

A FIRST-PRINCIPLES, TIGHT-BINDING AND COHERENT POTENTIAL STUDY  
OF 1-1 TYPE IRON-BASED SUPERCONDUCTOR  $\text{FeSe}_x\text{Te}_{1-x}$

by

Alexander P. Koufos  
A Dissertation  
Submitted to the  
Graduate Faculty  
of  
George Mason University  
In Partial Fulfillment of  
the Requirements for the Degree  
of  
Doctor of Philosophy  
Computational Sciences and Informatics

Committee:

---

Dr. Dimitrios A. Papaconstantopoulos,  
Dissertation Director

---

Dr. Howard Sheng, Committee Member

---

Dr. Estela Blaisten-Barojas, Committee  
Member

---

Dr. Maria Emelianenko, Committee Member

---

Dr. Chi Yang, Interim Director, School of  
Physics, Astronomy, and Computational  
Sciences

---

Dr. Donna M. Fox, Associate Dean, Office  
of Student Affairs & Special Programs,  
College of Science

---

Dr. Peggy Agouris, Dean, College  
of Science

Date: \_\_\_\_\_

Fall Semester 2014  
George Mason University  
Fairfax, VA

A First-Principles, Tight-Binding and Coherent Potential Study of 1-1 Type Iron-based  
Superconductor  $\text{FeSe}_x\text{Te}_{1-x}$

A dissertation submitted in partial fulfillment of the requirements for the degree of  
Doctor of Philosophy at George Mason University

By

Alexander P. Koufos  
Master of Science  
George Mason University, 2011  
Bachelor of Science  
George Mason University, 2008

Director: Dr. Dimitrios A. Papaconstantopoulos, Professor  
Department of School of Physics, Astronomy, and Computational Sciences (SPACS)

Fall Semester 2014  
George Mason University  
Fairfax, VA

Copyright © 2014 by Alexander P. Koufos  
All Rights Reserved

## **Dedication**

I would like to dedicate this dissertation to my role model, Peter Parker. You are everything I wish I could be.

## Acknowledgments

I would like to thank my committee: Dr. Dimitrios Papaconstantopoulos, my chair; Dr. Estela Blaisten-Barojas; Dr. Howard Sheng; and Dr. Maria Emelianenko. You have my sincere appreciation for all the knowledge, time and effort you put into me, my research and my studies. Dr. Papa, thank you for supporting me financially, academically and professionally for the past six years; now you can finally retire. In all sincerity, your guidance has been priceless. I honestly would not have accomplished this without you.

Dr. Michael Mehl, thank you for helping me to better understand space groups, crystal structures, and other general knowledge used in the field. Also, thank you for your help with my second publication.

I would also like to thank Dr. Michelle Johannes for sharing your expertise regarding the Wien2k code. The time you took to show me how to use the code helped immensely with this project. Without your insight, the calculations in this dissertation would have been much more limited.

A huge thank you to all my professors throughout my time at GMU. Your knowledge of physics, math and computational sciences, and your passions for teaching helped forge my understanding of the topics. I specifically wanted to thank Dr. Phil Rubin, for your mentorship and for everything you've done for me in the past. I greatly appreciate all the opportunities you have given me. Your guidance and those opportunities were extremely important in deciding to pursue this PhD. I can't thank you enough for all of it.

Thank you to my family for always being there for support, helping where you could, and providing me with the foundation that got me to this point. Without you, I would not have reached this milestone. Thank you for everything you have done for me in the past, present and future.

Finally, I would like to thank my friends for listening and helping solve problems associated with this dissertation. You have been there when I needed you and made sure I had a life outside of work. I specifically would like to thank Shea Hess Webber for all your help and support. You assisted with reading through my many edits and took time out of your own research to help. I greatly appreciate how helpful all of these acts were to finishing this work on time. Also, Cory, your psychomagick will always be invaluable.

## Table of Contents

	Page
List of Tables . . . . .	viii
List of Figures . . . . .	xi
Abstract . . . . .	xv
1 Introduction . . . . .	1
2 APW/LAPW - Preliminaries . . . . .	4
2.1 First-Principles Theory . . . . .	4
2.1.1 Applied Density Functional Theory . . . . .	4
2.1.2 Local Density and Generalized Gradient Approximations . . . . .	5
2.1.3 Additional Approximations . . . . .	6
2.1.4 Wave Function Expansions and Augmented Plane Wave Methods . .	7
2.1.5 Total Energy . . . . .	8
2.1.6 Elastic Constants . . . . .	9
2.1.7 Density of States . . . . .	10
2.2 Preliminary Calculations - Alkali Metals . . . . .	12
2.2.1 Introduction . . . . .	12
2.2.2 Computational Details of Alkali Metal Calculations . . . . .	12
2.2.3 Total Energy Calculations of the Alkali Metals . . . . .	13
2.2.4 Band Structure Calculations of Francium . . . . .	17
2.3 Preliminary Calculations - Inert Gas Solids . . . . .	24
2.3.1 Introduction . . . . .	24
2.3.2 Computational Details . . . . .	24
2.3.3 Total Energy Calculations . . . . .	25
2.3.4 Energy Band Calculations of the Inert Gases . . . . .	28
2.3.5 Insulator to Metal Transitions of the Inert Gases . . . . .	30
2.4 Conclusions of Preliminary Results . . . . .	36
3 FeSeTe . . . . .	37
3.1 Electronic Structure of Iron-Selenium . . . . .	37
3.1.1 Introduction . . . . .	37

3.1.2	Computational details . . . . .	37
3.1.3	Iron-Selenium total energy calculations . . . . .	38
3.1.4	DOS and energy band calculations of FeSe . . . . .	41
3.2	Electronic Structure of Iron-Tellurium . . . . .	47
3.2.1	Introduction . . . . .	47
3.2.2	Computational Details . . . . .	47
3.2.3	Total Energy Calculations . . . . .	47
3.2.4	Band Structure Calculations . . . . .	48
3.2.5	Energy Band Calculations . . . . .	51
3.3	Electronic Structure of $\text{FeSe}_x\text{Te}_{1-x}$ . . . . .	53
3.3.1	Introduction . . . . .	53
3.3.2	Computational Details . . . . .	53
3.3.3	Band Structure Calculations . . . . .	54
3.4	A Virtual Crystal Approach . . . . .	58
3.5	Final Conclusions . . . . .	61
4	Superconductivity . . . . .	63
4.0.1	Introduction . . . . .	63
4.1	Gaspari-Gyorffy-McMillan Theories of Superconductivity . . . . .	63
4.2	Superconductivity of the Iron-Selenium-Tellurium System . . . . .	66
4.2.1	Superconductivity of FeSe . . . . .	66
4.2.2	Superconductivity of Iron-Tellurium . . . . .	71
4.2.3	FeSeTe GGM Calculations . . . . .	73
4.2.4	Final Remarks on Superconductivity . . . . .	76
5	Tight-Binding . . . . .	77
5.1	Tight-Binding Methodology . . . . .	77
5.1.1	Tight-Binding Basics . . . . .	77
5.1.2	NRL Implementation of the TB Method . . . . .	79
5.2	Tight-binding Fits of FeSe and FeTe . . . . .	82
5.2.1	Introduction . . . . .	82
5.2.2	Computational Details . . . . .	84
5.2.3	Using the Fitted TB Parameters . . . . .	86
5.2.4	Conclusions . . . . .	95
6	VCA/CPA . . . . .	98
6.1	Virtual Crystal Approximation . . . . .	98
6.2	$\text{FeSe}_x\text{Te}_{1-x}$ with the Tight-Binding Virtual Crystal Approximation . . . . .	99

6.3	Coherent Potential Approximation . . . . .	102
6.4	Developed Code Discussion . . . . .	104
6.5	Coherent Potential Approximation of $\text{FeSe}_x\text{Te}_{1-x}$ . . . . .	106
6.5.1	Results of the TB-CPA . . . . .	106
6.6	Concluding Remarks . . . . .	111
7	Conclusions . . . . .	112
7.1	Summary . . . . .	112
7.2	Future Work . . . . .	113
A	Electronic Structure - Fr . . . . .	114
B	Electronic Structure - FeSe . . . . .	122
C	CPA Code . . . . .	127
	Bibliography . . . . .	174

## List of Tables

Table	Page
2.1 Calculated and experimental structural parameters of the Alkali metal. Calculations were performed using the LAPW method with LDA and GGA functionals. Experimental values were taken from Kittel[23]. . . . .	14
2.2 The total and decomposed DOS at the Fermi level for bcc cesium and bcc francium using LAPW with GGA functional at zero pressure. . . . .	19
2.3 Total energy and related results for francium with LDA functional with spin-orbit interaction. . . . .	21
2.4 Total and decomposed DOS at $E_F$ for bcc francium using LAPW with LDA functional, both with and without spin-orbit interaction . . . . .	22
2.5 Spin-orbit splitting and energies at high symmetry k-points of bcc francium at equilibrium . . . . .	23
2.6 Total energy and related results for the inert gases Ne, Ar, Kr, Xe, and Rn using the LAPW with LDA functional with experimental results[23]. . . .	26
2.7 Percent difference between calculated and experimental lattice parameters using LAPW with LDA and GGA functionals of inert gases (Ne, Ar, Kr, and Xe) . . . . .	27
2.8 Calculated and experimental pressures for the insulator to metal transition of the noble gases ( $GPa$ ) . . . . .	30
3.1 Structural parameters ( $V$ , $a$ , $c/a$ , $z$ ) and bulk mouduli ( $B$ ) of FeSe, both computational and experimental[44, 45]. . . . .	39
3.2 Structural parameters ( $V$ , $a$ , $c/a$ , $z$ ) and bulk mouduli ( $B$ ) of FeSe using the local density approximation and local spin density approximation (LSDA)..	41
3.3 Total and decomposed DOS of FeSe at the Fermi level, for both NRL-LAPW and Wien2k codes. Decomposed values do not add up to the total DOS due to the use of muffin-tin spheres. (Note: Wien2k does not calculate the $f$ DOS states.) . . . . .	43

3.4	Structural parameters ( $V$ , $a$ , $c/a$ , $z$ ) and bulk mouduli ( $B$ ) of FeTe, both computational and experimental[59, 60]. . . . .	48
3.5	Total and decomposed DOS of FeTe at the Fermi level, for both NRL-LAPW and Wien2k codes. Decomposed values do not add up to the total DOS due to the use of muffin-tin spheres. . . . .	50
3.6	Experimental structural parameters ( $V$ , $a$ , $c/a$ , $z$ ) used for LAPW calculations of FeSe, FeTe, $\text{FeSe}_{0.25}\text{Te}_{0.75}$ , $\text{FeSe}_{0.75}\text{Te}_{0.25}$ , and $\text{FeSe}_{0.50}\text{Te}_{0.50}$ systems. . . . .	55
3.7	Total and decomposed DOS at the Fermi level for $\text{FeSe}_x\text{Te}_{1-x}$ using the Wien2k code (NRL-LAPW $\text{FeSe}_{0.50}\text{Te}_{0.50}$ is provided as well.) Decomposed values do not add up to the total DOS due to the use of muffin-tin spheres. Values are represented based on the entire unit cell size (8 atoms for $x = 0.5$ and 16 atoms for $x = 0.25/0.75$ . . . . .	57
4.1	Total and decomposed DOS of FeSe at the Fermi level for two muffin-tin radii. Once again the decomposed values do not add up to the total DOS due to the use of muffin-tin spheres. . . . .	67
4.2	Superconductivity related parameters (Hopfield parameters ( $\eta$ ), electron-phonon coupling constants ( $\lambda$ ) and critical superconductivity temperature ( $T_c$ )) of FeSe using the GGM theory with NRL-LAPW code for two muffin-tin radii. A Debye temperature of 240K[45] and $\mu^* = 0.10$ were used for both sets of calculations. . . . .	69
4.3	Total DOS at $E_F$ , $N(E_F)$ , Hopfield parameters, $\eta$ , electron-phonon coupling constants, $\lambda$ , Debye temperature, $\Theta_D$ , Coulomb psuedopotential, $\mu^*$ , and critical superconductivity temperature, $T_c$ of FeSe at various volumes, corresponding to pressures as high as 8GPa. Values are calculated using a fixed $c/a$ and $z$ taken from experimental parameters ( $c/a=1.4656$ and $z=0.260$ ). Debye temperature is taken from equation (4.10). . . . .	70
4.4	Total DOS at $E_F$ , $N(E_F)$ , Hopfield parameters, $\eta$ , electron-phonon coupling constants, $\lambda$ , Debye temperature, $\Theta_D$ , Coulomb psuedopotential, $\mu^*$ , and critical superconductivity temperature, $T_c$ of FeTe under ambient conditions. Experimental values are calculated using a fixed $c/a$ and $z$ taken from experimental parameters ( $c/a=1.6406$ and $z=0.250$ ). . . . .	72

4.5	Superconductivity related parameters (Hopfield parameters ( $\eta$ ), electron-phonon coupling constants ( $\lambda$ ), specific heat ( $\gamma$ ), Debye temperature ( $\Theta_D$ ), and critical superconductivity temperature ( $T_c$ ) of FeSe, FeTe, and $\text{FeSe}_{0.50}\text{Te}_{0.50}$ systems using the GGM theory with NRL-LAPW code. . . . .	73
4.6	Calculated DOS and superconductivity related results of LaFeAsO using LAPW with LDA functional. Experimental critical temperature result is taken from Takahashi et. al[71] . . . . .	75
4.7	Superconductivity related parameters (total DOS at Fermi level ( $N(E_F)$ )), Hopfield parameters ( $\eta$ ), electron-phonon coupling constants ( $\lambda$ ), Debye temperature ( $\Theta_D$ ) and superconductivity temperature ( $T_c$ ) of $\text{FeAs}_{0.50}\text{Se}_{0.50}$ using the GG theory with NRL-LAPW code. The first row represents the direct LAPW VCA method, while the second is the averaged potential VCA method.	75
5.1	Tight-binding coefficients for the total energy-based FeSe fit. . . . .	88
5.2	Tight-binding coefficients for the total energy-based FeTe fit. . . . .	90
5.3	Final SK TB on-site and "hopping" parameters for the DOS-based FeSe fit.	96
5.4	Final SK TB on-site and "hopping" parameters for the DOS-based FeTe fit.	97
6.1	Total, Fe- <i>d</i> , Se- <i>p</i> and Te- <i>p</i> decomposed DOS of $\text{FeSe}_x\text{Te}_{1-x}$ at the Fermi level using the TB-CPA. . . . .	110

## List of Figures

Figure	Page
2.1 Calculated structural lattice parameters and bulk moduli of the bcc alkali metals using the LAPW with GGA functional. . . . .	16
2.2 Calculated total energy curves of Fr using the LAPW with GGA functional. Notice the hcp structure is calculated to have a lower total energy than the fcc structure by 0.05 $mRy$ at equilibrium. . . . .	17
2.3 Enthalpy calculations of Fr using the LAPW with GGA functional. A structural transition from hcp to bcc occurs at small pressure. . . . .	18
2.4 Density of States of bcc (a) Cs and (b) Fr using the LAPW method with GGA functional. Fermi level is given by the vertical line, given at zero. . . .	20
2.5 Total and $s, d$ -components of the DOS vs. pressure of francium at $E_F$ , using the GGA functional with no spin-orbit interaction. The $l$ -components of the DOS are normalized with respect to the equilibrium MT radius, $R_{eq}/R$ , to correct for the fact that we are using touching spheres. The hcp structure is given by a dashed (blue) line, and the bcc structure as a solid (red) line.	20
2.6 Energy bands of bcc Fr (a) under ambient conditions and (b) at 14 $GPa$ . Fermi level is given by the horizontal line, given at zero. . . . .	23
2.7 Total energy of radon using the LAPW method with LDA functional. Notice the total energy predicts the fcc structure to be less energy than the bcc and hcp. . . . .	27
2.8 The total and decomposed DOS of (a)Ne, (b)Ar, (c)Kr, (d)Xe, and (e)Rn at ambient pressure. . . . .	29
2.9 The energy bands of (a)Ne, (b)Ar, (c)Kr, (d)Xe, and (e)Rn under ambient conditions. . . . .	31
2.10 Energy bands of Ar at equilibrium and at the insulator to metal transition pressure. . . . .	33
2.11 Energy bands of Kr at equilibrium and at the insulator to metal transition pressure. . . . .	33

2.12	Energy bands of Xe at equilibrium and at the insulator to metal transition pressure. . . . .	34
2.13	Energy bands of Rn at equilibrium and at the insulator to metal transition pressure. . . . .	34
2.14	Band gap closure of the inert gases vs. pressure. Energy gap is calculated from the difference between $\Gamma_{15}$ and $X_1$ . Insulator to metal transitions occur at 513 $GPa$ , 392 $GPa$ , 147 $GPa$ , and 103 $GPa$ for Ar, Kr, Xe, and Rn, respectively. . . . .	35
3.1	Ground state structure of FeSe, <i>Strukturbereicht</i> designation B10. The space group is P4/nmm-D <sub>4d</sub> <sup>7</sup> (#129). The iron atoms are on (2a) Wyckoff sites, while the selenium atoms are on (2c) sites. . . . .	38
3.2	LAPW total energy plots of FeSe from the optimized LDA and GGA calculations. The LDA and GGA straddle the measured volume from Kumar, et. al.[44] . . . . .	40
3.3	Density of States of tetragonal (PbO-like) FeSe (a) using NRL-LAPW results and (b) using the Wien2k results. Fermi level is given by the dashed vertical line, given at zero. . . . .	42
3.4	Comparison of the calculated Density of States of FeSe using NRL-LAPW with Lorentzian broadening and the photoemission spectrum from Yamasaki, et., al.[42] . . . . .	44
3.5	Band structures of tetragonal (PbO-like) FeSe using NRL-LAPW results. Zoomed in section of the Fermi surface is given in (b). Fermi level is given at 0.0Ry. . . . .	45
3.6	Calculated (a) 2-D and (b) 3-D Fermi surface of tetragonal (PbO-like) FeSe using Wien2k and XCrysDen programs. . . . .	46
3.7	Total energy plots of the optimized LDA calculations of FeTe. The LDA underestimates the measured volume from Finlayson et. al.[59] . . . . .	49
3.8	Density of States of tetragonal (PbO-like) FeTe using (a) NRL-LAPW results and (b) Wien2k results. Fermi level is given by the dashed vertical line at 0.0Ry. . . . .	49
3.9	Calculated Density of States of FeTe using NRL-LAPW with Lorentzian broadening. These figures represent a prediction to experimental measurements of the photoemission spectrum of FeTe. . . . .	52

3.10	Band structures of tetragonal (PbO-like) FeTe using NRL-LAPW results. Zoomed in section of the Fermi surface is given in (b). Fermi level is given at 0.0Ry. . . . .	52
3.11	Density of States of tetragonal (PbO-like) (a) $\text{FeSe}_{0.50}\text{Te}_{0.50}$ using NRL-LAPW results, (b) $\text{FeSe}_{0.50}\text{Te}_{0.50}$ using the Wien2k results, (c) $\text{FeSe}_{0.25}\text{Te}_{0.75}$ using Wien2k and (d) $\text{FeSe}_{0.75}\text{Te}_{0.25}$ using Wien2k. . . . .	56
3.12	Band structures of tetragonal (PbO-like) $\text{FeSe}_{0.5}\text{Te}_{0.5}$ using NRL-LAPW results. Zoomed in section of the Fermi surface is given in (b). Fermi level is given at 0.0Ry. . . . .	58
3.13	Density of States with Virtual Crystal Approximation potentials of (a) $\text{FeSe}_{0.15}\text{Te}_{0.85}$ and (b) $\text{FeSe}_{0.50}\text{Te}_{0.50}$ . Potentials of FeSe and FeTe using NRL-LAPW code were averaged to perform the DOS calculations. . . . .	60
3.14	Density of States of $\text{FeAs}_{0.50}\text{Se}_{0.50}$ with virtual crystal approximation applied via (a) potential averaging and (b) virtual atom approach. Potentials of FeAs and FeSe using NRL-LAPW code were averaged to perform the DOS calculations of (a). For (b), self-consistent calculations were performed using same input parameters, but with an averaged atomic number for As/Se, 33.5, and averaged valence electrons, 27. . . . .	60
4.1	Density of States of tetragonal (PbO-like) FeSe using NRL-LAPW with (a) $r_{mt} = 2.0$ and (b) $r_{mt} = 2.2$ . Fermi level is given by the dashed vertical line, given at zero. . . . .	68
5.1	Total energy plots of the tetragonal PbO-like and hexagonal NiAs-like structures of FeSe using the Tight-Binding and LAPW results. The experimental volume is given by Kumar, et. al.[44]. . . . .	87
5.2	Total energy plots of the tetragonal PbO-like structure of FeTe using the Tight-Binding and LAPW results. Energy curves are based on the experimental $c/a$ and $z$ parameters. The experimental volume is given by Finlayson et. al.[59]. . . . .	89
5.3	Comparison of the total Density of States between NRL-LAPW (solid red) and NRL-TB (dashed green) of tetragonal (PbO-like) (a) FeSe and (b) FeTe. Fermi level is given at 0.0 Ry by the vertical dashed (blue) line. . . . .	91

5.4	Comparison of decomposed Density of States between NRL-LAPW (solid red) and NRL-TB (dashed green) of tetragonal (PbO-like) FeSe and FeTe. Comparison between Se- <i>p</i> states of FeSe are given in (a), Fe- <i>d</i> of FeSe are given in (b), Te- <i>p</i> states of FeTe are shown in (c), and Fe- <i>d</i> of FeTe are shown in (d). Fermi level is given at 0.0 <i>Ry</i> by the vertical dashed (blue) line. . . . .	92
5.5	Comparison of the energy bands between NRL-LAPW (solid red) and NRL-TB (dashed green) of tetragonal (PbO-like) (a) FeSe and (b) FeTe. Fermi level is given at 0.0 <i>Ry</i> by the horizontal solid (black) line. . . . .	93
6.1	Total and decomposed Density of States of $\text{FeSe}_x\text{Te}_{1-x}$ using the Virtual Crystal Approximation. Includes (a) $x = 0.0$ (FeTe) DOS, (b) $x = 0.1$ DOS, (c) $x = 0.2$ DOS, (d) $x = 0.3$ DOS, (e) $x = 0.4$ DOS, and (f) $x = 0.5$ DOS. . . . .	100
6.2	Total and decomposed Density of States of $\text{FeSe}_x\text{Te}_{1-x}$ using the Virtual Crystal Approximation. Includes (a) $x = 0.5$ DOS, (b) $x = 0.6$ DOS, (c) $x = 0.7$ DOS, (d) $x = 0.8$ DOS, (e) $x = 0.9$ DOS, and (f) $x = 1.0$ (FeSe) DOS	101
6.3	Total and decomposed Density of States of $\text{FeSe}_x\text{Te}_{1-x}$ using the Coherent Potential Approximation shifted by the calculated Fermi level. Includes (a) $x = 0.0$ (FeTe) DOS, (b) $x = 0.1$ DOS, (c) $x = 0.2$ DOS, (d) $x = 0.3$ DOS, (e) $x = 0.4$ DOS, and (f) $x = 0.5$ DOS. Fermi level ( $\varepsilon_F$ ) is given at 0.0 <i>Ry</i> by the vertical solid (blue) line. . . . .	107
6.4	Total and decomposed Density of States of $\text{FeSe}_x\text{Te}_{1-x}$ using the Coherent Potential Approximation shifted by the calculated Fermi level. Includes (a) $x = 0.5$ DOS, (b) $x = 0.6$ DOS, (c) $x = 0.7$ DOS, (d) $x = 0.8$ DOS, (e) $x = 0.9$ DOS, and (f) $x = 1.0$ (FeSe) DOS. Fermi level ( $\varepsilon_F$ ) is given at 0.0 <i>Ry</i> by the vertical solid (blue) line. . . . .	109
C.1	Coherent Potential Approximation subroutine flow chart. Level-1 subroutines that are called directly from the <b><i>mainn</i></b> subroutine are outlined in <b>red</b> . Level-2 subroutines called from any Level-1 program are outlined in <b>orange</b> . Similarly, Level-3 subroutines are outlined in <b>green</b> ; Level-4 subroutines in <b>blue</b> . The dashed lines indicate procedures that are called by more than one subroutine. . . . .	128

## Abstract

A FIRST-PRINCIPLES, TIGHT-BINDING AND COHERENT POTENTIAL STUDY OF  
1-1 TYPE IRON-BASED SUPERCONDUCTOR  $\text{FeSe}_x\text{Te}_{1-x}$

Alexander P. Koufos, PhD

George Mason University, 2014

Dissertation Director: Dr. Dimitrios A. Papaconstantopoulos

In this dissertation I performed first-principles calculations of the electronic structure for Iron-Selenium-Tellurium ( $\text{FeSeTe}$ ) systems and applied the results to study superconductivity in these materials. This dissertation discusses new first-principles calculations based on the Linearized Augmented Plane Wave (LAPW) method of Density Functional Theory (DFT) used in the Gaspari-Gyorffy-McMillan (GGM) theories of superconductivity. The LAPW results were also used to construct Tight-Binding (TB) Hamiltonians using the Naval Research Laboratory TB (NRL-TB) method. The code was expanded to include angular momentum contribution to the fits, to improve total and decomposed Density of States (DOS). Final fits for FeSe and FeTe showed total energy and total DOS calculations to compare well with the LAPW results up to the eighteenth band. These fits were further used to develop a computer program to treat disorder effects via the Coherent Potential Approximation (CPA) to the TB method. The new code incorporated diagonal disorder in the CPA and combined with the Virtual Crystal Approximation to study various concentrations of  $\text{FeSe}_x\text{Te}_{1-x}$ , where random substitutions of Se by Te were taken into account. Calculated DOS results with the CPA show similar features to the calculated LAPW DOS of  $\text{FeSe}_{0.50}\text{Te}_{0.50}$  by a supercell approach.

The results presented show that the GGM theories based on LAPW results can find good agreement with experimentally measured superconductivity temperatures,  $T_c$ . Specifically, we calculate  $T_c$ 's of 5.4  $K$  and 14.5  $K$  for FeSe and  $\text{FeSe}_{0.50}\text{Te}_{0.50}$ , respectively. The corresponding calculated electron-phonon coupling constants,  $\lambda$ , are 0.64 and 0.97, respectively. This suggests that the electron-phonon coupling interaction of the Bardeen-Cooper-Schrieffer (BCS) theory is an important mechanism in the superconductivity of these materials.

## Chapter 1: Introduction

In the field of computational materials science, a prime objective is to perform modeling and simulations via first-principles calculations. Such calculations are based on the principles of quantum mechanics and are performed using numerical and computational techniques of the Density Functional Theory (DFT), for which its main inventor Walter Kohn received the Nobel prize in Quantum Chemistry in 1998. DFT reduces an insoluble many-body problem to a tractable one-electron theory, based on the discovery that the total energy of an electron system is a functional of its electronic charge density. In the early 20th century Niels Bohr proposed his empirical model to explain the discrete energy levels of the hydrogen ( $H$ ) atom. Subsequently, the introduction of the Schrödinger equation led to the realization, that with the exception of the  $H$  atom, this equation can only be solved with numerical methods.

Schrödinger's equation can be treated as a system of linear equations by expanding the wave functions. This allows us to solve Schrödinger's equation with numerical band structure techniques. Two such techniques are used in this dissertation. The first is the Linearized Augmented Plane Wave (LAPW) method, which is a DFT-based all-electron technique that expands the wave functions into augmented plane waves. This method is one of the most accurate methods for calculating band structures of materials. The Tight-Binding (TB) method is the second technique used in this dissertation. This method expands the wave functions into linear combinations of the atomic orbitals. TB uses first-principles results to fit parameters that describe these atomic orbitals. Band structure techniques also allow for the calculation of superconductivity properties of materials.

Bardeen, Cooper, and Schrieffer developed the first comprehensive theory of superconductivity in 1957, coined the BCS theory[1]. This theory states that electrons can form into Cooper pairs mediated by lattice vibrations. The interaction between the electrons

and lattice vibration is known as electron-phonon interactions. Their work won them the Nobel prize in physics in 1972, for successfully describing all known superconductivity. In 1986, what are now known as high-temperature superconductors were discovered[2]. These materials can not be explained solely through electron-phonon interactions. Today computational methods based on the BCS theory, such as the Gaspari-Gyorffy-McMillan (GGM) theories of superconductivity, are used to understand superconductivity of most materials.

This dissertation discusses new contributions to computing the electronic structure of superconductors. Specifically, we performed first-principles, TB and Coherent Potential Approximation (CPA) calculations of the 1-1 type Fe-based superconductor,  $\text{FeSe}_x\text{Te}_{1-x}$ . I developed code based on the CPA, using the TB parameters to study a range of concentrations for this superconductor. First-principles calculations were performed using DFT with the LAPW method. The TB method was done using the Naval Research Laboratory implementation[3].

$\text{FeSeTe}$  has been studied previously by others[4–6] using first-principles methods. These studies suggest that the electron-phonon coupling mechanism of the BCS theory is inadequate in describing the superconductivity of this material. All previous work used linear-response methods to calculate the electron-phonon coupling. In this dissertation, I show that the coupling calculations based on the GGM theories of superconductivity find good agreement with experimental results for  $\text{FeSe}$  and  $\text{FeSe}_{0.5}\text{Te}_{0.5}$  under ambient conditions. As opposed to previous results, my calculations suggest that the electron-phonon coupling mechanism of the BCS theory is important in these materials.

Furthermore, this work provides the first TB parameters for the  $\text{FeSe}$  and  $\text{FeTe}$  systems. The fitted parameters are able to reproduce total energies and total DOS comparable to the first-principles results. Using these TB parameters, the virtual crystal approximation (VCA) and CPA were applied using code that I developed for this work. The diagonal disorder CPA calculations provide comparable results to the various first-principles supercell calculations of  $\text{FeSe}_x\text{Te}_{1-x}$ , where  $x = 0.75, 0.50$ , and  $0.25$ .

In Chapter 2, I discuss my previous research, showing that the GGM and general electronic structure calculations predict expected results for the alkali metals and inert gases. In Chapter 3, I discuss the general first-principles calculations and results of FeSe, FeTe and several concentrations of  $\text{FeSe}_x\text{Te}_{1-x}$ . Chapter 4 is an extension into the superconductivity first-principles calculations, specifically. Chapter 5 discusses the TB method and its results for FeSe and FeTe. Finally, I discuss the CPA as applied to my TB results, and compare to our first-principles calculations in Chapter 6.

## Chapter 2: Augmented Plane Wave Theories and Preliminary Work

### 2.1 First-Principles Theory

#### 2.1.1 Applied Density Functional Theory

Schrödinger's equation, given by equation (2.1), is the basis of all first-principles calculations for the properties of materials.

$$H\psi(r) = [-\nabla_i^2 + V(r)]\psi_i(r) = \varepsilon\psi(r) \quad (2.1)$$

$H$  is the Hamiltonian,  $\psi$  is the wave function,  $V(r)$  is a potential function with respect to distance  $r$ , and  $\varepsilon$  is eigenenergy. All first-principles calculations for this paper were based on the Density Functional Theory (DFT). The theory was developed by Kohn, *et. al.*[7] to include total energy in first-principles calculations. The method has two main criteria. First, the total energy,  $E$ , is given as a function of electronic density,  $\rho$ . Secondly, the ground state density minimizes  $E(\rho)$ . Here,  $\rho$  is the electronic density given by  $\rho = \sum \psi^* \psi$ . The electronic density is also coupled with a form of Poisson's equation

$$\nabla^2 V_c(r) = -8\pi\rho(r), \quad (2.2)$$

where  $V_c$  is the Coulomb potential. An exchange-and-correlation term is added to obtain the total potential of the system,  $V(r) = V_c(r) + V_{xc}(r)$ , which appears in equation (2.1). The evaluation of  $V_{xc}(r)$  is discussed in the next section. In DFT, the full total energy expression is given by

$$E(\rho) = E_H(\rho) + E_{xc}(\rho), \quad (2.3)$$

where

$$E_H(\rho) = E_k(\rho) + E_{e-e}(\rho) + E_{n-e} + E_{n-n}(\rho). \quad (2.4)$$

Here  $E_H$  is the Hartree energy,  $E_k$  is the kinetic energy of the system,  $E_{e-e}$  is the coulomb interaction,  $E_{n-e}$  is the interaction between electrons and nuclei and  $E_{n-n}$  is the interactions between nuclei. The  $E_{xc}$  in equation (2.3) is related to the  $V_{xc}$  potential by  $V_{xc}(r) = \frac{\partial E_{xc}(\rho)}{\partial \rho}$ .  $V_{xc}$  and  $E_{xc}$  are the exchange-and-correlation potential and energy, respectively, and are given by an energy equation that is determined by approximations such as those described in the following section.

### 2.1.2 Local Density and Generalized Gradient Approximations

There are many approximations one can use to calculate the exchange-and-correlation components. This research focuses on two such approximations, Local Density Approximation (LDA) and Generalized Gradient Approximation (GGA). Both approximations are a function of the electronic density, but the GGA is also a function of its gradient. The exchange-and-correlation energy equations for LDA and GGA approximations, respectively, are given by

$$E_{xc}^{LDA}(\rho) = \int d^3r \rho(r) \epsilon_{xc}(\rho(r)) \quad (2.5)$$

$$E_{xc}^{GGA}(\rho) = \int \rho(r) \epsilon_{xc}^{GGA}(\rho(r), |\nabla \rho(r)|, \nabla^2(\rho(r))) d^3r, \quad (2.6)$$

where  $\epsilon_{xc}$  is the exchange-and-correlation energy per particle.

One of the first exchange potentials developed was known as the  $X_\alpha$  method[8]. This “exchange” potential is given by

$$V_{ex}(r) = \alpha \left( \frac{3\rho(r)}{8\pi} \right)^{1/3} = \alpha U_{ex}(r), \quad (2.7)$$

where  $\alpha$  is usually varied between 2/3 and 1 to match the Hartree-Fock total energy for the atom,  $U_{ex}$ . Hedin and Lundqvist[9] improved upon this potential by adding a “correlation” term. This formalism of the LDA exchange-and-correlation potential is given by

$$V_{xc}(r) = \alpha\beta(r_s)U_{ex}(r), \quad (2.8)$$

where  $\alpha = 2/3$  is the Kohn-Sham parameter and  $\beta$  is the correlation enhancement factor

$$\beta(r_s) = 1 + B \ln\left(1 + \frac{1}{x}\right). \quad (2.9)$$

Here,  $r_s = (3/4\pi\rho(r))^{1/3}$ ,  $x = r_s/21$  and  $B = 0.7734$ .

### 2.1.3 Additional Approximations

Another approximation that was used, in conjunction with LDA or GGA, is the Born-Oppenheimer approximation[10]. This approximation considers the nuclei to have zero velocity, in other words they are frozen at the locations they would occupy in a crystal at  $T = 0$  K. The approximation applies since the mass of the electron is approximately 1/2000<sup>th</sup> the mass of a proton. Thus, electrons have little influence on the overall location of the nuclei in the systems. This allows for the separation of solving the electronic motion and nuclei motion. For elements heavier than the 3d transition metals, the Hamiltonian must include relativistic components, as well as the traditional non-relativistic Hamiltonian. This relativistic Hamiltonian is

$$H = H_{NR} - \frac{p^4}{8m^3c^2} + \frac{\hbar^2}{8m^2c^2}\nabla^2V + \frac{\hbar^2}{4m^2c^2r}\frac{1}{r}\frac{dV}{dr}(\boldsymbol{\sigma} \cdot \mathbf{L}), \quad (2.10)$$

where the first term,  $H_{NR}$ , is the non-relativistic Hamiltonian, the second term,  $\frac{p^4}{8m^3c^2}$ , accounts for the relativistic effects on the kinetic energy and is known as the mass-velocity term, the third term,  $\frac{\hbar^2}{8m^2c^2}\nabla^2V$ , is called the Darwin term and corrects for the centrifugal

potential, and the last term,  $\frac{\hbar^2}{4m^2c^2r} \frac{1}{r} \frac{dV}{dr} (\sigma \cdot L)$ , represents spin-orbit coupling. For some systems, the spin-orbiting effects can be ignored, if they have little influence on the occupied states. For example, spin-orbit effects are negligible for the alkali metals[11]. In this work we have also neglected spin-orbit interactions as having small effect on the Density of States.

#### 2.1.4 Wave Function Expansions and Augmented Plane Wave Methods

Solving equation (2.1) requires the use of wave functions, which can be approximated through various polynomial expansions. One such expansion is used in the Augmented Plane Wave (APW) method, which was proposed by Slater in 1937[8, 12]. This method, when proposed in conjunction with the Muffin-Tin Approximation (MTA), is called the MT-APW method. The MT-APW method considers that each atomic site is surrounded by a sphere, or “muffin-tin”. The muffin-tins are touching-spheres of radius  $r_{mt}$ . Inside these spheres we expand the wave functions in a spherically symmetric form,

$$\psi_{mt}(r) = \sum_{lm} A_{lm} Y_{lm}(r) u_l(r, \epsilon), \quad r \leq r_{mt}, \quad (2.11)$$

where  $Y_{lm}$  are the spherical harmonics and  $A_{lm}$  coefficients are determined by “augmented” boundary conditions. These boundary conditions make the wave functions inside the muffin-tin spheres continuous with the plane wave functions in the interstitial region,

$$\psi_{interstitial}(r) = e^{i(G+k) \cdot r}, \quad r \geq r_{mt}, \quad (2.12)$$

where  $G$  is the reciprocal lattice vector. The  $u_l$  in equation (2.11) is the radial wave function and is solved by the radial equation at each k-point in the Brillouin zone,

$$-\frac{1}{2r^2} \frac{d}{dr} \left( 2r^2 \frac{du_l(r)}{dr} \right) + \left[ \frac{l(l+1)}{r^2} + V(r) - \epsilon_l \right] u_l(r) = 0. \quad (2.13)$$

The potential inside the muffin-tin is also a spherically symmetric function  $V(|r - r_{mt}|)$ , while the potential outside is a constant,  $V_c$ . The MTA leads to very accurate results in close-packed structures such as fcc, bcc and hcp, where the packing ratio of the spheres is high.

A similar method, the Linearized Augmented Plane Wave (LAPW) method[13], removes the MTA and uses a general potential that is not spherically symmetric inside the spheres and not constant outside. Also, the LAPW method linearizes equation (2.11) by adding an additional energy derivative, such that equation (2.11) becomes

$$\psi_{mt}(r) = \sum_{lm} [A_{lm}u_l(r, \epsilon) + B_{lm}\dot{u}_l(r, \epsilon)]Y_{lm}(r), \quad r \leq r_{mt}. \quad (2.14)$$

The  $\dot{u}_l(r, \epsilon)$  in equation (2.14) is the energy derivative of the radial wave function, and  $A_{lm}$  and  $B_{lm}$  are determined by requiring that equation (2.14) equals equation (2.12) at  $r = r_{mt}$ . Furthermore, the radial equation (2.13) becomes

$$\left[ -\frac{d^2}{dr^2} + \frac{l(l+1)}{r^2} + V(r) - \epsilon_l \right] r\dot{u}_l(r) = r\dot{u}_l(r). \quad (2.15)$$

These methods allow scientists to calculate values of total energy, Density of States, energy bands, phonon frequencies, specific heat, elastic constants, and many more electronic and mechanical properties. These results usually compare very well with experimental results.

### 2.1.5 Total Energy

The APW/LAPW converged electronic densities, in conjunction with equation (2.3), determine the total energy of a system for a given volume. This is performed with calculations for multiple volumes using one of the DFT methods discussed above. An expansion of the

total energy is done via the Birch-fit formula[14],

$$E(V) = \sum_i^n a_i V^{2i/3}, \quad (2.16)$$

where  $a_i$  are the expansion coefficients and  $n$  is the order of the fit. Equation (2.17) provides the expanded version of equation (2.16) to third order.

$$E = E_0 + \frac{9}{8} B_0 V_0 \left[ \left( \frac{V_0}{V}^{2/3} \right) - 1 \right]^2 + \frac{9}{16} B_0 V_0 (B'_0 - 4) \left[ \left( \frac{V_0}{V}^{4/3} \right) - 1 \right]^3 \quad (2.17)$$

$E_0$  is the equilibrium energy,  $V_0$  is the equilibrium volume,  $B_0$  is the equilibrium bulk modulus and  $B'_0$  is the pressure derivative of the bulk modulus. Third order expansions are sufficient for most systems. However, second order expansions are often found to accurately give the lattice parameter at equilibrium. In some cases, higher order expansions are necessary. The bulk modulus is represented by the second derivative of the energy with respect to volume, given by

$$B = -V \frac{d^2 E}{dV^2}, \quad (2.18)$$

### 2.1.6 Elastic Constants

The calculations of elastic constants can be complicated and are explained by Mehl, *et al.*[15]. The description of cubic based elastic constant calculations are explained in some detail. For cubic systems, the overall symmetry reduces the elastic constant matrix,  $C_{ij}$ , to three independent components,  $C_{11}$ ,  $C_{12}$ , and  $C_{44}$ . With an orthorhombic strain,  $e$ , applied to the cubic structure, the energy becomes strained and can be expressed by

$$E = E_0 + V(C_{11} - C_{12})e^2, \quad (2.19)$$

where  $E_0$  is the undistorted energy and  $V$  is a fixed volume for the unit cell. Since the distorted energy has a linear dependence on the squared strain, the slope of the function is the  $C_{11} - C_{12}$  relation. Similarly,  $C_{44}$  can be found through another linear relation, applying a monoclinic strain

$$E = E_0 + \frac{1}{2}VC_{44}e^2. \quad (2.20)$$

Furthermore, the bulk modulus is related to the  $C_{11}$  and  $C_{12}$  elastic constants by

$$B = \frac{1}{3}(C_{11} + 2C_{12}). \quad (2.21)$$

A structure is mechanically stable if the following criteria are met:

$$B = \frac{1}{3}(C_{11} + 2C_{12}) > 0$$

$$C_{11} - C_{12} > 0$$

$$C_{44} > 0.$$

### 2.1.7 Density of States

The Density of States (DOS) is defined as the number of states per unit of energy. Determining the DOS requires the interpolation of first-principles results in k-space. One way to calculate the DOS is the tetrahedron method[16], in which the eigenvalues are interpolated linearly between four k-points placed on tetrahedron vertices. The eigenvalues are given by

$$\epsilon(\vec{k}) = \epsilon_0 + \vec{b} \cdot (\vec{k} - \vec{k}_0), \quad (2.22)$$

where  $\epsilon_0$  and  $\vec{b}$  are determined by the energies at the vertices. This method was used in this research for calculations of the DOS in cubic structures.

Another general method used to calculate the DOS was employed for non-cubic system[3,

17]. This method is based on a Fermi-style smearing function

$$f(x) = \frac{1}{1 + e^{\beta x}} , \quad (2.23)$$

where  $\beta$  is  $1/T$ , such that  $T$  is the Fermi temperature. The first derivative with respect to  $x$  is given by,

$$f'(x) = -\beta e^{\beta x} f(x)^2 . \quad (2.24)$$

The DOS at a given Fermi energy,  $E_F$ , can then be calculated by the formula

$$N(E_F) = \int_{-\infty}^{E_F} \rho(e) de . \quad (2.25)$$

Here,  $\rho(e)$  is the electronic DOS at the energy,  $e$ . Thus,  $\rho(e)$  can be written as

$$\rho(e) = - \sum_{k=1}^{nk} w(k) \sum_{i=1}^{ne} f'(\epsilon(i, k) - E_F) . \quad (2.26)$$

These equations can be generalized to any energy value, not just the Fermi energy.

The calculated DOS at the Fermi level can then be used to calculate other parameters, such as the specific heat. This is expressed by

$$C = \gamma T + \alpha T , \quad (2.27)$$

where  $\gamma T$  represents the electronic contribution and  $\alpha T$  the phonon contribution.  $\gamma$  is known as the electronic specific heat coefficient and is proportional to the total DOS at the Fermi level

$$\gamma = 0.1734(1 + \lambda)N(E_F) , \quad (2.28)$$

where  $N(E_F)$  is expressed in units of states/Ry per atom for both spins,  $\gamma$  is in units

$\frac{mJ}{mol \deg^2}$ , and  $\lambda$  is the electron-phonon coupling constant. The DOS at the Fermi level can be further used with the electron-phonon coupling constant, to provide superconductivity properties based on the BCS[1] theory.

## 2.2 Preliminary Calculations - Electronic Structure of Francium and the Alkali Metals

### 2.2.1 Introduction

The Alkali metals are given as the first group in the periodic table and are lithium (Li), sodium (Na), potassium (K), rubidium (Rb), cesium (Cs) and francium (Fr). These materials all contain one electron in their valence shell. This electronic configuration makes them highly reactive in water. Fr is the rarest material on the planet, with less than 30 g found in the Earth's crust at any given time. Its longest half-life of all its isotopes is about 20 minutes and is very radioactive, making this material extremely hard to study experimentally. So far the only experimental study of Fr involved optical traps and was unable to measure any of the structural or electronic structure properties of the material[18].

In our previous work, we presented the first and only band structure calculation of Fr, while for the other alkali metals discussed within had previous theoretical studies[11]. Our calculations were performed using the LAPW with both LDA and GGA functionals. The alkali metals using the LDA functional were previously studied by Sigalas, *et. al.*[19, 20]. The Fr results were published in the International Journal of Quantum Chemistry[11] (see Appendix A).

### 2.2.2 Computational Details of Alkali Metal Calculations

The LAPW method with both LDA in Hedin-Lundqvist form and GGA of Perdew-Wang were used to study the electronic structure of Fr and the other alkali metals using the NRL-LAPW code[21, 22]. (This code was originally written by Krakauer and Singh and modified by Mehl.) All calculations were performed with one electron in the valence shell.

This means that the core states consisted of the electronic configuration of the inert gas before the alkali metal. For example, Na used four core states (equilibrium state of Ne.) Thus, Fr used 24 core states (equilibrium of radon) with one electron in the valence shell of the calculations. The muffin-tin radii were kept constant at a specific value for each individual element's total energy calculations. For band structure calculations, the muffin-tin radii were varied to allow touching muffin-tin spheres for each volume. The  $rk_{max}$  value (8.5), basis set size (5x5x5) and local orbital energies ( $-1.8\text{ Ry}$  for s and  $-0.5\text{ Ry}$  for p states) were kept constant for all calculations. A k-point mesh of 55 and 89 points in the irreducible Brillouin zone were used for the bcc and fcc calculations, respectively. For Fr, these meshes were increased up to 285 and 505 k-points for bcc and fcc, respectively to check for convergence. The hcp calculations of Fr required another k-point mesh of 32x32x16 per direction was used. Another set of total energy calculations were performed for Fr with 22 core states, seven valence electrons, the local orbitals and 6s and 6p states treated as bands to obtain very accurate total energy values. The fixed muffin-tin radius of 4.3 *a.u.* was used for the Fr total energy calculations.

### 2.2.3 Total Energy Calculations of the Alkali Metals

Total energy calculations were performed for the alkali metals using the LDA and GGA functionals. Calculations were performed for the bcc and fcc structure for the alkali metals, with additional hcp lattice structure based calculations for Fr. Table 2.1 shows the total energy, structural lattice parameters and bulk moduli of the alkali metals using the two functionals. The total energy is zeroed at the lowest calculated total energy of the two or three lattice structure types. Experimental results of lattice parameters and bulk moduli are also included for comparison. It is important to note that all the alkali metals are experimentally found to be in the bcc structure under equilibrium conditions. However, as shown in Table 2.1, these calculations (and those of other workers) with the exception of Li give fcc as the ground state structure. This is in someway a failure of DFT due to the softness of these materials, which result in very small differences between total energies as

discussed below.

Table 2.1: Calculated and experimental structural parameters of the Alkali metal. Calculations were performed using the LAPW method with LDA and GGA functionals. Experimental values were taken from Kittel[23].

Generalized Gradient Approximation			Local Density Approximation			
	Tot. Energy (mRy)	Lat. Const. (a.u.)	Bulk Mod. (MBar)	Tot. Energy (mRy)	Lat. Const. (a.u.)	Bulk Mod. (MBar)
<b>Lithium (Li)</b>						
bcc	0	6.410	0.296	2.8	6.380	0.148
fcc	0.86	8.134	0.196	0	7.950	0.156
exp		6.597	0.116		6.597	0.116
<b>Sodium (Na)</b>						
bcc	0.08	7.964	0.076	0.96	7.690	0.087
fcc	0	10.040	0.076	0	9.680	0.090
exp		7.984	0.068		7.984	0.068
<b>Potassium (K)</b>						
bcc	0.23	10.432	0.029	0.75	9.540	0.047
fcc	0	13.379	0.025	0	12.010	0.046
exp		9.877	0.032		9.877	0.032
<b>Rubidium (Rb)</b>						
bcc	0.04	10.753	0.032	0	10.130	0.042
fcc	0	13.563	0.031	0.37	12.820	0.049
exp		10.558	0.031		10.558	0.031
<b>Cesium (Cs)</b>						
bcc	0.23	11.661	0.023	2.2	10.760	0.020
fcc	0	14.740	0.023	0	13.880	0.033
exp		11.423	0.020		11.423	0.020
<b>Francium (Fr)</b>						
bcc	0.29	11.702	0.014	0.22	10.842	0.017
fcc	0.05	14.815	0.015	0.20	13.809	0.022
hcp	0	$a = 10.491$	0.011	0	$a = 9.785$	0.021
		$c = 17.132$			$c = 15.657$	
exp			(0.020)			(0.020)

Table 2.1 shows that the LDA functional underestimates the structural lattice parameters for all the alkali metals. The GGA functional tends to overestimate these parameters for most of the alkali metals, with the exception of Li and Na, which it underestimates. All calculations, with both functionals, overestimate the experimental bulk moduli. Both the LDA and GGA functional calculations are unable to predict the correct lattice structure type of the materials. However, the GGA functional is able to predict the correct lattice structure of Li. Moreover, the GGA functional results have much less energy differences between the two structure types. It is also worth noting that the differences between these energies are on the order of less than 1  $mRy$ , which is within the computational accuracy of the code.

Total energy calculations were also performed for the hcp structure of Fr. Unlike the bcc and fcc cubic systems that require only the  $a$  parameter, the hcp structure has two structural lattice parameters,  $a$  and  $c$ . For the fcc and bcc structures, simply varying the  $a$  parameter is enough to find the calculated equilibrium of a system. Therefore, to find the true equilibrium of the hcp total energy calculations, optimization of the  $c/a$  ratio and volume must be performed via energy minimization. It was found that a  $c/a$  ratio of 1.60 was calculated via optimization of LDA calculations, while the ideal ratio ( $c/a = 1.633 = \sqrt{\frac{8}{3}}$ ) was found for the GGA optimized calculations.

Figure 2.1 provides a graphical representation of the calculated bcc results with GGA functional of the alkali metals. The lattice parameters are given as the solid (green) line, while bulk moduli are given as a dashed (blue) line. Two different trends appear in this figure. First, the lattice parameter  $a$  increases with the increase of atomic number. The other is the opposite trend for the bulk moduli, where the values decrease with increasing atomic number. The calculations for Fr seem to follow both of these trends. Spin-orbit calculations were also performed, but had little effect on the total energy results. It seems that the GGA functional provides an overall better description of the total energy related parameters of the alkali metals. The results shown in Figure 2.1 are in agreement with experiment, as was presented in Table 2.1.

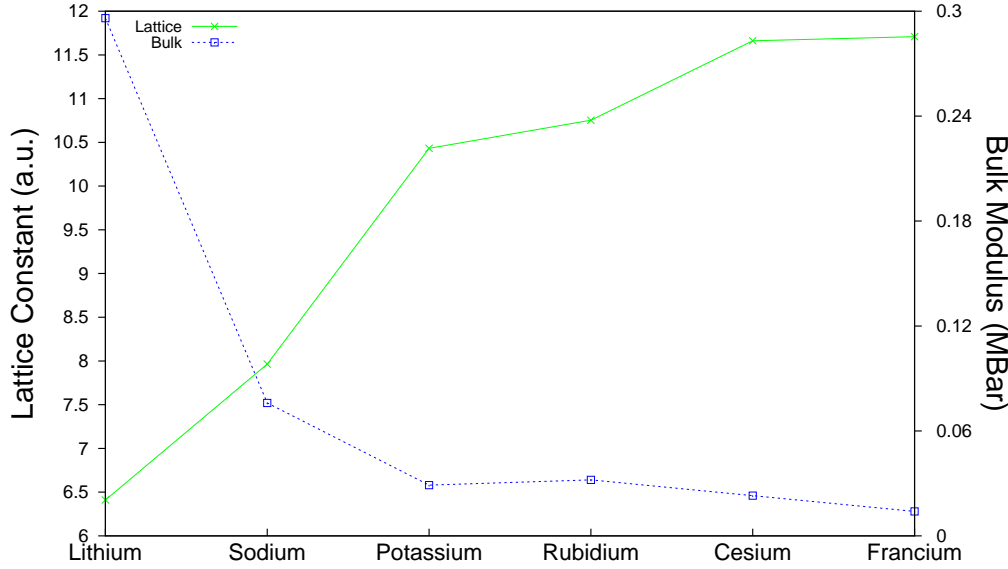


Figure 2.1: Calculated structural lattice parameters and bulk moduli of the bcc alkali metals using the LAPW with GGA functional.

Figure 2.2 shows the Birch fitted total energy curves of Fr for the three structural lattice types using the GGA functional. The lowest total energy is found for the hcp structure, but only by 0.05  $mRy$  for fcc and 0.25  $mRy$  for bcc. This is consistent with the description of Table 2.1. All three curves are relatively similar, providing comparable bulk modulus predictions.

Further calculations involving the enthalpy of the system were also performed. Enthalpy is given by  $H = E + pV$ , where  $p$  is pressure and  $V$  is the volume of the structure. The calculations of enthalpy can be used to predict structural transitions of the system under pressures. Figure 2.3 gives the enthalpy calculations for Fr. This figure shows there is a transition from hcp to bcc under small amounts of pressure and no transition thereafter for the given pressure range. The exact change in structure occurs around 0.57  $GPa$ . No experimental results are available to verify this prediction.

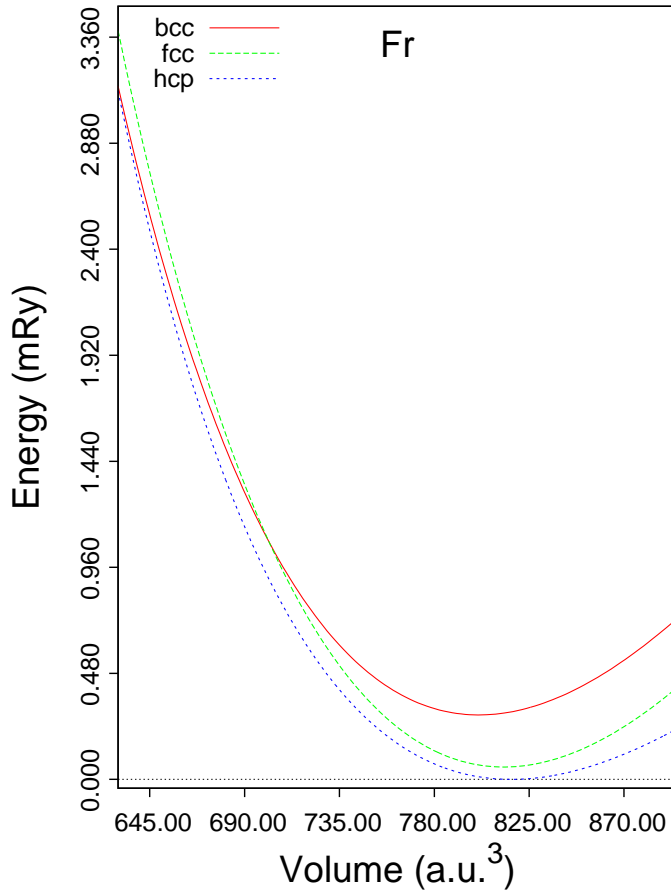


Figure 2.2: Calculated total energy curves of Fr using the LAPW with GGA functional. Notice the hcp structure is calculated to have a lower total energy than the fcc structure by 0.05  $mRy$  at equilibrium.

#### 2.2.4 Band Structure Calculations of Francium

This section discusses the DOS and energy band calculations of Fr using the LAPW with both LDA and GGA functionals. These calculations were done with touching muffin-tin spheres. The DOS and energy bands do not show any significant differences between the two functionals. Spin-orbit interaction calculations were performed with the LDA functional and were found to have little influence on the electronic structure of the system. Once again, these results compare well with the GGA functional calculations.

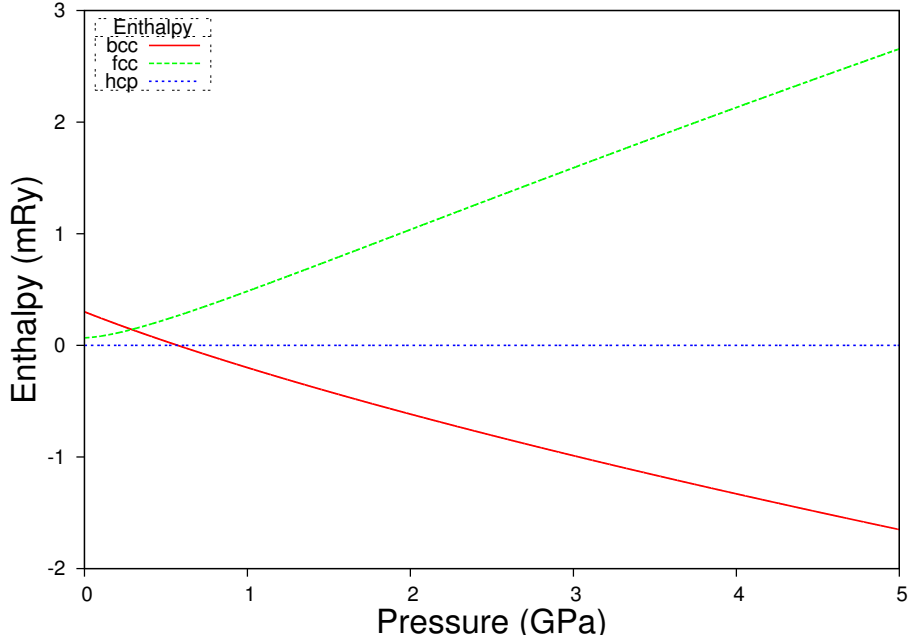


Figure 2.3: Enthalpy calculations of Fr using the LAPW with GGA functional. A structural transition from hcp to bcc occurs at small pressure.

### Francium DOS

The DOS of Fr were calculated with the tetrahedron method discussed in section 2.1.7. DOS calculations with the GGA functional are given in Figure 2.4(b), alongside the DOS of Cs. The figure shows the total and angular momentum ( $l$ -) decomposed DOS for the bcc structure. There are obvious similarities between the Cs and Fr DOS. The first panel of both figures show the total DOS in which we see four main features. One is given between  $-0.2 \text{ Ry}$  and  $0.05 \text{ Ry}$ , which is a flat peak containing mostly  $s$ - and  $d$ -like states. This energy range also contains the Fermi level ( $E_F$ ), which is given by the vertical line at  $0.0 \text{ Ry}$ . The second main feature is a pair of energy peaks ranging from  $0.05 \text{ Ry}$  to  $0.2 \text{ Ry}$ . Here we see  $p$ - and  $d$ - like states. A third major set of peaks appear between  $0.2 \text{ Ry}$  and  $0.35 \text{ Ry}$ . In this range, the  $d$ -states provide most of the contribution, with more than five times that of any other state. The last feature is another set of peaks ranging from  $0.35 \text{ Ry}$  to  $0.6 \text{ Ry}$ . The DOS here is comprised of  $s$ -,  $p$ -,  $d$ -, and  $f$ -like states. The similarities in this figure suggests an accurate prediction of the Fr true DOS.

Table 2.2: The total and decomposed DOS at the Fermi level for bcc cesium and bcc francium using LAPW with GGA functional at zero pressure.

Element	$N_{Total}$	$N_s$	$N_p$	$N_d$	$N_f$
Cs	21.113	6.621	2.772	4.228	0.070
Fr	19.772	7.198	1.897	3.909	0.094

DOS at the Fermi level for both Cs and Fr are given in Table 2.2. The summation of the decomposed DOS do not add up to the total as the decomposed are projections onto the muffin-tin spheres. This table shows good comparison between the two materials. Both materials suggest that  $s$ -like states are the largest contribution to the DOS of the system at  $E_F$ . Calculations of Fr were also performed under pressure to see the influence pressure had on the decomposed DOS of the material. It is found that as the pressure increases, the  $s$ -component of the DOS decreases, while the  $d$ -component increases. After about 2  $GPa$  the  $d$ -component of the DOS becomes the major contributor to the total DOS.

Figure 2.5 shows the total,  $s$ -, and  $d$ -components of the DOS at ambient conditions and under pressure. The total DOS is found to decrease during the structure transition of hcp to bcc. After this transition, the total DOS continues to decrease as  $s$ -like states seem to contribute the majority of the total DOS. However, at around 3  $GPa$ , the  $s$ -states continue to decrease as the total DOS and  $d$ -DOS jump significantly higher. For the remaining pressure range, the total and  $d$ -component of the DOS continue to increase monotonically, while the  $s$ -states monotonically decrease. This behavior is also found in the other alkali metals[24] and is due to  $s$ - $d$  hybridization under pressure. This behavior of increase of the  $d$ -DOS under pressure predicts superconductivity if Fr, similarly as in the other alkali metals. This is explained in detail in the paper of Appendix A and in the paper by Shi and Papaconstantopoulos[24].

### Spin-orbit Interactions

Spin-orbit calculations were performed on total energy and energy band calculations of Fr. The inclusion of spin-orbit interactions had little influence on the overall results of

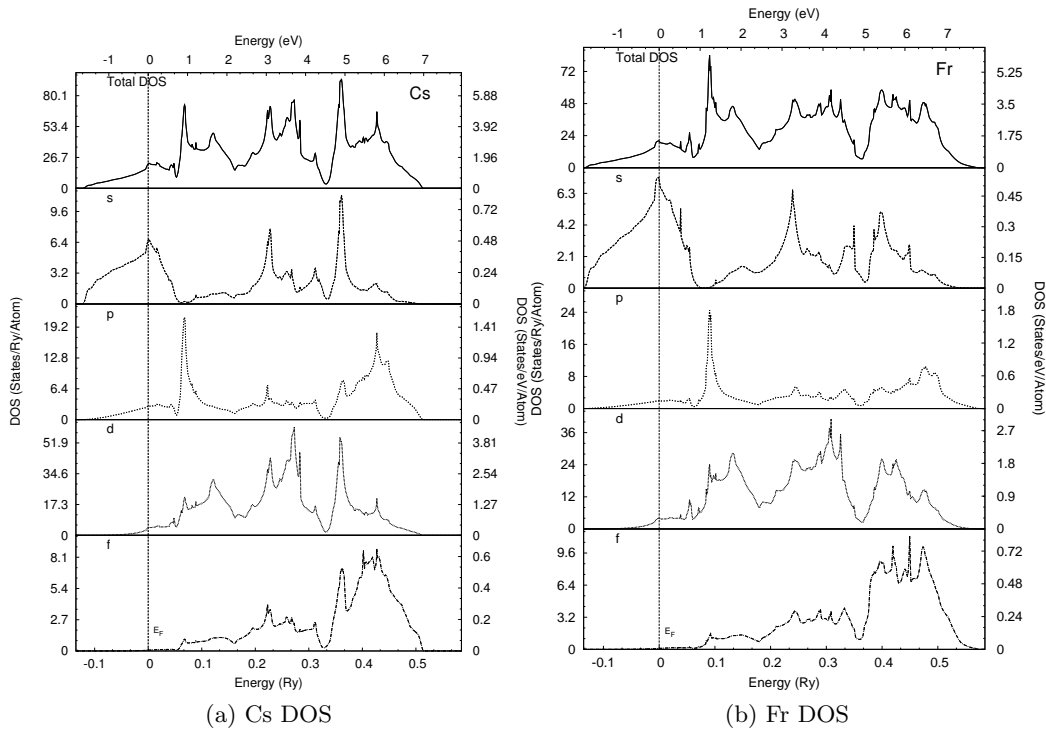


Figure 2.4: Density of States of bcc (a) Cs and (b) Fr using the LAPW method with GGA functional. Fermi level is given by the vertical line, given at zero.

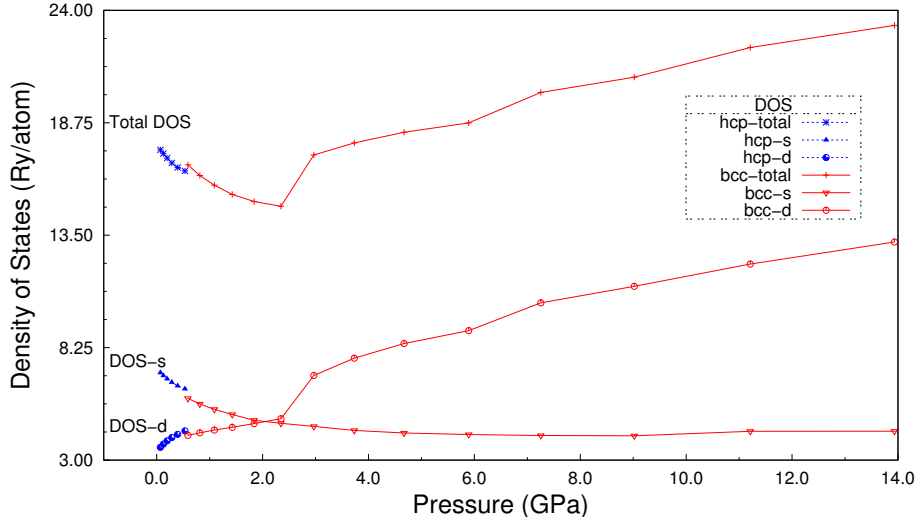


Figure 2.5: Total and  $s, d$ -components of the DOS vs. pressure of francium at  $E_F$ , using the GGA functional with no spin-orbit interaction. The  $l$ -components of the DOS are normalized with respect to the equilibrium MT radius,  $R_{eq}/R$ , to correct for the fact that we are using touching spheres. The hcp structure is given by a dashed (blue) line, and the bcc structure as a solid (red) line.

the electronic structure of Fr. Table 2.3 shows the total energy related results of bcc Fr with spin-orbit interactions. The total energy in the table compare very closely to those in Table 2.1. Both the fcc and bcc structure are calculated to be closer to the hcp structure by such a small amount, less than 0.05  $mRy$ . The hcp structure is once again found to be the ground state of the material. Lattice parameters, both  $a$  and  $c$ , for bcc, fcc, and hcp all come out to nearly the same values. Bulk modulus are also predicted to be nearly the same. Overall the spin-orbit interactions seem to have little to no influence over the total energy related parameters of Fr.

Table 2.3: Total energy and related results for francium with LDA functional with spin-orbit interaction.

	Total Energy ( $mRy$ )	Lattice Constant ( $a.u.$ )	Bulk Modulus ( $MBar$ )
bcc	0.20	10.836	0.018
fcc	0.17	13.802	0.022
hcp	0.0	$a = 9.788$ $c = 15.661$	0.020

Table 2.4 gives the total and decomposed DOS of the spin-orbit and no spin-orbit calculations under pressure. Like the total energy related results, we see very little difference between the two sets of calculations. Pressures are found to be nearly identical for the corresponding volumes. Total and decomposed DOS both find very similar results for the given volumes. Once again it would seem the spin-orbit interactions have little influence on the Fr system.

Fr, like the other alkali metals, has its lowest band half occupied and is almost entirely of  $s$ -character. Quantum mechanics tells us that there is no spin-orbit splitting for these “s” states. The states above  $E_F$  have  $p$ - and  $d$ -character, which do split, but are irrelevant to the Fermi level values of the DOS, phase shifts, etc. A latter chapter will discuss the role of superconductivity of this and other systems. As will be mentioned in section 4.1, DOS at the Fermi level are the important quantities needed for calculating the superconductivity

Table 2.4: Total and decomposed DOS at  $E_F$  for bcc francium using LAPW with LDA functional, both with and without spin-orbit interaction

Vol. ( <i>a.u.</i> <sup>3</sup> )	Press. ( <i>GPa</i> )	DOS Total	DOS s	DOS p	DOS d	DOS f
<b>No Spin-orbit</b>						
595.5	0.20	16.146	5.192	1.396	3.825	0.106
500	1.01	14.968	4.279	1.224	3.975	0.1280
364.5	4.39	18.289	3.230	1.083	6.771	0.276
275.7	11.57	23.069	3.080	1.283	9.147	0.650
<b>Spin-orbit</b>						
595.5	0.20	16.503	5.257	1.477	3.889	0.107
500	1.00	15.337	4.280	1.318	4.045	0.134
364.5	4.32	18.767	3.267	1.170	6.898	0.281
275.7	11.388	23.956	3.172	1.434	9.416	0.660

of a system.

Table 2.5 shows the splitting of the energy bands at three high symmetry k-points. For comparison, both spin-orbit (WSO) and no spin-orbit (NSO) results are displayed, with the energy difference between the splittings. The table shows how little influence the spin-orbit splitting has on the *s*-like bands around the Fermi level. Once again this is due to the lack of splitting that occurs in a quantum system with *s*-like character. The three points in the figure are;  $\Gamma_{25'}$ , which is a triple degenerate state that splits into a single degenerate state and a double degenerate state by spin-orbit coupling;  $H_{25'}$ , which is also a triple degenerate state splitting into a double and single degenerate state with spin-orbit interactions;  $P_4$  also splits from a triple degenerate state to a single and double degenerate one. These high symmetry points are displayed and labeled in Figure 2.6.

### Francium Band Structure

Figure 2.6 shows the LAPW with GGA functional energy bands of bcc Fr at equilibrium conditions (a) and under the largest pressure calculated, which corresponds to about 34% the equilibrium volume (b). As the pressure increases, *d*-like bands start to cross the Fermi

Table 2.5: Spin-orbit splitting and energies at high symmetry k-points of bcc francium at equilibrium

	$\Gamma_{25'}$	$H_{25'}$	$P_4$			
NSO	0.258	0.484	0.149			
WSO	0.255	0.264	0.479	0.493	0.121	0.161
$\Delta E$	0.009		0.014	0.040		

level, adding to the  $s-d$  band hybridization. For example, the  $H_{12}$  point is comprised of entirely  $d$ -character and drops below the Fermi level under pressure. Comparison between the other alkali metals show similar features with the energy bands[19]. Under these large pressures the alkali metals begin to show transition metal like behavior. This will be discussed further in the superconductivity chapter.

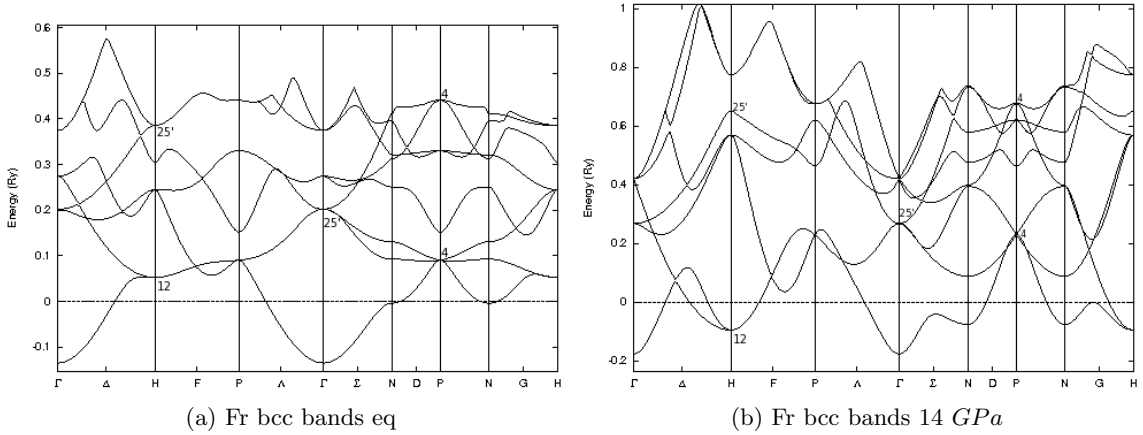


Figure 2.6: Energy bands of bcc Fr (a) under ambient conditions and (b) at 14 GPa. Fermi level is given by the horizontal line, given at zero.

## 2.3 Preliminary Calculations - Insulator-Metal Transition in the Inert Gases

### 2.3.1 Introduction

This section discusses first-principles calculations of the inert gases, or noble gases. All inert gases are found in group 18 of the periodic table and have their valence shells full. In 1927, Herzfeld suggested that all inert gases would become metals under high enough pressure[25]. As of today, only the element xenon has experimentally been measured as a metal under pressure[26, 27]. Other groups have studied the metalization of the other materials experimentally[28, 29]. Recently Veeser, *et. al.*[28] may have found krypton to conduct under significant pressure. Computationally, this metalization has been studied by various groups for most of the inert gases[30–34]. This work is a comprehensive study of the transition from insulator to metal for all the inert gases, including radon.

As with francium and the alkali metals, calculations were performed using the LAPW method with both the LDA and GGA functionals. The electronic structure of radon has not been published at the time of writing, computationally or experimentally. The other inert gases, neon, argon, krypton, and xenon, have various publications[29–34].

### 2.3.2 Computational Details

Calculations of the inert gas solids were performed using the NRL-LAPW code with the LDA and GGA functionals. All calculations used the equilibrium electronic configuration of the element, with the six valence electrons not considered as core states. For example, Rn used the core states contained the electronic configuration of mercury, with the  $6p$  states as valence electrons. The muffin-tin, like the alkali metals, were kept constant for total energy calculations at values that made sense for the specific element. However, during DOS and band structure calculations, the muffin-tin radii were kept constant as well. The k-point meshes of 55 and 89 were used for bcc and fcc, respectively. For hcp calculations, a k-point mesh of  $16 \times 16 \times 16$  was used. Rn calculations were also performed with a larger

meshes of 285 and 505 for bcc and fcc, respectively. An  $r k_{max}$  value of 8.5 was used for all calculations. Energies of  $-1.4 \text{ Ry}$  and  $-0.3 \text{ Ry}$  were used for the local orbitals of the last core  $s$ -state and the valence  $p$ -states.

### 2.3.3 Total Energy Calculations

Total energy calculations were performed for all the noble gases. These calculations were performed for both the LDA and GGA functionals. The LDA functional found the fcc structure to be the ground state for all the elements. This is consistent with the experimental results of the inert gases. The LDA results underestimated the experimental lattice parameters, while the GGA functional results overestimated these parameters.

Table 2.6 shows the total energy, lattice constants,  $a$  and  $c$ , and bulk modulus of the inert gases using the LAPW method with LDA functional. For these calculations the LDA functional was able to predict the correct equilibrium structure of the inert gases, which is fcc. Like the alkali metals, these total energy calculations had all three structures extremely close to each other. The largest difference between bcc and fcc results was less than  $1 \text{ mRy}$ . It is interesting to note that the bcc and fcc energy difference increases with the atomic mass. This suggests that the method is better able to predict the correct structure for the heavier elements, at least when comparing the two cubic structures.

Table 2.7 shows a comparison of the functionals, by comparing the percent difference of lattice parameters from experiment with the calculated values. The LDA tends to have a better agreement with experiment for the lattice parameters than the GGA, with the exception of Ne. The LAPW method is able to predict the correct ground structure, as well as other properties of these materials.

Total energy curves for the inert gases all find the fcc and hcp curves very close in minimum energy and shape, with the bcc minimum energy much higher than the other structures. Here we present the total energy results for the heaviest inert gas, Rn. Figure 2.7 shows the total energy of Rn with the bcc, fcc, and hcp structures using the LAPW method with LDA functional. The fcc structure was found to be the ground state for Rn, as

Table 2.6: Total energy and related results for the inert gases Ne, Ar, Kr, Xe, and Rn using the LAPW with LDA functional with experimental results[23].

	Total Energy (mRy)	Lat. Const., $a$ (a.u.)	Lat. Const., $c$ (a.u.)	Bulk Modulus $B$ (MBar)
<b>Neon (Ne)</b>				
bcc	0.29	5.795		0.100
hcp	0.005	5.134	8.383	0.097
fcc	0.0	7.260		0.100
exp		8.428		0.010
<b>Argon (Ar)</b>				
bcc	0.55	7.453		0.070
hcp	0.01	6.629	10.673	0.076
fcc	0.0	9.326		0.076
exp		10.034		0.013
<b>Krypton (Kr)</b>				
bcc	0.68	8.060		0.066
hcp	0.06	7.131	11.644	0.071
fcc	0.0	10.088		0.076
exp		10.658		0.018
<b>Xenon (Xe)</b>				
bcc	0.9	8.876		0.060
hcp	0.05	7.858	12.730	0.066
fcc	0.0	11.092		0.065
exp		11.584		
<b>Radon (Rn)</b>				
bcc	0.96	9.134		0.063
hcp	0.02	8.081	13.196	0.067
fcc	0	11.420		0.068
exp				

suggested by Table 2.6, where we present results for the rest of the inert gases. For the Rn hcp calculations, the ideal  $c/a$  ratio of  $\sqrt{\frac{8}{3}}$ , or  $\approx 1.633$ , gave the lowest total energy of all  $c/a$  calculated between 1.5-1.7.

Table 2.7: Percent difference between calculated and experimental lattice parameters using LAPW with LDA and GGA functionals of inert gases (Ne, Ar, Kr, and Xe)

	Local Density (LDA)	General Gradient (GGA)
Neon (Ne)	-13.86%	+4.08%
Argon (Ar)	-7.06%	+15.35%
Krypton (Kr)	-5.35%	+15.88%
Xenon (Xe)	-4.25%	+17.54%

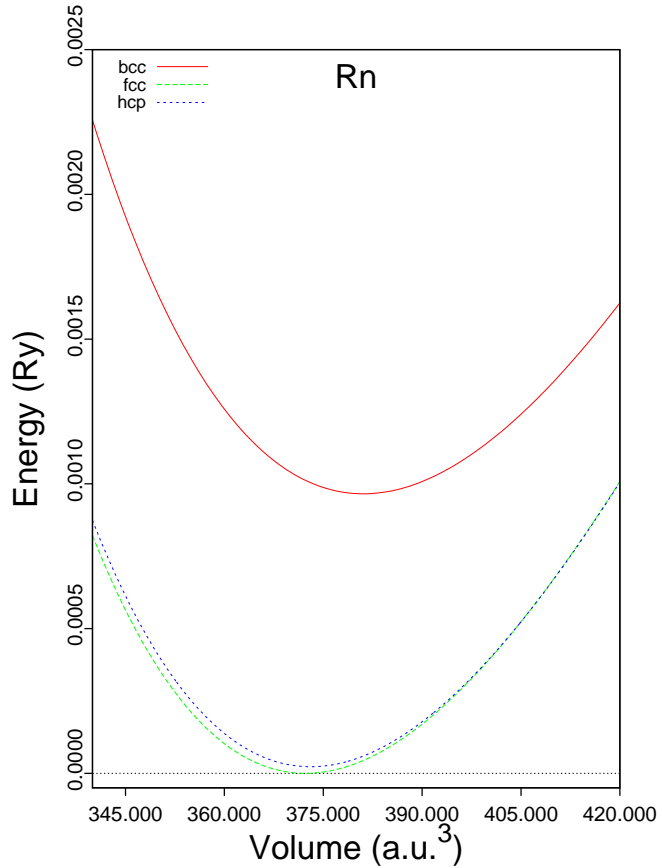


Figure 2.7: Total energy of radon using the LAPW method with LDA functional. Notice the total energy predicts the fcc structure to be less energy than the bcc and hcp.

### 2.3.4 Energy Band Calculations of the Inert Gases

This section discusses the calculations of the DOS and energy bands of the inert gases under equilibrium conditions and under pressure. We find that the inert gases transition from an insulator to metal under certain amounts of pressure. Neon, however, was not found to transition under the calculated pressures involved. The results of the DOS and energy bands are presented below with a discussion of the mechanism for the metalization transition.

#### Density of States of the Inert Gases

Figure 2.8 shows the Density of States (DOS) of Ne, Ar, Kr, Xe, and Rn, respectively, under ambient conditions. The DOS of Ne, Ar, Kr, Xe, and Rn show a gap between the occupied and unoccupied states, confirming that these materials are insulators at ambient conditions. Interestingly, the energy gap between these two states decreases as we go from the lightest element, Ne, to the heaviest, Rn. The Fermi level is given as a vertical dashed (blue) line at the top of the  $p$ -states at 0.0  $Ry$ .

The valence  $p$ -states of the inert gases are found between  $-0.2 Ry$  and  $0.0 Ry$  in all these figures. These  $p$ -states are more compressed in the lighter elements. The higher unoccupied states have a similar shape between all these figures. They are comprised of mostly  $d$ -like states which span a much wider energy range than the  $p$ -states. There are also traces of  $s$ -like and higher  $p$ -like states found within this range as well. However, no  $s$ - or  $d$ -states are found in the higher unoccupied bands of Ne. A large energy gap appears between the occupied and unoccupied states. The gap gets narrower as the atomic number of the element increases. Since the valence shell is entirely filled and the materials are found to be insulators, there are no DOS at the Fermi level for any of these material under equilibrium conditions.

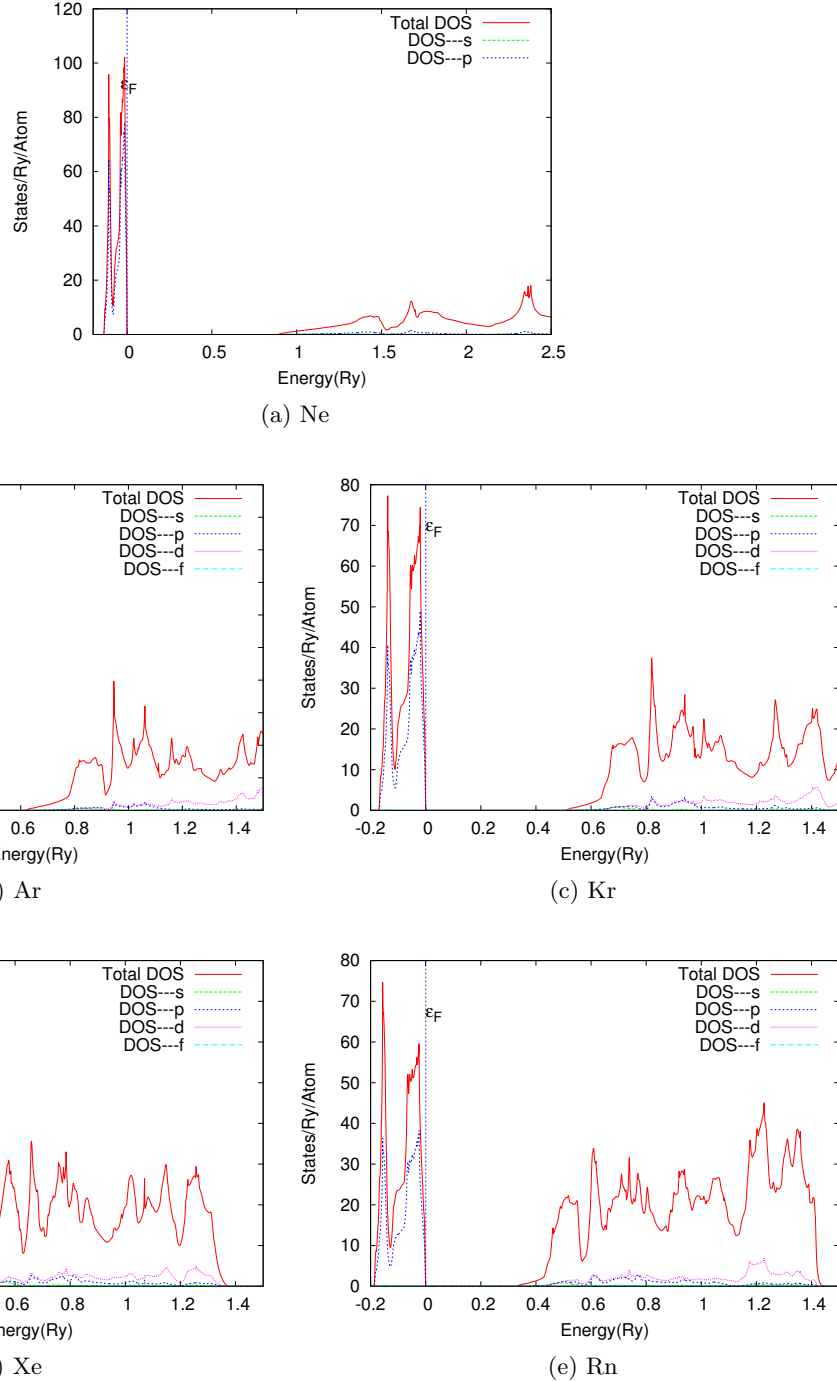


Figure 2.8: The total and decomposed DOS of (a)Ne, (b)Ar, (c)Kr, (d)Xe, and (e)Rn at ambient pressure.

## Energy Bands of the Inert Gases

Figure 2.9 shows the energy bands of the inert gases under equilibrium conditions. These figures have the Fermi level as a horizontal solid line at 0.0  $Ry$ . Like the DOS figures, the Fermi level is calculated directly above the  $p$ -like bands found between  $-0.2 Ry$  and  $0.0 Ry$ . Once again, a gap appears between these  $p$ -like bands and the higher unoccupied bands. This gap suggests the material are insulators, as no bands cross the Fermi level. These unoccupied bands are found to contain mostly  $d$ - and  $p$ -like bands, with a single  $s$ -like band appearing closest to the occupied  $p$ -bands. Under ambient conditions, none of the inert gases show signs of any metallic behavior. However, under pressure, these materials undergo significant changes in the electronic structure that suggest metal-like properties.

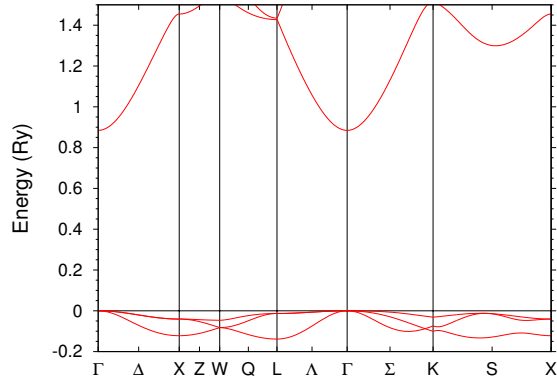
### 2.3.5 Insulator to Metal Transitions of the Inert Gases

The inert gas calculations were also performed under pressure to understand the effect this had on the materials. Using the LAPW method with LDA functional, predictions of the pressures needed to cause a transition from insulator to metal were made. This method has been able to accurately predict the confirmed experimental pressure needed for the xenon material.

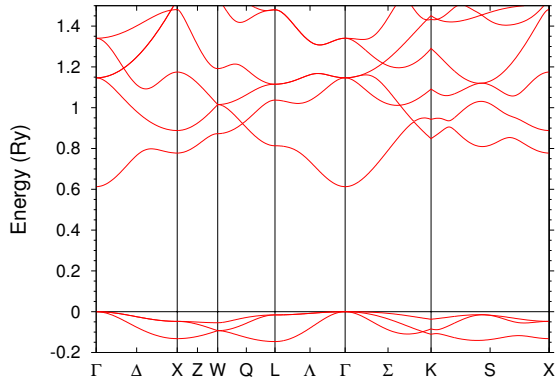
Table 2.8: Calculated and experimental pressures for the insulator to metal transition of the noble gases ( $GPa$ )

	LAPW LDA	Other Calculations	Experiment
argon	513	550[26]	
krypton	392		
xenon	147	123,104,128[35]	132±5[26],150[36],155[27]
radon	103		

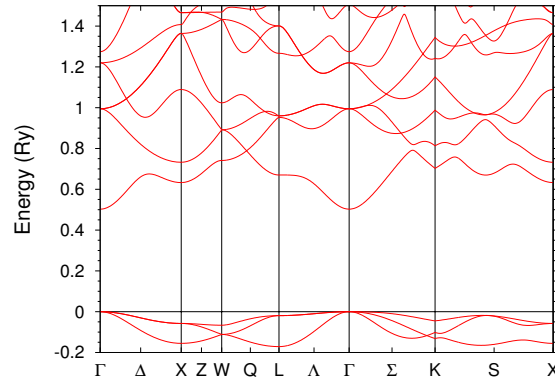
Table 2.8 provides our LAPW with LDA calculations, other group calculations and experimental pressures needed to force an insulator to a metal transition to occur. As there aren't very many papers that provide a direct value for the transition pressure, the table only



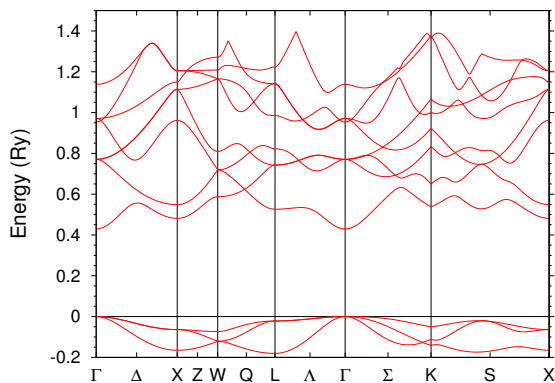
(a) Ne



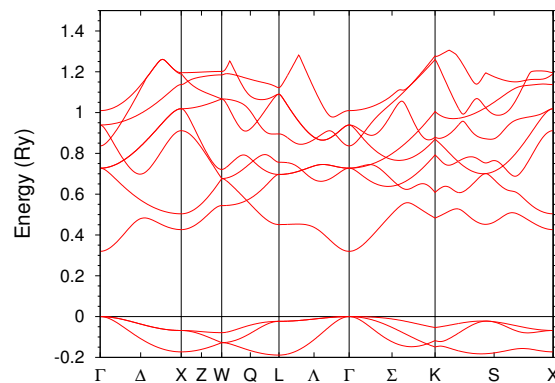
(b) Ar



(c) Kr



(d) Xe



(e) Rn

Figure 2.9: The energy bands of (a)Ne, (b)Ar, (c)Kr, (d)Xe, and (e)Rn under ambient conditions.

contains a few values to compare to directly. However, the table shows good comparison of the calculated values with those of both experiment and other groups' calculations.

Comparing with experiment, the xenon calculations performed agree extremely well with those found by references [36] and [27]. In particular, reference [27] used x-rays to study the structure of Xe under pressures up to 155  $GPa$ . They directly measured the electrical conductivity while compressing the material. Their results suggest that Xe is predominantly metallic around 121 – 138  $GPa$  and purely metallic at 155  $GPa$ . Goettal, *et. al.*[26] found the transition pressure to be 132  $GPa$ , while Reichlin, *et. al.*[36] found the pressure to be around 150  $GPa$ .

Other experimental groups have studied these materials under pressure, but did not find any transitions to metal under the pressures used. Although one group may have recently found Kr to undergo the insulator to metal transition, but lack of access to the article made this difficult to confirm[28].

Computational results from other groups also seem to agree well with the calculations performed here. Three other groups found similar results to our calculations for the Xe transition. These values were slightly less than the ones calculated here. For Ar, one group found a comparable pressure to the one calculated here, but unlike Xe, this result was predicted at a higher pressure. Overall it seems that the LAPW with LDA functional is able to correctly predict the experimental Xe transition pressure and other computational predictions.

Our LAPW results displayed in Table 2.8 suggest that the pressure needed to transition the material from an insulator to a metal decreases as the atomic number increases. The pressure needed for Ar is nearly four times that of Xe. The band structure of these materials undergo a significant change under the pressure required for the transition. Figures 2.10, 2.11, 2.12, and 2.13 present the equilibrium and metalization pressure band structure results of Ar, Kr, Xe, and Rn, respectively.

Figure 2.10 shows the energy bands of Ar under ambient conditions and the metalization pressure. The figure shows that as pressure increases in this material, all bands begin to

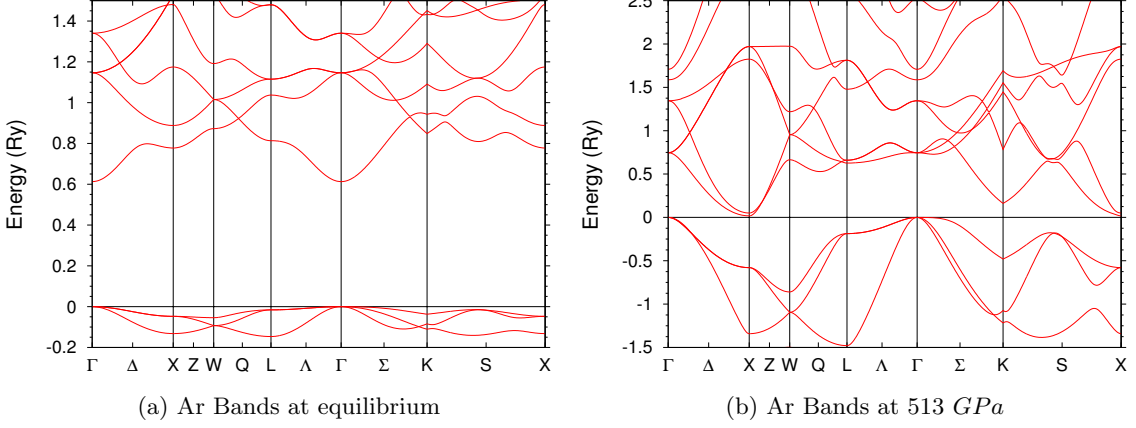


Figure 2.10: Energy bands of Ar at equilibrium and at the insulator to metal transition pressure.

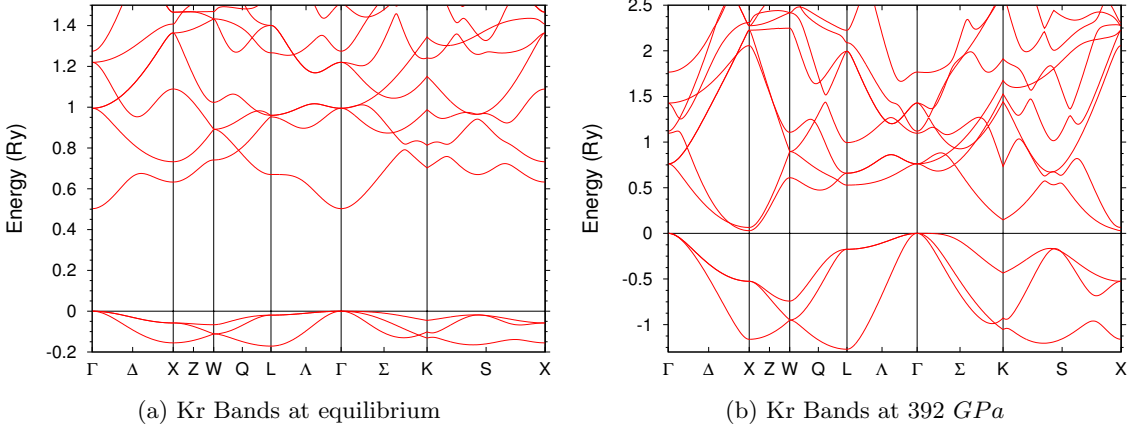


Figure 2.11: Energy bands of Kr at equilibrium and at the insulator to metal transition pressure.

broaden. Specifically, the  $p$  bands near the Fermi level begin to broaden from a range of approximately 0.2 Ry to 1.5 Ry at the point of metalization. The above unoccupied  $d$  bands also begin to broaden when pressure is applied. Figure 2.11 shows the energy bands of Kr under ambient conditions and 392 GPa pressure. Again, we see a large broadening of the  $p$  bands around the Fermi level as pressure is increased, albeit to a lesser extent than Ar.

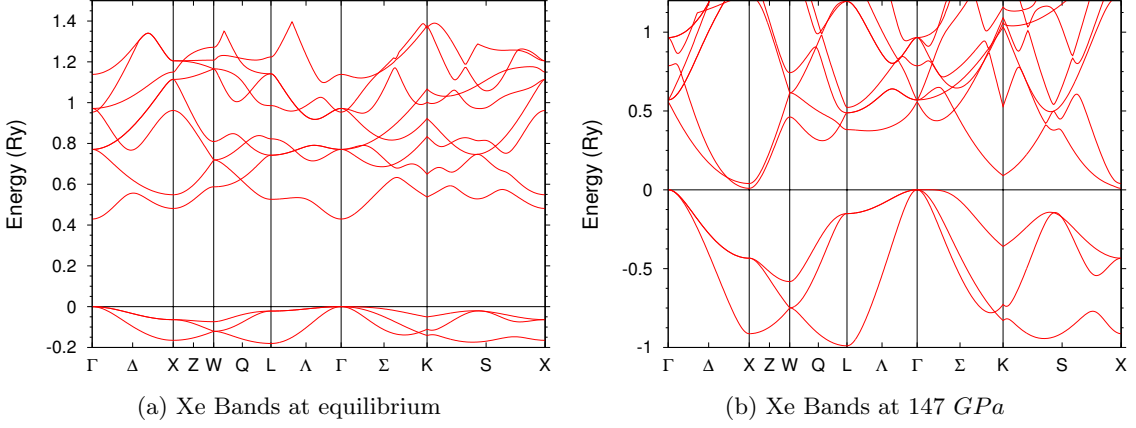


Figure 2.12: Energy bands of Xe at equilibrium and at the insulator to metal transition pressure.

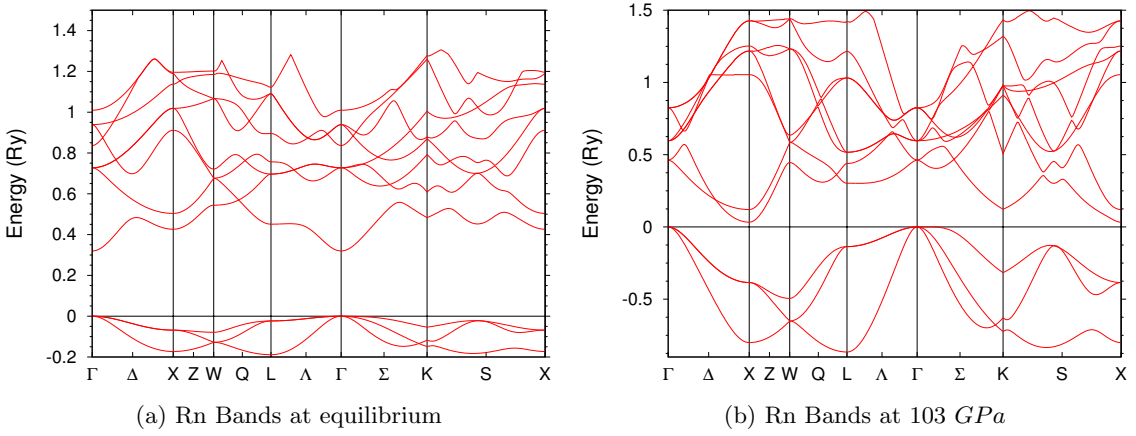
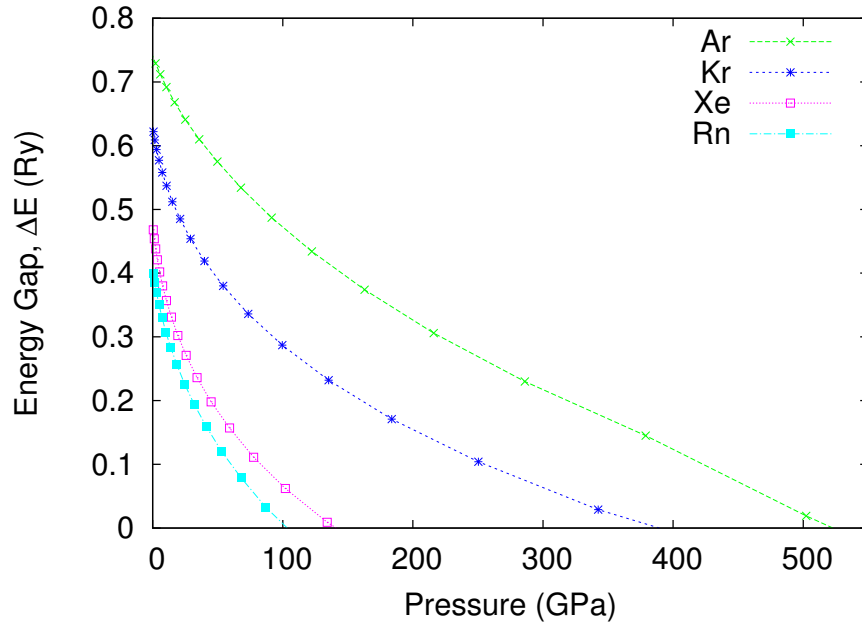


Figure 2.13: Energy bands of Rn at equilibrium and at the insulator to metal transition pressure.

For the Kr figure, the bands broaden from approximately 0.2 Ry to 1.3 Ry at the transition pressure. Figure 2.12 and Figure 2.13 also show the two sets of bands structures for Xe and Rn, respectively. These figures also show the same broadening features as those shown in the Figure 2.10 and Figure 2.11.

For all the pressure-based band figures mentioned above, both  $p$  bands below the Fermi

level and unoccupied bands above the Fermi level expand a great deal. However, the size of the broadening decreases as the atomic number increases. This is true for both the  $p$  bands and those found above the Fermi level. In the ambient condition figures, the lowest energy band at the  $\Gamma$  point is of  $s$  angular momentum character. However, as pressure is applied, this band begins to move higher in energy, while the  $d$ -like band begins to move closer to the Fermi level. At the point of metalization, the  $X$  point intersects the Fermi level, closing the gap between the  $d$ -like bands and the  $p$  bands. Specifically, the gap is between the  $\Gamma_{15}$  point and the  $X_1$  point.



(a) Band gap closure of the inert gases

Figure 2.14: Band gap closure of the inert gases vs. pressure. Energy gap is calculated from the difference between  $\Gamma_{15}$  and  $X_1$ . Insulator to metal transitions occur at 513 GPa, 392 GPa, 147 GPa, and 103 GPa for Ar, Kr, Xe, and Rn, respectively.

Figure 2.14 provides curves of the  $\Gamma_{15}$ - $X_1$  energy gap of each element under pressure. This figure shows the gap is initially wider for the lighter elements and decrease under pressure until eventually becoming zero. For example, the energy gap between these points in Rn is almost half that of Ar. We show that the heavier the element, the less pressure

required to undergo the insulator to metal transition.

It is important to note that results for Ne were not presented for this section. This is due to the fact under the pressures studied, Ne  $d$  states are at much higher energies above the Fermi level. The bands above the Fermi level shown in Figure 2.9a begin to move higher as pressure is increased. It is possible that the much higher  $d$  bands move closer to the Fermi level when pressure is increased, but this was not found for pressures up to 960  $GPa$ .

## 2.4 Conclusions of Preliminary Results

This chapter presented information on some of the computational theories used to calculate the electronic structure of materials, as well as calculations using these theories for the alkali metals and inert gases. It was shown that the LAPW method with both GGA and LDA functionals can provide good agreement with experiments when calculating total energy and DOS related parameters. Although both functionals can provide great detail on the nature of a material, any functional is not universally best. It was shown that the GGA functional provided much better agreement with experimental structural parameters for the alkali metals, while the LDA did a better job for the inert gases. The LDA consistently underestimated these structural parameters for both groups of materials, while the GGA overestimated them. Energy band calculations and DOS results were well represented by both functionals. These results have been useful to better understanding the general electronic structure of the materials. A very interesting transition from insulator to metal has been confirmed for the inert gases except for Ne. A paper on this work is under preparation.

## Chapter 3: First-Principles Study of the Electronic Structure of Iron-Selenium-Tellurium Superconductor Systems

### 3.1 Electronic Structure of Iron-Selenium

#### 3.1.1 Introduction

Iron-selenium (FeSe) is one of the structurally simplest iron-based superconductors. Under ambient conditions[5, 37–40] it forms in the tetragonal PbO structure, *Strukturbericht* B10,[41], space group P4/nmm-D<sub>4d</sub><sup>7</sup> (#129). Fe atoms are found at the (2a) Wyckoff position (000) and Se atoms are fixed at the (2c) Wyckoff position (01/2z). Figure 3.1 shows the PbO structure of the system. The *z* found in the (2c) Wyckoff position is called the internal parameter of Se. This internal parameter is the distance of the Se atom plane from the Fe atom plane, as seen in Figure 3.1.

FeSe is found to superconduct at a critical transition temperature,  $T_c$ , of about 8 K[5,37–39,42]. It has been found that  $T_c$  increases substantially, up to 37 K under pressure[38,39]. It is important to note that although FeSe is an iron-based material, there is no magnetic order of the material in the superconducting temperature range. There are several studies, both computational and experimental[4–6, 37–40, 42–48].

#### 3.1.2 Computational details

Calculations were performed using the NRL-LAPW and Wien2k[49] codes. Both codes require various input parameters, and were kept as identical as possible to compare the calculations with one another. LAPW wave functions were used for the valence band, further augmented by local orbitals for the semi-core states, using codes mentioned. Exchange-and-correlation effects were approximated by the Hedin-Lundqvist parametrization of the Local

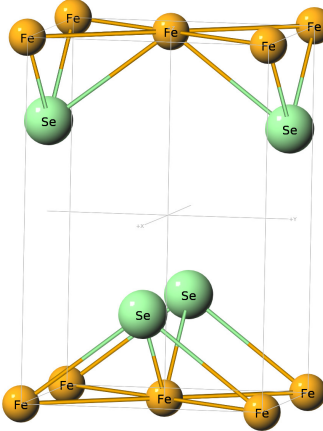


Figure 3.1: Ground state structure of FeSe, *Strukturbereicht* designation B10. The space group is  $P4/nmm-D_{4d}^7$  (#129). The iron atoms are on (2a) Wyckoff sites, while the selenium atoms are on (2c) sites.

Density Approximation (LDA), as well as the Purdue-Wang implementation of the Generalized Gradient Approximation (GGA). The Rigid Muffin-Tin Approximation (RMTA) code developed by Papaconstantopoulos and Klein[51] was used to apply the Gaspari-Gyorffy (GG) theory[52] to the NRL-LAPW results. A  $\Gamma$ -centered k-point mesh of 196 points, or  $12 \times 12 \times 12$  per direction, was used for total energy and Density of States calculations. A larger mesh of 904 k-points was used for the calculations of energy bands in the NRL-LAPW code. All calculations used a basis set size of  $6 \times 6 \times 6$ , 7 core states (equilibrium state of argon) for iron and 9 core states (argon +  $3d$  states) for selenium resulting in 28 total valence electrons for FeSe calculations. Estimates of the local orbital energies were approximately  $-0.3$  Ry,  $0.2$  Ry and  $-2.0$  Ry for  $3s$ ,  $3p$  and  $3d$  states, respectively. All calculations used fixed muffin-tin radii of  $2.0$  a.u. for Fe and Se atoms, with the cutoff parameter,  $rk_{max}$ , set to 8.5.

### 3.1.3 Iron-Selenium total energy calculations

Structural optimization was executed via energy minimization with respect to both the tetragonal lattice constants  $a$  and  $c$  and the internal Selenium parameter  $z$  for FeSe with

the NRL-LAPW code with both LDA and GGA. As discussed in Koufos, et. al.[47], the LDA optimization underestimates the experimental lattice parameters. Specifically, the calculations underestimate the experimental lattice parameters by 4.5% and 2.2% for  $a$  and  $c$ , respectively. For the GGA optimization, the  $c$  lattice parameter was overestimated by 10.6%, while the  $a$  lattice parameter was only underestimated by 1.8%, and the  $c/a$  ratio was largely overestimated for the GGA. Table 3.1 is a comparison of these parameters calculated with both functionals and the parameters measured by experiment. The table shows that the GGA and LDA calculated volumes are on either side of the experimental volume. The calculated internal parameters are also underestimates of the measured  $z$ . However, it is interesting to note that other groups find a range of  $z$  from 0.260-0.270[5, 37, 53, 54]. The calculated LDA bulk modulus is in very good agreement with experiment, while the GGA value is too low.

Table 3.1: Structural parameters ( $V$ ,  $a$ ,  $c/a$ ,  $z$ ) and bulk mouduli ( $B$ ) of FeSe, both computational and experimental[44, 45].

$V$ (a.u. <sup>3</sup> )	$a$ (a.u.)	$c/a$	$z$	$B$ (GPa)
LDA				
472.5	6.804	1.50	0.255	32.2
GGA				
564.4	6.994	1.65	0.230	6.6
Experiment				
529.5	7.121	1.465	0.269	31.0

Figure 3.2 shows the structural optimization results of energy vs. volume. The solid (red) line is the fit to the NRL-LAPW LDA optimized calculations, while the dashed (green) line is the fit to the optimized NRL-LAPW GGA calculations. As discussed in section 2.1.5, the second derivative of the energy curve is related to the bulk moduli of the system. These values are also provided in the figure for convenience. As the fits suggest, the bulk modulus of the GGA calculations is quite small, due to the flatness of the GGA curve. As mentioned, the LDA underestimates the experimental volume and GGA overestimates,

straddling the experimentally measured volume. Structural optimization was not performed with the Wien2k code. This was mainly due to the fact that another set of optimized LDA calculations were performed for the paper[47] by Mehl with the Vienna ab initio simulation package (VASP)[55]. The calculations agreed exceptionally well with the NRL-LAPW optimized LDA calculations.

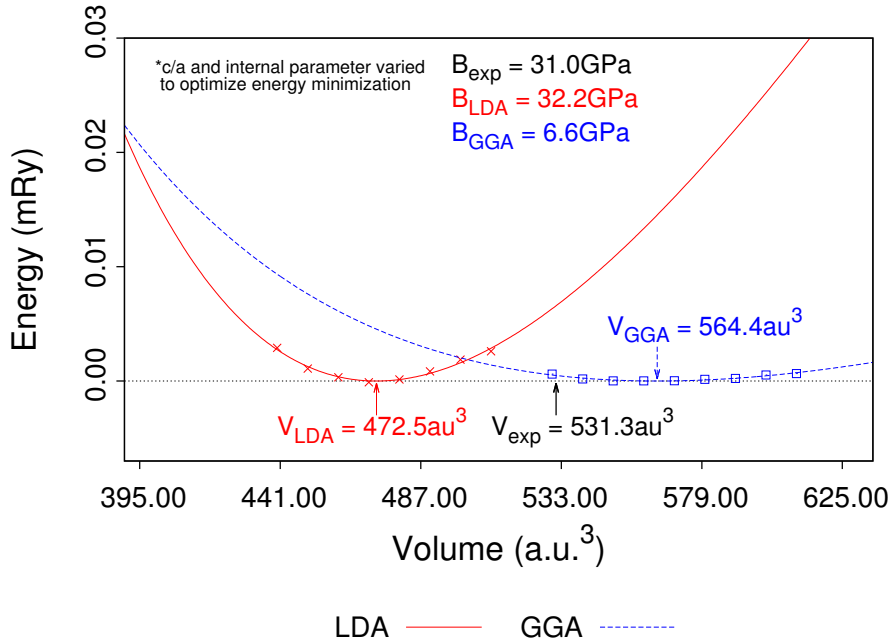


Figure 3.2: LAPW total energy plots of FeSe from the optimized LDA and GGA calculations. The LDA and GGA straddle the measured volume from Kumar, et. al.[44]

Ferromagnetic optimization calculations were also performed for FeSe, but found little difference from the above paramagnetic calculations. These calculations were done using the local spin density approximation (LSDA), which incorporates spin-polarization into the calculations of LDA. Table 3.2 shows the resulting optimized calculations of both the LDA and LSDA functionals. Hence no magnetic moment was found. As can be seen from the table, these values are extremely comparable to each other. The LSDA results presented underestimate the volume and  $a$  parameter slightly more than the LDA. The  $c/a$  ratio remains the same, while the internal parameter increases slightly. The largest difference

here is the bulk modulus, which is due to a steeper energy curve of the fit. It is important to note that the LDA results were based on a larger database of calculation than the LSDA, approximately 33% more. Thus the LSDA may be found to have even closer results to the LDA.

Table 3.2: Structural parameters ( $V$ ,  $a$ ,  $c/a$ ,  $z$ ) and bulk mouduli ( $B$ ) of FeSe using the local density approximation and local spin density approximation (LSDA).

$V$ (a.u. $^3$ )	$a$ (a.u.)	$c/a$	$z$	$B$ (GPa)
LDA				
472.5	6.804	1.50	0.255	32.2
LSDA				
466.4	6.774	1.50	0.260	61.0

Since FeSe is not found to be ferromagnetic[5, 37, 38, 44], all calculations reported in the next section were performed without spin-polarization. As the GGA and LSDA are computationally more expensive than LDA and LDA results agree well with experiment, the LDA functional was used for the section 3.1.4 calculations. In order to make more meaningful comparisons with experiment, the band structure calculations discussed in detail in the following section were performed using the experimental lattice parameters. Lastly, spin-orbit coupling was not included since the effects of spin-orbit on the energy bands was found to be minimal.

### 3.1.4 DOS and energy band calculations of FeSe

Band structure calculations were performed with the two codes mentioned in section 3.1.2. Having these two sets of calculations allow for direct comparison of the codes. This also allows one form of validation of the calculations performed. Calculations by other groups[4, 6, 43, 56] and experimental work[48, 57] give us the opportunity to verify our calculations further. The parameters used by other calculation groups differed slightly from those used here and may affect the details of the band structure calculations.

## Calculated Density of States

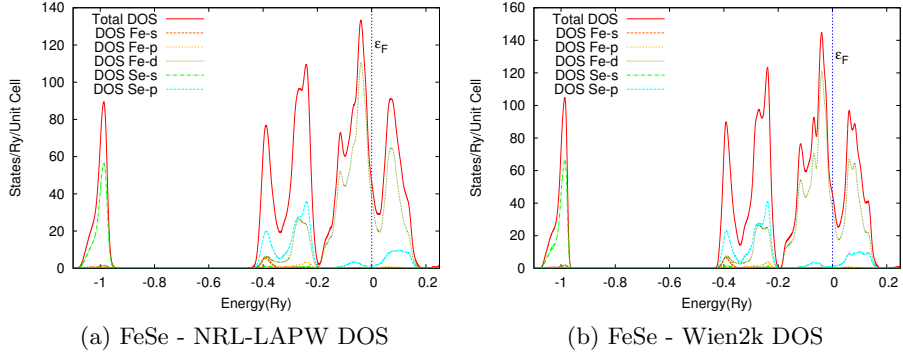


Figure 3.3: Density of States of tetragonal (PbO-like) FeSe (a) using NRL-LAPW results and (b) using the Wien2k results. Fermi level is given by the dashed vertical line, given at zero.

Figure 3.3 shows the DOS of FeSe for both the NRL-LAPW and Wien2k calculations. The two FeSe DOS, Figure 3.3a and Figure 3.3b, show near identical results. No significant difference were found between the two calculations. Overall the picture is extremely similar, even giving a small gap between the majority of Se *p*-states and the Fe *d*-states. This shows that the codes perform DOS calculations similarly and therefore suggest either code would be adequate for other calculations of FeSe.

Figure 3.3 shows a tall DOS peak well below the Fermi level. In both figures, the Fermi level is given as a vertical (blue) line at 0.0 *Ry*. This peak is composed of mostly Se-*s* (lime green), with less than 3% from all the other states. In Figure 3.3 this peak appears approximately between  $-1.1$  *Ry* and  $-0.9$  *Ry*. As we approach the Fermi level, two other peaks appear between  $-0.4$  *Ry* and  $-0.2$  *Ry* below the Fermi energy for both figures. These two peaks are composed of both Se-*p* (blue) and Fe-*d* (green) states, with a small contribution from the Fe-*s* (dashed red) and Fe-*p* (orange) like states. The peaks end fairly abruptly, creating a gap between them and the next peak. This next peak is also approximately 0.2 *Ry* wide and contains the Fermi energy. It is comprised of mostly Fe-*d*,

with some Se-*p* states. At the Fermi level, we find that Fe-*d* is the largest contributor to the DOS. The exact values of the DOS at the Fermi level are given in Table 3.3.

The states excluded from Figure 3.3 (Se-d, Se-f, and Fe-f) do not show up in the energy range presented in these figures. This is because the Se *d*-states are found in the core, much further below the Fermi level, and even the Se *s*-states. Both Fe-f and Se-f are found far above the unoccupied bands shown in these figures. Trace amounts of contribution of these ignored states can be found near the Fermi level, as shown in Table 3.3, but are negligible in the discussion of DOS of these materials. This information is still of interest, as it is important in the implementation of the Gaspari-Gyorffy theory and tight-binding calculations discussed in later sections.

Table 3.3: Total and decomposed DOS of FeSe at the Fermi level, for both NRL-LAPW and Wien2k codes. Decomposed values do not add up to the total DOS due to the use of muffin-tin spheres. (Note: Wien2k does not calculate the *f* DOS states.)

Code	$N(E_F)$	$Fe_s$	$Fe_p$	$Fe_d$	$Fe_f$	$Se_s$	$Se_p$	$Se_d$	$Se_f$
NRL	44.82	0.03	0.40	36.71	0.01	0.01	1.18	0.21	0.06
Wien2k	46.66	0.02	0.40	32.60	0.00	0.00	1.16	0.20	0.00

### Photoemission of Iron-Selenium

Experimental groups have also performed photoemission studies on FeSe. This provides another way to validate DOS calculations performed by the codes used. Photoemissions of experiments are unable to obtain a full picture of the DOS like Figure 3.3. However, these experiments are able to provide an idea of the overall DOS picture. Figure 3.4 shows the photoemission measurements of FeSe from Yamasaki, et. al.[42] overlaid with Lorentz broadened figures of the NRL-LAPW DOS. The photoemission presented in Figure 3.4a is the data collected from the 690eV off resonance beam source (dashed orange line), with the NRL-LAPW total DOS with Lorentz broadening (solid red line.) The off resonance beam source represents the overall measurable DOS in the given energy range. Figure 3.4b

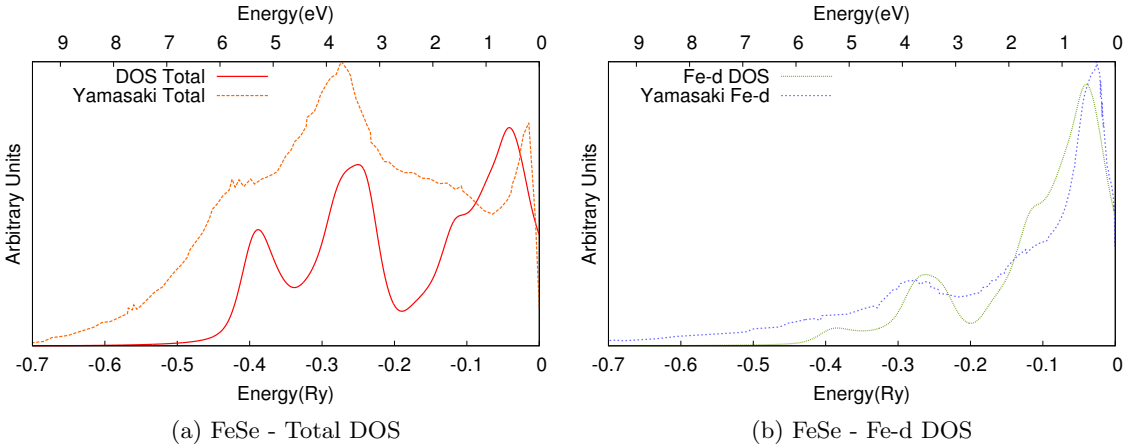


Figure 3.4: Comparison of the calculated Density of States of FeSe using NRL-LAPW with Lorentzian broadening and the photoemission spectrum from Yamasaki, et., al.[42]

provides the data collected from the subtraction of the off resonance beam with the “Fe- $2p$  anti-resonance” beam (dashed blue line) and the NRL-LAPW Fe- $d$  DOS with Lorentz broadening (solid green line.) The “Fe- $2p$  anti-resonance” beam has an energy just below the Fe  $2p$ - $3d$  absorption edge, 702eV.

Both Figure 3.4a and Figure 3.4b show the Lorentzian broadened DOS, at DOS peak positions compare well with the experimentally measured values. The Lorentz total DOS shows three main peaks, one around  $-0.4$  Ry,  $-0.25$  Ry and near the Fermi level. As found in ref. [42], the first two peaks are mostly hybridized Fe- $d$ /Se- $p$  states. The third peak is a slight hybridization of Fe- $d$ /Se- $p$ , but mainly pure Fe- $d$  states. This is confirmed by Figure 3.4b, where the Fe- $d$  states appear at the two lower energy levels ( $-0.4$  Ry and  $-0.25$  Ry) and largely near the Fermi level.

### Calculations of Energy Bands

Energy band plots of the system are given in Figure 3.5. The energy range of Figure 3.5a is the same range shown in the DOS Figure 3.3. As seen from the aforementioned Figure 3.5a

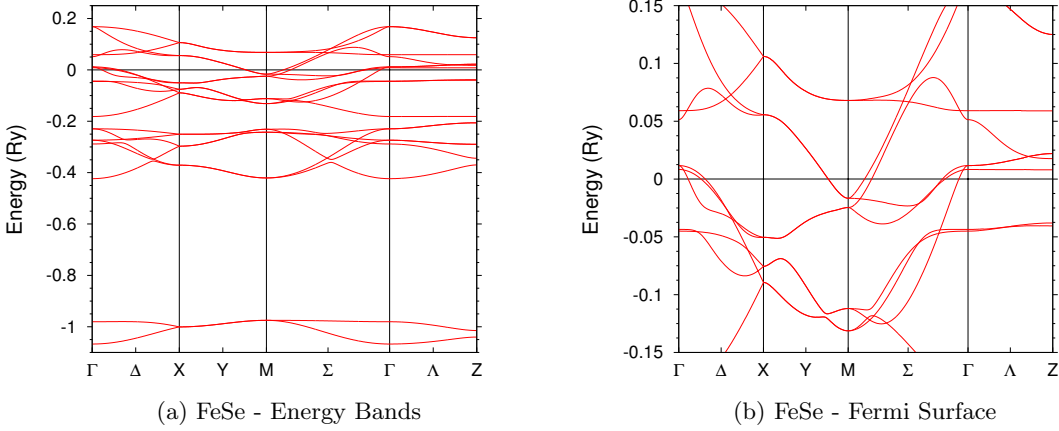


Figure 3.5: Band structures of tetragonal (PbO-like) FeSe using NRL-LAPW results. Zoomed in section of the Fermi surface is given in (b). Fermi level is given at 0.0Ry.

shows two bands at  $-1.0\text{ Ry}$  below the Fermi level, corresponding to the Se  $s$ -states. The gap between the Se- $s$  bands and the next set of bands at the  $\Gamma$  point is found to be approximately  $0.5\text{ Ry}$ . This next set of six bands are comprised of Se- $p$  and Fe- $d$  bands. A small gap is found between this set of Se-p/Fe- $d$  bands and the next set of ten bands. The gap between these calculated points was found to be the smallest between the  $Z$  and  $\Gamma$  points, with  $\Delta E = 24.6\text{mRy}$ . The following set of bands is also comprised of Se- $p$  and Fe- $d$  states, but mostly that of Fe- $d$ .

Figure 3.5b shows a zoomed in section of the energy bands around the Fermi level which we use to plot the Fermi surface. There are two notable features of the Fermi surface. At the  $M$  point, there are two intersecting electron pockets, while at the  $\Gamma$  point there exists three holes. Figure 3.6a and Figure 3.6b show the two- and three-dimensional representations of the Fermi surface using the Wien2k code, respectively. We see that these two electron pockets at the  $M$  point correspond to two elliptical cylindrical electron Fermi surfaces at the center of Figure 3.6. At the corners, the holes are shown as three concentric cylinders. These Fermi surface results are in agreement with those obtained by Subedi, et. al.[4].

Our band structure calculations agree well with each other and those calculated by previous groups[4,6,43,56]. It is important to note that the calculations performed by others,

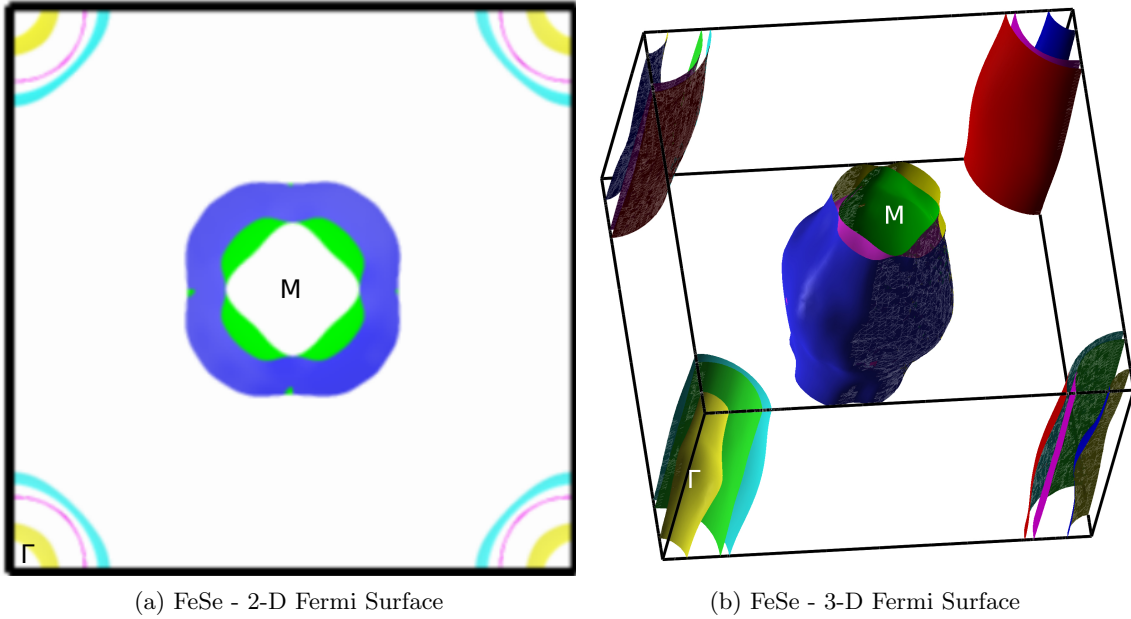


Figure 3.6: Calculated (a) 2-D and (b) 3-D Fermi surface of tetragonal (PbO-like) FeSe using Wien2k and XCrysDen programs.

used slightly different structural parameters. Even with this difference, the overall band structures are quite comparable. Differences can arise between all these calculations due to the parameters used, including that of k-point mesh size, muffin-tin radii, and methods used to calculated the DOS and band plots.

## 3.2 Electronic Structure of Iron-Tellurium

### 3.2.1 Introduction

Iron-tellurium is an isoelectronic material to that of iron-selenium. For one thing, FeTe is also found to be in the PbO structure, discussed in section 3.1.1, under ambient conditions[53, 57, 58]. Another similarity is the electronic configuration of the valence electrons. Both materials have Fe with 8 valence electrons, and Se/Te with 6 valence electrons, making them isoelectronic.

### 3.2.2 Computational Details

The computational details of FeTe calculations are very similar to that of FeSe in section 3.1.2. Both NRL-LAPW and Wien2k codes were used to perform calculations of the band structure of this material. Exchange-and-correlation was again approximated by the Hedin-Lundqvist implementation of the LDA. However, no calculations were performed with the GGA functional. This was mainly due to the fact that in FeSe the GGA calculations did not reveal anything interesting. Furthermore, k-point meshes (12x12x12 and 904), basis set size (6x6x6), muffin-tin radii (2.0 for both atom types) and  $r_{k_{max}}$  (8.5) were all kept the same as in FeSe. The only main differences in the calculations were the core states; Fe atoms continued to have the seven cores states of equilibrium argon and the Te atoms had fourteen core states (krypton + 4d states.) This resulted in 28 valence electrons once again. Local orbitals were applied as well with the same energies ( $-0.3\text{ Ry}$ ,  $0.2\text{ Ry}$  and  $-2.0\text{ Ry}$ ), but for 4s, 4p and 4d states, respectively.

### 3.2.3 Total Energy Calculations

While calculating the electronic structure of FeTe, structural optimization was performed using the NRL-LAPW code with the LDA functional. Again, this was performed through energy minimization with respect to the tetragonal lattice constants  $a$  and  $c$  and the internal Tellurium parameter  $z$ . It was found that the LDA calculations underestimate the experimental structural lattice parameters. Specifically, calculated optimized parameters found the volume to be approximately  $570\text{ a.u.}^3$  and  $c/a$  ratio to be 1.60.

Table 3.4: Structural parameters ( $V$ ,  $a$ ,  $c/a$ ,  $z$ ) and bulk mouduli ( $B$ ) of FeTe, both computational and experimental[59, 60].

$V$ (a.u. $^3$ )	$a$ (a.u.)	$c/a$	$z$	$B$ (GPa)
LDA				
568.1	7.081	1.60	0.260	55.4
Experiment				
617.4	7.224	1.641	0.280	36.0

Exact values of calculated and experimental parameters can be found in Table 3.4. The lattice parameter  $a$  is 1.9% below the measured experimental value, while  $c$  is 4.2% below. These underestimates are consistent with the calculations of FeSe. FeTe  $c/a$  ratio was found to be close to experiment, similar to the FeSe LDA calculations, but in this case underestimated. The internal parameter was also underestimated for the FeTe optimization. Bulk modulus was calculated and found to overestimate the measured experimental value[60].

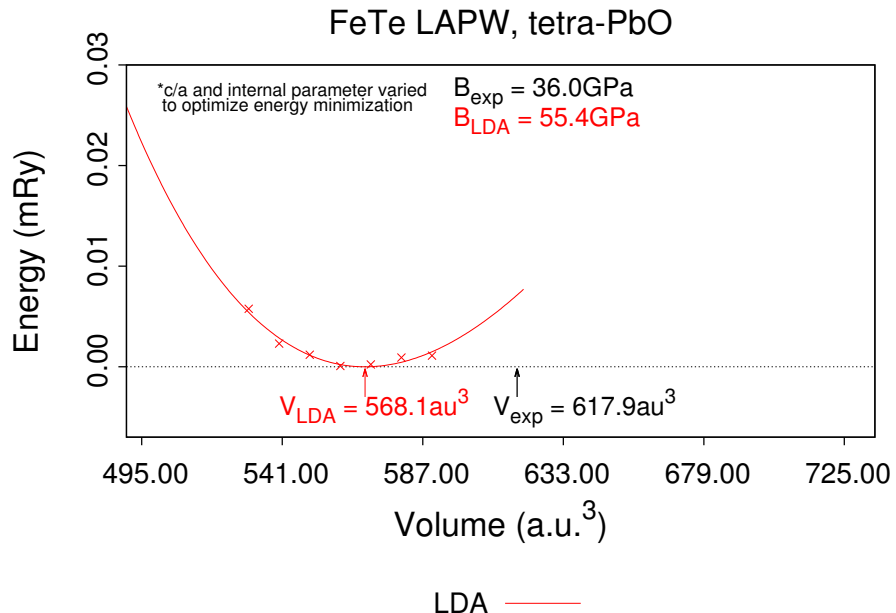


Figure 3.7: Total energy plots of the optimized LDA calculations of FeTe. The LDA underestimates the measured volume from Finlayson et. al.[59]

Figure 3.7 shows the structural optimized LDA total energy versus volume of FeTe. The solid (red) line is the fit of the NRL-LAPW LDA optimized calculations. This LDA energy curve is slightly sharper than that of the LDA calculations for FeSe and thus predicts a larger bulk modulus for FeTe. Overall this figure compares well with the LDA fit from Figure 3.2 in FeSe.

Since the differences between ferromagnetic and paramagnetic calculations of FeSe were minor, no ferromagnetic calculations were performed. Although FeTe is suggested to be on

the verge of magnetic instability, no experiments have found ferromagnetic order in FeTe.

### 3.2.4 Band Structure Calculations

The band structure calculations performed for FeTe used both the NRL-LAPW and Wien2k codes. These extra calculations provide us with another validation of the DOS calculated by the NRL-LAPW code. Similarly to the FeSe band structure calculations, the FeTe calculations used the experimental structural parameters given above.

### Calculated Density of States

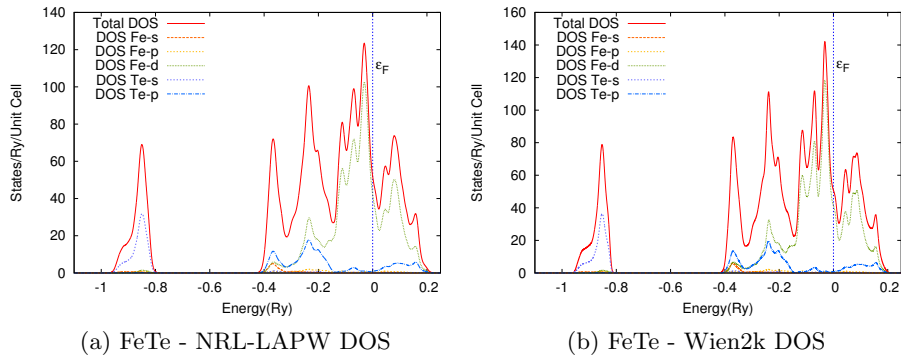


Figure 3.8: Density of States of tetragonal (PbO-like) FeTe using (a) NRL-LAPW results and (b) Wien2k results. Fermi level is given by the dashed vertical line at 0.0 Ry.

Figure 3.8 provides the total (red) and decomposed DOS of FeTe for both the NRL-LAPW and Wien2k programs. The Fermi level is given at 0.0  $Ry$  by a vertical (blue) line. In the figure, a peak comprised mainly of Te- $s$  (dotted blue) semicore states is found between  $-1.0\text{ }Ry$  and  $-0.8\text{ }Ry$  below the Fermi level. This is followed by a gap of approximately  $0.4\text{ }Ry$ . Two large DOS peaks appear between  $-0.4\text{ }Ry$  to  $-0.15\text{ }Ry$ . Their main contribution is from both Fe- $d$  (green) and Te- $p$  (dashed blue) DOS. There is a significant decrease in the total DOS around  $-0.15\text{ }Ry$ , but does not reduce to near zero, like that found in Figure 3.3 of FeSe. The fourth major peak is found between  $-0.15\text{ }Ry$  and  $0.05\text{ }Ry$ .

and contains the Fermi level. This energy range contains mostly Fe *d*-states, with small contribution of Te *p*-states. Above the Fermi level, we see some more Te-*p* and Fe-*d* states until another gap appears. The exact values of the total and decomposed DOS at the Fermi level is given in Table 3.5.

Table 3.5: Total and decomposed DOS of FeTe at the Fermi level, for both NRL-LAPW and Wien2k codes. Decomposed values do not add up to the total DOS due to the use of muffin-tin spheres.

Code	$N(E_F)$	$\text{Fe}_s$	$\text{Fe}_p$	$\text{Fe}_d$	$\text{Fe}_f$	$\text{Te}_s$	$\text{Te}_p$	$\text{Te}_d$	$\text{Te}_f$
NRL	50.83	0.05	0.43	41.07	0.01	0.03	0.87	0.17	0.10
Wien2k	49.92	0.04	0.42	40.66	0.00	0.01	0.80	0.02	0.00

The values in Table 3.5 suggest the Wien2k and NRL-LAPW results compare extremely well with each other. The decomposed DOS agree particularly well, with the exception of Te-*d* DOS. Which is unimportant and, as discussed previously, the Te-*d* like states appear well below the lowest DOS energy range pictured above.

Since FeSe and FeTe are isoelectronic in terms of the valence electrons the DOS, including the decomposed, have the same characteristic general features. For example, both Figure 3.8 and Figure 3.3 show four large DOS peaks at and below the Fermi level. However, the width of the gap between the first peak and the second peak is different for the two systems. There is a major difference in the DOS between FeSe and FeTe. That is, FeSe shows a small gap between the third and fourth peaks at  $-0.2 \text{ Ry}$ , which is not present at FeTe.

Table 3.5 suggests similar results to those of FeSe. Total DOS from the NRL-LAPW code is comparable to that of Table 3.3, but larger for FeTe. Since the NRL-LAPW total DOS is larger, the Fe-*d* DOS is also increased from the FeSe calculations. The remaining decomposed DOS values are very similar. Se-*p* is, however, a little larger than the Te-*p* values.

## Photoemission of FeTe

Experimental photoemission spectrum for FeTe were not found at the time of writing. We present here a predicted photoemission spectrum from our calculations, which is very similar to that of FeSe. However, Lorentz broadening was applied to the calculated NRL-LAPW DOS results. Total broadened DOS are given in Figure 3.9a and broadened Fe-*d* DOS are given in Figure 3.9b. A large peak of Fe-*d* like states are found near the Fermi level and correspond to the majority of the large peak in the total DOS figure. Between the energies of  $-0.3 \text{ Ry}$  and  $-0.15 \text{ Ry}$  there is another large peak in Figure 3.9a, which corresponds to a much smaller peak in the second figure. A final peak appears between  $-0.45 \text{ Ry}$  and  $-0.3 \text{ Ry}$  in both figures. These results are quite similar to those found for FeSe. If the results are indicative of the experimental photoemission, we would once again expect the two peaks between  $-0.45 \text{ Ry}$  and  $-0.15 \text{ Ry}$  are a hybridization of Fe-*d* and Te-*p* states. This assumption can also be obtained from the DOS Figure 3.8.

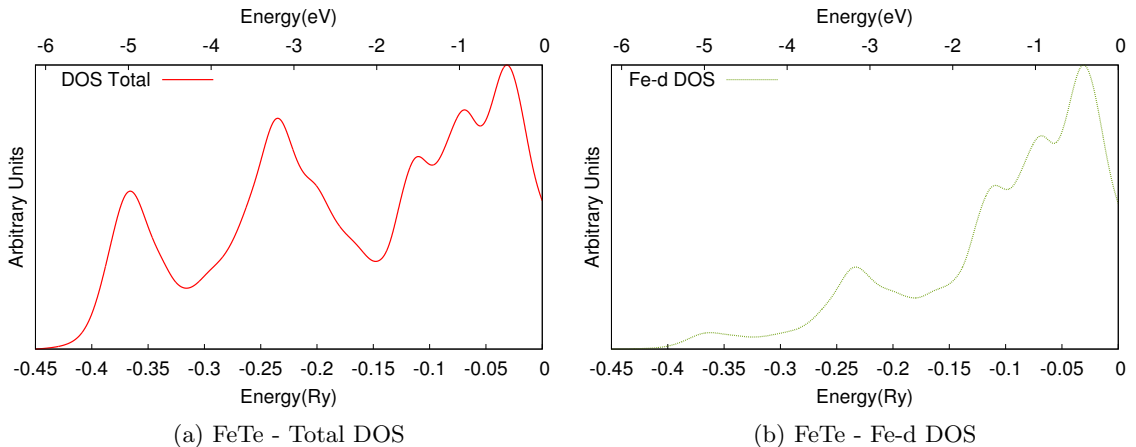


Figure 3.9: Calculated Density of States of FeTe using NRL-LAPW with Lorentzian broadening. These figures represent a prediction to experimental measurements of the photoemission spectrum of FeTe.

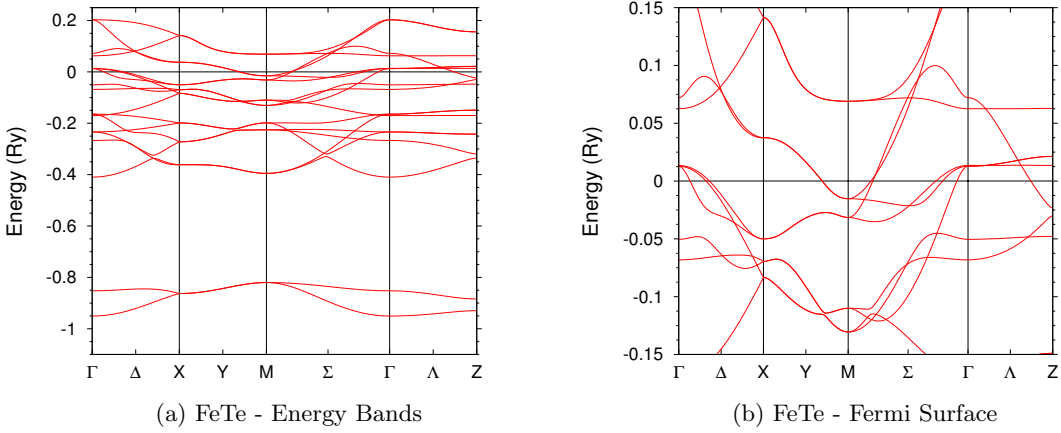


Figure 3.10: Band structures of tetragonal (PbO-like) FeTe using NRL-LAPW results. Zoomed in section of the Fermi surface is given in (b). Fermi level is given at 0.0Ry.

### 3.2.5 Energy Band Calculations

Figure 3.10 shows the energy bands of FeTe calculated with the NRL-LAPW with LDA are consistent with the DOS figure. This figure shows a set of two bands located between  $-1.0 \text{ Ry}$  and  $-0.8 \text{ Ry}$ . These bands are found to be Te *s*-like. A gap of approximately  $0.4 \text{ Ry}$  (compared with  $0.5 \text{ Ry}$  for FeSe) exists from these Te-*s* bands and the band around  $-0.4 \text{ Ry}$ . These remaining bands, ranging from  $-0.4 \text{ Ry}$  to  $0.2 \text{ Ry}$ , are comprised of Fe-*d* and Te-*p* like states. The Fermi level, solid horizontal (black) line, is given at  $0.0 \text{ Ry}$  and intersects these bands. Unlike the FeSe bands, no gap appears between the majority of Te-*p* and Fe-*d* bands.

Figure 3.10b shows a zoomed in section of the FeTe energy bands around the Fermi level. These results are very similar to those of FeSe. Again, we see two electron Fermi surfaces at the M point. At the  $\Gamma$  point, we show three hole Fermi surfaces. The two- and three-dimensional representations of the Fermi surface are predicted to be similar to the FeSe results of Figure 3.6.

### 3.3 Electronic Structure of $\text{FeSe}_x\text{Te}_{1-x}$

#### 3.3.1 Introduction

As discussed in the previous two introductions in this chapter (section 3.1.1 and section 3.2.1)  $\text{FeSe}_x\text{Te}_{1-x}$  also exists in the PbO structure under ambient conditions[5,53,57]. Both Se and Te are chalcogenides; elements found in the 16th column of the periodic table. This similarity allows for substitutions of Te for Se in the PbO type FeSe system. The substitution of Te in FeSe creates the  $\text{FeSe}_x\text{Te}_{1-x}$  system, where  $x$  is the concentration of Se and is between 0 and 1. There have been many studies of various concentrations of Se in the  $\text{FeSe}_x\text{Te}_{1-x}$  system. It was found that the  $x=0.5$  system superconducts at a higher temperature than FeSe at zero pressure, around 15 K[5,53,57]. The addition of Te in FeSe seems to increase the superconductivity temperature for all concentrations of  $x \geq 0.1$ [48]. Concentrations of Se less than 10% induces magnetic instability and destroys all superconductivity in the systems[48]. This section discusses LAPW calculations performed for the  $x = 0.75$ , 0.50, and 0.25 systems.

#### 3.3.2 Computational Details

FeSeTe system required many of the same computational details as both the FeSe and FeTe systems. Specifically, k-point meshes (196 and 904),  $rk_{max}$  values (8.5), core states (7 Fe, 9 Se and 14 Te), local orbital energies ( $-0.3\text{ Ry}$ ,  $0.2\text{ Ry}$  and  $-2.0\text{ Ry}$ ), and muffin-tin radii were kept at 2.0. However, certain input parameters had to be changed, due to the additional atoms needed in the computations. Since FeSeTe systems require the addition of Te atoms in the FeSe calculations, larger computational cells (supercells) had to be employed. In the FeSe and FeTe calculations, we had a total of 4 atoms in the computational cells, two Fe atoms and two Se or Te atoms. For the  $x = 0.5$  system, a simple substitution of one Se atom for one Te would seem adequate, but was not possible with the limitations of the codes used. Therefore, more atoms needed to be added to the computations of all FeSeTe systems. Specifically, the  $\text{FeSe}_{0.5}\text{Te}_{0.5}$  required 8 atoms (4 Fe, 2 Se and 2 Te) and

the  $\text{FeSe}_{0.75}\text{Te}_{0.25}/\text{FeSe}_{0.25}\text{Te}_{0.75}$  systems required 16 atoms per computational cell (8 Fe, 6/2 Se and 2/6 Te.) The computational cell size was doubled for the  $\text{FeSe}_{0.5}\text{Te}_{0.5}$  system and quadrupled for the  $\text{FeSe}_{0.75}\text{Te}_{0.25}/\text{FeSe}_{0.25}\text{Te}_{0.75}$  systems. The computation cell was increased along the direction of the  $c$  parameter, [001] direction for both systems. Larger computational cells also increased the computational time of these calculations from the simpler FeSe and FeTe calculations. The supercells calculations also required an increase in the basis set size from  $6 \times 6 \times 6$  to  $7 \times 7 \times 7$ , further adding to computational costs. Calculations for  $\text{FeSe}_{0.75}\text{Te}_{0.25}/\text{FeSe}_{0.25}\text{Te}_{0.75}$  were performed only with the Wien2k code, due to these factors. However, both codes were used to calculate  $\text{FeSe}_{0.5}\text{Te}_{0.5}$ .

### 3.3.3 Band Structure Calculations

We did not perform optimized calculations of any of the FeSeTe systems. With the underestimation of structural lattice parameters of both FeSe and FeTe using the LDA functional, the time required to perform such optimization, and the lack of necessity of these types of calculations for the later tight-binding based chapter, this would have been an overkill. Therefore, only the band structure calculations are discussed here. They were performed with experimental structural parameters as inputs to the codes.

Table 3.6: Experimental structural parameters ( $V$ ,  $a$ ,  $c/a$ ,  $z$ ) used for LAPW calculations of FeSe, FeTe,  $\text{FeSe}_{0.25}\text{Te}_{0.75}$ ,  $\text{FeSe}_{0.75}\text{Te}_{0.25}$ , and  $\text{FeSe}_{0.50}\text{Te}_{0.50}$  systems.

	$V$ (a.u. <sup>3</sup> )	$a$ (a.u.)	$c/a$	$z$
FeSe	530	7.1244	1.4656	0.260
$\text{FeSe}_{0.75}\text{Te}_{0.25}$	550	7.1708	1.4917	0.260
$\text{FeSe}_{0.50}\text{Te}_{0.50}$	580	7.1804	1.5667	0.2674
$\text{FeSe}_{0.25}\text{Te}_{0.75}$	605	7.2118	1.6129	0.250
FeTe	620	7.2299	1.6406	0.2496

Table 3.6 provides the structural parameters used in the calculations. These correspond to roughly the measured experimental parameters. The lattice parameter ratio,  $c/a$ , were

taken exactly from experiment, while the final lattice parameters used in the calculations were based on a volume rounded to the nearest 5  $a.u.^3$ . For example, FeSe was rounded to 530  $a.u.^3$ , while experimental volume was measured as 531.3  $a.u.^3$ . This was done for simplicity in the optimization calculations of FeSe and FeTe as well as errors associated with experimental findings.

Examining Table 3.6, some obvious trends appear. Specifically, the value of volume almost increases linearly as the concentration of Se is decreased. A similar trend also appears for  $a$  parameter and  $c/a$  ratio. This implies that as Te is added to the system, the unit cell begins to expand. This is most likely due to the increased size of Te atoms compared to Se. That is the atomic radius of Se is 1.98 and that of Te is 2.21, see table 9 of Kittel[23]. As discussed in Gomez, et. al.[53], the increased ionic radius increases the bond lengths in the materials. The internal parameters in this table are interesting on their own. Different experiments have found different values of  $z$  for all these materials. For example, FeTe was found to be 0.280 in one experiment, but as low as 0.250 in others. Therefore, it is hard to really understand how these internal parameters affect the materials experimentally. However, Panfilov, et. al. try to understand the influence of  $z$  with magnetic susceptibility. In Table 3.6 we see an increase of  $z$  from FeSe as we approach the 50% concentration material followed by a decrease as we approach FeTe. Using other measured internal parameters, we could possibly see a linear increase. Whatever the true nature of the internal parameter distance of these absolute pure materials, the values presented here are those used for our calculations.

As discussed, both the Wien2k and NRL-LAPW codes were used to perform the calculations of  $\text{FeSe}_{0.50}\text{Te}_{0.50}$ , and Wien2k was used to calculate  $\text{FeSe}_{0.75}\text{Te}_{0.25}$  and  $\text{FeSe}_{0.25}\text{Te}_{0.75}$ . The total and decomposed DOS of these systems can be found in Figure 3.11. Each figure has the Fermi level given at 0.0  $Ry$  by a vertical (blue) line. Figures 3.11 show two semicore states between  $-1.1 Ry$  and  $-0.8 Ry$ . The first semicore state is comprised of almost entirely Se-s, while the second is almost entirely Te-s. Above these semicore states exists a gap up to about  $-0.4 Ry$ . Between  $-0.4 Ry$  and  $-0.2 Ry$  there are two peaks comprised mainly

of Se/Te-*p* and Fe-d. A sharp decrease in the DOS is found around  $-0.2 \text{ Ry}$  for each figure. Another large peak appears between  $-0.2 \text{ Ry}$  and approximately  $0.0 \text{ Ry}$  which contains the Fermi level. This peak is comprised of mostly Fe-*d* states, with small contributions from Se/Te-*p* states. Overall, the features are quite similar between all four parts of the figure.

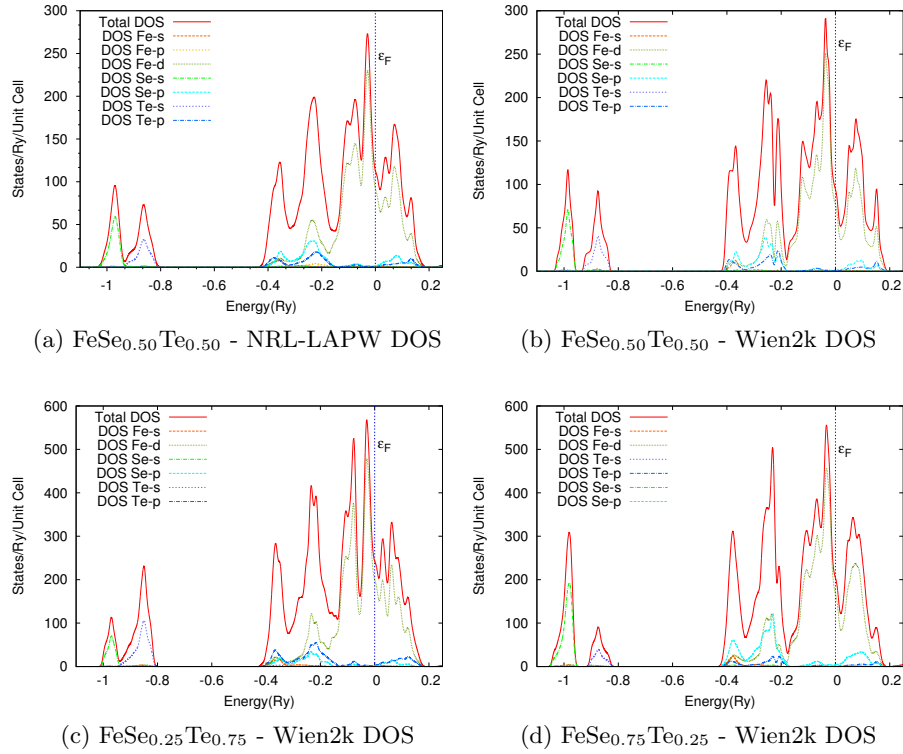


Figure 3.11: Density of States of tetragonal (PbO-like) (a)  $\text{FeSe}_{0.50}\text{Te}_{0.50}$  using NRL-LAPW results, (b)  $\text{FeSe}_{0.50}\text{Te}_{0.50}$  using the Wien2k results, (c)  $\text{FeSe}_{0.25}\text{Te}_{0.75}$  using Wien2k and (d)  $\text{FeSe}_{0.75}\text{Te}_{0.25}$  using Wien2k.

Figures 3.3, 3.8 and 3.11 provide a lot of important information for the general electronic structure of the FeSeTe systems. It seems that no matter the concentration number, features are prominent in all. Specifically, we continue to see DOS peaks around  $-1.0 \text{ Ry}$  that represent the majority of Se-*s* and Te-*s* DOS. To the right is a gap until the next DOS peaks appear. Just like those found in the FeSe and FeTe systems, these peaks contain mostly Fe-*d* and Se-*p* states. The peak that contains the Fermi level is once again dominated by

Fe-*d* contributions, with traces of the Se/Te *p*-states. In comparing these DOS the most striking difference of the alloy calculations from the pure FeSe and FeTe is the double peak.

Table 3.7: Total and decomposed DOS at the Fermi level for  $\text{FeSe}_x\text{Te}_{1-x}$  using the Wien2k code (NRL-LAPW  $\text{FeSe}_{0.50}\text{Te}_{0.50}$  is provided as well.) Decomposed values do not add up to the total DOS due to the use of muffin-tin spheres. Values are represented based on the entire unit cell size (8 atoms for  $x = 0.5$  and 16 atoms for  $x = 0.25/0.75$ .

$x$	$N(E_F)$	$\text{Fe}_s$	$\text{Fe}_p$	$\text{Fe}_d$	$\text{Se}_s$	$\text{Se}_p$	$\text{Se}_d$	$\text{Te}_s$	$\text{Te}_p$	$\text{Te}_d$
0.50 (NRL)	106.95	0.08	0.84	43.72	0.01	1.67	0.19	0.02	0.84	0.14
0.50 (Wien)	96.84	0.08	0.79	39.90	0.01	1.22	0.20	0.02	0.66	0.16
0.75 (Wien)	208.68	0.08	0.79	86.10	0.02	1.91	0.33	0.01	0.33	0.08
0.25 (Wien)	240.62	0.12	0.86	99.28	0.01	1.01	0.11	0.03	1.40	0.24

Table 3.7 gives the calculated total and decomposed DOS at the Fermi level for the three FeSeTe systems. These values are given in terms of the entire unit cell, meaning eight atoms for  $x = 0.5$  and sixteen atoms for  $x = 0.75/0.25$ . The results also show that the total and decomposed DOS have similar features regardless of the concentration number. Specifically, the total DOS are all comparable, when compared to a per atom basis, and the Fe-*d* DOS is the major contributor to the total DOS at the Fermi level. The Se/Te-*p* are the next highest contribution to the DOS at the Fermi level.

Figure 3.12a shows the energy bands of  $\text{FeSe}_{0.5}\text{Te}_{0.5}$  using the NRL-LAPW code. These bands look very comparable to the pure FeSe and FeTe results, but with near double the total number of bands in this energy region due to the use of an 8-atom supercell. Both Se-*s* and Te-*s* like bands appear between  $-1.1 \text{ Ry}$  and  $-0.8 \text{ Ry}$  energy range. The gap of approximately  $0.4 \text{ Ry}$  exists between these Se/Te-*s* bands and the next set of bands. Between  $-0.45 \text{ Ry}$  and  $0.2 \text{ Ry}$  we find the remaining sets of bands. The Fermi level is given as the horizontal (black) line at  $0.0 \text{ Ry}$ .

Figure 3.12b shows a zoomed picture near the Fermi level. This figure implies electron Fermi surface centered at the  $M$  high symmetry k-point. At the  $\Gamma$  point, there are four concentric holes at the center. A small closed hole section appears in the inner most. This

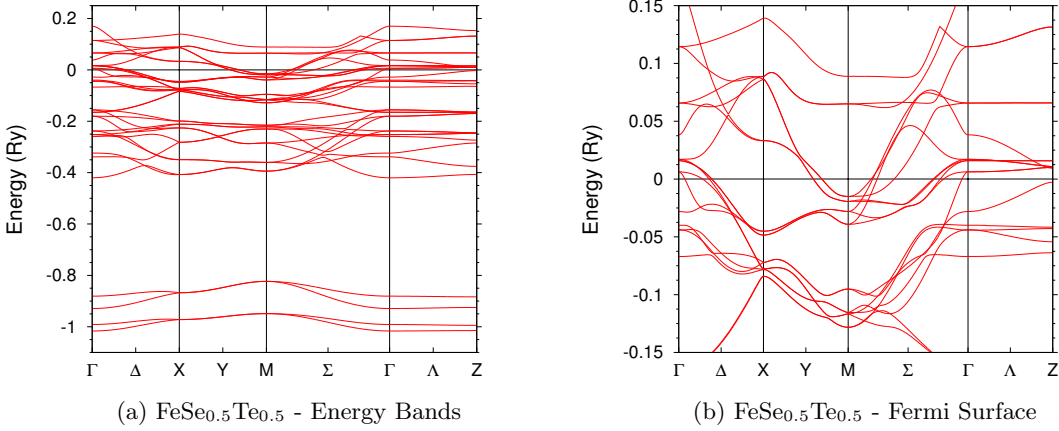


Figure 3.12: Band structures of tetragonal (PbO-like)  $\text{FeSe}_{0.5}\text{Te}_{0.5}$  using NRL-LAPW results. Zoomed in section of the Fermi surface is given in (b). Fermi level is given at 0.0Ry.

is very similar to the results of the Fermi surface for  $\text{FeTe}$ .

### 3.4 A Virtual Crystal Approach

The Virtual Crystal Approximation (VCA) within the LAPW method was studied for the  $\text{FeSeTe}$  system. It was initially thought that since  $\text{FeSe}$  and  $\text{FeTe}$  have similar atomic properties (DOS, bands, etc.) and are isoelectronic that the VCA could be applied to these calculations to predict other  $\text{FeSeTe}$  systems. In general the VCA can be performed with LAPW calculations by replacing the atomic sites with virtual atoms. These virtual atoms are given as a weighted average of the atomic number and valence electrons of the elements being replaced. Specifically, the atomic number is replaced by

$$Z_{VCA} = Z_A x - Z_B (1 - x) , \quad (3.1)$$

where  $Z_{A/B}$  are the atomic numbers of element  $A/B$ . The number of valence electrons are averaged in a similar way

$$ne_{VCA} = ne_A x - ne_B (1 - x) , \quad (3.2)$$

where  $ne_{A/B}$  is the number of valence electrons for element type  $A/B$ .

Usually this procedure works well for elements in the same row of the periodic table. However, Se and Te are in different rows and have different numbers of core electrons. Hence, the above way of performing a VCA calculation gave completely unphysical results. Therefore, we attempted an averaging of the self-consistent crystal potentials of the FeSe and FeTe systems to perform VCA calculations. This was done by taking the final potentials from the two systems and performing weighted averages to create approximate potentials to be used in direct non-self-consistent LAPW calculations.

### FeSeTe VCA Results Averaging Potentials

The final potentials from the self-consistent LAPW calculations for FeSe and FeTe were averaged to perform non-self-consistent LAPW DOS calculations for  $\text{FeSe}_{0.50}\text{Te}_{0.50}$  and  $\text{FeSe}_{0.15}\text{Te}_{0.85}$ . These calculations gave the DOS results presented in Figure 3.13 for (a) 15%/50% FeSe/FeTe and (b) 50% of each. We show that the “potentials VCA” does not produce reasonable total or decomposed DOS. Due to the lack of the self-consistent procedure, this approach cannot compute accurate wave functions. As a result, the method completely fails to calculate the DOS of these systems.

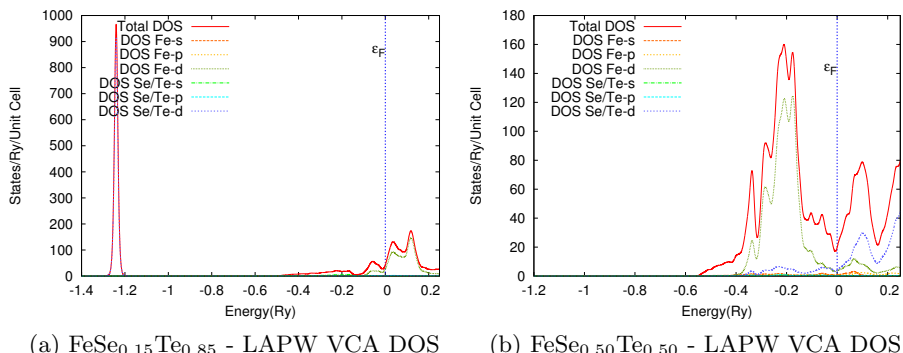


Figure 3.13: Density of States with Virtual Crystal Approximation potentials of (a)  $\text{FeSe}_{0.15}\text{Te}_{0.85}$  and (b)  $\text{FeSe}_{0.50}\text{Te}_{0.50}$ . Potentials of FeSe and FeTe using NRL-LAPW code were averaged to perform the DOS calculations.

## VCA for the FeAsSe System

As an example of a situation that a self-consistent VCA based on Equation (3.1) and Equation (3.2) works well, we performed calculations on the FeAsSe system, in which As and Se are neighbors in the periodic table. First, a direct self-consistent LAPW calculation for the FeAs system was performed. This was done using the same computational details expressed in Section 3.1.2. The only differences between the calculation of FeAs and FeSe were the atomic number of As (33) was used in replace of Se and the total valence electrons were changed from 28 to 26, due to As having one less valence electron.

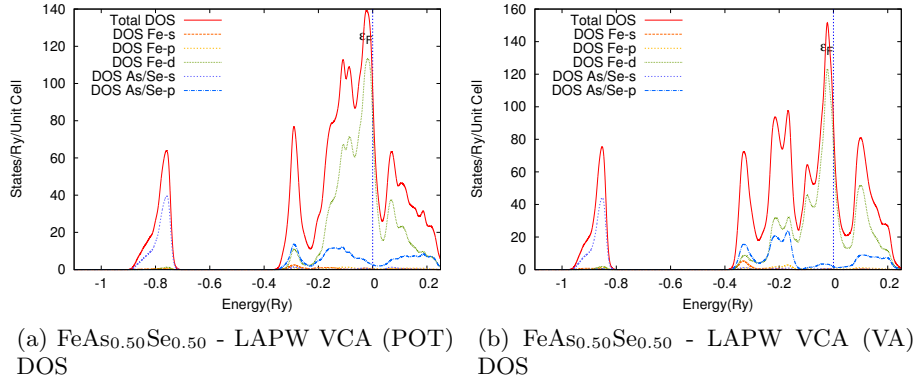


Figure 3.14: Density of States of  $\text{FeAs}_{0.5}\text{Se}_{0.5}$  with virtual crystal approximation applied via (a) potential averaging and (b) virtual atom approach. Potentials of FeAs and FeSe using NRL-LAPW code were averaged to perform the DOS calculations of (a). For (b), self-consistent calculations were performed using same input parameters, but with an averaged atomic number for As/Se, 33.5, and averaged valence electrons, 27.

Figure 3.14 gives the total and decomposed DOS for both the (a) “potentials VCA” and (b) the virtual atom VCA approach. It is clearly visible that the VCA method does an adequate job predicting the total and decomposed DOS of  $\text{FeAs}_{0.5}\text{Se}_{0.5}$ . The virtual atom calculations are more robust, as the self-consistent procedure calculates accurate wave functions. However, the Fermi level, decomposed DOS and overall shape of the DOS of the “potentials VCA” approach, compare well with the self-consistent virtual atom VCA.

With these calculations, it seems we can extrapolate a few interesting bits of information. For one, similar properties (DOS, decomposed DOS, bands, valence energy levels, etc.) between systems does not justify the use of the “potentials VCA”. Even though the LAPW results of FeSe and FeTe are similar, the lack of similar core electronic configurations are enough to impair the use of VCA for the FeSeTe systems. However, for similar core electronic configurations, the VCA is able predict the electronic structure of these systems. Specifically, the VCA calculations of  $\text{FeAs}_{0.5}\text{Se}_{0.5}$  were able to produce reasonable DOS for the FeAsSe system.

### 3.5 Final Conclusions

The electronic structure of FeSe, FeTe, and  $\text{FeSe}_x\text{Te}_{1-x}$  was calculated with two different codes using the Linearized Augmented Plane Wave method. Total energy, band structure, DOS, and prediction of experimental photoemission spectrum were performed in this chapter. Using these first-principles results, the contents of this chapter paint a fairly convincing picture of the overall electronic structure of the FeSeTe system. It was shown that optimized calculations using the local density functional underestimate the experimental lattice parameters by less than 5%, while generalized gradient approximation functional calculations overestimate by slightly more. Calculations of the DOS show very similar features between all three systems. Specifically, the DOS of all systems have the Se/Te-*s* states far below the Fermi level, in semicore states. Near the Fermi level, both Se/Te-*p* and Fe-*d* states play a major role in the overall DOS. Furthermore, the Fermi level is always found on the large sloped end of a Fe-*d* dominated peak. The band structure of all systems also looked quite comparable, with bands of similar type found in the same locations. Lorentz broadened DOS calculations have been shown to compare well to photoemission spectrum of FeSe and have been given as predictions for the FeTe and  $\text{FeSe}_{0.5}\text{Te}_{0.5}$  systems. Calculations using the virtual crystal approximation of the LAPW by averaging crystal potentials of FeSe and FeTe are inadequate, failing in predicting correct total and *l*-components of the DOS of the FeSeTe systems. Although the systems relate extremely well with each other, direct

calculations seem to be necessary for an adequate representation of the electronic structure of FeSeTe. On the other hand, VCA calculations on the FeAsSe system give reasonable results due to the proximity of As and Se in the periodic table.

## Chapter 4: Computational Studies of Superconductivity

### 4.0.1 Introduction

Superconductivity has been an interest to many physicists and engineers over the last hundred years. Due to this, first-principles based theories have been developed to understand and study the superconductivity of materials. This chapter discusses one of these first-principles based approaches to calculating superconductivity properties and the results of this method for the materials discussed in the previous chapters.

As mentioned in chapter 2 and chapter 3, the DOS results were used to calculate superconductivity properties using the Gaspari-Gyorffy-McMillan (GGM) theories of superconductivity. Some of these results have been previously discussed in references [11] and [47], but will be expanded in this section.

### 4.1 Gaspari-Gyorffy-McMillan Theories of Superconductivity

In 1968, McMillan[61] developed a formalism for calculating the electron-phonon coupling constant,  $\lambda$ , and critical superconductivity transition temperature,  $T_c$ , of the BCS theory[1]. The electron-phonon coupling constant is defined by the following formula

$$\lambda = \frac{\eta}{M < \omega^2 >} , \quad (4.1)$$

where  $\eta$  is the Hopfield parameter[62],  $M$  is the atomic mass and  $\langle \omega^2 \rangle$  is the renormalized phonon frequency. The Hopfield parameter is defined as

$$\eta = N(E_F) \langle I^2 \rangle , \quad (4.2)$$

using the Rigid Muffin-Tin Approximation (RMTA). Here,  $\langle I^2 \rangle$  is the electron-ion coupling matrix which is derived from multiple scattering theory and the RMTA prescription of Gaspari-Gyorffy[52]:

$$\langle I^2 \rangle = \frac{E_F}{\pi^2 N^2(E_F)} \sum_{l=0}^{\infty} \frac{2(l+1) \sin^2(\delta_{l+1} - \delta_l) N_{l+1} N_l}{N_{l+1}^{(1)} N_l^{(1)}} , \quad (4.3)$$

where  $N_l$  are the spin angular momenta ( $l$ ) components of the DOS at the Fermi level,  $N_l^{(1)}$  are the so-called free-scatterer DOS, and  $\delta_l$  are the scattering phase shifts calculated at the muffin-tin radius and at  $E_F$ . Free-scatterer DOS are calculated by

$$N_l^{(1)} = \frac{\sqrt{E_F}}{\pi} (2l+1) \int_0^{r_{mt}} r^2 u_l^2(r, E_F) dr \quad (4.4)$$

and scattering phase shifts are given by

$$\tan \delta_l(r_{mt}, E_F) = \frac{j_l'(kr_{mt}) - j_l(kr_{mt}) L_l(r_{mt}, E_F)}{n_l'(kr_{mt}) - n_l(kr_{mt}) L_l(r_{mt}, E_F)} , \quad (4.5)$$

where  $j_l$  are spherical Bessel functions,  $n_l$  are spherical Newnaun functions,  $L_l = u'_l/u_l$  is the logarithmic derivative of the radial wave function evaluated at  $r_{mt}$  (recall section 2.1.4), and  $k = \sqrt{E_F}$ . The  $\langle \omega^2 \rangle$  can be calculated through phonon calculations, or taken from

experimental measurements of the Debye temperature,  $\Theta_D$ , such that

$$\langle \omega^2 \rangle = \frac{1}{2} \Theta_D^2. \quad (4.6)$$

However, the Debye temperature can also be expressed by the Moruzzi formula[63]

$$\Theta_D = A \sqrt{\frac{r_0 B}{M}}, \quad (4.7)$$

where  $A$  is a proportionality constant between 131.6 and 213.4,  $B$  is the bulk modulus in GPa, and  $r_0$  is the Wigner-Seitz radius in atomic units.

The critical superconductivity transition temperature is given by the McMillan equation

$$T_c = \frac{\Theta_D}{1.45} \exp \left[ \frac{-1.04(1+\lambda)}{\lambda - \mu^*(1+0.62\lambda)} \right], \quad (4.8)$$

where  $\mu^*$  is the Coulomb pseudopotential which is usually between the value of 0.1 and 0.2. The Coulomb pseudopotential can also be calculated from the DOS at the Fermi level, given by the Bennemann-Garland equation

$$\mu^* = C_\mu \frac{N(E_F)}{1 + N(E_F)}, \quad (4.9)$$

where  $C_\mu$  is a constant chosen in such a way to make  $\mu^*$  equal to a specific value at equilibrium.

## 4.2 Superconductivity of the Iron-Selenium-Tellurium System

This section discusses the results of the GGM theory with the LAPW calculations performed by the NRL-LAPW code for the FeSeTe systems. As mentioned in section 3.1.3, experimental volumes and  $c/a$  were used to calculate the superconductivity properties of FeSe. The results were found to compare quite well with those found experimentally.

### 4.2.1 Superconductivity of FeSe

The computational study of superconductivity for the FeSe system using the GGM theory was discussed in a previous publication[47]. We found that the GGM theory was able to predict superconductivity for FeSe adequately at ambient pressure, but was not sufficient for the prediction of the significant increase of  $T_c$  under pressure. This section discusses the results from reference [47] in detail and some further calculations performed after publication.

Superconductivity calculations were performed using the same computational details discussed in section 3.1.2. However, further calculations were performed to understand the influence of muffin-tin radii on the GGM calculations of FeSe. Before talking about the GGM results, a brief discussion of the DOS calculations will be discussed for the FeSe using two different muffin-tin radii.

#### The Role of Muffin-tin Radii

All previously mentioned calculations for FeSe used the 2.0 *a.u.* muffin-tin radius discussed in section 3.1.2. However, the use of muffin-tins can influence the decomposed DOS and GGM calculations. As mentioned, the decomposed values of the DOS from the NRL-LAPW do not add up to the total DOS at any given energy level. This was due to the fact that the calculations for decomposed DOS take place only in the muffin-tin spheres. Therefore, it was important to understand how the choice of muffin-tin radii can influence the calculations of

the parameter  $\eta$ .

The choice of a muffin-tin radius of 2.0 *a.u.* came from the decision to perform optimized calculations. It is impossible to perform energy minimization correctly with the varying of the muffin-tin size. Varying the muffin-tin radius influences the total energy calculation and thus needs to be set constant. Since muffin-tin radii are not allowed to overlap in the NRL-LAPW code, a muffin-tin radius that met the overlap criteria at smaller volumes had to be chosen. The value of 2.0 *a.u.* was chosen, since this met the overlap criteria at low volumes and still provided good coverage of the atomic space in the computational cell. Once the optimization was complete and the choice of experimental parameters for the DOS calculations were made, secondary calculations with another muffin-tin radius were performed to understand their effect on the calculations.

Table 4.1: Total and decomposed DOS of FeSe at the Fermi level for two muffin-tin radii. Once again the decomposed values do not add up to the total DOS due to the use of muffin-tin spheres.

$r_{mt}$	$N(E_F)$	$Fe_s$	$Fe_p$	$Fe_d$	$Fe_f$	$Se_s$	$Se_p$	$Se_d$	$Se_f$
2.0	45.11	0.03	0.40	36.80	0.01	0.01	1.25	0.22	0.06
2.2	45.10	0.04	0.60	37.80	0.02	0.01	1.49	0.34	0.11

Table 4.1 shows the total and decomposed DOS of FeSe with experimental structural parameters for two different muffin-tin radii, 2.0 *a.u.* and 2.2 *a.u..* The first thing to note about this table, is how similar the DOS values are for each radii. In other words, the muffin-tin radius seems to have little influence on the total and decomposed DOS at the Fermi level for FeSe. Figure 4.1 shows the total and decomposed DOS of both muffin-tin radii calculations. Just like the table of values at the Fermi level, this figure shows remarkable similarities between the two calculations. A first glance would suggest there are no differences at all between the two. However, upon closer inspection, one can see that the decomposed Se-p states (lime green) in the first peak fill in the total DOS (red) slightly more in figure 4.1(b), where  $r_{mt} = 2.2$  *a.u..* The second difference that is noticeable is the

Se-p (blue) states filling more total space than the  $r_{mt} = 2.0$  *a.u.* figure. Although the figures are near identical and the values in Table 4.1 seem very close, the  $r_{mt} = 2.2$  *a.u.* calculations, do hint that some information of the decomposed DOS was missing from the 2.0 case. This is much more noticeable for the Se states. Due to these minor, yet potentially significant differences, superconductivity calculations must also be performed for both choices of muffin-tin radii.

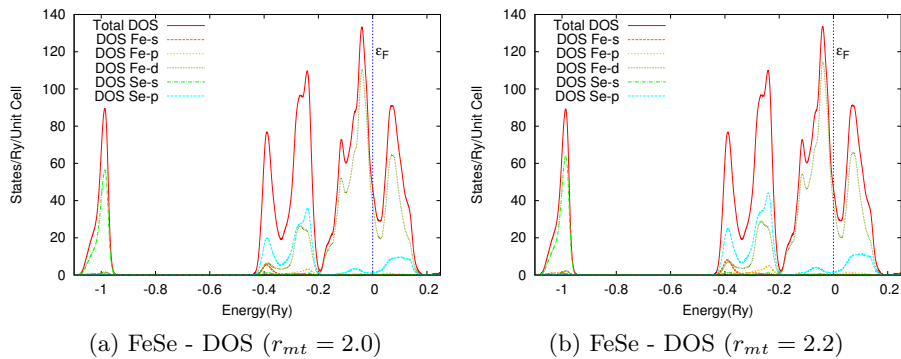


Figure 4.1: Density of States of tetragonal (PbO-like) FeSe using NRL-LAPW with (a)  $r_{mt} = 2.0$  and (b)  $r_{mt} = 2.2$ . Fermi level is given by the dashed vertical line, given at zero.

### GGM Calculations of Iron-Selenium

As Table 4.1 and Figure 4.1 have shown, the muffin-tin radius seems to have little influence on the DOS at the Fermi level and other energy levels. However, the muffin-tin radius can still potentially influence the calculations of the GGM theory. Table 4.2 gives the Hopfield parameters, electron-phonon coupling constants, and critical superconductivity temperature of FeSe using the two different muffin-tin radii. These calculations were performed using the experimental lattice parameters, experimental Debye temperature[45] and a Coulomb pseudopotential of 0.10. The table shows extremely similar results between the two different muffin-tin radii.

As discussed prior to the GGM calculations, the DOS at the Fermi level were quite

Table 4.2: Superconductivity related parameters (Hopfield parameters ( $\eta$ ), electron-phonon coupling constants ( $\lambda$ ) and critical superconductivity temperature ( $T_c$ )) of FeSe using the GGM theory with NRL-LAPW code for two muffin-tin radii. A Debye temperature of 240K[45] and  $\mu^* = 0.10$  were used for both sets of calculations.

$r_{mt}$ ( <i>a.u.</i> )	$\eta_{Fe}$ (eV/ $\text{\AA}^2$ )	$\eta_{Se}$	$\lambda_{Fe}$	$\lambda_{Se}$	$\lambda$	$T_c$ (K)
2.0	1.50	0.36	0.513	0.090	0.6032	4.6
2.2	1.52	0.46	0.522	0.115	0.6373	5.4

comparable between the two muffin-tin radii. However, the Se contribution to the DOS does increase some. This translates into a slightly larger Hopfield parameter and electron-phonon coupling constant of Se. The increases contribute to an increase to the total electron-phonon coupling constant and thus an overall higher superconductivity temperature. These increases are worth noting, but do not suggest any significant changes in the overall picture of the electron-phonon coupling mechanism of superconductivity.

Returning to the calculations performed with a muffin-tin radius of 2.0 *a.u.*, further GGM calculations were performed for FeSe under pressure. The 2.0 *a.u.* muffin-tin radius had to be used, as overlapping spheres became an issue at volumes less than 510 *a.u.*<sup>3</sup>. To perform these calculations under pressure, a modification of the Debye temperature had to be made in order to approximate its change under pressure. The following linear representation of the Debye temperature for our calculations is given as

$$\Theta_D = C(V - \bar{V}) + \bar{\Theta}_D , \quad (4.10)$$

where  $C$  is given as the slope between experimental Debye temperature[45] at ambient and 6.9 *GPa* pressures,  $\bar{V}$  is the experimental volume, and  $\bar{\Theta}_D$  is the experimental Debye temperature at ambient pressure.

Table 4.3 gives the total DOS at the Fermi level, Hopfield parameters, electron-phonon coupling constants, Debye temperature, Coulomb pseudopotential, and critical superconductivity temperature of FeSe using the GGM theory. Calculations were performed with the

Table 4.3: Total DOS at  $E_F$ ,  $N(E_F)$ , Hopfield parameters,  $\eta$ , electron-phonon coupling constants,  $\lambda$ , Debye temperature,  $\Theta_D$ , Coulomb pseudopotential,  $\mu^*$ , and critical superconductivity temperature,  $T_c$  of FeSe at various volumes, corresponding to pressures as high as 8GPa. Values are calculated using a fixed c/a and z taken from experimental parameters (c/a=1.4656 and z=0.260). Debye temperature is taken from equation (4.10).

V (au <sup>3</sup> )	$N(E_F)$ ( $\frac{\text{states}}{\text{Ry}/\text{cell}}$ )	$\eta_{Fe}$	$\eta_{Se}$	$\lambda_{Fe}$	$\lambda_{Se}$	$\lambda$	$\mu^*$	$\Theta_D$ (K)	$T_c$ (K)
530	45.11	1.52	0.46	0.522	0.115	0.637	0.10	240.0	5.4
460	37.05	2.15	0.47	0.558	0.088	0.646	0.0951	276.1	6.8
430	34.23	2.58	0.53	0.600	0.089	0.689	0.0930	291.4	8.5
420	33.44	2.75	0.55	0.618	0.088	0.707	0.0927	296.6	9.4

experimental lattice parameters and experimental internal parameter, with one calculation of the optimized internal parameter for comparison. The Coulomb pseudopotential in the table were taken from equation (4.9), such that the constant was made to make  $\mu^* = 0.10$  at the equilibrium volume. Again, these calculation were performed with a muffin-tin radius of 2.0 *a.u.*, with the exception of the 530 *a.u.*<sup>3</sup>, which used the  $r_{mt} = 2.2$  *a.u.* results.

Before discussing the pressure related GGM calculations, it is important to discuss the differences found between these results and those performed by other groups[4, 64]. These groups have performed calculations of superconductivity properties for FeSe under ambient conditions, but found the electron-phonon coupling constant to be insufficient at describing superconductivity. Linear response theory was used for describing the electron-phonon coupling interaction in the system. With this method, both groups found total electron-phonon coupling constants of around 0.15. The real reasons for this discrepancy are not certain, but possible reasons could be the use of Debye temperature is an oversimplification, or the Brillouin-zone sampling for the linear response calculations are not sufficiently converged. Further understanding of this dependency would be useful for future study of high-temperature superconductors. However, if the experimental results of Ksenofontov[45] are used to invert the McMillan equation, a total  $\lambda$  of 0.65 is calculated. This value is comparable to the one shown in Table 4.3.

Returning to the NRL-LAPW calculations, the calculated superconductivity temperature of FeSe at ambient pressure agrees reasonably well to experimentally measured  $8\text{ K}$ . The larger muffin-tin radius calculation raised the calculated  $T_c$  closer to experiment. Although the total DOS monotonically decreases with increasing pressure (decreasing volume,) the parameters  $\eta$  experiences monotonic increases. The calculated Debye temperature is also found to increase under pressure. Equations (4.1) and (4.6) tell us that both values are important for the electron-phonon coupling of the system. So although the  $\eta$  parameters increase to almost double at approximately  $8\text{ GPa}$ , the increased Debye temperature limits the increase in  $\lambda$ . However, we still see an increase in  $\lambda$  over the pressure range. Thus, the influence of the electron-phonon coupling of the system seems to increase only slightly under pressure. The overall trend of increasing superconductivity temperature exists for the calculations performed. However, these values do not get anywhere near the experimentally measured values of about  $37\text{ K}$  under  $6\text{ GPa}$ . This suggests that electron-phonon coupling mechanism is adequate for superconductivity of FeSe in equilibrium conditions, but not under pressure.

#### 4.2.2 Superconductivity of Iron-Tellurium

GGM calculations were performed for the FeTe system as well. For these calculations, the experimental structural parameters were used with the experiment internal parameter. FeTe was found to not superconduct under equilibrium conditions using the GGM theory. This is consistent with experimental measurements of the superconductivity of FeTe. Superconductivity calculations were performed using the same computational details as discussed in section 3.2.2.

The experimental Debye temperature of FeTe,  $290\text{ K}$ [65], was used to perform the GGM calculations. Like the FeSe calculations, a  $\mu^*$  of 0.1 was used at the equilibrium volume. Unlike FeSe, there were no experimental values of the Debye temperature of FeTe under pressure. Therefore, calculations of superconductivity under pressure were not performed for FeTe. Assuming the Debye temperature behaves similarly to the FeSe system, the

superconductivity of FeTe should remain non-superconducting under pressure.

Table 4.4: Total DOS at  $E_F$ ,  $N(E_F)$ , Hopfield parameters,  $\eta$ , electron-phonon coupling constants,  $\lambda$ , Debye temperature,  $\Theta_D$ , Coulomb pseudopotential,  $\mu^*$ , and critical superconductivity temperature,  $T_c$  of FeTe under ambient conditions. Experimental values are calculated using a fixed c/a and z taken from experimental parameters (c/a=1.6406 and z=0.250).

V (au <sup>3</sup> )	$N(E_F)$ ( $\frac{\text{states}}{\text{Ry}/\text{cell}}$ )	$\eta_{Fe}$ (eV/Å <sup>2</sup> )	$\eta_{Te}$ (eV/Å <sup>2</sup> )	$\lambda_{Fe}$	$\lambda_{Te}$	$\lambda$	$\mu^*$	$\Theta_D$ (K)	$T_c$
620	50.83	1.62	0.16	0.388	0.017	0.405	0.10	290.0	1.1

Table 4.4 gives the total DOS at the Fermi level, Hopfield parameters, electron-phonon coupling constants, Coulomb pseudopotential, Debye temperature and critical superconductivity temperature of FeTe under ambient conditions. The Hopfield parameters of FeTe are found to be comparable to those of FeSe. The total DOS is larger in the FeTe system than in FeSe. This leads to a larger value of the Hopfield parameter of Fe. However, the Hopfield parameter of Te is less than the Se of FeSe. This seems reasonable as the decomposed DOS of Te were less than the decomposed DOS of Se which were shown in Table 3.3 and Table 3.5. Although the Hopfield parameter of Fe is larger in this system, the Debye temperature is also much larger. This increase in Debye temperature suppresses the effects of the increased Hopfield parameter in the electron-phonon coupling interaction. The suppressed Fe contribution and generally reduced chalcogen Hopfield parameters produce a total electron-phonon coupling constant of  $\frac{2}{3}$  that of the FeSe system. All of these factors lead to a superconductivity temperature of 1.1 K. Although this value is not zero, it suggests the material is not superconducting under these conditions.

### 4.2.3 FeSeTe GGM Calculations

The GGM theory seems to accurately predict superconductivity in FeSe and suggests no superconductivity for FeTe under ambient conditions. With this success, it seems reasonable

to expect the theory to continue to provide an adequate representation of the superconductivity of the other FeSeTe systems. Due to limitations in the NRL-LAPW code, GGM theory based calculations were only performed for the  $\text{FeSe}_{0.5}\text{Te}_{0.5}$  system. These results are discussed in this section.

Table 4.5: Superconductivity related parameters (Hopfield parameters ( $\eta$ ), electron-phonon coupling constants ( $\lambda$ ), specific heat ( $\gamma$ ), Debye temperature ( $\Theta_D$ ), and critical superconductivity temperature ( $T_c$ )) of FeSe, FeTe, and  $\text{FeSe}_{0.50}\text{Te}_{0.50}$  systems using the GGM theory with NRL-LAPW code.

	$\eta_{Fe}$	$\eta_{Se}$	$\eta_{Te}$	$\lambda_{Fe}$	$\lambda_{Se}$	$\lambda_{Te}$	$\lambda$	$\gamma$ ( $\frac{mJ}{molK^2}$ )	$\Theta_D$ (K)	$T_c$ (K)
FeSe	1.52	0.46		0.522	0.115		0.637	6.23	240	5.4
$\text{FeSe}_{0.50}\text{Te}_{0.50}$	3.17	0.18	0.06	0.928	0.037	0.008	0.973	9.09	262	14.5
FeTe	1.62		0.16	0.388		0.017	0.405	6.19	290	1.1

Table 4.5 gives the Hopfield parameters, electron-phonon coupling constants, electronic specific heat, Debye temperature and critical superconductivity temperature of all three FeSeTe based systems under ambient conditions. As previously mentioned the results of FeSe and FeTe calculations compare well with each other. The addition of the 50% system follows these results as well, although significant increases in the Fe contribution are seen. For the  $\text{FeSe}_{0.50}\text{Te}_{0.50}$  system, we again see an increase of  $\eta_{Fe}$ , specific heat and Debye temperature from FeSe. In this calculation, we see the  $\eta_{Fe}$  is about double that of either FeSe or FeTe. Both chalcogen Hopfield parameters are reduced by almost half those found in the corresponding extreme systems. This is consistent with the DOS values discussed previously for  $\text{FeSe}_{0.50}\text{Te}_{0.50}$ . The increase in  $\eta_{Fe}$  is obviously the largest contribution to the electron-phonon coupling interactions of this system. These electron-phonon coupling constants calculate a specific heat of FeSe that is comparable to the experimental results of  $9.17\text{ mJ/molK}^2$ [66]. The calculated specific heat of FeTe is significantly underestimated from the experimental value of  $34\text{ mJ/molK}^2$ [67]. Experimental specific heat for  $\text{FeSe}_{0.50}\text{Te}_{0.50}$  could not be found, but our calculated value is a prediction of experiment.

The Debye temperature is found to be in between the FeSe and FeTe Debye temperatures. This increase in Debye temperature is much less significant than the large increase of  $\eta_{Fe}$ . Thus, the electron-phonon coupling constant is calculated to be nearly double the FeSe value. This increase in  $\lambda$  causes the calculated  $T_c$  to be larger than both FeSe and FeTe. The calculated value of  $T_c = 14.5 K$  agrees particularly well with the experimentally measured temperature of  $13 K$ [5].

Table 4.5 tells us a few things about the FeSeTe system as a whole. For one thing, the addition of Te into the FeSe system seems to greatly increase the electron-ion interactions of Fe. However, the chalcogenides themselves do not contribute much directly to the overall electron-ion and electron-phonon coupling interactions in the systems. The electron-phonon coupling interaction is able to predict superconductivity in both FeSe and the 50% system, while predicting no superconductivity for FeTe. While these Fe-based superconductors can be explained by electron-phonon interactions, other interactions are needed to explain more complex Fe-based superconductors.

Calculations of the LaFeAsO system were performed by various groups[68–70]. In all these calculations, the electron-phonon coupling constants of LaFeAsO were in agreement, approximately  $\lambda = 0.2$ . Reference [70] and reference [69] both performed the superconductivity calculations using linear response methods. However, the LAPW calculation based on ref. [68] find  $\lambda = 0.23$  when using the Gaspari-Gyorffy-McMillan theories of superconductivity. It is important to note that LaFeAsO is on the verge of magnetic instability, which may suggest spin-fluctuations are important in this material. Table 4.6 provides the superconductivity related parameters of the LaFeAsO material.

Gaspari-Gyorffy-McMillan calculations of the VCA based  $FeAs_{0.50}Se_{0.50}$  systems were also performed. Table 4.7 show the calculated total DOS, Hopfield parameters, electron-phonon coupling constants, Debye temperature and superconductivity temperature for the two VCA methods. The total DOS of these calculations are much higher than those found for FeSe and FeTe. Fe  $\eta$  values are significantly higher than FeSe and FeTe, but As/Se

Table 4.6: Calculated DOS and superconductivity related results of LaFeAsO using LAPW with LDA functional. Experimental critical temperature result is taken from Takahashi et. al[71]

LaFeAsO						
$N(E_F)$ (states/Ry/cell)						
	53.964					
	$N_s(E_F)$	$N_p(E_F)$	$N_d(E_F)$	$N_f(E_F)$	$\eta$ (eV/ $\text{\AA}^2$ )	$\lambda$
Fe	0.029	0.562	44.052	0.014	0.967	0.19
As	0.006	0.826	0.439	0.119	0.186	0.03
La	0.006	0.126	0.330	0.278	0.034	0.003
O	0.009	0.264	0.042	0.005	0.008	0.006
$\Theta_D$ (K)	$\lambda_{Total}$	$\mu^*$	$T_c$	$T_c$ (exp)		
319	0.23	0.13	0.0	45.0		

$\eta$  results are comparable. Using an estimated Debye temperature of 240 K, the experimental FeSe result, we calculate total  $\lambda$  values close to 1. This provides superconductivity temperatures much higher than those found for FeSe.

Table 4.7: Superconductivity related parameters (total DOS at Fermi level ( $N(E_F)$ )), Hopfield parameters ( $\eta$ ), electron-phonon coupling constants ( $\lambda$ ), Debye temperature ( $\Theta_D$ ) and superconductivity temperature ( $T_c$ ) of  $\text{FeAs}_{0.50}\text{Se}_{0.50}$  using the GG theory with NRL-LAPW code. The first row represents the direct LAPW VCA method, while the second is the averaged potential VCA method.

	$N(E_F)$ ( $\frac{\text{states}}{\text{Ry}/\text{unitcell}}$ )	$\eta_{Fe}$	$\eta_{As/Se}$	$\lambda_{Fe}$	$\lambda_{As/Se}$	$\lambda_{Total}$	$\Theta_D$ (K)	$T_c$ (K)
VCA	77.85	2.62	0.39	0.898	0.010	0.998	240	13.8
Pot/VCA	83.23	2.07	0.42	0.711	0.107	0.818	240	9.7

As of this dissertation, experimental and computational work on this material have not been published. It is possible this material is difficult to produce in a laboratory setting. Without an experimental Debye temperature to base further calculations on, the electron-phonon coupling and superconductivity temperatures are estimates. However, if a larger Debye temperature is used, such as the experimental FeTe value, the results still

provide electron-phonon coupling constants large enough to suggest superconductivity in this material.

#### 4.2.4 Final Remarks on Superconductivity

The results discussed here reiterate the claim that the Gaspari-Gyorffy-McMillan theories do an adequate job in predicting superconductivity of FeSe, as well as FeTe and  $\text{FeSe}_{0.50}\text{Te}_{0.50}$ . This affirms that the electron-phonon coupling cannot be ignored in these materials. For more complex iron-based superconductors such as LaFeAsO, the electron-phonon picture is clearly not enough. The calculations presented here, lead to the conclusion that electron-phonon coupling has a significant role in explaining superconductivity in the FeSeTe system under ambient conditions. However, spin-fluctuations may become important to explain the increase of  $T_c$  under pressure and also in the more complex Fe-based superconductors.

## Chapter 5: Tight-Binding Theory and Calculations

### 5.1 Tight-Binding Methodology

In Chapter 2, we discussed solving Schrödinger’s equation using first-principles methods. This chapter considers another approach for solving Schrödinger’s equation known as the Tight-Binding (TB) method of Slater and Koster (SK)[72]. This method is much faster than the first-principles based APW/LAPW methods owing to the size reduction of matrices that need to be diagonalized. The TB method was originally developed to reduce the large number of integrals involved in the Linear Combination of Atomic Orbitals (LCAO) method. The reduction considers the integrals to be adjustable constants, determined by first-principles calculations.

#### 5.1.1 Tight-Binding Basics

In the TB method, the atomic orbitals are replaced by Bloch sums, which give wave functions of the form

$$\psi_{\vec{k}i\alpha} = N^{-1/2} \sum_n e^{i\vec{k}\cdot\vec{R}_n} \psi_{i\alpha}(\vec{r} - \vec{R}_n - \vec{b}_i) , \quad (5.1)$$

where  $\vec{k}$  is the Bloch wave vector,  $N$  is the number of unit cells in the sum,  $\vec{R}_n$  are the lattice vectors,  $i$  is the atom type associated with position  $\vec{b}_i$ , and  $\alpha$  denotes both orbital and angular quantum numbers of the atomic site. The Hamiltonian with an orthogonal basis set can then be written as

$$H_{i\alpha,j\beta}(\vec{k}) = \sum_n e^{i\vec{k}\cdot\vec{R}_n} \int \psi_{i\alpha}^*(\vec{r} - \vec{R}_n - \vec{b}_i) H \psi_{j\beta}(\vec{r} - \vec{b}_j) d^3r. \quad (5.2)$$

The potential associated with this Hamiltonian is given by

$$V(\vec{r}) = \sum_{nk} V_k (\vec{r} - \vec{R}_n - \vec{b}_k). \quad (5.3)$$

Using equation (5.2), there are four different categories of integrals:

1. On-site integrals: Used if all three locations are on the same atom;
2. Two-center integrals: Used if the location of the potential is the same as one of the wave functions;
3. Three-center integrals: Used when the potential and wave functions are located at different sites;
4. Crystal field integrals: Used when wave functions come from the same site, but the potential is on a different site.

In general, implementations of the TB method use only the first two integral types. This means that the integrals only depend on the displacement between two atoms. The Slater-Koster TB formalism skips the calculation of the integrals all together and replaces them by disposable parameters. These parameters are determined by fitting first-principles calculations at points in the Brillouin zone. The best fit parameters can then be used to interpolate the eigenvalues in the entire Brillouin zone. The parameter fitting is done using a non-linear least squares method.

Using the SK formalism, there are three kinds of TB parameters: on-site, Hamiltonian and overlap parameters. On-site parameters describe the energy needed to place an electron in a specific orbital. The Hamiltonian parameters represent the orthogonal "hopping" of electrons from one atomic site to another. Overlap parameters express the "hopping" interactions between non-orthogonal orbitals. These parameters construct the TB Hamiltonian, which is given by

$$H = \sum_{i\alpha} h_{i\alpha} c_{i\alpha}^\dagger c_{i\alpha} + \sum_{ij,\alpha\beta} P_{i\alpha,j\beta} c_{i\alpha}^\dagger c_{j\beta}, \quad (5.4)$$

where  $ij$  are atomic sites,  $\alpha\beta$  are the atomic orbitals,  $h$  are the on-site parameters, and  $P$  are the Hamiltonian and overlap matrix elements. The total number of parameters that are used in a fit depends on the system in question.

### 5.1.2 NRL Implementation of the TB Method

In DFT, the total energy can be written as

$$E[\rho(r)] = \sum_i f(\mu - \varepsilon_i) \varepsilon_i + F[\rho(r)] , \quad (5.5)$$

where  $\rho(r)$  is the electronic density,  $\mu$  is the chemical potential,  $\varepsilon_i$  is the Kohn-Sham eigenvalue of the  $i^{\text{th}}$  electronic state and  $F[\rho(r)]$  is the total energy from Equation (2.3) without the kinetic term. The NRL-TB formalism uses a unique method for solving Equation (5.5), based on the fact that the Kohn-Sham method allows for an arbitrary shift in the potential. This is done by shifting the first-principles eigenvalues by a constant potential,  $V_0$ , prior to the fit. This potential is defined by

$$V_0 = F[\rho(r)] / N_e , \quad (5.6)$$

where  $N_e$  is the number of valence electrons in the system. The total energy with the shift applied becomes

$$E[\rho(r)] = \sum_i f(\mu' - \varepsilon'_i) \varepsilon'_i , \quad (5.7)$$

where ' designates the shifted value and specifically  $\varepsilon'_i = \varepsilon_i + V_0$ .

In general, on-site parameters have off-diagonal terms due to overlapping of wave functions. However, traditionally only the diagonal terms are used, as they correspond to the orbital type ( $s, p, d, \dots$ ). The on-site parameters take the form

$$h_{i\gamma} = a_{\alpha\gamma} + b_{\alpha\gamma} \rho_i^{2/3} + c_{\alpha\gamma} \rho_i^{4/3} + d_{\alpha\gamma} \rho_i^2 , \quad (5.8)$$

where  $\gamma$  denotes the orbital type,  $a, b, c, d$  are coefficients, and  $\rho$  is the atomic density of the atoms. In the NRL-TB formalism, the density of each atom is given by

$$\rho_i = \sum_{j \neq i} e^{-\lambda_{\alpha\beta}^2 R_{ij}} F(R_{ij}) , \quad (5.9)$$

where  $R_{ij}$  is the distance between the atomic sites  $i$  and  $j$ ,  $\alpha\beta$  is the type of atom on the  $ij$  sites, respectively, and  $\lambda$  is an additional fitting coefficient.  $F(R_{ij})$  is the smoothing function

$$F^{-1}(R_{ij}) = (1 + e^{\frac{R_{ij} - R_c}{l}}) . \quad (5.10)$$

Here,  $R_c$  is a constant cut-off distance, usually determined by the number of nearest neighbors to include in the fit. The smoothing function helps to limit the interactions between the current atom and distant atoms, which have a negligible effect relative to nearest neighbors.

Originally, the NRL-TB method used four types of on-site parameters corresponding to the  $s, p, d_{t_2g}$  and  $d_{e_g}$  interactions. This leads to sixteen coefficients for the on-site parameters. However, these can be expanded into  $s, p_x, p_y, p_z, d_{xy}, d_{xz}, d_{yz}, d_{x^2-y^2}$  and  $d_{3z^2-r^2}$ , requiring nine on-site parameters. These extra on-site parameters can potentially improve the fit for a system where common orbital symmetries are not found.

Both the Hamiltonian and overlap parameters take the form

$$P_\mu = (e_\mu + f_\mu R + \bar{f}_\mu R^2) e^{-g_\mu^2 R} F(R) , \quad (5.11)$$

where  $e, f, \bar{f}, g$  are coefficients and  $\mu$  corresponds to the type of orbital interactions involved. For example,  $\mu = ss\sigma$  would represent the interaction between the  $s$  orbital of the first atom with the  $s$  orbital of the second atom parallel to the bond,  $\sigma$ . Two other types of bonds are used in the NRL-TB implementation, which include  $\pi$  and  $\delta$  bonds[73–75]. For a binary system, there are a possible total of fourteen Hamiltonian parameters and fourteen overlap parameters. The fourteen orbital interactions for these parameters are  $ss\sigma, sp\sigma,$

$sd\sigma$ ,  $ps\sigma$ ,  $pp\sigma$ ,  $pp\pi$ ,  $pd\sigma$ ,  $pd\pi$ ,  $ds\sigma$ ,  $dp\sigma$ ,  $dp\pi$ ,  $dd\sigma$ ,  $dd\pi$  and  $dd\delta$ . Symmetry reduces the number of interactions when both atoms are the same element. The symmetry couples  $sp\sigma = -ps\sigma$ ,  $sd\sigma = ds\sigma$ ,  $pd\sigma = -dp\sigma$  and  $pd\pi = -dp\pi$ .

For monoatomic TB calculations, a total of 97 coefficients are used. As previously discussed, a total of seventeen coefficients are used to describe the on-site parameters for a single element. The on-site parameters include  $s$ ,  $p$ ,  $d_{eg}$  and  $d_{t_{2g}}$ , and the  $\lambda$  coefficient. The Hamiltonian and overlap parameters require four coefficients for all ten symmetric parameters above. This corresponds to eighty total coefficients for the Hamiltonian and overlap parameters.

For diatomic materials, a total of 346 parameters are used, disregarding the  $p$  and  $d$  symmetries of  $p_x = p_y = p_z$  and  $d_{eg}/d_{t_{2g}}$ . Instead of seventeen coefficients, there are now  $9*4 + \lambda \rightarrow 37$  for each element, which is 74 coefficients for the on-site parameters. Considering only the Hamiltonian parameters, we have  $4*10$  coefficients for each monoatomic pair of elements; for two types of elements, this comes to eighty coefficients. We also have  $4*14$  coefficients for the cross-element pair. The same goes for the overlap parameters, which gives a total of 272 coefficients between both sets of "hopping" parameters.

The NRL-TB method minimizes total energies, eigenvalues and their corresponding charge contributions by differencing the TB and first-principles calculations. This is done using a Levenberg-Marquardt least squares algorithm. Minimization is written as

$$\text{Minimize} \left[ \sum_s \left( w_s (E_s^{TB} - E_s^{LAPW})^2 + \sum_k \sum_b w_{sb} (\epsilon_{skb}^{TB} - \epsilon_{skb}^{LAPW})^2 + \sum_k \sum_b \sum_e w_{sbe} (q_{skbe}^{TB} - q_{skbe}^{LAPW})^2 \right) \right]^{1/2}, \quad (5.12)$$

where  $s$  are the lattice structures to be fit,  $k$  are the k-points used,  $b$  is the band number for a given k-point. The eigenvalues at band  $b$  of k-point  $k$  are given by  $\epsilon$  and  $q$  are the charges for a given eigenvalue. The weight for the total energy fit is  $w_s$ ,  $w_{sb}$  is the weight

of the  $b$  band for the  $s$  structure, and  $w_{sbe}$  is the weight of the charge type of eigenvalue of the given band and structure.

In the end, we are left with a Hamiltonian of size  $n \times n$ , where  $n$  is the total number of atoms and orbitals included. A Hamiltonian is calculated at each k-point. The number of on-site parameters and k-points are determined on a per system basis. This means that the size of the Hamiltonian will vary depending on the total number of atoms and the type of structure of the system. These details are discussed in the following sections.

## 5.2 Tight-binding Fits of FeSe and FeTe

### 5.2.1 Introduction

First-principles results of FeSe and FeTe from the NRL-LAPW code (see Chapter 3) were fit using the NRL-TB method, with up to eighteen bands from the LAPW results. These bands include the Se/Te s-states well below the Fermi level, the rest of the bands that are below the Fermi level, and around four bands above the Fermi level. Other calculations with 14, 16 and 20 bands were also performed, but either did not contain enough information to accurately fit, or contained more data than was necessary for a good fit. One fit concentrated on fitting the total energy accurately and used multiple lattice structures and volumes results from the LAPW. Another fit particularly focused on the energy bands, using only the experimental lattice parameter structure. The primary fit was based on the DOS and charge information of the systems under experimental equilibrium conditions. This DOS fit was later used to perform further calculations for the FeSeTe systems.

#### Tight-Binding Fitting Process

Before discussing the exact details of the fits and their final results, it is important to understand the process for finding good fits for a system. The process has several iterative steps. The first step is to perform first-principles based calculations of the total energy and energy bands, as a function of volume and  $c/a$ . For this study, this step was performed

using the NRL-LAPW code. These results were used as an input to the NRL-TB code, which follows Eq. (5.12), to produce good transferability of the TB parameters for different volumes. The starting point of the minimization requires an initial set of TB coefficients estimated from the eigenvalues calculated by the first-principles results. This is done by setting the first coefficient of each on-site parameter to the eigenvalues calculated at the  $\Gamma$  point. The remaining coefficients are usually set to values below  $10^{-3}$ , but sometimes need adjustments to begin iteration. Once the initial coefficients are set, these coefficients and some chosen structural lattice parameters are input into the fit. The initial structural inputs were chosen as the calculated LAPW equilibrium result, plus one or two results that straddle the calculated minimum LAPW total energy. Next, the TB fitting is run until convergence is met. Recall, the initial coefficients may need to be adjusted to achieve convergence. Once a good fit is produced, additional structures are added to the previous best fit coefficients and then input into the fitting process. This procedure is done as many times as desired, but is stopped once the additions start negatively effecting the fit. A good fit is usually considered to have an overall RMS band error of about  $10 \text{ mRy}$  and an overall total energy RMS error of  $1 \text{ mRy}$ . However, these values are only estimates and can vary from system to system.

During the fitting process, additional steps can be taken to produce good fits. For example, we can add block diagonalization of high symmetry k-points to the fit input. This can either be done prior to the initial fit or after a decent initial fit is obtained. Block diagonalization better determines the proper placement of bands and their angular momentum character. It is also common to remove certain parameters from the fit if they become too large or too small, which leads to poor fits. For the Hamiltonian and overlap parameters, this is done by setting the poor parameter to zero and forcing the program to ignore that term. For on-site parameters, removal is done by setting the first coefficient of the on-site parameter to a large value and freezing it there. We cannot set these parameters to zero because instead of removing them from the fit, this would set the orbital interaction at  $0.0 \text{ Ry}$ .

After a good fit is found the coefficients are used to calculate properties of the material, such as total energies, band structures, phonon frequencies, and DOS. A complete set of TB coefficients should be transferable, meaning the coefficients can be used to calculate properties for structural information not input directly into the fit. The TB based results can then be compared to first-principles results or experimental data.

This entire process requires intuition, as well as physical understanding from the user. There are no universal initial sets of coefficients that can be used for every case.

### 5.2.2 Computational Details

As mentioned in the previous section, FeSe and FeTe were fit emphasizing total energy, energy bands and DOS, in turn. For these fits, the 346 coefficient base was used. However, we reduced the number of coefficients owing to results found in section 3.1.4 and section 3.2.4. In these sections, the Fe-*p* and Se/Te-*d* states had little influence on the electronic structure of the fitted bands. This allowed for the removal of all the related parameters in the TB fits. Specifically, the Fe-*p* on-site parameters were frozen to 10 and the Se/Te-*d* on-site parameters were frozen to 20; The Hamiltonian parameters involving the Se/Te-*d* interactions were frozen to 0. However, the Hamiltonian parameters involving Fe-*p* interactions were allowed to vary because traces of Fe-*p* DOS were calculated in the fitted LAPW results; This reduced the fits of 346 coefficients to as low as 130 coefficients. However, some fits were performed with the Fe-*p* states included to see if they could provide a better fit. The following few paragraphs explain the explicit details of the best overall fits for the total energy, energy bands, and DOS/charge based fits.

All fits were based on the NRL-LAPW with LDA functional results of FeSe and FeTe. Recall, these calculations had four atoms in the unit cells. These TB fits contained the *s*, *p*, and *d* character for each atom. Therefore, the size of secular equation, or the size of the Hamiltonian at each k-point, was a 36x36 matrix, which was effectively reduced to 20x20 by removing the Fe-*p* and Se/Te-*d* states.

For the total energy based fit, seventeen structure calculations of FeSe were used to

fit the system. This fit also included calculations of the hexagonal NiAs-type structure of FeSe that experimentally only exists at high pressures, greater than 12  $GPa$ . A total of twelve PbO-type structures were fit, with the remaining five as NiAs-type. Both sets of structures were based on experimental  $c/a$  and  $z$ . This fit was also performed with most of the coefficients free to vary. Since Fe- $p$  states were found slightly above the included bands, these parameters were not frozen. However, Se- $d$  states have much higher energy and were therefore excluded from the system. The on-site parameters of Fe were reduced to the  $p$  and  $d$  symmetries, meaning  $p_x = p_y = p_z$ ,  $d_{xy} = d_{xz} = d_{yz}$  and  $d_{3r^2-z^2} = d_{x^2-y^2}$ . The Se on-site parameters used the  $p$  symmetries, but  $d$  was frozen, as mentioned above. This fit used only orthogonal interactions, which further reduced the overall number of coefficients used. Only bands of the calculated equilibrium PbO-type structure were included and the charges were weighted at zero. The overall RMS energy error was 0.83  $mRy$ , while the overall RMS band error was 14  $mRy$ . These errors suggest a very good fit of the FeSe system.

The total energy based fit of FeTe used less total structures in the minimization. Specifically, twelve NRL-LAPW with LDA calculations were fitted, with eight of these being based on the experimental  $c/a$  and  $z$ , and the remaining four were based on the optimized LDA calculations. Since the Fe- $p$  states were again found just above the contained bands, these Fe- $p$  on-site parameters were allowed to vary. The Te- $d$  on-site parameters were removed entirely. Only the  $p$  symmetry was used, meaning all the Fe- $d$  on-site parameters were allowed to vary independently. The fit was orthogonal and thus only the Hamiltonian parameters were used. Again, only bands of the calculated equilibrium structure of FeTe were fit, with no weight given to the charges. The overall total energy RMS error was 1.03  $mRy$ , while the overall RMS error of the bands was 18  $mRy$ .

Energy band based fits were performed for FeSe and FeTe using the NRL-LAPW with LDA functional band calculations with the nonuniform 904 k-point mesh. Total energy and charges were weighted to zero for both fits. The FeSe fit used only the experimental  $c/a$  ratio and  $z$  parameter calculation. Only the Se- $d$  on-site parameters were removed from the fit. The  $p$  symmetry was used for both atom types, while the Fe- $d$  on-site parameters

were all independent of each other, except for  $d_{xz} = d_{yz}$ . The overall RMS band error was found to be 10.7  $mRy$  and was a non-orthogonal fit. For FeTe, the best fit used the experimental calculation. This fit included the Fe- $p$  on-site parameters and allowed  $p_z$  to vary independently from  $p_x$  and  $p_y$ . The Fe- $d_{xz}$  and  $d_{yz}$  parameters were set equal to each other. The fit used an orthogonal base. The overall RMS band error for this fit was found to be 15.1  $mRy$ .

For DOS based calculations, only the experimental lattice parameter results of the NRL-LAPW code with LDA functional were fit for both the FeSe and FeTe systems using the uniform 196 k-point mesh. The total energy weight was set to zero, while the charge weight was set to 1/500. The Fe- $p$  and Se/Te- $d$  on-site parameters were removed. All other on-site parameters were allowed to vary independently of the others. Although the Fe- $p$  on-site parameters were removed, the "hopping" Fe- $p$  parameters were allowed to vary. Again, these fits were orthogonal based. An overall RMS band error for FeSe was 13.5  $mRy$ , with the largest band error found in the eighth band at 23.3  $mRy$ . For FeTe, the overall RMS band error was given as 12.5  $mRy$ , with the largest error of 18.5  $mRy$  at the third band. Both of these fits provide good RMS errors for the DOS.

### 5.2.3 Using the Fitted TB Parameters

#### Tight-Binding Total Energy Calculations

Figure 5.1 shows the total energy plots of FeSe in the PbO-like structure and NiAs-like structure using the TB results. Both of these structures were fit with the NRL-TB method. Recall, the fit used the experimental  $c/a$  ratio and  $z$  parameters as input. The energy curve of the PbO-like calculations predict the equilibrium volume to be 464.5  $a.u.^3$ . This is fairly close to the optimized NRL-LAPW with LDA functional result of 472.5  $a.u.^3$ . The NiAs-like calculations had a higher energy than the PbO-like calculations, which was expected. These calculations predict the equilibrium volume to be 371.1  $a.u.^3$ . The bulk modulus was also calculated for both curves. For the PbO-like structure, the bulk modulus was 142.2  $GPa$ , while the NiAs-like bulk modulus was 376.4  $GPa$ . These values are significantly higher than

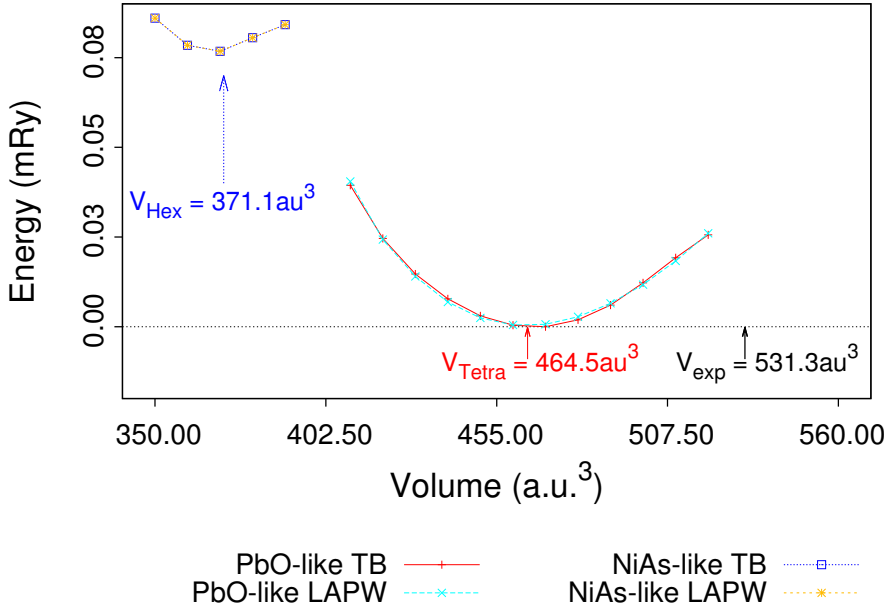


Figure 5.1: Total energy plots of the tetragonal PbO-like and hexagonal NiAs-like structures of FeSe using the Tight-Binding and LAPW results. The experimental volume is given by Kumar, et. al.[44].

the NRL-LAPW results.

Table 5.1 provides the final TB coefficients for the FeSe total energy-based fit. Only the coefficients that were included in the fit are presented in the table. Again, both the on-site and "hopping" parameters that contained Se-*d* interactions were removed from the fit. This fit was orthogonal, meaning all overlap coefficients were zero and not included in the table. A total of 141 coefficients were used in this fit.

Figure 5.2 shows the total energy plot of NRL-TB experimental PbO-like FeTe. This fit predicts the equilibrium volume of FeTe to be  $592.7 \text{ a.u.}^3$ , which is actually closer to experiment than the NRL-LAPW results. Again, this was fit using the experimental  $c/a$  and  $z$  parameters as well as some of the optimized results discussed in Chapter 3. Although some optimized results were involved in the fit, the NRL-TB parameters were unable to produce a smooth energy curve when using their structural input for the calculation of total energy. The bulk modulus was predicted to be much higher though, with a value of

Table 5.1: Tight-binding coefficients for the total energy-based FeSe fit.

	Coefficient		Coefficient		Coefficient
Fe $\lambda$	1.04074550	Se $c_y$	-98.35725403	Se $\bar{f}_{ss\sigma}$	-14.50675297
Fe $a_s$	0.79037011	Se $d_y$	2916.05786133	Se $g_{ss\sigma}$	1.00000000
Fe $b_s$	-3.85532212	Se $a_z$	0.57968342	Se $e_{sp\sigma}$	771.53460693
Fe $c_s$	-67.57326508	Se $b_z$	-3.73370290	Se $f_{sp\sigma}$	-9.23446369
Fe $d_s$	678.48132324	Se $c_z$	-98.35725403	Se $\bar{f}_{sp\sigma}$	-15.20286655
Fe $a_x$	0.24236092	Se $d_z$	2916.05786133	Se $g_{sp\sigma}$	1.00000000
Fe $b_x$	0.31090668	Fe $e_{ss\sigma}$	3.28240132	Se $e_{pp\sigma}$	-1009.02374268
Fe $c_x$	-16.81315804	Fe $\bar{f}_{ss\sigma}$	-0.86473733	Se $f_{pp\sigma}$	35.72250748
Fe $d_x$	382.52609253	Fe $\bar{f}_{ss\sigma}$	0.05531130	Se $\bar{f}_{pp\sigma}$	15.99949074
Fe $a_y$	0.24236092	Fe $g_{ss\sigma}$	0.56201625	Se $g_{pp\sigma}$	1.02264977
Fe $b_y$	0.31090668	Fe $e_{sp\sigma}$	-30.88891983	Se $e_{pp\pi}$	-782.80541992
Fe $c_y$	-16.81315804	Fe $f_{sp\sigma}$	-6.08658648	Se $f_{pp\pi}$	165.16844177
Fe $d_y$	382.52609253	Fe $\bar{f}_{sp\sigma}$	2.16998196	Se $\bar{f}_{pp\pi}$	-6.97320604
Fe $a_z$	0.24236092	Fe $g_{sp\sigma}$	1.00000000	Se $g_{pp\pi}$	1.00000000
Fe $b_z$	0.31090668	Fe $e_{pp\sigma}$	-67.24925995	Fe-Se $e_{ss\sigma}$	-41.44359589
Fe $c_z$	-16.81315804	Fe $f_{pp\sigma}$	-48.48870087	Fe-Se $f_{ss\sigma}$	1.99207914
Fe $d_z$	382.52609253	Fe $\bar{f}_{pp\sigma}$	-4.34365797	Fe-Se $\bar{f}_{ss\sigma}$	2.74189496
Fe $a_{yz}$	0.13475570	Fe $g_{pp\sigma}$	1.30933940	Fe-Se $g_{ss\sigma}$	1.08950412
Fe $b_{yz}$	1.03740466	Fe $e_{pp\pi}$	7.62456083	Fe-Se $e_{sp\sigma}$	-22.89796448
Fe $c_{yz}$	-7.07714081	Fe $f_{pp\pi}$	-21.28631592	Fe-Se $f_{sp\sigma}$	3.68959713
Fe $d_{yz}$	103.08042145	Fe $\bar{f}_{pp\pi}$	4.27471066	Fe-Se $\bar{f}_{sp\sigma}$	-0.01981102
Fe $a_{xz}$	0.13475570	Fe $g_{pp\pi}$	1.01926863	Fe-Se $g_{sp\sigma}$	1.00000000
Fe $b_{xz}$	1.03740466	Fe $e_{sd\sigma}$	688.70593262	Fe-Se $e_{pp\sigma}$	456.01055908
Fe $c_{xz}$	-7.07714081	Fe $f_{sd\sigma}$	-1.57170069	Fe-Se $f_{pp\sigma}$	-161.15187073
Fe $d_{xz}$	103.08042145	Fe $\bar{f}_{sd\sigma}$	-19.81988144	Fe-Se $\bar{f}_{pp\sigma}$	-77.10799408
Fe $a_{xy}$	0.13475570	Fe $g_{sd\sigma}$	1.31946468	Fe-Se $g_{pp\sigma}$	1.46372819
Fe $b_{xy}$	1.03740466	Fe $e_{pd\sigma}$	1.63366520	Fe-Se $e_{pp\pi}$	-0.73331422
Fe $c_{xy}$	-7.07714081	Fe $f_{pd\sigma}$	-0.40202522	Fe-Se $f_{pp\pi}$	2.01693559
Fe $d_{xy}$	103.08042145	Fe $\bar{f}_{pd\sigma}$	0.02712457	Fe-Se $\bar{f}_{pp\pi}$	-0.44232374
Fe $a_{x^2-y^2}$	0.32691318	Fe $g_{pd\sigma}$	0.49895480	Fe-Se $g_{pp\pi}$	1.00000000
Fe $b_{x^2-y^2}$	-2.46214676	Fe $e_{pd\pi}$	41.19293213	Fe-Se $e_{ps\sigma}$	-4.36741066
Fe $c_{x^2-y^2}$	-20.80017281	Fe $f_{pd\pi}$	-0.48562828	Fe-Se $f_{ps\sigma}$	0.44560799
Fe $d_{x^2-y^2}$	470.00033569	Fe $\bar{f}_{pd\pi}$	-1.31066239	Fe-Se $\bar{f}_{ps\sigma}$	0.23779057
Fe $a_{3z^2-r^2}$	0.32691318	Fe $g_{pd\pi}$	1.00262678	Fe-Se $g_{ps\sigma}$	0.85807490
Fe $b_{3z^2-r^2}$	-2.46214676	Fe $e_{dd\sigma}$	-211.16706848	Fe-Se $e_{ds\sigma}$	36.48718643
Fe $c_{3z^2-r^2}$	-20.80017281	Fe $f_{dd\sigma}$	69.73640442	Fe-Se $f_{ds\sigma}$	-7.03932142
Fe $d_{3z^2-r^2}$	470.00033569	Fe $\bar{f}_{dd\sigma}$	-5.48511600	Fe-Se $\bar{f}_{ds\sigma}$	-1.17955494
Se $\lambda$	0.99533558	Fe $g_{dd\sigma}$	1.00000000	Fe-Se $g_{ds\sigma}$	1.02513921
Se $a_s$	-0.53249127	Fe $e_{dd\pi}$	-494.84747314	Fe-Se $e_{dp\sigma}$	5.59420156
Se $b_s$	1.27065158	Fe $f_{dd\pi}$	-161.00187683	Fe-Se $f_{dp\sigma}$	0.40000820
Se $c_s$	-80.07010651	Fe $\bar{f}_{dd\pi}$	53.25040436	Fe-Se $\bar{f}_{dp\sigma}$	-0.16165493
Se $d_s$	1305.34814453	Fe $g_{dd\pi}$	1.20045924	Fe-Se $g_{dp\sigma}$	0.86289167
Se $a_x$	0.57968342	Fe $e_{dd\delta}$	1.23081100	Fe-Se $e_{dp\pi}$	0.33103356
Se $b_x$	-3.73370290	Fe $f_{dd\delta}$	-0.02199572	Fe-Se $f_{dp\pi}$	-1.23522317
Se $c_x$	-98.35725403	Fe $\bar{f}_{dd\delta}$	-0.07591713	Fe-Se $\bar{f}_{dp\pi}$	-0.01363446
Se $d_x$	2916.05786133	Fe $g_{dd\delta}$	0.76730031	Fe-Se $g_{dp\pi}$	1.00000000
Se $a_y$	0.57968342	Se $e_{ss\sigma}$	-503.39953613		
Se $b_y$	-3.73370290	Se $f_{ss\sigma}$	172.37174988		

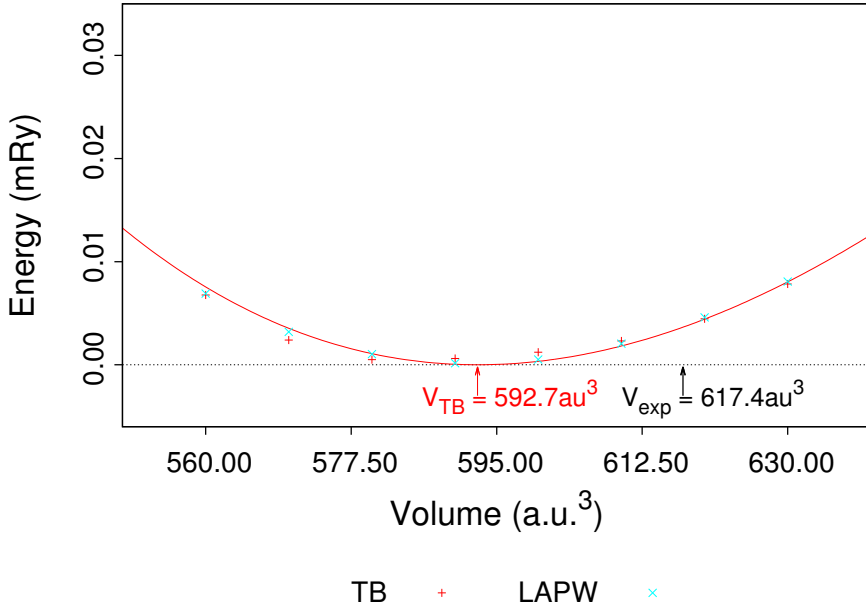


Figure 5.2: Total energy plots of the tetragonal PbO-like structure of FeTe using the Tight-Binding and LAPW results. Energy curves are based on the experimental  $c/a$  and  $z$  parameters. The experimental volume is given by Finlayson et. al.[59].

$$B = 111.8 \text{ GPa}.$$

Table 5.2 presents the final TB coefficients of the FeTe total energy-based fit. Again, only the used coefficients of the fit are presented in the table. The orthogonal base removed all overlap parameters from the fit. The coefficients that involved Se- $d$  were also removed from the fit. Like the FeSe total energy-based fit, we were left with a total of 142 coefficients for this fit.

### Tight-Binding DOS

The DOS were calculated using the NRL-TB method for FeSe and FeTe using the fits discussed above. Figure 5.3 shows the total DOS from the NRL-LAPW results overlaid with the NRL-TB results for FeSe (5.3a) and FeTe (5.3b). Both panels of the figure show that the NRL-TB DOS is in good agreement with the NRL-LAPW DOS. We see in Figure 5.3a that the TB results predict the same general structure of the DOS throughout the energy

Table 5.2: Tight-binding coefficients for the total energy-based FeTe fit.

	Coefficient		Coefficient		Coefficient
Fe $\lambda$	1.02972209	Te $c_y$	-137.05931091	Te $\bar{f}_{ss\sigma}$	10.04300117
Fe $a_s$	0.09575267	Te $d_y$	2359.46508789	Te $g_{ss\sigma}$	1.30949759
Fe $b_s$	0.41640300	Te $a_z$	0.53245795	Te $e_{sp\sigma}$	-160.84097290
Fe $c_s$	-14.95510197	Te $b_z$	-2.63346338	Te $f_{sp\sigma}$	-14.18148613
Fe $d_s$	441.91253662	Te $c_z$	-137.05931091	Te $\bar{f}_{sp\sigma}$	4.53809547
Fe $a_x$	0.18364148	Te $d_z$	2359.46508789	Te $g_{sp\sigma}$	1.00000000
Fe $b_x$	1.12482858	Fe $e_{ss\sigma}$	29.05669785	Te $e_{pp\sigma}$	15.11514091
Fe $c_x$	1.73608065	Fe $f_{ss\sigma}$	0.40643018	Te $f_{pp\sigma}$	-25.25718307
Fe $d_x$	253.34585571	Fe $\bar{f}_{ss\sigma}$	-0.95387864	Te $\bar{f}_{pp\sigma}$	3.17394638
Fe $a_y$	0.18364148	Fe $g_{ss\sigma}$	1.00000000	Te $g_{pp\sigma}$	0.94583619
Fe $b_y$	1.12482858	Fe $e_{sp\sigma}$	-21.99173737	Te $e_{pp\pi}$	5.10377073
Fe $c_y$	1.73608065	Fe $f_{sp\sigma}$	-1.13533175	Te $f_{pp\pi}$	9.46372223
Fe $d_y$	253.34585571	Fe $\bar{f}_{sp\sigma}$	0.70573235	Te $\bar{f}_{pp\pi}$	-1.31177461
Fe $a_z$	0.18364148	Fe $g_{sp\sigma}$	1.00358689	Te $g_{pp\pi}$	0.84871167
Fe $b_z$	1.12482858	Fe $e_{pp\sigma}$	-90.53153229	Fe-Te $e_{ss\sigma}$	240.07279968
Fe $c_z$	1.73608065	Fe $f_{pp\sigma}$	-11.25663948	Fe-Te $f_{ss\sigma}$	1.50956428
Fe $d_z$	253.34585571	Fe $\bar{f}_{pp\sigma}$	0.34707510	Fe-Te $\bar{f}_{ss\sigma}$	-13.64760685
Fe $a_{yz}$	0.04489431	Fe $g_{pp\sigma}$	1.16995907	Fe-Te $g_{ss\sigma}$	1.19084144
Fe $b_{yz}$	0.66583282	Fe $e_{pp\pi}$	-6.62954378	Fe-Te $e_{sp\sigma}$	-0.02917978
Fe $c_{yz}$	2.74255347	Fe $f_{pp\pi}$	0.25033674	Fe-Te $f_{sp\sigma}$	-0.61173117
Fe $d_{yz}$	146.71618652	Fe $\bar{f}_{pp\pi}$	0.80212069	Fe-Te $\bar{f}_{sp\sigma}$	-0.01327198
Fe $a_{xz}$	0.07733063	Fe $g_{pp\pi}$	1.11986697	Fe-Te $g_{sp\sigma}$	1.00000000
Fe $b_{xz}$	0.77684200	Fe $e_{sd\sigma}$	6.99462032	Fe-Te $e_{pp\sigma}$	-23.21195412
Fe $c_{xz}$	1.47659814	Fe $f_{sd\sigma}$	2.21414852	Fe-Te $f_{pp\sigma}$	4.16017389
Fe $d_{xz}$	92.89398956	Fe $\bar{f}_{sd\sigma}$	0.03787647	Fe-Te $\bar{f}_{pp\sigma}$	0.23646605
Fe $a_{xy}$	0.05892282	Fe $g_{sd\sigma}$	1.06904840	Fe-Te $g_{pp\sigma}$	1.00000000
Fe $b_{xy}$	0.78196758	Fe $e_{pd\sigma}$	1.78592587	Fe-Te $e_{pp\pi}$	22.04906845
Fe $c_{xy}$	4.92304897	Fe $f_{pd\sigma}$	-0.00601421	Fe-Te $f_{pp\pi}$	-0.37230593
Fe $d_{xy}$	248.75355530	Fe $\bar{f}_{pd\sigma}$	-0.02007457	Fe-Te $\bar{f}_{pp\pi}$	-0.99022424
Fe $a_{x^2-y^2}$	0.51376987	Fe $g_{pd\sigma}$	0.63095170	Fe-Te $g_{pp\pi}$	0.94103771
Fe $b_{x^2-y^2}$	-3.29643798	Fe $e_{pd\pi}$	17.81668091	Fe-Te $e_{ps\sigma}$	4.74289131
Fe $c_{x^2-y^2}$	-8.38007259	Fe $f_{pd\pi}$	-1.30904233	Fe-Te $f_{ps\sigma}$	3.54650187
Fe $d_{x^2-y^2}$	71.75533295	Fe $\bar{f}_{pd\pi}$	-0.45424110	Fe-Te $\bar{f}_{ps\sigma}$	-0.65310216
Fe $a_{3z^2-r^2}$	0.44508547	Fe $g_{pd\pi}$	0.93507278	Fe-Te $g_{ps\sigma}$	1.00000000
Fe $b_{3z^2-r^2}$	-3.62744522	Fe $e_{dd\sigma}$	-3.57384205	Fe-Te $e_{ds\sigma}$	5.80567646
Fe $c_{3z^2-r^2}$	-7.73834181	Fe $f_{dd\sigma}$	-1.20072317	Fe-Te $f_{ds\sigma}$	-3.48812079
Fe $d_{3z^2-r^2}$	110.53488159	Fe $\bar{f}_{dd\sigma}$	0.57797039	Fe-Te $\bar{f}_{ds\sigma}$	0.49473786
Te $\lambda$	0.97154653	Fe $g_{dd\sigma}$	1.00000000	Fe-Te $g_{ds\sigma}$	0.89484090
Te $a_s$	-0.54105967	Fe $e_{dd\pi}$	-74.66387177	Fe-Te $e_{dp\sigma}$	0.11398563
Te $b_s$	1.19040513	Fe $f_{dd\pi}$	-13.86046124	Fe-Te $f_{dp\sigma}$	0.22444968
Te $c_s$	-87.54024506	Fe $\bar{f}_{dd\pi}$	5.26521397	Fe-Te $\bar{f}_{dp\sigma}$	0.02621157
Te $d_s$	1212.64270020	Fe $g_{dd\pi}$	1.05696487	Fe-Te $g_{dp\sigma}$	0.82138622
Te $a_x$	0.53245795	Fe $e_{dd\delta}$	-1.36689031	Fe-Te $e_{dp\pi}$	7.33093166
Te $b_x$	-2.63346338	Fe $f_{dd\delta}$	0.38245890	Fe-Te $f_{dp\pi}$	-0.54200119
Te $c_x$	-137.05931091	Fe $\bar{f}_{dd\delta}$	-0.03361005	Fe-Te $\bar{f}_{dp\pi}$	-0.31840372
Te $d_x$	2359.46508789	Fe $g_{dd\delta}$	0.61812407	Fe-Te $g_{dp\pi}$	0.92311865
Te $a_y$	0.53245795	Te $e_{ss\sigma}$	6965.93408203		
Te $b_y$	-2.63346338	Te $f_{ss\sigma}$	-1280.79101562		

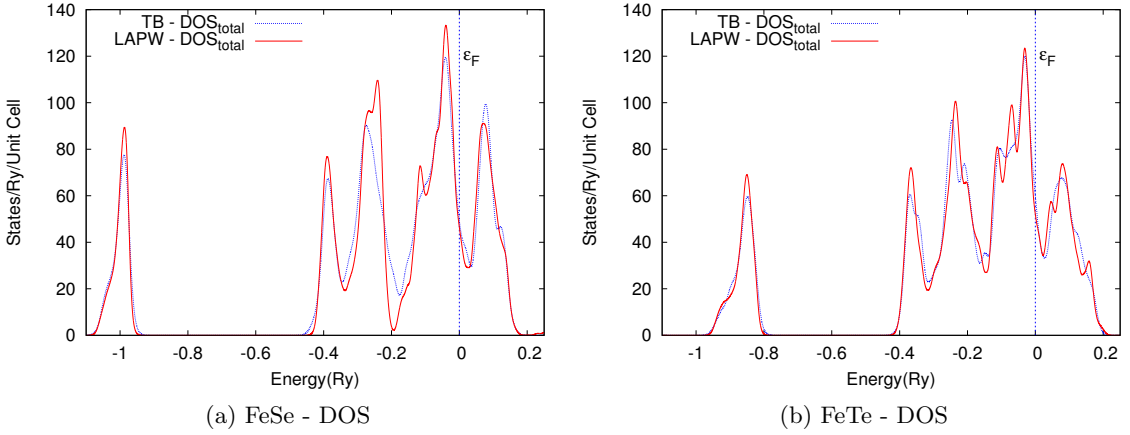


Figure 5.3: Comparison of the total Density of States between NRL-LAPW (solid red) and NRL-TB (dashed green) of tetragonal (PbO-like) (a) FeSe and (b) FeTe. Fermi level is given at  $0.0 \text{ Ry}$  by the vertical dashed (blue) line.

region, with minor discrepancies. The only difference is the prediction of a small gap in the LAPW DOS around  $-0.2 \text{ Ry}$ , which is shown as a minimum in the TB results. The TB DOS in Figure 5.3b for FeTe has very good overall agreement with the LAPW DOS.

Figure 5.4 shows the comparisons of the Se/Te-*p* and Fe-*d* DOS between the TB and LAPW methods. The differences in decomposed DOS are quite pronounced for the Figure 5.4a and Figure 5.4c. Between the energies of  $-0.20 \text{ Ry}$  and  $0.0 \text{ Ry}$  in Figure 5.4a, the decomposed *p* states are more than doubled for the TB method. This energy range shows a decrease in the Fe-*d* DOS for the corresponding Figure 5.4b. Outside this energy range, the TB decomposed DOS of FeSe are in good agreement with the LAPW decomposed DOS. The TB decomposed DOS of FeTe have a broader range of energies in which significant differences in the decomposed DOS are found. The energy range between  $-0.30 \text{ Ry}$  and  $0.0 \text{ Ry}$  in Figure 5.4c and Figure 5.4d shows approximately double the Te-*p* DOS and less decrease of the Fe-*d* DOS for the TB method. The remainder of the energies in these figures are in good agreement with decomposed DOS of the LAPW calculations.

Overall the DOS-based TB fit seem to suggest great agreement with the total DOS of the LAPW calculations. This is specifically true between  $-0.15 \text{ Ry}$  and  $0.1 \text{ Ry}$ , which

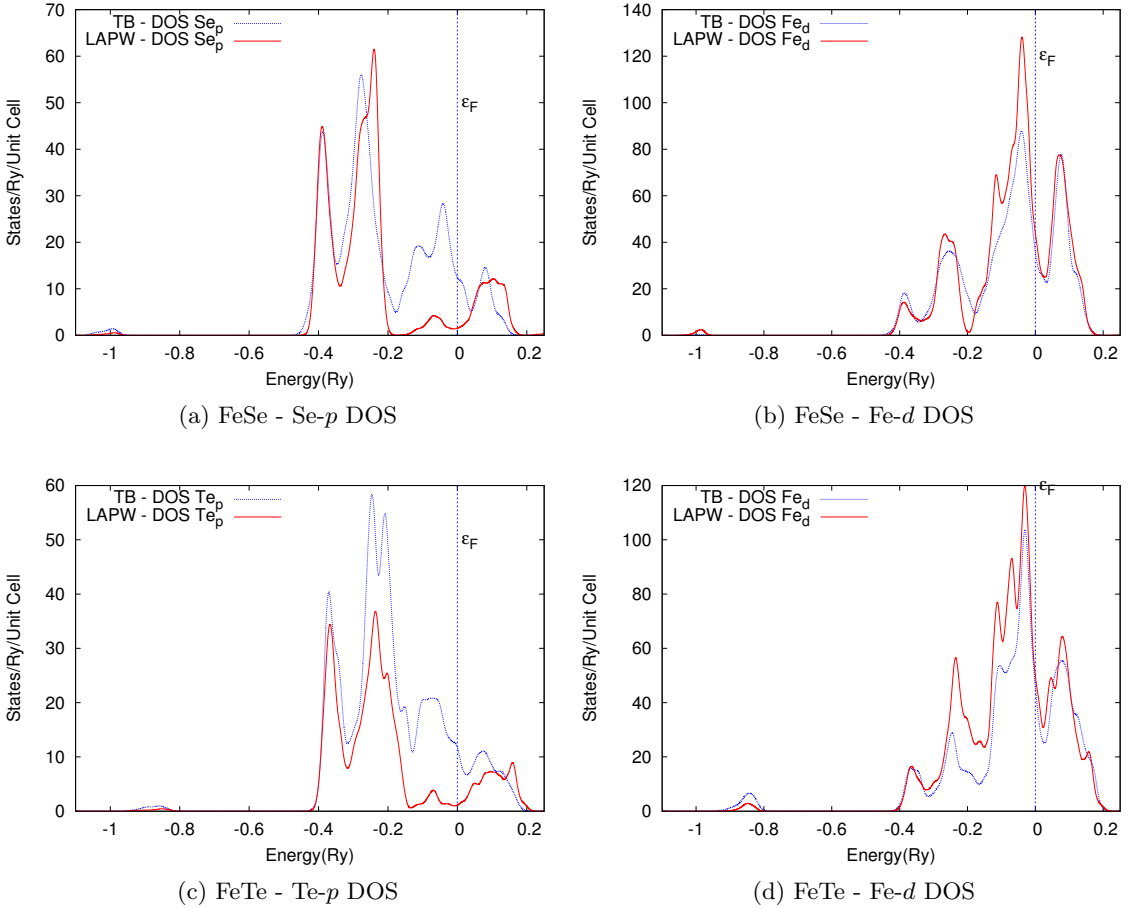


Figure 5.4: Comparison of decomposed Density of States between NRL-LAPW (solid red) and NRL-TB (dashed green) of tetragonal (PbO-like) FeSe and FeTe. Comparison between Se-*p* states of FeSe are given in (a), Fe-*d* of FeSe are given in (b), Te-*p* states of FeTe are shown in (c), and Fe-*d* of FeTe are shown in (d). Fermi level is given at 0.0 *Ry* by the vertical dashed (blue) line.

contains the Fermi level in both panels of Figure 5.3. Decomposed DOS produced by the TB method has substantially more Se/Te-*p* states. This difference is most sizable between  $-0.3$  *Ry* and  $0.0$  *Ry*. In this region, the Fe-*d* DOS is reduced by a comparable amount, due to the increase of Se/Te-*p*. The reasons for these significant difference in the decomposed DOS, while total DOS is essentially the same, is discussed in more detail below.

## Tight-Binding Bands

Energy bands calculations of the TB method were performed using the band-based fit discussed above. Figure 5.5 shows a comparison of the energy bands of the TB and LAPW methods. In both panels of this figure, we see comparable band structures between the two methods. Specifically, the energy ranges for the 18 bands that are plotted are comparable. The two methods agree particularly well for the Se/Te-*s* like bands, given between  $-1.1 \text{ Ry}$  and  $-0.8 \text{ Ry}$ . Outside of these *s* character bands, the remaining bands do not compare quite as well as the DOS results discussed previously. Some high symmetry points, specifically between X and M, do show good agreement between methods. In fact, the entire direction of the Brillouin zone, X-M, have TB energy bands that show the same features as the LAPW energy bands. The  $\Gamma$  point shows the worst agreement. Single degenerate bands that were predicted by the LAPW method are calculated to be double degenerate with the TB method. As mentioned previous, this is caused by misplaced eigenvalues at the k-points. Even though the overall RMS band error is good, the specific eigenvalues are not always found with the right angular momentum character.

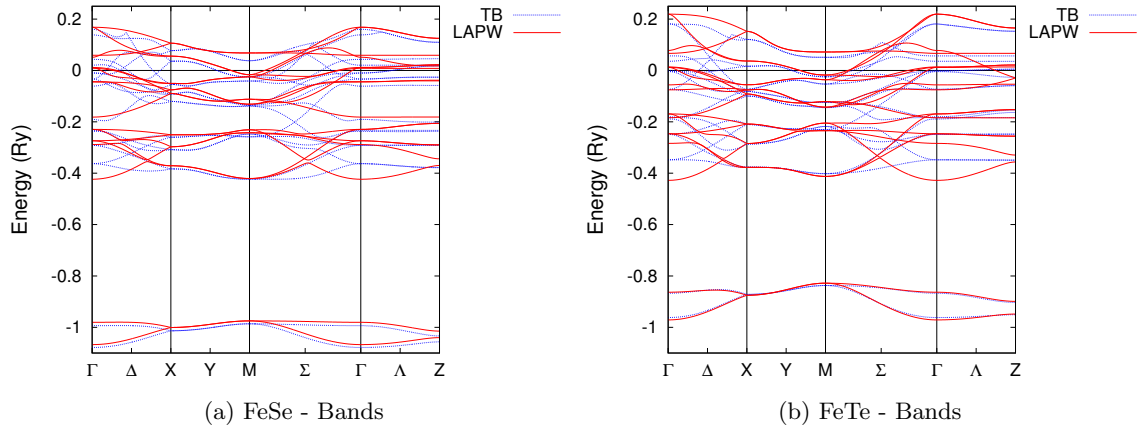


Figure 5.5: Comparison of the energy bands between NRL-LAPW (solid red) and NRL-TB (dashed green) of tetragonal (PbO-like) (a) FeSe and (b) FeTe. Fermi level is given at  $0.0 \text{ Ry}$  by the horizontal solid (black) line.

Recall, the results presented in Figure 5.5 are calculated based on the energy band-based fit and not the DOS-based fit discussed for the DOS comparisons. Therefore, the results in Figure 5.5 are not produced from the same parameters used in Figure 5.3. Even if the latter parameters are used to calculate the energy bands, the results look comparable to those presented here. So, even though the decomposed DOS compared well between the two methods, they do not fix the problem with eigenvalue placement at the k-points.

Block diagonalization of some high symmetry k-points were attempted to correct for the band issues. However, attempts at finding such block diagonalization were not satisfactory. The addition of charge information (see last term of Equation (5.12) in Section 5.1.2) to the fitting process was proposed to help with this issue. Although the charges did help reduce the RMS error of specific bands, it did not solve the problem at the  $\Gamma$  point. Even with this limitation, the overall DOS and bands calculated by the TB parameters compared well with the NRL-LAPW results.

### The Final TB Parameters

Table 5.3 provides the calculated on-site and "hopping" parameters from the uniform DOS k-point mesh fit of FeSe. We show the ten on-site parameters and six sets of Hamiltonian parameters that were used in this fit. The on-site parameters that were removed from the fit are not presented in this table. As for the Hamiltonian parameters, there were found to be six different distances between atom types within the provided cutoff length. Two of these distances are between the Fe atoms, one three are between Se atoms, and only one distance is found for the unlike atoms. There are no overlap parameters presented, as the fit was orthogonal. Recall the Fe-*p* "hopping" interactions were allowed to vary, while the Se-*d* "hopping" interactions were not. Therefore, the table shows the parameters involving Fe-*p* interactions have large values, which keep the Fe *p*-like states high above  $E_F$ . The parameters involving Se-*d* are all zero.

Table 5.4 shows the on-site and "hopping" parameters from the uniform DOS k-point mesh fit of FeTe. Similar to the FeSe parameters, there are ten on-site parameters and six

sets of Hamiltonian parameters. All removed on-site parameters are not shown in this table. The sets of Hamiltonian parameters are given for the six different atomic distances found within the cutoff length. Again, we have two sets from Fe-Fe distances, three sets from Te-Te distances and one set from a Fe-Te distance. Since this was also an orthogonal fit, no overlap parameters are calculated. The Hamiltonian parameters involving Fe-*p* interactions are nonzero, while parameters involving Se-*d* interactions are zero.

These final parameters from the Table 5.3 and Table 5.4 are used in the follow chapter (Chap.6.) The values of each parameter is different between the two tables, but the corresponding on-site and Hamiltonian parameters between the tables are comparable. For example, the Se/Te-*p* on-sites are similar between the two systems and Fe-*d*<sub>xy</sub> are identical in the two tables. Other parameters can be compared to see the similarities between the two fits. Overall these final parameters should prove adequate in use of the TB virtual crystal and coherent potential approximations discussed in the next chapter.

#### 5.2.4 Conclusions

Total energy, DOS, and energy bands calculations using the NRL-LAPW were fit with the TB method. The best parameters for these fits produced comparable total energies, DOS, and energy bands to those found in Chapter 3. Total energies compared with experiment just as accurately, and in the case of FeTe better than, as the LAPW results. The total DOS, but not the *l*-components of the DOS, calculated by the TB method showed very good agreement with the LAPW method DOS. This was specifically true near the Fermi level. The TB energy bands were in less agreement with those calculated by the LAPW method, showing small differences in some directions, which are not detectable in the DOS. This has shown that the produced parameters have good transferability to be used in further calculations. We consider the RMS error of 15 *mRy* in this fit, good enough to proceed with the tight-binding virtual crystal approximation and coherent potential approximation for the FeSeTe system. These methods and their results are discussed in Chapter 6.

Table 5.3: Final SK TB on-site and "hopping" parameters for the DOS-based FeSe fit.

On-site parameters						
Fe- <i>s</i>	0.110					
Fe- <i>d</i> <sub>yz</sub>	-0.108					
Fe- <i>d</i> <sub>xz</sub>	-0.128					
Fe- <i>d</i> <sub>xy</sub>	0.041					
Fe- <i>d</i> <sub>x<sup>2</sup>-y<sup>2</sup></sub>	-0.034					
Fe- <i>d</i> <sub>3z<sup>2</sup>-r<sup>2</sup></sub>	0.039					
Se- <i>s</i>	-0.968					
Se- <i>p</i> <sub>x</sub>	-0.211					
Se- <i>p</i> <sub>y</sub>	-0.192					
Se- <i>p</i> <sub>x</sub>	-0.017					
"Hopping" parameters						
$R_{Fe-Fe} = 5.03774$						
<i>ss</i> $\sigma$	<i>sp</i> $\sigma$	<i>pp</i> $\sigma$	<i>pp</i> $\pi$	<i>sd</i> $\sigma$	<i>pd</i> $\sigma$	<i>pd</i> $\pi$
<i>dd</i> $\sigma$	<i>dd</i> $\pi$	<i>dd</i> $\delta$				
-0.0264	-0.2634	5.4976	5.6591	0.0110	0.0509	-0.2874
-0.0040	-0.0335	0.0088				
$R_{Fe-Fe} = 7.12444$						
<i>ss</i> $\sigma$	<i>sp</i> $\sigma$	<i>pp</i> $\sigma$	<i>pp</i> $\pi$	<i>sd</i> $\sigma$	<i>pd</i> $\sigma$	<i>pd</i> $\pi$
<i>dd</i> $\sigma$	<i>dd</i> $\pi$	<i>dd</i> $\delta$				
-0.0017	0.1231	0.4302	0.8125	0.0251	0.740	0.2321
0.0505	0.0255	-0.0039				
$R_{Fe-Se} = 4.47883$						
<i>ss</i> $\sigma$	<i>sp</i> $\sigma$	<i>pp</i> $\sigma$	<i>pp</i> $\pi$	<i>sd</i> $\sigma$	<i>pd</i> $\sigma$	<i>pd</i> $\pi$
<i>dd</i> $\sigma$	<i>dd</i> $\pi$	<i>dd</i> $\delta$	<i>ps</i> $\sigma$	<i>ds</i> $\sigma$	<i>dp</i> $\sigma$	<i>dp</i> $\pi$
-0.0421	-0.0617	0.7255	0.4696	0.0000	0.0000	0.0000
0.0000	0.0000	0.0000	-0.1882	0.0145	-0.0189	-0.0686
$R_{Se-Se} = 7.10630$						
<i>ss</i> $\sigma$	<i>sp</i> $\sigma$	<i>pp</i> $\sigma$	<i>pp</i> $\pi$	<i>sd</i> $\sigma$	<i>pd</i> $\sigma$	<i>pd</i> $\pi$
<i>dd</i> $\sigma$	<i>dd</i> $\pi$	<i>dd</i> $\delta$				
-0.0021	0.0024	0.0329	0.0046	0.0000	0.0000	0.0000
0.0000	0.0000	0.0000				
$R_{Se-Se} = 7.12444$						
<i>ss</i> $\sigma$	<i>sp</i> $\sigma$	<i>pp</i> $\sigma$	<i>pp</i> $\pi$	<i>sd</i> $\sigma$	<i>pd</i> $\sigma$	<i>pd</i> $\pi$
<i>dd</i> $\sigma$	<i>dd</i> $\pi$	<i>dd</i> $\delta$				
-0.0024	0.0088	0.0344	0.0042	0.0000	0.0000	0.0000
0.0000	0.0000	0.0000				
$R_{Se-Se} = 7.40680$						
<i>ss</i> $\sigma$	<i>sp</i> $\sigma$	<i>pp</i> $\sigma$	<i>pp</i> $\pi$	<i>sd</i> $\sigma$	<i>pd</i> $\sigma$	<i>pd</i> $\pi$
<i>dd</i> $\sigma$	<i>dd</i> $\pi$	<i>dd</i> $\delta$				
-0.0047	0.0639	0.0504	-0.0002	0.0000	0.0000	0.0000
0.0000	0.0000	0.0000				

Table 5.4: Final SK TB on-site and "hopping" parameters for the DOS-based FeTe fit.

On-site parameters						
Fe- <i>s</i>	0.529					
Fe- <i>d</i> <sub>yz</sub>	-0.082					
Fe- <i>d</i> <sub>xz</sub>	-0.106					
Fe- <i>d</i> <sub>xy</sub>	0.041					
Fe- <i>d</i> <sub>x<sup>2</sup>-y<sup>2</sup></sub>	-0.051					
Fe- <i>d</i> <sub>3z<sup>2</sup>-r<sup>2</sup></sub>	0.072					
Te- <i>s</i>	-0.754					
Te- <i>p</i> <sub>x</sub>	-0.144					
Te- <i>p</i> <sub>y</sub>	-0.153					
Te- <i>p</i> <sub>x</sub>	-0.078					
"Hopping" parameters						
$R_{Fe-Fe} = 5.11229$						
<i>ss</i> $\sigma$	<i>sp</i> $\sigma$	<i>pp</i> $\sigma$	<i>pp</i> $\pi$	<i>sd</i> $\sigma$	<i>pd</i> $\sigma$	<i>pd</i> $\pi$
<i>dd</i> $\sigma$	<i>dd</i> $\pi$	<i>dd</i> $\delta$				
-0.1974	0.3592	7.9431	3.7398	0.0686	-0.2748	0.2662
-0.0079	0.0255	-0.0306				
$R_{Fe-Fe} = 7.22988$						
<i>ss</i> $\sigma$	<i>sp</i> $\sigma$	<i>pp</i> $\sigma$	<i>pp</i> $\pi$	<i>sd</i> $\sigma$	<i>pd</i> $\sigma$	<i>pd</i> $\pi$
<i>dd</i> $\sigma$	<i>dd</i> $\pi$	<i>dd</i> $\delta$				
0.02836	0.6355	0.8218	0.9121	-0.0382	-0.1125	0.1230
0.0404	0.0239	0.0024				
$R_{Fe-Te} = 4.67255$						
<i>ss</i> $\sigma$	<i>sp</i> $\sigma$	<i>pp</i> $\sigma$	<i>pp</i> $\pi$	<i>sd</i> $\sigma$	<i>pd</i> $\sigma$	<i>pd</i> $\pi$
<i>dd</i> $\sigma$	<i>dd</i> $\pi$	<i>dd</i> $\delta$	<i>ps</i> $\sigma$	<i>ds</i> $\sigma$	<i>dp</i> $\sigma$	<i>dp</i> $\pi$
0.0325	-0.0199	0.7119	0.5169	0.0000	0.0000	0.0000
0.0000	0.0000	0.0000	-0.1802	-0.1117	-0.0092	-0.0666
$R_{Te-Te} = 7.22988$						
<i>ss</i> $\sigma$	<i>sp</i> $\sigma$	<i>pp</i> $\sigma$	<i>pp</i> $\pi$	<i>sd</i> $\sigma$	<i>pd</i> $\sigma$	<i>pd</i> $\pi$
<i>dd</i> $\sigma$	<i>dd</i> $\pi$	<i>dd</i> $\delta$				
-0.0142	-0.0229	-0.0072	0.0286	0.0000	0.0000	0.0000
0.0000	0.0000	0.0000				
$R_{Te-Te} = 7.82274$						
<i>ss</i> $\sigma$	<i>sp</i> $\sigma$	<i>pp</i> $\sigma$	<i>pp</i> $\pi$	<i>sd</i> $\sigma$	<i>pd</i> $\sigma$	<i>pd</i> $\pi$
<i>dd</i> $\sigma$	<i>dd</i> $\pi$	<i>dd</i> $\delta$				
-0.0064	-0.0152	0.0120	-0.0044	0.0000	0.0000	0.0000
0.0000	0.0000	0.0000				
$R_{Te-Te} = 7.83712$						
<i>ss</i> $\sigma$	<i>sp</i> $\sigma$	<i>pp</i> $\sigma$	<i>pp</i> $\pi$	<i>sd</i> $\sigma$	<i>pd</i> $\sigma$	<i>pd</i> $\pi$
<i>dd</i> $\sigma$	<i>dd</i> $\pi$	<i>dd</i> $\delta$				
-0.0062	-0.0149	0.0122	-0.0048	0.0000	0.0000	0.0000
0.0000	0.0000	0.0000				

## Chapter 6: Coherent Potential Approximation and Related Methods

### 6.1 Virtual Crystal Approximation

A form of the Virtual Crystal Approximation (VCA) was discussed previously in Section 3.4. This section discusses the VCA used in conjunction with the TB method (TB-VCA). The TB-VCA uses the results of the TB method to calculate results for virtual systems. This is done by first performing TB fits for two systems to be coupled, using the coefficients of the final TB fit to create independent Hamiltonians for each system, and then averaging the Hamiltonians to produce a single Hamiltonian for the virtual system. The averaging is performed similarly to the potential-based VCA discussed previously. Specifically, the virtual system's Hamiltonian is given by

$$\mathbf{H}_{VCA} = \mathbf{H}_A(x) - \mathbf{H}_B(1-x) , \quad (6.1)$$

where  $\mathbf{H}_A$  and  $\mathbf{H}_B$  represent the Hamiltonian of systems  $A$  and  $B$ , respectively, and  $x$  is the concentration number between 0 and 1.

For this method of the VCA to produce reasonable results, the fits of both systems have to be performed using the same number of orbitals and bands, as well as similar starting parameters. For example, if an on-site parameter is removed from the fit of system  $A$ , then system  $B$  must also freeze this on-site parameter. Moreover, the removed on-site parameters must be frozen with similar values, otherwise the virtual Hamiltonian will have significantly different values compared to either of the original Hamiltonians. In addition, the individual fits should be of the same quality, i.e. have similar RMS errors.

## 6.2 FeSe<sub>x</sub>Te<sub>1-x</sub> with the Tight-Binding Virtual Crystal Approximation

We studied the substitutional alloy FeSe<sub>x</sub>Te<sub>1-x</sub> with the TB-VCA. This was accomplished using the Hamiltonians from the DOS-based fits discussed in Section 5.2.3. Calculations were done for  $x = 0.0, 0.1, 0.2, 0.3, 0.4, 0.5, 0.6, 0.7, 0.8, 0.9, 1.0$ . The values of 0.0 and 1.0 correspond to the TB results given in the previous chapter for FeTe and FeSe, respectively.

Figure 6.1 shows the total and decomposed DOS of the Te heavy TB-VCA calculations. The first panel shows the total (red) DOS with the same features as discussed in Section 5.2.3. It is clear that the Se/Te-*s* states (light blue) are the major contributors to the first peak of the total DOS. The Se/Te-*p* states (blue) supply the bulk DOS for the next three DOS peaks below the Fermi level. However, the Fe-*d* states (green) make up the majority of the DOS near and above the Fermi level. These results look similar to the DOS results discussed in Section 3.2.4. They differ primarily in the amount of Se/Te-*p* contribution to the total DOS. This is largely owing to the fact that these decomposed DOS are not limited to the projections onto the muffin-tin spheres.

The total DOS with  $x = 0.0$  is very close to the TB FeTe results Figure 5.3. However, it is not identical because we used the coherent potential approximation code, in which we set the self-energy to zero and calculate the DOS using Green's function (see Equation (6.5) in Section 6.3.) As the concentration of Te decreases (Figs. 6.1a→6.1f) the DOS peaks found between  $-0.4$  Ry and  $-0.15$  Ry change dramatically, merging into a single peak when  $x = 0.5$ . The contributions from the Se/Te-*p* states is also enhanced near the Fermi level. The biggest difference between these results and the NRL-LAPW results is the lack of two independent Se-*s* and Te-*s* peaks near the  $-1.0$  Ry energy level.

Figure 6.2 shows the total and decomposed DOS of the Se heavy TB-VCA results. These results are similar to those in Figure 6.1. The results of Figure 6.2(f) correspond to  $x = 1.0$  and the TB FeSe DOS found in the previous chapter. As mentioned for the TB results,

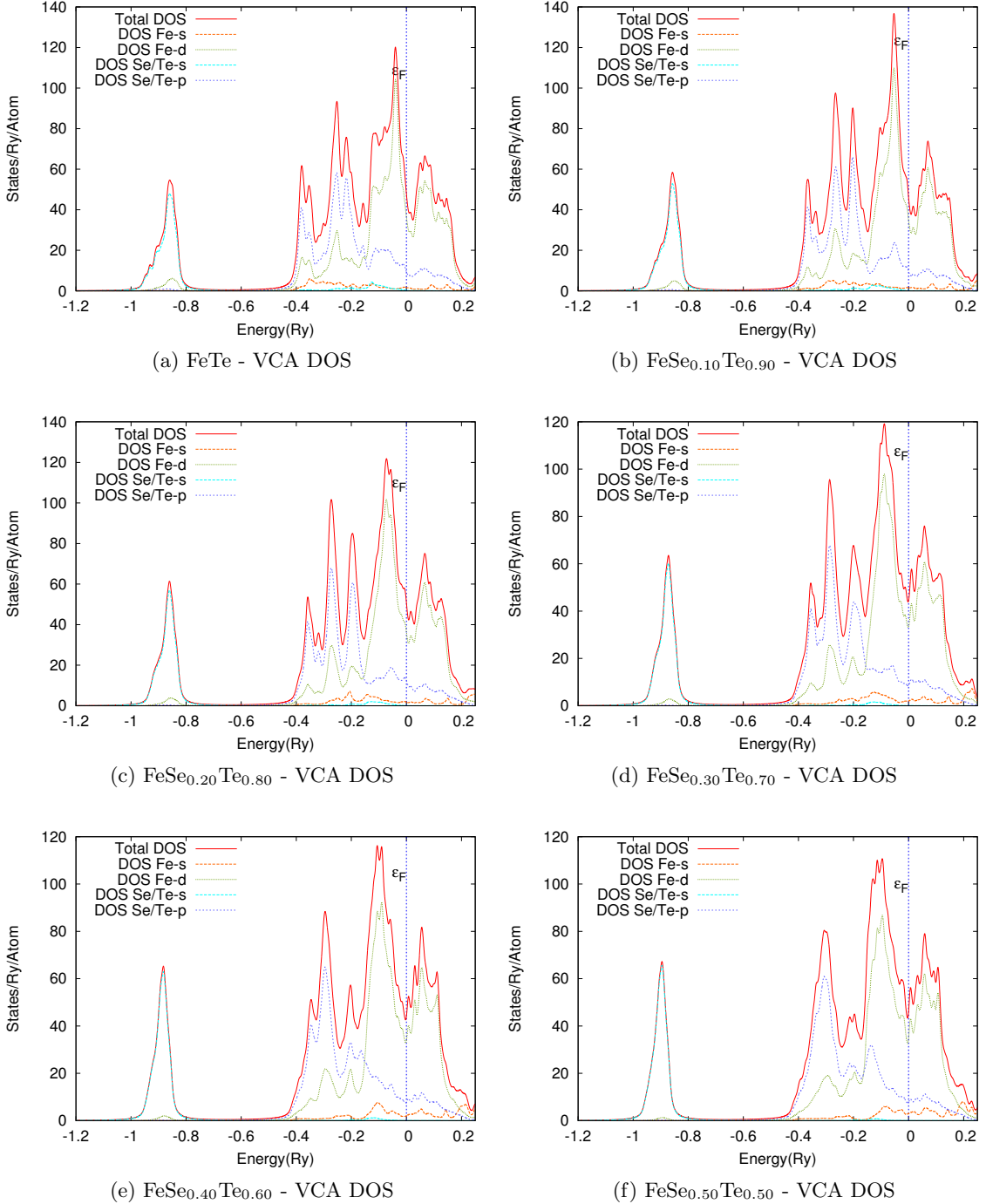


Figure 6.1: Total and decomposed Density of States of  $\text{FeSe}_x\text{Te}_{1-x}$  using the Virtual Crystal Approximation. Includes (a)  $x = 0.0$  (FeTe) DOS, (b)  $x = 0.1$  DOS, (c)  $x = 0.2$  DOS, (d)  $x = 0.3$  DOS, (e)  $x = 0.4$  DOS, and (f)  $x = 0.5$  DOS.

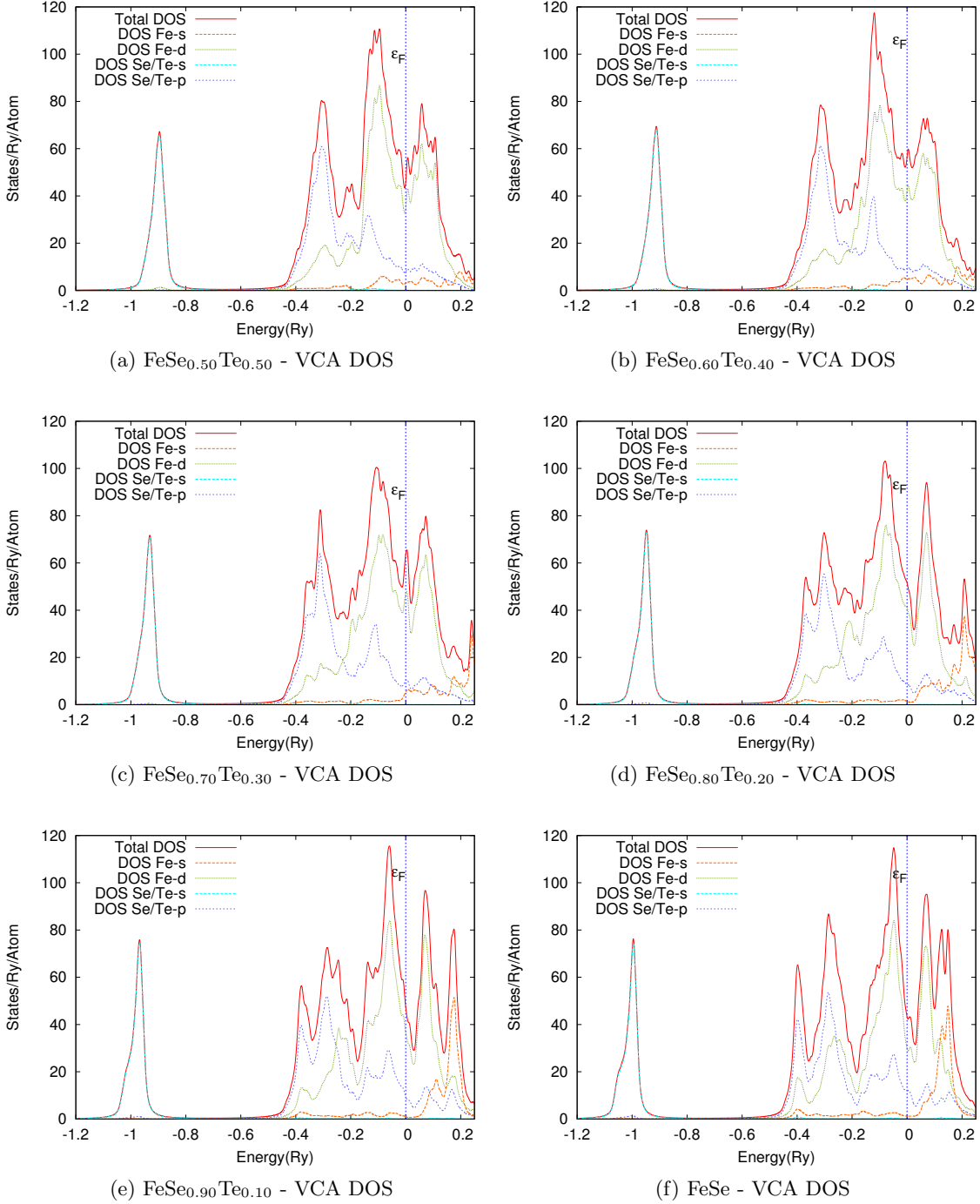


Figure 6.2: Total and decomposed Density of States of  $\text{FeSe}_x\text{Te}_{1-x}$  using the Virtual Crystal Approximation. Includes (a)  $x = 0.5$  DOS, (b)  $x = 0.6$  DOS, (c)  $x = 0.7$  DOS, (d)  $x = 0.8$  DOS, (e)  $x = 0.9$  DOS, and (f)  $x = 1.0$  (FeSe) DOS

the total DOS compares well with the NRL-LAPW DOS of FeSe. The decomposed DOS also show similar overall results to the NRL-LAPW calculations. Again, the Se/Te-*p* states are contributions are higher than those in Figure 3.3 at the two DOS peaks that appear between  $-0.4 \text{ Ry}$  and  $-0.15 \text{ Ry}$ . Between  $-0.15 \text{ Ry}$  and  $0.05 \text{ Ry}$ , both methods agree that the largest contribution comes from the Fe-*d* states. Around  $-1.0 \text{ Ry}$ , Figure 6.2 indicates that the lowest energy peak contains mostly Se/Te-*s* states, which is also consistent with the LAPW calculations. The primary difference is occurs above the Fermi level, where the Fe-*s* contribution is significant for the VCA results. However, this high energy level corresponds to unoccupied energy bands that do not play a role in the electronic structure for ambient conditions.

Just as in Figure 6.1, we see a dramatic change in the overall DOS between  $-0.4 \text{ Ry}$  and  $-0.15 \text{ Ry}$  when the concentration of Se is decreased (Figs. 6.2a→6.2f). The two peaks that exist in this energy range in Figure 6.2f merge into one peak as the Se concentration approaches 50%. Again, the Se/Te-*s* states near  $-1.0 \text{ Ry}$  do not split into the two independent Se-*s* and Te-*s* dominated DOS peaks that are found in the LAPW calculations.

This shows that the TB-VCA method is unable to predict the two independent Se/Te-*s* state DOS peaks that exist in the supercell LAPW calculations. The averaging of the Hamiltonians does not provide the individual Se/Te-*s* and Se/Te-*p* states to be stored. The following section discusses a method to retain the full information and improve these results.

### 6.3 Coherent Potential Approximation

The Coherent Potential Approximation (CPA) was introduced by Soven[76] to study the electronic states of random substitutional alloys. The randomness, with which the different sites are treated, is ignored in the TB-VCA. It is a mean-field theory that treats the alloys as an effective medium with zero average scattering. The effective medium is determined

self-consistently within the CPA. Zero average scattering must satisfy

$$\sum_i^N c_i \mathbf{t}_i = 0 , \quad (6.2)$$

where  $c_i$  is the concentration of the corresponding element,  $i$ , in the alloy, and  $N$  is the number of elements in the alloy. The  $\mathbf{t}_i$  in Equation (6.2) is the scattering matrix, which has the form

$$\mathbf{t}_i = (\boldsymbol{\epsilon}_i - \boldsymbol{\Sigma})[1 - (\boldsymbol{\epsilon}_i - \boldsymbol{\Sigma})\mathbf{G}]^{-1} , \quad (6.3)$$

such that  $\boldsymbol{\epsilon}_i$  is the matrix of the on-site SK parameters, discussed in Section 5.1.2. The  $\boldsymbol{\Sigma}$  in Equation (6.3) is the diagonal CPA self-energy matrix, and  $\mathbf{G}$  is Green's function over the irreducible Brillouin zone, given by

$$\mathbf{G}(\mathbf{z}, \boldsymbol{\Sigma}) = \int_{IBZ} \frac{dk}{\mathbf{z} - \mathbf{H}_{CPA}(\boldsymbol{\Sigma}, k)} . \quad (6.4)$$

Here,  $\mathbf{z}$  is the complex energy matrix, such that the real component represents a given energy level and the imaginary part relates to temperature broadening. The  $\mathbf{H}_{CPA}(\boldsymbol{\Sigma}, k)$  in Equation (6.4) is related to the periodic Hamiltonian from Section 5.1.1. For this study, only diagonal disorder was applied, meaning that  $\mathbf{H}_{CPA} = \mathbf{H}_{VCA}$  from Equation (6.1), except that the diagonal elements replaced by  $\boldsymbol{\Sigma}$ . Both  $\mathbf{G}$  and  $\boldsymbol{\Sigma}$  are solved self-consistently through a Newton-Raphson procedure[77]. After solving for  $\mathbf{G}$ , the decomposed DOS,  $N_l(E)$ , can be calculated by

$$N_l(E) = -\frac{1}{\pi} \lim_{z \rightarrow E^+} \text{Im}[\text{Tr} \mathbf{G}_l(\mathbf{z}, \boldsymbol{\Sigma})] , \quad (6.5)$$

where  $l$  is the decomposed angular momentum. However, Equation (6.5) does not produce the individual contributions of each substitutional element. The decomposed DOS for the

substitutional element is given by

$$N_l^A(E) = -\frac{1}{\pi} \lim_{z \rightarrow E^+} \text{Tr} \frac{\mathbf{G}_l^R + \mathbf{G}_l^I(\boldsymbol{\Sigma} - \boldsymbol{\epsilon}_B)}{\boldsymbol{\epsilon}_B - \boldsymbol{\epsilon}_A}, \quad (6.6)$$

where  $A$  and  $B$  are the two substitutional atoms, and  $\mathbf{G}_l^R$  and  $\mathbf{G}_l^I$  are the real and imaginary parts of the Green function, respectively.

We can also solve for the spectral density function,  $A(k, E)$ . This is analogous to the energy function,  $E(k)$ , in the band structure of ordered solids. It is given by

$$A(k, E) = -\frac{1}{\pi} \text{Im} \sum_l G_{ll}(k, E) \quad (6.7)$$

## 6.4 Developed Code Discussion

An elaborated discussion of the code developed for this dissertation is given in Appendix C. However, the general procedures and methods are discussed in this section. Specifically, I discuss the Newton-Raphson method and matrix inversion. These procedures can be found in most numerical method books as well.

The Newton-Raphson method is an iterative procedure designed to locate roots of a function[78]. For this method, an initial guess of the solution is chosen,  $x_1$ . This initial guess is then used to calculate the function's value,  $f(x_1)$ , and the function's derivative,  $f'(x_1)$ . The value of  $\frac{f(x_1)}{f'(x_1)}$  is then subtracted from  $x_1$  to get a new solution. This is done multiple times until a convergence criterion is met. For one-dimensional functions, the general solution is given by

$$x_{n+1} = x_n - \frac{f(x_n)}{f'(x_n)}, \quad (6.8)$$

where  $n$  is the number of iterations performed,  $f(x)$  is the function value at  $x$  and  $f'(x)$  is the derivative of the function at  $x$ . Convergence is met when two consecutive solutions have the same value up to a given decimal place. The procedure can also be performed for higher dimensional functions:

$$\vec{x}_{n+1} = \vec{x}_n - \mathbf{J}^{-1}(\vec{x}_n) \mathbf{F}(\vec{x}_n) , \quad (6.9)$$

where  $\vec{x}$  are vectors,  $\mathbf{F}(\vec{x})$  is a matrix of solutions to the functions at  $\vec{x}$ , and  $\mathbf{J}^{-1}(\vec{x})$  is the inverted Jacobian of  $\mathbf{F}(\vec{x})$ . The Jacobian is the derivative matrix given as  $\mathbf{J} = \frac{\partial \mathbf{F}}{\partial \vec{x}}$ . Since the inverse of the Jacobian is used to solve for this general case,  $\mathbf{J}$  must be non-singular, or invertible. Mathematically, this means that  $\mathbf{J}\mathbf{J}^{-1} = \mathbf{I}$ , where  $\mathbf{I}$  is the identity matrix.

Matrix inversion can be performed in many ways. This code used *LU* decomposition in conjunction with forward and backward substitution to find the inverse of a matrix. *LU* decomposition converts any general  $n \times n$  matrix,  $\mathbf{A}$ , into a lower triangular matrix,  $\mathbf{L}$ , and an upper triangular matrix,  $\mathbf{U}$ . This is given by

$$\mathbf{L}\mathbf{U} = \mathbf{A} . \quad (6.10)$$

The *LU* decomposition was performed using Crout's algorithm with partial pivots. For our code, matrix inversion is used to solve for Green's function (Eq. (6.4).)

Once Green's function is found for a given self-energy, our multidimensional function from Equation (6.9) becomes

$$\mathbf{F}_{CPA}(\Sigma) = \mathbf{G}\Sigma^2 + (\mathbf{I} - \boldsymbol{\varepsilon}_B\mathbf{G} - \boldsymbol{\varepsilon}_A\mathbf{G})\Sigma + \mathbf{G}\boldsymbol{\varepsilon}_A\boldsymbol{\varepsilon}_B - \frac{1}{2}(\boldsymbol{\varepsilon}_A + \boldsymbol{\varepsilon}_B) , \quad (6.11)$$

such that  $A$  and  $B$  represent our FeSe and FeTe parameters, respectively. The Jacobian of  $\mathbf{F}_{CPA}$  is thus

$$\mathbf{J}_{CPA}(\Sigma) = 2\mathbf{IG}\Sigma + (\mathbf{I} - \boldsymbol{\varepsilon}_B\mathbf{G} - \boldsymbol{\varepsilon}_A\mathbf{G}) . \quad (6.12)$$

Therefore, for our calculations, Equation (6.9) can be written as

$$\Sigma_{n+1} = \Sigma_n - \mathbf{F}_{CPA}(\Sigma_n)/\mathbf{J}_{CPA}(\Sigma_n) . \quad (6.13)$$

This is done until some specified convergence is met for each self-energy. The final converged self-energies are then used to solve for a final Green's function for the given energy level and DOS can be calculated. The following section discusses the results calculated by the code for  $\text{FeSe}_x\text{Te}_{1-x}$ .

## 6.5 Coherent Potential Approximation of $\text{FeSe}_x\text{Te}_{1-x}$

Using the parameters discussed in Section 6.2, the CPA was applied to the substitutional alloy,  $\text{FeSe}_x\text{Te}_{1-x}$ . A diagonal disordered CPA was used for this study. The Hamiltonian discussed in Section 6.2 was modified for the CPA by replacing the diagonal elements of Se/Te with self-energies. These modified elements correspond to the Se/Te-*s* and *p* on-site parameters, specifically diagonal matrix elements 19-22 and 28-31 in the secular equations. The Se/Te-*d* on-site parameters are ignored as they were already removed from the fit. Initial guesses for these self-energies are approximated by the average of the two systems' on-site parameters. The off-diagonal terms are treated in a VCA manner, i.e. they are evaluated as an arithmetic mean.

### 6.5.1 Results of the TB-CPA

#### TB-CPA DOS of $\text{FeSe}_x\text{Te}_{1-x}$

The concentrations investigated for this system were the same as discussed in Section 6.2. Figure 6.3 shows the total and some decomposed DOS calculated using the CPA for the Te rich systems,  $x = 0.0$  to  $x = 0.5$ . The Fermi level,  $E_F$ , is given by the vertical solid (blue) line at 0.0 Ry. Panel 6.3a of this figure shows the pure FeTe system. The TB-CPA DOS results are identical to the TB-VCA results shown in Figure 6.1. As we move from the pure FeTe system to the 50% concentration (6.3a→6.3f), we see some significant changes between

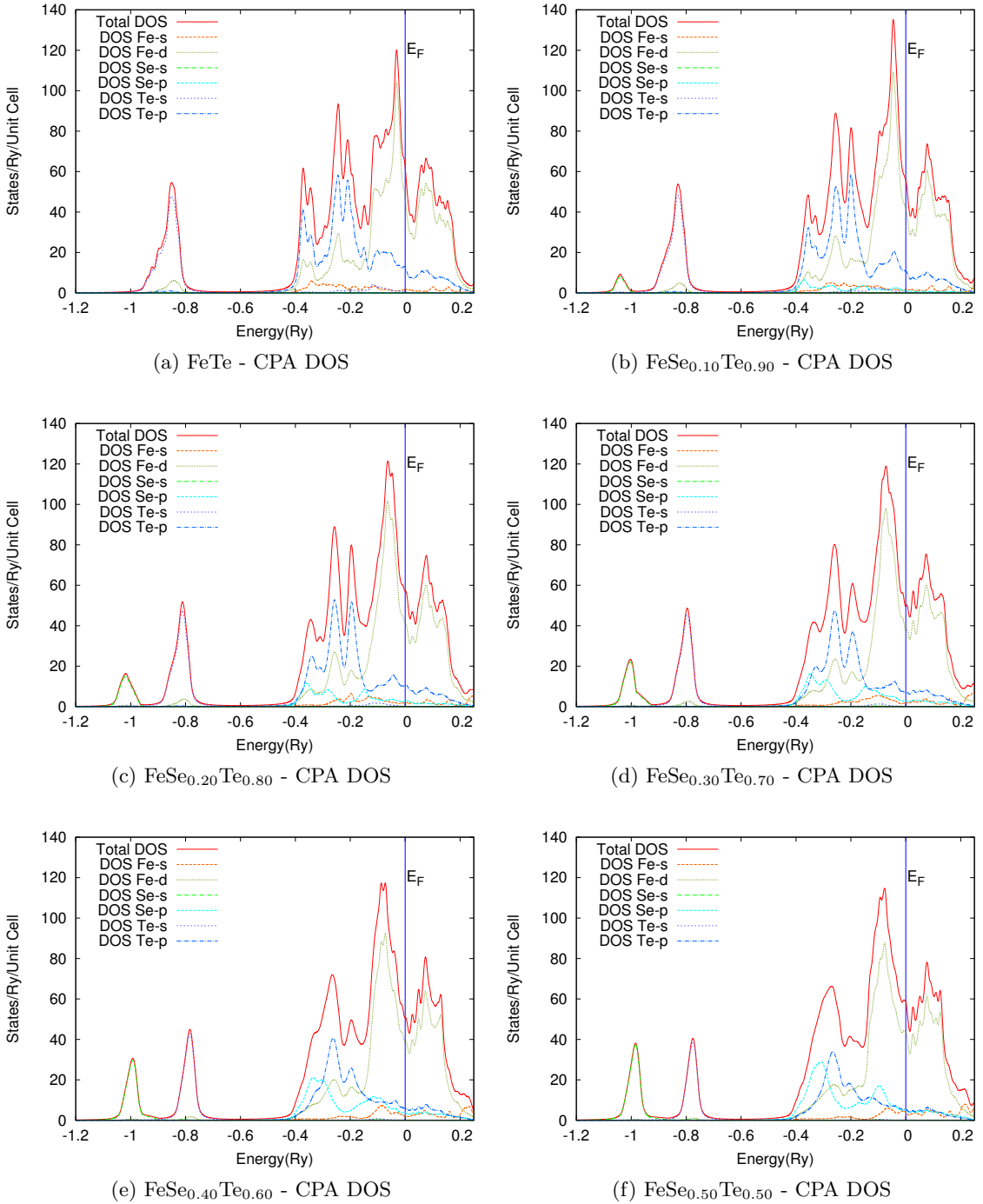


Figure 6.3: Total and decomposed Density of States of  $\text{FeSe}_x\text{Te}_{1-x}$  using the Coherent Potential Approximation shifted by the calculated Fermi level. Includes (a)  $x = 0.0$  (FeTe) DOS, (b)  $x = 0.1$  DOS, (c)  $x = 0.2$  DOS, (d)  $x = 0.3$  DOS, (e)  $x = 0.4$  DOS, and (f)  $x = 0.5$  DOS. Fermi level ( $\varepsilon_F$ ) is given at 0.0 Ry by the vertical solid (blue) line.

the TB-VCA and TB-CPA global DOS features. Between the energy range of  $-0.4 \text{ Ry}$  and  $-0.15 \text{ Ry}$  we see two DOS peaks that contain Te-*p* states, Fe-*d* states, and trace amounts of Fe-*s* states. These two DOS peaks merge into one single peak as we approach  $x = 0.5$ , Figure 6.3f. This merged DOS peak is still comprised mainly of Se/Te-*p* states with some Fe-*d* states as well. Near the Fermi level, the DOS features stay relatively consistent as Se is added to the system. In this range, between  $-0.15 \text{ Ry}$  and  $0.25 \text{ Ry}$ , the DOS is comprised mainly of Fe-*d* states, some Se/Te-*p* states and trace amounts of Fe-*s* states. The most significant changes to the DOS occur between  $-1.2 \text{ Ry}$  and  $-0.8 \text{ Ry}$ . In Figure 6.3a, one peak of Te-*s* states, with trace amounts of Fe-*s*, is located within this energy range. When Se is added to the system, a second DOS peak begins to form at an energy below the Te-*s* DOS peak. As the Se concentration continues to increase, the Te-*s* peak decreases, while the lower energy peak increases. This secondary peak contains almost entirely Se-*s* states. When the concentration of Se and Te are equal, these two peaks are comparable in total DOS value, but are now composed entirely of Se-*s* and Te-*s*, respectively.

Figure 6.4 shows the DOS of the Se rich systems. Panel 6.4f displays the pure FeSe system, which is equivalent to the TB-VCA results. The global DOS changes dramatically as Te is added to the system (6.4f→6.4a). The energy range surrounding the Fermi level, between  $-0.15 \text{ Ry}$  and  $0.05 \text{ Ry}$ , changes insignificantly as Te is added. Here, the major contributor to the DOS is Fe-*d*, with some Se/Te-*p* states. The DOS above this energy range changes greatly with increased concentration of Te. This is because of the large amount of Fe-*s* like states found around  $0.2 \text{ Ry}$ , which decreases with increasing Te. Between  $-0.4 \text{ Ry}$  and  $-0.15 \text{ Ry}$ , the two DOS peaks that exist in Figure 6.4f merge into one as Te is added to the system. This range contains mostly Se/Te-*p* and Fe-*d* states, with the Fe-*d* contribution decreasing somewhat as Te concentration increases. DOS peaks between  $-1.2 \text{ Ry}$  and  $-0.8 \text{ Ry}$  undergo a significant change in the features. Specifically, in Figure 6.4f, only one DOS peak of entirely Se-*s* is found within this energy range. A small addition of Te to the system, Figure 6.4e, creates a small DOS peak of Te-*s* states at slightly higher energy than the original. As Te concentration increases, the total DOS of the first peak decreases while

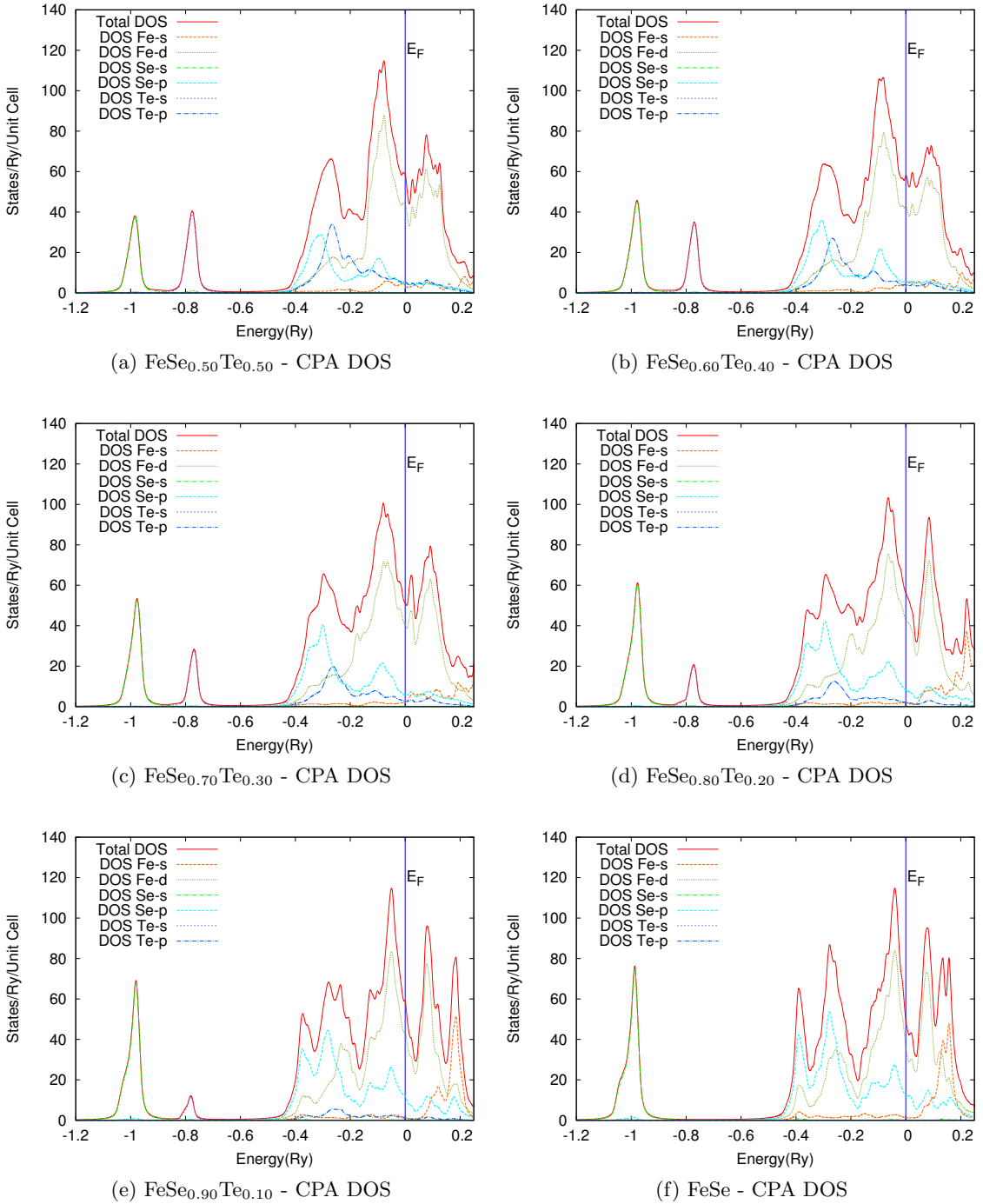


Figure 6.4: Total and decomposed Density of States of  $\text{FeSe}_x\text{Te}_{1-x}$  using the Coherent Potential Approximation shifted by the calculated Fermi level. Includes (a)  $x = 0.5$  DOS, (b)  $x = 0.6$  DOS, (c)  $x = 0.7$  DOS, (d)  $x = 0.8$  DOS, (e)  $x = 0.9$  DOS, and (f)  $x = 1.0$  (FeSe) DOS. Fermi level ( $\varepsilon_F$ ) is given at 0.0 Ry by the vertical solid (blue) line.

the second increases. In Figure 6.4a, these two peaks have comparable total DOS values.

Table 6.1: Total, Fe-*d*, Se-*p* and Te-*p* decomposed DOS of  $\text{FeSe}_x\text{Te}_{1-x}$  at the Fermi level using the TB-CPA.

$x$	$E_F$	$N(E_F)$	$\text{Fe}_d$	$\text{Se}_p$	$\text{Te}-p$	$\text{Se}/\text{Te}-p$
0.0	0.0086	23.97	18.28	0.00	4.72	4.72
0.1	0.0120	20.43	15.42	0.40	3.74	4.13
0.2	0.0257	23.47	17.32	1.01	3.97	4.97
0.3	0.0357	24.51	18.08	1.52	3.51	5.02
0.4	0.0392	25.59	19.84	1.63	2.60	4.21
0.5	0.0418	26.70	20.25	2.12	2.34	4.45
0.6	0.0206	29.02	21.49	2.90	1.96	4.86
0.7	0.0197	31.96	23.54	3.67	1.60	5.27
0.8	0.0150	25.55	20.13	3.57	0.89	4.46
0.9	0.0111	22.97	17.77	4.18	0.40	4.58
1.0	0.0083	21.70	14.98	6.01	0.00	6.01

As mentioned in Section 5.2.3, the TB Hamiltonians that were used in the TB-CPA calculations were shifted such that the calculated Fermi level was natively set to 0.0 *Ry*. Theoretically, the calculated Fermi level should remain very close to 0.0 *Ry*, since the shift was applied prior to the TB-CPA calculations. However, due to the merging of the Se/Te-*p* states, the calculated Fermi levels were higher than 0.0 *Ry*. The calculated Fermi level is based on the integration of the total DOS, which is also the number of electrons in the system at each energy level.

Table 6.1 presents the total, Fe-*d*, Se-*p*, and Te-*p* decomposed DOS calculated by the TB-CPA method at the calculated Fermi energies. The table shows the total and decomposed DOS are sporadic throughout the Se/Te concentrations. The only clear DOS trend is the near monotonic increase/decrease of Se/Te-*p* DOS when Se is added to the system. However, the total, Fe-*d*, and Se/Te-*p* decomposed DOS values have large fluctuations. We see some trends emerging from the  $E_F$  values. The calculated  $E_F$  at the two extremes are essentially the same (approximately 0.008,) but monotonically increase to 0.04 at the 50% concentration. It is important to note that in all the TB-CPA calculations, integrated

electron count of the two DOS peaks between  $-1.2 \text{ Ry}$  and  $-0.8 \text{ Ry}$  provides four of the 28 valence electrons, as found in the LAPW calculations.

## 6.6 Concluding Remarks

When comparing the figures in the VCA section (Sec. 6.2) with the figures of the CPA section (Sec. 6.5.1), there are only minor differences. The largest, and most significant difference, is found in the  $-1.2 \text{ Ry}$  and  $-0.8 \text{ Ry}$  energy range. Recall that the VCA gives only one DOS peak within this region for all concentration values. This is because the TB-VCA method is unable to provide independent information for the Se and Te contributions. Within the diagonal disorder of TB-CPA method, this information is recoverable. Specifically, within this low energy region, both Se- and Te-*s* states are contained within two separate DOS peaks, comparable to the NRL-LAPW results.

The diagonal disorder CPA results are consistent with the NRL-LAPW supercell calculations. In more detail, the two separate Se- and Te-*s* DOS peaks are found, the specific features are not identical between the NRL-LAPW and the TB-CPA results. The TB-CPA finds both of these peaks with comparable total DOS values, while the NRL-LAPW results find the Se-*s* peak to be broader and shorter than the Te-*s* peak. However, the primary problem is the merging of the two DOS peaks within the  $-0.4 \text{ Ry}$  and  $-0.15 \text{ Ry}$  energy range. Although integration of the DOS suggests approximately the same number of electrons are contained in this region as the NRL-LAPW results. The total DOS in this region is misrepresented, however, which causes the minor changes in the Fermi level location for the TB-CPA results.

## Chapter 7: Final Conclusions and Future Work

### 7.1 Summary

First-principles electronic structure calculations of FeSe, FeTe, FeSe<sub>0.75</sub>Te<sub>0.25</sub>, FeSe<sub>0.25</sub>Te<sub>0.75</sub>, and FeSe<sub>0.50</sub>Te<sub>0.50</sub> were performed with the NRL-LAPW and Wien2k software. I present the total energies, energy bands, DOS, and Fermi surface first-principles results agree well with other computational and experimental findings. Specifically, the DOS have similar features in all calculations, with Fe-*d* DOS the major contribution to the total DOS at the Fermi level. The Lorentzian broadened DOS calculations of FeSe were compared with experimental photoemission spectrum. Predictions of photoemission spectrum for FeTe and FeSe<sub>0.50</sub>Te<sub>0.50</sub> showed comparable results to those found for FeSe.

Superconductivity first-principles calculations from the Gaspari-Gyorffy-McMillan theories also show good agreement with the experimental results of FeSe and FeSe<sub>0.50</sub>Te<sub>0.50</sub> in ambient conditions. The main conclusion of this work regarding superconductivity is that the electron-phonon mechanism can explain the modest  $T_c = 7.5\text{ K}$  observed in FeSe at ambient conditions. Also, electron-phonon explains qualitatively the increase of  $T_c$  under pressure, but cannot provide a quantitative agreement with the observed  $T_c = 35\text{ K}$ . The Gaspari-Gyorffy-McMillan superconductivity calculations of the FeSe<sub>*x*</sub>Te<sub>1-*x*</sub> systems suggest that the electron-phonon coupling interaction of the BCS theory is important in these materials.

The NRL-TB method was used with the first-principles results of FeSe and FeTe to fit TB parameters. These parameters were able to reproduce total energy curves and total DOS of the first-principles LAPW results. I developed code to perform coherent potential approximation calculations on the FeSe<sub>*x*</sub>Te<sub>1-*x*</sub> material, using the fitted TB parameters and their corresponding Hamiltonians. These results also find good agreement with the total

DOS of the LAPW calculations.

## 7.2 Future Work

My current coherent potential approximation code only applies diagonal disorder to the Se and Te atoms, but treats off-diagonal effects within the virtual crystal approximation of the  $\text{FeSe}_x\text{Te}_{1-x}$  system. The introduction of off-diagonal disorder would further improve the coherent potential approximation calculations and I hope to attempt such a calculation in the future. Molecular dynamics calculations could also be performed based of the TB parameters fit for this system. This is also a project to consider in future work.

# Appendix A: Electronic Structure of Francium - Published

## Electronic Structure of Francium

Alexander P. Koufos\* and Dimitrios A. Papaconstantopoulos

This article presents the first calculations of the electronic structure of francium for the bcc, fcc, and hcp structures, using the linearized augmented plane wave (LAPW) method. Both the local density approximation (LDA) and generalized gradient approximation (GGA) were used to calculate the electronic structure and total energy of francium (Fr). The GGA and LDA both found the total energy of the hcp structure to be slightly below that of the fcc and bcc structures, respectively. This is in agreement with similar results for the other alkali metals where the bcc structure is found not to be the ground state in contradiction to experiment. The equilibrium lattice constant, bulk modulus, and

superconductivity parameters were calculated. Calculations of the enthalpy of the system suggest a structural transition from hcp to bcc under a pressure of 0.57 GPa. Using the McMillan-Gaspari-Gyorffy theories, we found that under further pressures, in the range of 3–14 GPa, Fr could be a superconductor with critical temperature up to 7 K. This is consistent with the other alkali metals and originates from an increase of the d-like density of states at the Fermi level, which makes the alkali metals behave like transition metals.  
© 2013 Wiley Periodicals, Inc.

DOI: 10.1002/qua.24466

### Introduction

Francium (Fr) is one of the rarest elements on the planet. Around 20–30 g of the element is found on the earth's crust at any given moment and the longest half-life of all its isotopes is about 20 min.<sup>[1]</sup> Fr is the last element in the alkali metal group, thus having one electron in its valence shell. It has an atomic number of 87 and atomic weight of 223.0197.<sup>[2]</sup> Fr also has radioactive properties similar to cesium (Cs). Due to Fr's rare nature, the only current way to study any of these properties is to optically trap it.<sup>[3]</sup> Even with these methods, the study of its electronic structure is hard to conduct.

In this article, we perform calculations of the electronic structure of Fr using density functional theory, more specifically using the linearized augmented plane wave (LAPW) method in its full potential form. These calculations were performed for the local density approximation (LDA) and the generalized gradient approximation (GGA). The calculations were performed using a scalar-relativistic Hamiltonian. Tests incorporating spin-orbit coupling were performed to study the effect of spin-orbit interaction.

### Computational Details

All calculations performed in this article used the NRL LAPW code (This LAPW code was originally written by Krakauer and Singh, modified by Mehl. The rigid muffin-tin approximation (RMTA) code was written by Papaconstantopoulos and Klein<sup>[4]</sup> using the Hedin-Lundqvist method, for LDA calculations, or Purdue-Wang 1991 (PW91) method for GGA calculations. Various  $\Gamma$ -centered k-point meshes were used for the calculations contained in the manuscript. Specifically, k-point meshes of 285, 505, and 918 were used for the bcc, fcc, and hcp calculations, respectively. All calculations used a basis set size of  $5 \times 5 \times 5$ , 24 core states (equilibrium state of radon), one valence electron, and local orbitals with energies of  $-1.8$  and

$-0.47$  Ry. However, we also performed total energy calculations with 22 core states, seven valence electrons, the local orbitals, and the 6s and 6p states treated as bands. Calculations involving superconductivity, those found in Superconductivity section, used touching muffin-tin radii, while all other calculations used a fixed muffin-tin radius of 4.3 bohr.

### Total Energy of Fr

In this section, we discuss the results for the total energy of Fr, and related properties, calculated using the LAPW with both the LDA and GGA functionals. All LAPW calculations performed for the total energy of Fr found that the fcc and hcp structures have slightly lower total energy than the bcc structure. This is consistent with similar calculations for the other alkali metals,<sup>[4,5]</sup> which are experimentally known to be bcc. Table 1 shows the total energies, lattice parameters and bulk moduli of the alkali metals using the LAPW method with both functionals. The LDA results contained in Table 1 for all the alkali metals, excluding Fr, were obtained from the paper by Sigalas et al.<sup>[4]</sup> Additional calculations were performed to obtain the GGA information presented in Table 1. The GGA functional improves the total energy results by making the difference in

---

This article was published online on 13 May 2013. An error was subsequently identified. This notice is included in the online and print versions to indicate that both have been corrected on 17 May 2013.

A. P. Koufos and D. A. Papaconstantopoulos  
School of Physics, Astronomy, and Computational Sciences, George Mason University, Fairfax, Virginia 22030  
E-mail: akoufos@gmu.edu

Contract grant sponsor: Schools, University 'N' (and) Resources in the Sciences and Engineering-A (SUNRISE; NSF/GMU GK-12 Fellows Project); contract grant number: DGE 0638680 (07/07-06/12).

Contract grant sponsor: ONR; contract grant number: N00014-09-1-1025.  
© 2013 Wiley Periodicals, Inc.

Table 1. Total energy, lattice parameters, and bulk moduli for all alkali metals Li, Na, K, Rb, Cs, and Fr

	Generalized gradient approximation			Local density approximation		
	Tot. energy (mRy)	Lat. const. (au)	Bulk mod. (MBar)	Tot. energy (mRy)	Lat. const. (au)	Bulk mod. (MBar)
<b>Lithium (Li)</b>						
bcc	0	6.410	0.296	2.8 <sup>[4]</sup>	6.380 <sup>[4]</sup>	0.148 <sup>[4]</sup>
fcc	0.86	8.134	0.196	0 <sup>[4]</sup>	7.950 <sup>[4]</sup>	0.156 <sup>[4]</sup>
exp <sup>[6]</sup>	6.597	0.116		6.597	0.116	
<b>Sodium (Na)</b>						
bcc	0.08	7.964	0.076	0.96 <sup>[4]</sup>	7.690 <sup>[4]</sup>	0.087 <sup>[4]</sup>
fcc	0	10.040	0.076	0 <sup>[4]</sup>	9.680 <sup>[4]</sup>	0.090 <sup>[4]</sup>
exp <sup>[6]</sup>	7.984	0.068		7.984	0.068	
<b>Potassium (K)</b>						
bcc	0.23	10.432	0.029	0.75 <sup>[4]</sup>	9.540 <sup>[4]</sup>	0.047 <sup>[4]</sup>
fcc	0	13.379	0.025	0 <sup>[4]</sup>	12.010 <sup>[4]</sup>	0.046 <sup>[4]</sup>
exp <sup>[6]</sup>	9.877	0.032		9.877	0.032	
<b>Rubidium (Rb)</b>						
bcc	0.04	10.753	0.032	0 <sup>[4]</sup>	10.130 <sup>[4]</sup>	0.042 <sup>[4]</sup>
fcc	0	13.563	0.031	0.37 <sup>[4]</sup>	12.820 <sup>[4]</sup>	0.049 <sup>[4]</sup>
exp <sup>[6]</sup>	10.558	0.031		10.558	0.031	
<b>Cesium (Cs)</b>						
bcc	0.23	11.661	0.023	2.2 <sup>[4]</sup>	10.760 <sup>[4]</sup>	0.020 <sup>[4]</sup>
fcc	0	14.740	0.023	0 <sup>[4]</sup>	13.880 <sup>[4]</sup>	0.033 <sup>[4]</sup>
exp <sup>[6]</sup>	11.423	0.020		11.423	0.020	
<b>Francium (Fr)</b>						
bcc	0.29	11.702	0.014	0.22	10.842	0.017
fcc	0.05	14.815	0.015	0.20	13.809	0.022
hcp	0	$a = 10.491$ ; 0.011	0	$a = 9.785$ ; 0.021		
		$c = 17.132$		$c = 15.657$		
exp <sup>[6]</sup>		(0.020)		(0.020)		

Total energies are given with respect to the lowest total energy for the given structures represented by 0 mRy.

fcc and bcc energies,  $\Delta E$ , smaller, but only lithium (Li) is calculated to have bcc as the equilibrium structure. The lattice parameter results are, in general, closer to experimental values

using the GGA functional rather than the LDA. With the exception of Li and sodium (Na), the GGA generally overestimates the lattice parameter while the LDA typically underestimates the experimental value. For all the LDA calculations, we find the fcc has lower energy than bcc, with the exception of rubidium (Rb). With the GGA functional we see that  $\Delta E = 0.04$  mRy for Rb, but the fcc structure is still found to have lower energy than the bcc structure. Table 1 suggests that Fr is very malleable. This is in agreement with the well-known malleable properties of the other alkali metals. The bulk modulus of this material is extremely small, 0.014 MBar at equilibrium, implying a compressibility of  $71.4 \times 10^{-11} \text{ m}^2/\text{N}$ .

Figure 1 shows the general trends of the lattice constants and bulk moduli from the lighter alkalis to heavier ones for the bcc structure. The general trend for the lattice constant is to increase with increasing atomic number, while the bulk modulus follows the opposite trend, that is, decreases with atomic number (in agreement with experiment). The results found for Fr follow both trends.

We also examined the hcp structure of Fr using the LAPW method with both LDA and GGA functionals. The value of  $c/a = 1.60$  was found to be the optimized value for the LDA functional, while  $c/a = 1.633$  was obtained for the GGA functional. We calculated the lattice constants for the two functionals as well as the total energies. The results are shown in Table 1. Spin-orbit calculations for the LDA functional were also performed, as discussed in Spin-orbit calculations section, and showed little effect in the total energy results.

Figure 2 shows the total energy of Fr using the GGA functional. Following the trends of the other alkali elements, the total energy of the fcc structure is lower than the bcc structure by only 0.24 mRy.

We also examined the possibility of phase transition in Fr. As with many materials, pressure can have a significant impact

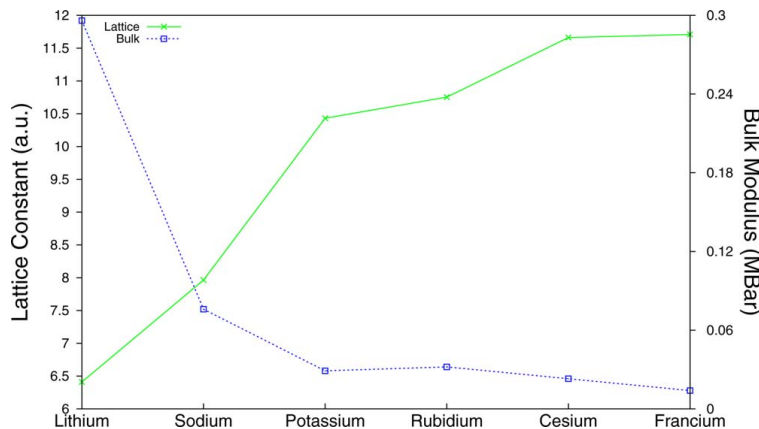
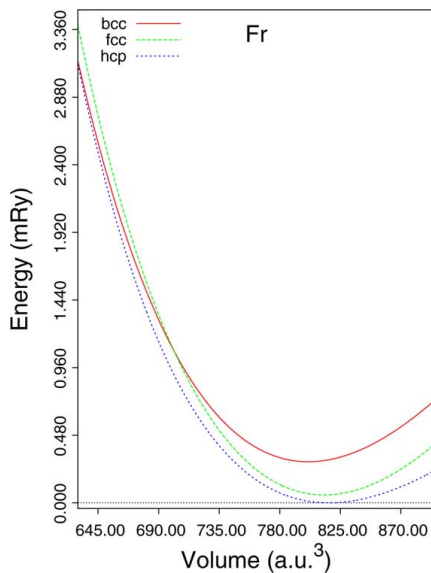
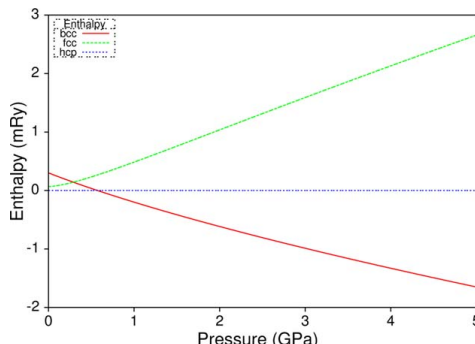


Figure 1. Lattice constants and bulk moduli with bcc structure of the alkali metals. Information within the figure corresponds to calculated values using the LAPW method with the GGA functional. [Color figure can be viewed in the online issue, which is available at [wileyonlinelibrary.com](http://wileyonlinelibrary.com).]



**Figure 2.** Total energy of Fr using the LAPW method with GGA functional. Notice the hcp structure is calculated to have lower total energy than the fcc structure by 0.05 mRy at equilibrium. [Color figure can be viewed in the online issue, which is available at [wileyonlinelibrary.com](http://wileyonlinelibrary.com).]

on the structure of the material. Therefore, enthalpy,  $H=E+pV$ , where  $E$  is total energy,  $p$  is pressure, and  $V$  is volume, was calculated to locate any structural transitions that might occur under pressure. These results all suggest a transition from hcp to bcc under some small pressure, with no other transitions for the pressures investigated. Figure 3 shows the enthalpy plot of the LAPW with GGA, without spin-orbit interaction. The transition from hcp to bcc occurs around 0.57 GPa for the GGA functional.



**Figure 3.** Enthalpy of the three structures, fcc, bcc, and hcp, calculated using LAPW with GGA functional. All enthalpies are given with respect to the hcp enthalpy. A transition from hcp to bcc occurs at 0.572 GPa. [Color figure can be viewed in the online issue, which is available at [wileyonlinelibrary.com](http://wileyonlinelibrary.com).]

## Electronic Structure

In this section, we discuss the Density of States (DOS) and energy band calculations of Fr performed for various lattice parameters. The DOS and energy bands discussed in this section correspond to touching muffin-tin LAPW. Our use of the RMTA, which requires touching muffin-tin spheres, makes the results consistent with scattering theory. This method is discussed in the Superconductivity section in regards to calculating the electron-phonon interaction. The DOS and bands do not show any significant differences between LDA and GGA. Calculations with spin-orbit interaction were obtained using the LDA functional. We find little difference between the GGA and LDA functional calculations with the spin-orbit coupling, as discussed in more detail in the Spin-orbit calculations section.

### Density of states

The DOS of Fr were calculated by the tetrahedron method<sup>[7]</sup> and are shown in Figure 4(b). This figure shows the total DOS and the angular momentum ( $I$ ) decomposed DOS of Fr for the bcc structure. There are great similarities in the calculated DOS when compared with Cs, Figure 4(a), and other alkali metals.<sup>[8]</sup> In both images of Figure 4, the Fermi level,  $E_F$ , is shown by the vertical dashed line. At  $E_F$  and below, the DOS of both elements have s- and p-like character, while the d-states appear well above  $E_F$ . The similarities between these figures suggest an accurate prediction of Fr's true DOS, which are consistent with the other alkali metals. Table 2 shows the calculated values of the total, and  $I$ -decomposed, DOS at the Fermi energy for both Cs and Fr using the GGA functional. Summation of the  $I$ -decomposed DOS do not equal the total DOS, since these are projections on to the muffin-tin spheres.

Table 2 shows that the s-component of the DOS, at  $E_F$ , is the largest contributor to the total DOS of Fr at equilibrium. We also perform band structure calculations as a function of pressure. When pressure is increased the s-component begins to decrease, while the d-component increases. The d-component becomes the largest contribution to the total DOS after a pressure of 2 GPa as shown in Figure 5. In Figure 5, the values of  $N(E_F)$  and its angular momentum components are plotted as a function of pressure as Fr transitions from hcp to bcc. This behavior is also found in other alkali metals and is due to increased s-d hybridization under pressure, see Energy bands and Superconductivity sections.

### Spin-orbit calculations

Spin-orbit interaction calculations were performed for the LDA functional to observe any influences on the total energy and DOS of the system. These results showed little difference from the non-spin-orbit interaction calculations for the occupied states. Table 3 shows the total energy results for the LDA functional with spin-orbit interaction. The results given in Table 3 compare well with the LDA functional without spin-orbit interaction results, with less than 1% difference when compared to Table 1.

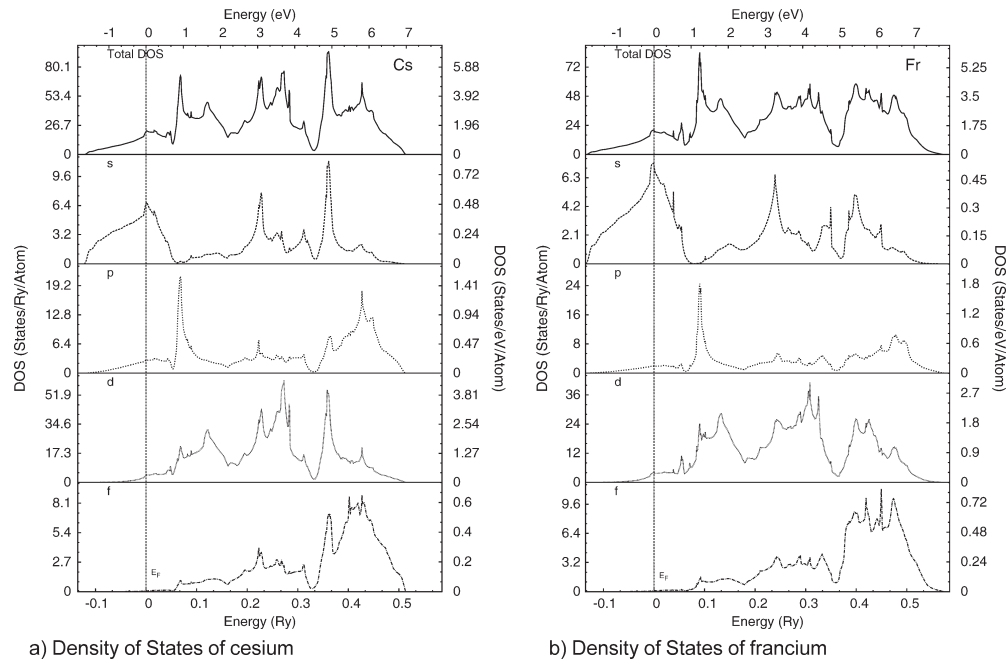


Figure 4. The total and decomposed density of states for bcc Cs (a) and Fr (b). The total, s-component, p-component, d-component, and f-component of the DOS, is given from top to bottom, respectively. The Fermi level is shown by the vertical dotted line.

Table 2. The total and decomposed DOS at the Fermi level for bcc cesium and bcc francium using LAPW with GGA functional at zero pressure

Element	$N_{\text{Total}}$	$N_s$	$N_p$	$N_d$	$N_f$
Cs	21.113	6.621	2.772	4.228	0.070
Fr	19.772	7.198	1.897	3.909	0.094

Table 3. Total energy and related results for francium with LDA functional with spin-orbit interaction

	Total energy (mRy)	Lattice constant (au)	Bulk modulus (mBar)
bcc	0.20	10.836	0.018
fcc	0.17	13.802	0.022
hcp	0.0	$a = 9.788; c = 15.661$	0.020

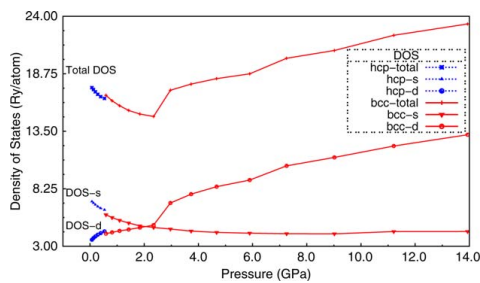


Figure 5. Total and s,d-components of the DOS vs. pressure of Fr at  $E_F$ , using the GGA functional with no spin-orbit interaction. The l-components of the DOS are normalized with respect to the equilibrium MT radius,  $R_{\text{eq}}/R$ , to correct for the fact that we are using touching spheres. The hcp structure is given by a dashed (blue) line and the bcc structure as a solid (red) line. [Color figure can be viewed in the online issue, which is available at [wileyonlinelibrary.com](http://wileyonlinelibrary.com).]

We performed calculations using the LDA functional with spin-orbit interaction for volumes down to 34% of the equilibrium volume. The total and l-decomposed DOS with spin-orbit interaction had similar results to the LDA without spin-orbit interaction in the calculations. This is demonstrated in Table 4,

Table 4. Total and decomposed DOS at  $E_F$  for bcc francium using LAPW with LDA functional, both with and without spin-orbit interaction

Vol. ( $\text{Å}^3$ )	Press. (GPa)	DOS, total	DOS, s	DOS, p	DOS, d	DOS, f
<b>No spin-orbit</b>						
595.5	0.20	16.146	5.192	1.396	3.825	0.106
500	1.01	14.968	4.279	1.224	3.975	0.1280
364.5	4.39	18.289	3.230	1.083	6.771	0.276
275.7	11.57	23.069	3.080	1.283	9.147	0.650
<b>Spin-orbit</b>						
595.5	0.20	16.503	5.257	1.477	3.889	0.107
500	1.00	15.337	4.280	1.318	4.045	0.134
364.5	4.32	18.767	3.267	1.170	6.898	0.281
275.7	11.388	23.956	3.172	1.434	9.416	0.660

for four bcc pressures. The inclusion of spin-orbit results in the DOS values at the Fermi level show negligible differences from the non-spin-orbit calculations. The largest percent difference is between the total DOS at 275.5 au<sup>3</sup> at 3.7%.

Fr, similarly to the other alkali metals, has its lowest band half occupied and is almost entirely of s-character. We know from quantum mechanics that there is no spin-orbit splitting for these "s" states. Although the states above  $E_F$  have p- and d-character, which do split, they are irrelevant to the Fermi level values of the DOS, phase shifts, etc.

Table 5 shows splitting at high-symmetry k-points. The  $\Gamma_{25'}$  state is a triple degenerate state that splits into a single degenerate state and a double degenerate state by spin-orbit interaction.  $H_{25'}$  is also a triple degenerate state that splits into a single degenerate and a double degenerate state. The  $P_4$  point also splits from triple degenerate states to a single and a double degenerate state, with the values given respectively in the WSO row of Table 5. Figure 6, in Energy bands section, shows the location of these points. As  $E_F$  is at 0, we conclude that the spin-orbit interaction effects only the states above  $E_F$ . This is the case both at equilibrium and under pressure.

**Table 5.** Spin-orbit splitting and energies at high symmetry k-points of bcc francium at equilibrium

	$\Gamma_{25'}$	$H_{25'}$	$P_4$		
NSO	0.258	0.484	0.149		
WSO	0.255	0.264	0.479	0.493	0.121
$\Delta E$	0.009	0.014		0.040	

We find that the results using the GGA functional, which does a better job with predicting total energy related calculations, without spin-orbit interaction can accurately describe the properties of Fr, including superconductivity.

### Energy bands

Figure 6 shows the energy bands of Fr for the bcc structure using the LAPW method with GGA functional. Figure 6(a)

shows the bcc band structure at equilibrium pressure, while Figure 6(b) shows the bcc band structure under the largest calculated pressure, corresponding to a volume of 34% of the GGA equilibrium volume. As pressure is increased, the d-like energy bands begin to cross the Fermi level, allowing increased s- and d-band hybridization. For example, Figure 6 shows  $H_{12}$ , which is of entirely d-character, drop below the Fermi level. Comparisons with the other alkali metals show similar features in the energy bands.<sup>[8]</sup> With the increased contribution of the d-bands, these metals begin to show characteristics of the transition metals, which is discussed further in Superconductivity section.

### Superconductivity

The results presented in this section were produced with touching muffin-tin spheres. Using the touching muffin-tin results makes the calculations consistent with the scattering theory of the RMTA. To calculate the electron-ion matrix element known as the Hopfield parameter,  $\eta$ ,<sup>[9]</sup> we use the following formula,<sup>[10]</sup>

$$\eta = N(E_F) \langle l^2 \rangle \quad (1)$$

where  $N$  is the total DOS and  $\langle l^2 \rangle$  is the electron-ion coupling matrix, which is calculated with the Gaspari and Gyorffy theory (GG)<sup>[10]</sup> using the angular momentum components of the DOS and the phase shifts. The following equation gives the electron-ion coupling matrix,

$$\langle l^2 \rangle = \frac{E_F}{\pi^2 N^2(E_F)} \sum_{l=0}^{\infty} \frac{2(l+1) \sin^2(\delta_{l+1} - \delta_l) N_{l+1} N_l}{N_{l+1}^{(1)} N_l^{(1)}} \quad (2)$$

where  $N_l$  are the angular momenta,  $l$ -, components of the DOS at  $E_F$ ,  $\delta_l$  are scattering phase shifts calculated at the muffin-tin radius and at  $E_F$ , and  $N_l^{(1)}$  is the so-called free-scatterer DOS calculated from the radial wave functions,  $u_l$ . The Hopfield parameter is then used to calculate the electron-phonon

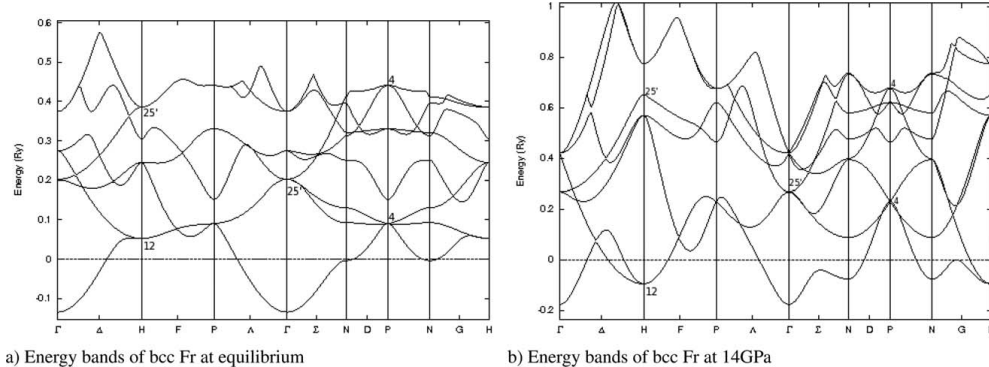


**Figure 6.** The GGA energy bands for bcc Fr at equilibrium (a) and a pressure of ~14 GPa (b).

coupling constant, which is obtained using the following equation from McMillan's strong-coupling theory<sup>[11]</sup>

$$\lambda = \frac{\eta}{M\langle\omega^2\rangle} \quad (3)$$

where  $M$  is the atomic mass and  $\langle\omega^2\rangle$  is the average of the phonon frequency squared, which is related to the Debye temperature by

$$\langle\omega^2\rangle = \frac{1}{2}\Theta_D^2 \quad (4)$$

Since there are no experimental values for the Debye temperature of Fr, the formula by Moruzzi et al.<sup>[12]</sup> was used to calculate the Debye temperature,

$$\Theta_D = 131.6 \sqrt{\frac{r_0 B}{M}} \quad (5)$$

where  $r_0$  is the Wigner-Seitz radius in au and  $B$  is the bulk modulus in GPa. The equilibrium volume was found to be  $V_{GGA_{eq}} = 801,182 \text{ au}^3$  for the bcc structure, with a Debye temperature from eq. (5),  $\Theta_D = 25 \text{ K}$ , which is consistent with the experimental trend of reducing  $\Theta_D$  as we go from the lighter to the heavier alkali metals. The critical temperature is given by the McMillan equation,<sup>[11]</sup>

$$T_C = \frac{\Theta_D}{1.45} \exp \left[ \frac{-1.04(1+\lambda)}{\lambda - \mu^*(1+0.62\lambda)} \right] \quad (6)$$

where  $\mu^*$  is the Coulomb pseudopotential, which was set to 0.13 for our calculations. We also calculated  $T_C$  for values of  $\mu^*$  between 0.1 and 0.16. These are the most accepted values used, based on fits to experimental data. The critical temperature varies, between 5.9 and 7.8 K, at the highest pressure calculated.

The GG theory has been criticized as being designed for transition metals only. However, we have shown that the GG also works well for the alkali metals, which behave like transition metals under pressure.<sup>[13,14]</sup> These results not only compare well with experimental results for Li,<sup>[15–18]</sup> but are equivalent, if not better, than those produced by other recent methods.<sup>[19–21]</sup> Furthermore, Profeta et al.<sup>[22]</sup> and Sanna et al.<sup>[23]</sup> using an elaborate DFT formalism, predict superconductivity for potassium in agreement with our earlier results,<sup>[13]</sup> which were based on the GG and McMillan theories. We also point out that while calculations for the hcp structure neglect the nonspherical corrections, we expect these corrections to be small. Furthermore, superconductivity occurs at pressures after the transition to the bcc structure.

Returning to Fr, our calculations of the Debye temperature, superconducting critical temperature, electron-phonon coupling constant, bulk modulus, and pressure were performed using the GGA functional for volumes down to 34%  $V_{GGA_{eq}}$ . Results discussed in this section correspond to the GGA

functional. We calculated, similarly to the other alkali metals, that Fr has near-zero superconducting critical temperature at equilibrium.

Figure 7(a) shows a monotonic increase of Debye temperature with increased pressure. The Debye temperature continues to increase past 110 K at pressures beyond the plotted pressures. In Figures 7(b) and 7(c), we show the electron-ion interaction and electron-phonon coupling constant values. Both the trends increase with increased pressure. The  $\lambda$  values stay under 1.5 for pressures beyond those plotted in the figures, corresponding to a percent volume below 34%  $V_{GGA_{eq}}$ . As discussed in Energy bands section, the increased contribution of the d band at the Fermi level greatly influences the electron-ion interaction. This contribution is demonstrated by the monotonic increase in the  $\eta$  values for increased pressure. We also see in Figure 7(b) that the p-d component of  $\eta$  has the largest contribution to the overall  $\eta$  values. These features are similar to those found for the other alkali metals.<sup>[14]</sup> The transition metals, at equilibrium pressures, also see  $\eta$  values similar to the alkalis under compression, due to the influence of the d-bands at the Fermi surfaces. Figure 7(d) shows the increasing trend of the superconducting critical temperatures with increasing pressure, reaching 7 K for pressures up to 14 GPa for GGA.

Integration of the DOS suggests a transfer of charge from s- to d-like under pressure. We calculate the initial charge at zero pressure to be 72% s-like, 16% p-like, 12% d-like, and 0% f-like. However, under a pressure of 14 GPa, we see the charge become 59% d-like, 30% s-like, 8% p-like, and 3% f-like. Calculations for pressures in between show charge transfer to d-like, while the s-like decrease, with p- and f-like charges remaining approximately constant.

It should be noted that superconductivity seems to occur for even the most compressible metal when under pressure. Furthermore, our prediction of superconductivity in Fr is consistent with the results of Shi and Papaconstantopoulos,<sup>[13,14]</sup> who predicted that the alkali metals, with the exception of Sodium, will become superconducting at temperatures between 5 and 20 K when subjected to high pressure. It has also been experimentally verified that lithium becomes superconducting above pressures of 20 GPa at temperatures of 15 K.<sup>[15]</sup>

## Ferromagnetism

Since the d-DOS dominates at pressures beyond 2 GPa, we performed calculations for the possible ferromagnetism of Fr. The Stoner parameter,<sup>[24]</sup>  $I$  given by Eq. (7), and DOS at the Fermi level are used to calculate the ferromagnetism criterion of Stoner ( $N(E_F)I > 1$ ).

$$I = \int dr \gamma^2(r) |K(r)| \quad (7)$$

where  $\gamma = \frac{1}{N(E_F)} \sum_i N_i(E_F) u_i^2(E_F)$

In Eq. (7),  $u_i(E_F)$  is the value of the radial wave function at the Fermi level and  $K(r)$  is a kernel giving the exchange and

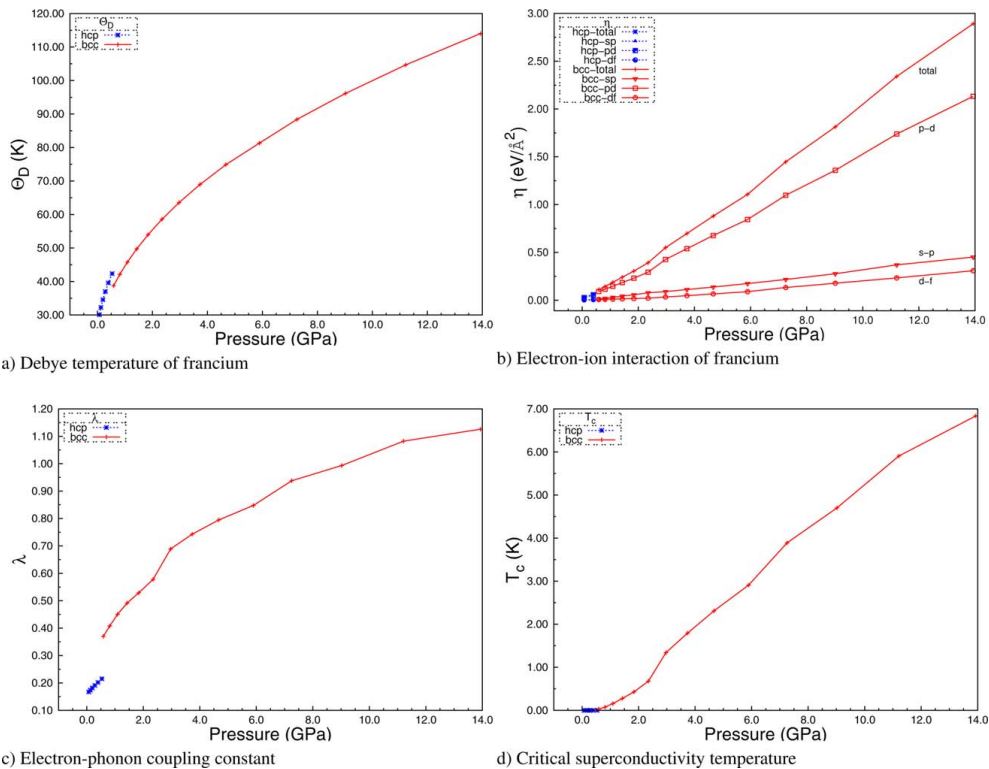


**Figure 7.** Debye temperature,  $\Theta_D$  (a), electron-ion interaction,  $\eta$  (b), electron-phonon coupling constant,  $\lambda$  (c), and critical temperature,  $T_C$  (d), versus pressure of Fr. LAPW using GGA functional with no spin-orbit interaction. The hcp structure is given by a dashed (blue) line, and the bcc structure as a solid (red) line. [Color figure can be viewed in the online issue, which is available at [wileyonlinelibrary.com](http://wileyonlinelibrary.com).]

correlation enhancement of an external magnetic field. When  $N(E_F)/l < 1$ , there is no implied ferromagnetism. We found that the alkali metals have Stoner parameter values that suggest no ferromagnetism at equilibrium or under pressure. Table 6 shows values of the Stoner parameter for various volumes.

Table 6. Stoner parameter and Stoner criterion of bcc francium for various volumes		
Volume (au <sup>3</sup> )	Stoner parameter, $l$ (Ry)	$N(E_F)l$
595.5	0.020	0.333
500	0.018	0.273
364.5	0.014	0.271
275.7	0.013	0.293
Results using LAPW with GGA functional.		

## Conclusions

Fr is a rare element and very little work has been done experimentally or theoretically. This article has predicted the properties and structure of Fr using density functional theory. These

calculations complete the systematic study of superconductivity in the alkali metals discussed by Shi et al.<sup>[13,14]</sup>

In most alkali metals using the GGA or LDA functional, it is found that fcc is the ground state instead of bcc. However, due to energy differences of much less than 1 mRy between hcp, fcc, and bcc, we conclude that density functional theory has difficulty obtaining an accurate description of the equilibrium structure for the alkali metals. This is due to the very small  $\Delta E$ , which are within the computational error of the methods used, and possibly due to zero point motion effects. Fr was calculated to be an hcp structure but with an energy difference of only 0.29 mRy between bcc and hcp. The material displayed neither superconducting properties at equilibrium nor did it display any ferromagnetic properties. This is consistent with the other alkali metals. However, under small pressure we see a phase transition from hcp to bcc, and under larger pressures we see superconducting properties, with a superconducting critical temperature of approximately 7 K at 14 GPa. This was found to be caused by increasing s-d hybridization that begins to appear at the Fermi surface under pressure. We also found the spin-orbit interaction to have little effect on Fr at equilibrium or under pressure because it only effects the states above the Fermi energy.

**Acknowledgments**

The authors thank Lane Nixon for helpful discussions during the beginning of the project.

**Keywords:** francium · electronic structure · superconductivity · density functional theory

How to cite this article: A. P. Koufos, D. A. Papaconstantopoulos, *Int. J. Quantum Chem.* **2013**, 113, 2070–2077. DOI: 10.1002/qua.24466

- [1] S. Aubin, E. Gomez, L. A. Orozco, G. D. Sprouse, *Rev. Sci. Instrum.* **2003**, 74, 4342.
- [2] D. R. Lide, Ed. CRC Handbook of Chemistry and Physics, 89th Edition (Internet Version 2009); CRC Press/Taylor and Francis, Boca Raton, FL, 2008.
- [3] G. D. Sprouse, L. A. Orozco, J. E. Simsarian, W. Z. Zhao, *Nucl. Phys.* **1998**, A630, 316.
- [4] M. Sigalas, N. C. Bacalis, D. A. Papaconstantopoulos, M. J. Mehl, A. C. Switendick, *Phys. Rev. B* **1990**, 42, 11637.
- [5] D. A. Papaconstantopoulos, D. J. Singh, *Phys. Rev. B* **1991**, 45, 7507.
- [6] C. Kittel, Introduction to Solid State Physics, 8th Edition; Wiley, Hoboken, NJ, 2005.
- [7] O. Jepsen, O. K. Andersen, *Solid State Commun.* **1971**, 9, 1763.
- [8] D. A. Papaconstantopoulos, Handbook of the Band Structure of Elemental Solids; Plenum, New York, New York; **1986**.
- [9] J. J. Hopfield, *Phys. Rev.* **1969**, 186, 443.
- [10] G. D. Gaspari, B. L. Gyorffy, *Phys. Rev. Lett.* **1972**, 28, 801.
- [11] W. L. McMillan, *Phys. Rev.* **1968**, 167, 331.
- [12] V. L. Moruzzi, J. F. Janak, K. Schwarz, *Phys. Rev. B* **1988**, 37, 790.
- [13] Lei Shi, D. A. Papaconstantopoulos, M. J. Mehl, *Solid State Commun.* **2003**, 127, 13.
- [14] L. Shi, D. A. Papaconstantopoulos, *Phys. Rev. B* **2006**, 73, 184516.
- [15] T. Tomita, S. Deemyad, J. J. Hamlin, J. S. Schilling, V. G. Tissen, B. W. Veal, L. Chen, H. Claus, *J. Phys. Condens. Matter* **2005**, 17(11), S921.
- [16] S. Deemyad, J. S. Schilling, *Phys. Rev. Lett.* **2003**, 91, 167001.
- [17] K. Shimizu, H. Ishikawa, D. Takao, T. Yagi, K. Amaya, *Nature (London)* **2002**, 419, 597.
- [18] V. V. Struzhkin, M. I. Eremets, W. Gan, H. Mao, R. J. Hemley, *Science* **2002**, 298, 1213.
- [19] D. Kasinathan, K. Koepernik, J. Kunes, H. Rosner, W. E. Pickett, *Phys C* **2007**, 460.
- [20] Y. Yao, J. S. Tse, K. Tanaka1, F. Marsiglio, Y. Ma, *Phys. Rev. B* **2009**, 79, 054524.
- [21] T. Bazhirov, J. Noffsinger, M. L. Cohen, *Phys. Rev. B* **2010**, 82, 184509.
- [22] G. Profeta, C. Franchini, N. N. Lathiotakis, A. Floris, A. Sanna, M. A. L. Marques, M. Lders, S. Massidda, E. K. U. Gross, A. Continenza, *Phys. Rev. Lett.* **2006**, 96, 047003.
- [23] A. Sanna, C. Franchini, A. Floris, G. Profeta, N. N. Lathiotakis, M. Lders, M. A. L. Marques, E. K. U. Gross, A. Continenza, S. Massidda, *Phys. Rev. B* **2006**, 73, 144512.
- [24] J. F. Janak, *Phys. Rev. B* **1977**, 16, 255.

Received: 3 April 2013

Revised: 3 April 2013

Accepted: 5 April 2013

Published online on 13 May 2013

# Appendix B: Electronic Structure of Iron-Selenium - Published

PHYSICAL REVIEW B 89, 035150 (2014)

## First-principles study of the electronic structure of iron-selenium: Implications for electron-phonon superconductivity

Alexander P. Koufos and Dimitrios A. Papaconstantopoulos

School of Physics, Astronomy, and Computational Sciences, George Mason University, Fairfax, Virginia 22030, USA

Michael J. Mehl

Center of Computational Material Sciences, Naval Research Laboratory, Washington, D.C., USA

(Received 21 November 2013; revised manuscript received 6 January 2014; published 31 January 2014)

We have performed density functional theory calculations using the linearized augmented plane wave method (LAPW) with the local density approximation (LDA) functional to study the electronic structure of the iron-based superconductor iron-selenium (FeSe). In our study, we have performed a comprehensive set of calculations involving structural, atomic, and spin configurations. All calculations were executed using the tetragonal lead-oxide or  $P4/nmm$  structure, with various volumes,  $c/a$  ratios, and internal parameters. Furthermore, we investigated the spin polarization using the LDA functional to assess ferromagnetism in this material. The paramagnetic LDA calculations find the equilibrium configuration of FeSe in the  $P4/nmm$  structure to have a volume of 472.5 a.u.<sup>3</sup> with a  $c/a$  ratio of 1.50 and internal parameter of 0.255, with the ferromagnetic having comparable results to the paramagnetic case. In addition, we calculated total energies for FeSe using a pseudopotential method, and found comparable results to the LAPW calculations. Superconductivity calculations were done using the Gaspari-Gyorffy and the McMillan formalisms and found substantial electron-phonon coupling. Under pressure, our calculations show that the superconductivity critical temperature continues to rise, but underestimates the measured values.

DOI: 10.1103/PhysRevB.89.035150

PACS number(s): 71.15.Mb, 71.20.-b, 74.20.Pq, 74.70.Xa

### I. INTRODUCTION

Iron-based superconductors are the newest addition to high-temperature superconductivity. Current experimental findings have made many believe that the superconductivity may not be due to electron-phonon interaction [1–3]. Spin fluctuations and spin-density waves have been suggested as mechanisms for the high-temperature superconductivity, but without quantitative assessment. It is therefore important to fully study the electronic structure of these materials, and its implications on superconductivity.

Iron-selenium (FeSe) has the simplest structure of the current iron-based superconductors. As shown in Fig. 1, under ambient conditions [1–5] it forms in the tetragonal PbO structure, *Strukturbericht* B10 [6], space group  $P4/nmm-D_{4d}^7$  (No. 129). The Fe atoms are fixed at the (2a) Wyckoff position (000), while the Se atoms are at the (2c) Wyckoff position (01/2z).

There have been several studies of iron-selenium both computationally and experimentally [1–5,7–12]. Most of the computational works use the experimental equilibrium results as input without optimization of all parameters through first principles. In this work we have performed calculations using the experimental parameters as well as calculations based on first-principles energy minimization.

### II. COMPUTATIONAL DETAILS

Most calculations performed in this paper used the linearized augmented plane wave (LAPW)[13] implementation of density functional theory [14]. LAPW wave functions were used for the valence band, further augmented by local orbitals for the semicore states, using a code developed by Krakauer, Wei, and Singh [15,16]. Exchange and correlation effects were

approximated by the Hedin-Lundqvist [17] parametrization of the local density approximation (LDA) [18]. The rigid muffin-tin approximation code developed by Papaconstantopoulos and Klein [19] was used to apply the Gaspari-Gyorffy theory [20]. A  $\Gamma$ -centered  $k$ -point mesh of 75 points was used for total energy and density of states (DOS) calculations. A larger mesh of 904  $k$  points was used for the calculations of energy bands. All calculations used a basis set size of  $6 \times 6 \times 6$ , seven core states (equilibrium state of argon) for iron and nine core states (argon + 3d states) for selenium resulting in 28 total valence electrons. Local orbitals were also used with energies of 0.308 Ry for 3s and 3p iron and −0.548 Ry and 0.158 Ry for 3s and 3p selenium, respectively. All calculations used fixed muffin-tin radii of 2.0 a.u. for Fe and Se atoms. Structural optimization was executed via energy minimization with respect to both the tetragonal lattice constants  $a$  and  $c$  and the internal selenium parameter  $z$ . As a check on our LAPW results, we performed calculations on the B10 structure using the Vienna *ab initio* simulation package (VASP) [21–23] using the VASP implementation [24] of the projector augmented-wave (PAW) method [25]. To ensure convergence we used a plane-wave cutoff of 500 eV, and used the same  $k$ -point mesh as in the LAPW calculations.

### III. TOTAL ENERGY OF IRON-SELENIUM

Figure 2 shows the optimized (variation of volume,  $c/a$ , and internal parameter  $z$ ) total energy calculations performed with our LAPW code, as well as our optimized VASP calculations with the LDA functional. Both LAPW and VASP methods with the LDA functional underestimate the measured lattice parameters by 4.5% and 2.2% for the  $a$  and  $c$  parameters, respectively. This was expected since the LDA functional

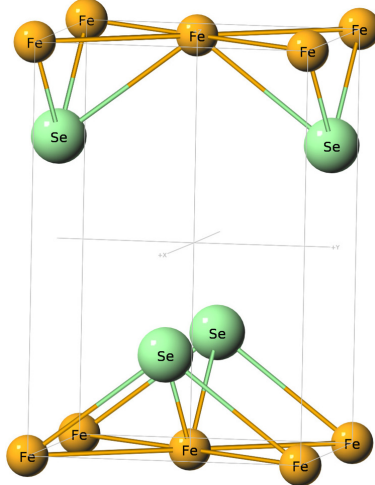


FIG. 1. (Color online) Ground state structure of FeSe, *Strukturbericht* designation B10. The space group is  $P4/nmm-D_{3d}^2$  (No. 129). The iron atoms are on (2a) Wyckoff sites, while the selenium atoms are on (2c) sites.

usually underestimates the lattice parameters, although for simple materials the difference is usually smaller. Bulk modulus results were overestimated by 3.9% using the LAPW method. The calculated and experimental structural results and bulk moduli of FeSe are given in Table I. Structural results from another optimized study of FeSe using PAW and the LDA functional completed by Winiarski *et al.* [12] agree with our calculations. They found lattice parameters of  $a = 6.7902$  a.u.,  $c = 10.177$  a.u., and  $z = 0.257$ . Although it is not explicitly stated in their paper, these correspond to underestimations of experimental values of 4.7% and 2.5%

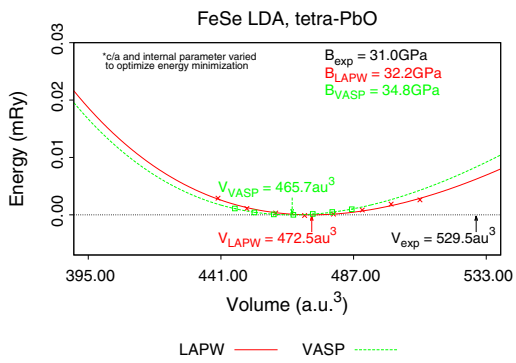


FIG. 2. (Color online) Total energy of FeSe using the LAPW with the LDA functional and VASP code with the LDA functional. Both methods performed energy minimization to obtain the optimal energy for each volume. Although the equilibrium volume is underestimated, the bulk modulus value is in very good agreement with experiment.

TABLE I. Volume, structural parameter,  $a$ ,  $c/a$  ratio, internal parameter,  $z$ , and bulk moduli for FeSe at ambient pressure. Calculated results are from optimized calculations of the corresponding method and the LDA functional. Experimental results are taken from Kumar *et al.* [10] and Ksenofontov *et al.* [11].

Volume (a.u. $^3$ )	$a$ (a.u.)	$c/a$	$z$	Bulk mod. (GPa)
472.5	6.804	LAPW	0.255	32.2
		VASP	1.50	34.8
465.7	6.771	Experiment	0.256	
529.5 [10]	7.121 [10]	1.465 [10]	0.269 [10]	31.0 [11]

for  $a$  and  $c$  parameters, respectively. Comparing our structural results under pressure with the Winiarski [12] paper, we find comparable results for all pressures.

All calculations presented in this paper are for paramagnetic FeSe. We also performed ferromagnetic calculations which yield nearly the same results for total energy to the paramagnetic calculations. Furthermore, the calculated equilibrium parameters are nearly equivalent to the paramagnetic case, and therefore show no significant difference between the two cases. Further calculations using the ferromagnetic, antiferromagnetic, and other magnetic orders should be considered for further study, but are beyond the scope of this paper.

#### IV. ELECTRONIC STRUCTURE

DOS and energy band calculations were performed using the LAPW results from the optimized LDA total energy calculations. These calculations are performed down to 76%  $V_{\text{exp}}$ , where  $V_{\text{exp}} = 529.5$  a.u. $^3$  from Table I. This corresponds to pressures as high as 8 GPa. The DOS results are then used to calculate superconductivity properties.

Figure 3 shows the total, Se- $p$ , and Fe- $d$  decomposed DOS for FeSe at ambient pressure, i.e.,  $V_{\text{exp}}$ . The  $d$  component of

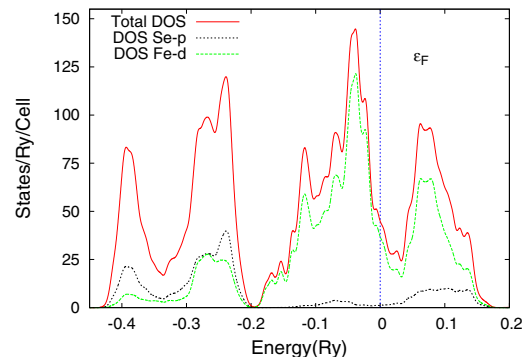


FIG. 3. (Color online) Total, Se- $p$ , and Fe- $d$  density of states of FeSe at ambient pressure. Notice that the Fe- $d$  component is the largest contributor to the total DOS around the Fermi level. Dashed vertical (blue) line represents the Fermi level.

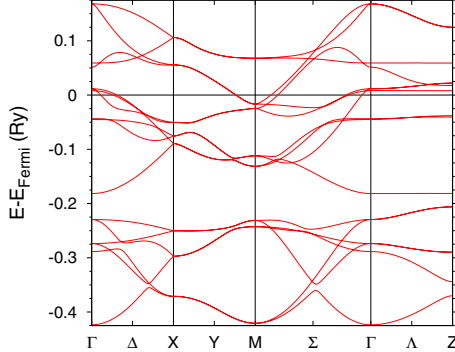


FIG. 4. (Color online) Energy bands of FeSe at ambient pressure. Solid horizontal (black) line represents the Fermi level.

the Fe DOS is the largest contributor to the total DOS near and at the Fermi level,  $E_F$ . Around  $E_F$ , these Fe- $d$  states are localized and do not extend into the interstitial region, while the Se- $p$  and the Fe- $d$  tails have significant contributions in the interstitial space as shown in Fig. 3. The Se- $s$  semicore states, not shown in Fig. 3, are found approximately 1 Ry below  $E_F$ . Figure 4 displays the energy bands of FeSe at ambient pressure. These two figures are in agreement with calculations of the DOS and energy bands performed by other groups [7–9]. Table II gives a comparison of the DOS between our results for the experimental lattice parameters with those from Subedi *et al.* [7] and Bazhirov and Cohen [9]. The specific lattice parameters used for the DOS calculations presented in Table II are  $a = 7.114$  a.u.,  $c = 10.1154$  a.u., and  $z = 0.2343$  for both Subedi *et al.* [7] and us. However, it is unclear what structural parameters were used in Ref. [9]. DOS calculations for various  $a$ ,  $c$ , and  $z$  lead to different values at the Fermi surface. These differences in structural parameters are influencing the calculation of superconducting properties and will be discussed in more detail in the following section. The differences in  $N(E_F)$  shown in Table II are probably due to the details of the method used to calculate the DOS and possibly the number of  $k$  points.

## V. SUPERCONDUCTIVITY

As mentioned, the DOS calculations are used to calculate superconductivity parameters. For each atom type, we

TABLE II. Comparison of the total DOS at the ambient pressure. Our DOS calculations, as well as those of Subedi *et al.* [7], are for the experimental structural parameters with the internal parameter  $z = 0.2343$ . It is not entirely certain what were the structural parameters used to calculate the values given by Bazhirov and Cohen [9].

	$N(E_F)$ (states/Ry/cell)
This paper	32.3
Subedi [7]	26.0
Bazhirov [9]	21.0

calculate the electron-ion matrix element known as the Hopfield parameter,  $\eta_i$  [26], using the following formula [20]:

$$\eta_i = N(E_F)\langle I^2 \rangle_i, \quad (1)$$

where  $N(E_F)$  is the total DOS per spin at  $E_F$  and  $\langle I^2 \rangle_i$  is the electron-ion matrix element for each atom type, which is calculated by the Gaspari and Gyorffy theory [20]. The electron-ion matrix element is given by the following equation:

$$\langle I^2 \rangle_i = \frac{E_F}{\pi^2 N^2(E_F)} \sum_{l=0}^2 \frac{2(l+1) \sin^2(\delta_{l+1}^i - \delta_l^i) N_{l+1}^i N_l^i}{N_{l+1}^{(1),i} N_l^{(1),i}}, \quad (2)$$

where  $N_l^i$  are the per spin angular momenta ( $l$ ) components of the DOS at  $E_F$  for atom type  $i$ ,  $N_l^{(1),i}$  are the so-called free-scatterer DOS for atom type  $i$ , and  $\delta_l^i$  are scattering phase shifts calculated at the muffin-tin radius and at  $E_F$  for atom type  $i$ . Free-scatterer DOS are calculated by

$$N_l^{(1)} = \frac{\sqrt{E_F}}{\pi} (2l+1) \int_0^{R_s} r^2 u_l^2(r, E_F) dr \quad (3)$$

and scattering phase shifts are calculated by

$$\tan \delta_l(R_S, E_F) = \frac{j'_l(kR_S) - j_l(kR_S)L_l(R_S, E_F)}{n'_l(kR_S) - n_l(kR_S)L_l(R_S, E_F)}, \quad (4)$$

where  $R_S$  is the muffin-tin radius;  $j_l$  are spherical Bessel functions;  $n_l$  are spherical Neumann functions;  $L_l = u'_l/u_l$  is the logarithmic derivative of the radial wave function,  $u_l$ , evaluated at  $R_S$  for different energies;  $k = \sqrt{E_F}$ ; and  $u_l$  is computed by solving the radial wave equation at each  $k$  point in the Brillouin zone. The Hopfield parameter is then used to calculate the electron-phonon coupling constant, which is obtained using the following equation from McMillan's strong-coupling theory [27]:

$$\lambda = \sum_{i=1}^2 \frac{\eta_i}{M_i \langle \bar{\omega}^2 \rangle}, \quad (5)$$

where  $M_i$  is the atomic mass of atom type  $i$ , and  $\langle \bar{\omega}^2 \rangle$  is the average of the squared phonon frequency taken from the experimentally calculated Debye temperature of Ksenofontov *et al.* [11]. The Debye temperature is related to the phonon frequency by

$$\langle \bar{\omega}^2 \rangle = \frac{1}{2} \overline{\Theta_D^2}, \quad (6)$$

where  $\overline{\Theta_D}$  is found to be 240 K [11]. The critical superconductivity temperature is given by the McMillan equation [27]

$$T_c = \frac{\Theta_D}{1.45} \exp \left[ \frac{-1.04(1+\lambda)}{\lambda - \mu^*(1+0.62\lambda)} \right], \quad (7)$$

where  $\mu^*$  is the Coulomb pseudopotential, given by the Bennemann-Garland equation [28]

$$\mu^* = 0.13 \frac{N(E_F)}{1 + N(E_F)}. \quad (8)$$

In Eq. (8),  $N(E_F)$  is expressed in eV and given in a per cell basis. The prefactor 0.13 was chosen such that  $\mu^* = 0.10$  at

TABLE III. Total DOS at  $E_F$ ,  $N(E_F)$ , Hopfield parameters,  $\eta$ , electron-phonon coupling constants,  $\lambda$ , Coulomb pseudopotentials,  $\mu^*$ , and critical superconductivity temperature,  $T_c$ , for FeSe at various volumes, corresponding to pressures as high as 8 GPa. Experimental values are calculated using a fixed  $c/a$  and  $z$  taken from experimental parameters ( $c/a = 1.4656$  and  $z = 0.260/z = 0.2343$ ).

$V$ (a.u. <sup>3</sup> )	$N(E_F)$ (states/Ry/cell)	$\eta_{\text{Fe}}$ (eV/Å <sup>2</sup> )	$\eta_{\text{Se}}$	$\lambda_{\text{Fe}}$	$\lambda_{\text{Se}}$	$\lambda$	$\mu^*$	$T_c$ (K)
Experimental $c/a$ ; optimized $z$ ( $c/a = 1.4656$ ; $z = 0.2343$ )								
530	32.28	1.47	0.46	0.500	0.114	0.614	0.10	4.9
Experimental parameters ( $c/a = 1.4656$ ; $z = 0.260$ )								
530	44.82	1.50	0.36	0.513	0.090	0.603	0.10	4.6
460	37.05	2.15	0.47	0.558	0.088	0.646	0.095	6.8
430	34.23	2.58	0.53	0.600	0.089	0.689	0.093	8.5
420	33.44	2.75	0.55	0.618	0.088	0.707	0.0927	9.4

the experimental volume.  $\Theta_D$  was calculated as a function of volume,  $V$ , by the following formula:

$$\Theta_D = C(V - \bar{V}) + \bar{\Theta}_D, \quad (9)$$

where  $C$  is given as the slope between the experimental Debye temperature of Ksenofontov *et al.* [11] at ambient and 6.9 GPa pressures at their corresponding volumes. We have  $C = -0.513$ , where  $\bar{V} = 530.3$  a.u.<sup>3</sup>.

In Table III, we show the total DOS at the Fermi level, Hopfield parameters, electron-phonon coupling constants, Coulomb pseudopotentials, and critical superconductivity temperature for FeSe at various volumes, using our LAPW results. We have included constant  $c/a$  and  $z$  calculations in Table III, where  $c/a$  is set at the experimental value.

First we note that at the experimental volume we obtain  $T_c \approx 5$  K reasonably close to the measured value of 8 K. We also note that if the  $c/a$  ratio and  $z$  are held constant, specifically at the experimental values, throughout the DOS calculations for the given volumes, an increase in all  $T_c$  values is found for increased pressure (decreasing volume), as seen in Table III. Although the total  $N(E_F)$  is found to monotonically decrease during the increase in pressure, the parameter  $\eta$  undergoes a rapid increase. This decrease in total  $N(E_F)$  also contributes to a subtle reduction in the  $\mu^*$  at larger pressures. It is also of interest that the change of internal parameter does not seem to influence the overall superconductivity properties. We continue to see the increase of  $\eta$  due to the complexity of Eq. (2), which gives the electron-ion matrix elements  $\langle I^2 \rangle$ . This shows that the total DOS at the Fermi level is not the only, or the major, influence in calculating superconductivity properties. It is important to note from Table III that  $\lambda_{\text{Fe}}$  is approximately six to seven times larger than  $\lambda_{\text{Se}}$ . This is not surprising since the Fe states dominate near  $E_F$ , but also justifies our use of the Debye temperature in estimating the average phonon frequency. Varying the  $c/a$  ratio for a given volume does, however, cause a significant change in the superconductivity properties. This makes the search of absolute optimized parameters quite hard and time consuming. We show the trend of increasing superconductivity critical temperature for increasing pressure using the experimental

TABLE IV. Calculated DOS and superconductivity related results of LaFeAsO using LAPW with the LDA functional. Experimental critical temperature result is taken from Takahashi *et al.* [32].

LaFeAsO						
$N(E_F)$ (states/Ry/cell)						
53.964						
	$N_s(E_F)$	$N_p(E_F)$	$N_d(E_F)$	$N_f(E_F)$	$\eta$ (eV/Å <sup>2</sup> )	$\lambda$
Fe	0.029	0.562	44.052	0.014	0.967	0.19
As	0.006	0.826	0.439	0.119	0.186	0.03
La	0.006	0.126	0.330	0.278	0.034	0.003
O	0.009	0.264	0.042	0.005	0.008	0.006
$\Theta_D$ (K)	$\lambda_{\text{total}}$	$\mu^*$	$T_c$	$T_c$ (exp)		
319	0.23	0.13	0.0	45.0		

structural parameters, with a value of about 9 K, which is too small to account for the measured value of 30 K.

At ambient conditions, our electron-phonon coupling constant calculation  $\lambda = 0.603$  is consistent with the value calculated by Ksenofontov *et al.* [11],  $\lambda = 0.65$ , by inverting the McMillan equation using the measured  $\theta_D$ .

Other computational papers [7,9] find values of approximately  $\lambda = 0.15$  using linear response theory. It is not clear to us what is the source of discrepancy between our calculations based on the Gaspari-Gyorffy theory and the linear response theory-based calculations. It is possible that our use of the relationship between average phonon frequency and the Debye temperature is an oversimplification or, on the other hand, the Brillouin-zone samplings performed in the linear response codes are not sufficiently converged. It would be helpful for resolving this issue to have separate calculations of  $\langle I^2 \rangle$  by the linear response method. In any case, our results presented in the following paragraphs regarding our agreement with the small  $\lambda = 0.23$  we obtained for LaFeAsO need to be understood.

In this other iron-based superconducting material, LaFeAsO, electron-phonon coupling constants of approximately 0.2 [29,30] have been reported. We have also performed superconductivity calculations of LaFeAsO using the results of Ref. [31]. Our calculations of the electron-phonon coupling constant for LaFeAsO is consistent with the results of these groups. LaFeAsO is known to be on the verge of magnetic instability [29,30]. This suggests that spin fluctuations are important in this material.

Table IV shows our calculated LAPW DOS and superconductivity results using the LDA functional and experimental parameters for LaFeAsO. The Hopfield parameter of the Fe atom is seen to be quite low for the LaFeAsO material, in contrast to what we find in FeSe. Similarly, the electron-phonon coupling is much larger for FeSe.

## VI. CONCLUSIONS

In this paper we present calculations of the band structure of FeSe which are in good agreement with other works regarding mechanical and electronic properties of this material. We

have also presented calculations of the parameters entering the McMillan equation for the superconducting critical temperature. Our view is that an electron-phonon mechanism can explain superconductivity in FeSe at zero pressure, but it does not give enough of an enhancement to the value of  $T_c$  under pressure. Comparing with the multicomponent compound LaFeAsO we see the following picture emerging: In LaFeAsO, a combination of the small value of the calculated parameter  $\eta$  and a large value of the measured  $\theta_D$  invalidates the electron-phonon coupling. On the other hand,

in the case of FeSe, the combination of large  $\eta$  and small  $\theta_D$  supports electron-phonon coupling, at least at zero pressure.

#### ACKNOWLEDGMENTS

This research was funded in part by DOE Grant No. DE-FG02-07ER46425 and by ONR Grant No. N00014-09-1-1025. We wish to thank Igor Mazin and Michelle Johannes for useful discussions.

- 
- [1] Y. Mizuguchi, F. Tomioka, S. Tsuda, T. Yamaguchi, and Y. Takano, *Appl. Phys. Lett.* **93**, 152505 (2008).
  - [2] S. Medvedev, T. M. McQueen, I. A. Troyan, T. Palasyuk, M. I. Eremets, R. J. Cava, S. Naghavi, F. Casper, V. Ksenofontov, G. Wortmann *et al.*, *Nat. Mater.* **8**, 630 (2009).
  - [3] D. Louca, K. Horigane, A. Llobet, R. Arita, S. Ji, N. Katayama, S. Konbu, K. Nakamura, T.-Y. Koo, P. Tong *et al.*, *Phys. Rev. B* **81**, 134524 (2010).
  - [4] T. M. McQueen, Q. Huang, V. Ksenofontov, C. Felser, Q. Xu, H. Zandbergen, Y. S. Hor, J. Allred, A. J. Williams, D. Qu *et al.*, *Phys. Rev. B* **79**, 014522 (2009).
  - [5] P. Diko, V. Antal, V. Kavečansky, C. Yang, and I. Chen, *Physica C: Superconductivity* **476**, 29 (2012), <http://linkinghub.elsevier.com/retrieve/pii/S0921453412000226>.
  - [6] P. P. Ewald and C. Hermann, *Strukturbericht 1913–1928* (Akademische Verlagsgesellschaft M.B.H., Leipzig, 1931).
  - [7] A. Subedi, L. Zhang, D. J. Singh, and M. H. Du, *Phys. Rev. B* **78**, 134514 (2008).
  - [8] P. P. Singh, *J. Phys.: Condens. Matter* **22**, 135501 (2010).
  - [9] T. Bazhirov and M. L. Cohen, *Phys. Rev. B* **86**, 134517 (2012).
  - [10] R. S. Kumar, Y. Zhang, S. Sinogeikin, Y. Xiao, S. Kumar, P. Chow, A. L. Cornelius, and C. Chen, *J. Phys. Chem. B* **114**, 12597 (2010).
  - [11] V. Ksenofontov, G. Wortmann, A. I. Chumakov, T. Gasi, S. Medvedev, T. M. McQueen, R. J. Cava, and C. Felser, *Phys. Rev. B* **81**, 184510 (2010).
  - [12] M. J. Winiarski, M. Samsel-Czekaa, and A. Ciechan, *Europhys. Lett.* **100**, 47005 (2012).
  - [13] D. Singh and L. Nordstrom, *Planewaves, Pseudopotentials, and the LAPW Method*, 2nd ed. (Springer, New York, 2006).
  - [14] P. Hohenberg and W. Kohn, *Phys. Rev.* **136**, B864 (1964).
  - [15] S. H. Wei and H. Krakauer, *Phys. Rev. Lett.* **55**, 1200 (1985).
  - [16] D. Singh, *Phys. Rev. B* **43**, 6388 (1991).
  - [17] L. Hedin and B. I. Lundqvist, *J. Phys. C* **4**, 2064 (1971).
  - [18] W. Kohn and L. J. Sham, *Phys. Rev.* **140**, A1133 (1965).
  - [19] D. A. Papaconstantopoulos, L. L. Boyer, B. M. Klein, A. R. Williams, V. L. Moruzzi, and J. F. Janak, *Phys. Rev. B* **15**, 4221 (1977).
  - [20] G. Gaspari and B. Gyorffy, *Phys. Rev. Lett.* **28**, 801 (1972).
  - [21] G. Kresse and J. Hafner, *Phys. Rev. B* **48**, 13115 (1993).
  - [22] G. Kresse and J. Hafner, *Phys. Rev. B* **49**, 14251 (1994).
  - [23] G. Kresse, Ph.D. thesis, Universität Wien, Vienna, 1993.
  - [24] G. Kresse and D. Joubert, *Phys. Rev. B* **59**, 1758 (1999).
  - [25] P. E. Blöchl, *Phys. Rev. B* **50**, 17953 (1994).
  - [26] J. Hopfield, *Phys. Rev.* **186**, 443 (1969).
  - [27] W. McMillan, *Phys. Rev.* **167**, 331 (1968).
  - [28] K. H. Bennemann and J. W. Garland, *AIP Conf. Proc.* **4**, 103 (1972).
  - [29] L. Boeri, O. V. Dolgov, and A. A. Golubov, *Phys. Rev. Lett.* **101**, 026403 (2008).
  - [30] I. I. Mazin, D. J. Singh, M. D. Johannes, and M. H. Du, *Phys. Rev. Lett.* **101**, 057003 (2008).
  - [31] D. A. Papaconstantopoulos, M. J. Mehl, and M. D. Johannes, *Phys. Rev. B* **82**, 054503 (2010).
  - [32] H. Takahashi, K. Igawa, K. Arii, Y. Kamihara, M. Hirano, and H. Hosono, *Nature (London)* **453**, 376 (2008).

## Appendix C: Coherent Potential Approximation Code

This appendix includes all source code written for the Coherent Potential Approximation program. All code was written in Fortran, with each subroutine as its own file. Global variables were used and stored in global.f90. The file cpagen.f90 is the Fortran program, which sets the overall verboseness of the code and calls the "mainn" subroutine. The "mainn" subroutine calls some initialization subroutines, the subroutine to calculate the self-energies, the subroutine to calculate DOS using the final Green's function, and the subroutine to integrate the Fermi level.

Initialization for most of the global variables are performed in the subroutines "readin", "setOnsites", "kpts", "readSec", set "setInitHam". Descriptions of the function of each subroutine are given at the start of the files. The subroutine "calcSig" calls and performs the mathematics to solve for the self-energies, such as initializing the Hamiltonian with the diagonal disorder, calling the greens subroutine for solving Green's function and performing the Newton-Raphson method for an energy level. Once the Green's function and self-energies are solved for, the "cpaDOS" subroutine is run to calculated the DOS from the final Green's function. Using the calculated DOS at each energy level, the subroutine "simp" calculates the Fermi level. Figure C.1 shows the connection of each of these subroutines. The remainder of the appendix is the source code.

```
program cpagen
!<hr>
!> This program is for tetragonal perovskites with disorder in the s & p
!! orbitals of the second atom i.e. FeSe/Te, where Se/Te is the second atom.
!<hr>
use global
implicit none
v1v1 = 0
verbose = .false.
call mainn()
```

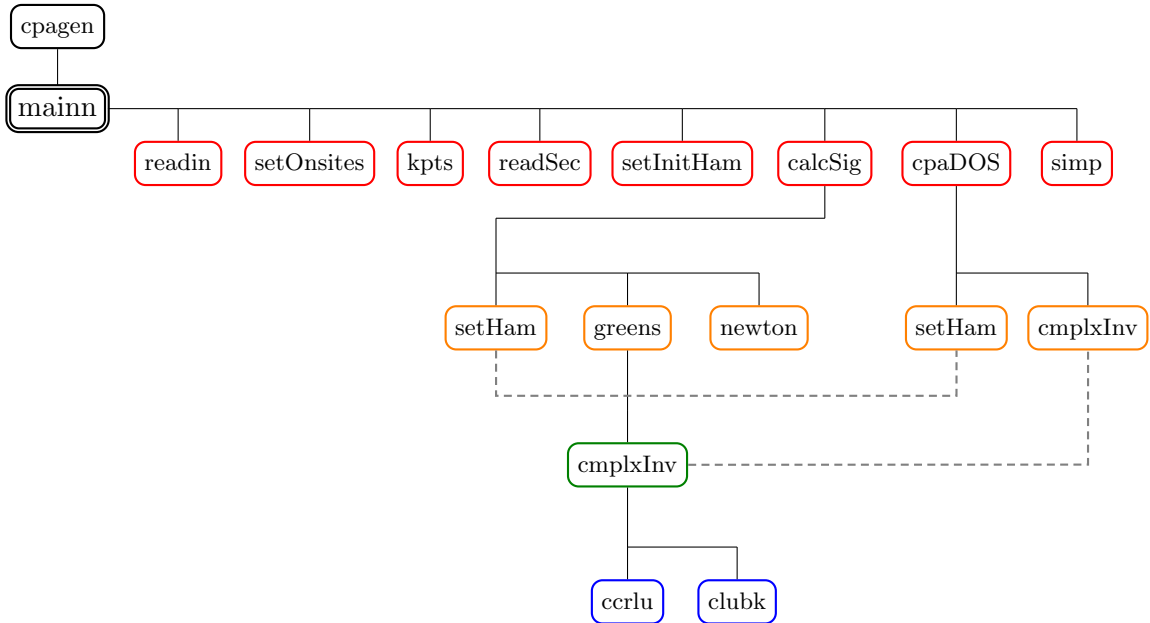


Figure C.1: Coherent Potential Approximation subroutine flow chart. Level-1 subroutines that are called directly from the `mainn` subroutine are outlined in red. Level-2 subroutines called from any Level-1 program are outlined in orange. Similarly, Level-3 subroutines are outlined in green; Level-4 subroutines in blue. The dashed lines indicate procedures that are called by more than one subroutine.

```

write(*,1000)
stop
1000 format( /, 'Program_finished_running..Check_cpaper.out_for_final &
..results',/)
end program cpagen

module global
!
!> Currently this global file is setup for calculations of P4/nmm Fe2Se/Te2
!
! Variables:
!> @param jsz - Number of kpoints
!> @param mode - Used to decide how the program is run
!! 1 - Perform full CPA prgoram, including GG calculations
!! 2 - Perform only GG calculations. Must have run mode 1 or 3 previously

```

```

!! 3 - Perform VCA with DOS and GG calculations. Essentially skips
!!      setting and calculating self-energies.

!> @param ntype - Number of different atom types
!> @param natom(ntype) - Number of different atoms (# of atoms in should
!!      be given alphabetical order; i.e. UPd2Al3 should be (3,2,1))
!> @param nse - Number of self energies
!> @param pi Mathematical value of pi
!> @param sec - Number of secular equations
!> @param small Real value considered to be "small"
!> @param title - Title from cpaper.in to be used in all output files
!> @param verbose - Logical for debugging flags (.true. = debug info on)
!> @param vlvl - Level of debugging verboseness
!-----
! Notes for future release:
!
! Some of these parameters should not be explicitly set in the global
! module and just declared to be set from one of the reading subroutines.
! This will allow for more flexibility in the future and make it easier
! to modify the code for more than just the FeSe/Te system.
!-----
implicit none
integer(kind=4) :: vlvl
integer(kind=4) :: mode
integer(kind=4), parameter :: jsz = 196 !904 ! From TB band calculation
integer(kind=4), parameter :: ntype = 2 ! Fe & Se
integer(kind=4), parameter :: natom(ntype) = (/ 2, 2 /) ! Fe = 2 , Se/Te = 2
integer(kind=4), parameter :: nse = 4*natom(2) ! s(1) + p(3) for each Se/Te
integer(kind=4), parameter :: sec = 9*2*2 !sum(natom) ! 9 (s(1) + p(3) + d(5))
logical :: verbose
real(kind=8), parameter :: pi = 4.0d0*datan(1.0d0), pp = 1.0d0/pi
real(kind=8), parameter :: small = 1.0d-20

```

```
character(len=75) :: title  
save  
end module global
```

---

```
!  
module converge  
!  
!> Module for the convergence criterion related variables  
!  
! Variables:  
!> @param cr - Convergence criterion for the real part of the  
!! Newton-Raphson procedure  
!> @param ci - Convergence criterion for the imaginary part of the  
!! Newton-Raphson procedure  
!  
implicit none  
real(kind=8) :: cr  
real(kind=8) :: ci  
save  
end module converge
```

---

```
!  
module concentration  
!  
!> Module for the concentration related variables of the CPA program  
!  
! Variables:  
!> @param con - The concentration of the first atom type (e.g.  
!! \f$FeSe_{con}Te_{1-con}\f$)  
!  
implicit none
```

```

real(kind=8) :: con
save
end module

!-----
module onsites
!-----
!> Module for the onsites parameters and related variables
!-----
! Variables:
!> @param ons(natom(2),sec) - The onsite parameters of the systems
!> @param ons_bar(sec) - Average onsite parameters between the two systems
!-----
use global
implicit none
real(kind=8) :: ons(natom(2),sec)
real(kind=8) :: ons_bar(sec)
complex(kind=8) :: onsA(nse,nse)
complex(kind=8) :: onsB(nse,nse)
complex(kind=8) :: onsAvg(nse,nse)

save
end module onsites

!-----
module hamiltonians
!-----
!> Module for hamiltonians of the two systems and related variables
!-----
! Variables:
!> @param hma(jsz,sec,sec) - Real part of initial Hamiltonian of system A
!!    (e.g. FeSe)

```

```

!> @param vsa(jsz ,sec ,sec) - Imaginary part of initial Hamiltonian of
!!    system A

!> @param hmb(jsz ,sec ,sec) - Real part of initial Hamiltonian of system B
!!    (e.g. FeTe)

!> @param vsb(jsz ,sec ,sec) - Imaginary part of initial Hamiltonian of
!!    system B

!> @param ham(jsz ,sec ,sec) - Average Hamiltonian between the two systems
!-----  

use global  

implicit none  

real(kind=8) :: hma(jsz ,sec ,sec )
real(kind=8) :: hmb(jsz ,sec ,sec )
real(kind=8) :: vsa(jsz ,sec ,sec )
real(kind=8) :: vsb(jsz ,sec ,sec )
complex(kind=8) :: ham(jsz ,sec ,sec )  

save  

end module hamiltonians  

!-----  

module green  

!-----  

!> Module for greens function matrix and related variables
!-----  

! Variables:  

!> @param grn(sec ,sec) - Green's function
!-----  

use global  

implicit none  

complex(kind=8) :: grn(sec ,sec )  

save  

end module green

```

```

!-----  

module sigma  

!-----  

!> Module for the self-energies and related variables  

!-----  

! Variables:  

!> @param sig(nse) - Self energies of the system  

!-----  

use global  

implicit none  

complex(kind=8) :: sig(nse)  

save  

end module sigma  

!-----  

module unitconvert  

!-----  

!> Module for all unit conversions  

!-----  

! Variables:  

!> @param ang2m - Angstroms to si units , meters  

!> @param bohr2ang - Atomic radius , bohrs , to angstroms  

!> @param bohr2m - Atomic radius , bohrs , to si units , meters  

!> @param eV2J - Electron volts to si units , Joules (kgm^2/s^2 or Nm)  

!> @param K2eV - Kelvin to electron volts  

!> @param u2kg - Atomic mass to si units , kilograms  

!> @param u2eVc2 - Atomic mass to electron volts per speed of light squared  

!-----  

use global  

implicit none

```

```

real(kind=8), parameter :: ang2m = 1.0d-10
real(kind=8), parameter :: bohr2ang = 0.52917721092d0
real(kind=8), parameter :: bohr2m = 0.52917721092d-11
real(kind=8), parameter :: eV_AA2kg_ss = 16.0217656d0
real(kind=8), parameter :: eV2Hz = 2.417989348d14
real(kind=8), parameter :: eV2J = 1.602176565d-18
real(kind=8), parameter :: K2eV = 8.621738d-5
real(kind=8), parameter :: K2meV = 8.621738d-2
real(kind=8), parameter :: kg_ss2eV_AA = 6.2415094d-2
real(kind=8), parameter :: meV2Hz = 2.417989348d11
real(kind=8), parameter :: Ry2ev = 13.60569253d0
real(kind=8), parameter :: u2kg = 1.660538921d-27
real(kind=8), parameter :: u2eV_c2 = 931.494061d6
real(kind=8), parameter :: uKK2eV_AA = 1.776386273d-6
real(kind=8), parameter :: uKK2eV_AA2 = 4.504401531323d-8
save
end module unitconvert

```

---

```

!> Description of function.
!> @brief
! Function for doing interpolation of the Fermi level.
!
!> @param[in] j1
!
real(kind=8) function interp(xx,x,f,j1,n)
implicit none
integer(kind=4) :: i, istart, j, j2
integer(kind=4), intent(in) :: j1, n
real(kind=8) :: fx, p
real(kind=8), intent(in) :: f(1), x(1), xx

```

```

fx = 0.0d0

istart = j1 - n + n/2 + 1

j2 = istart + n - 1

do j = istart , j2

  p = f(j)

  do i = istart , j2

    if (i.eq.j) cycle

    p = p*(xx-x(i))/(x(j)-x(i))

  end do

  fx = fx + p

end do

interp = fx

return

end function interp



---


subroutine mainn()

!> Subroutine to run the main parts of the CPA program. Specifically this
!! subroutine does the Newton-Raphson procedure, applies concentrations
!! and most of the initialization.

!> Variables:
!! del - Temperature broadening ?
!! epi - Pivot energy (helps with N-R iterations [usually around E_F])
!! eps - Imaginary part of energy shift ?
!! emax/emin - Maximum and minimum of energy window, respectively
!! sag**1 - Real and imaginary parts, respectively, of s & p initial onsite
!! parameters (should be average between two substitution atoms)
!! sig** - Real and imaginary parts, respectively, of s & p self-energies
!! sig - Complex self-energies
!! method - String used to decide which zero finding procedure to use

```

---

```

use global
use hamiltonians
use sigma
implicit none
common /d2/ emin, emax, eps, del, epiv
integer(kind=4) :: i, l, ll
integer(kind=4) :: iss, iss1, itop, ixyz, l9, m, mc, mcm, mcount, &
n, nchk, ndim, nmode, num99
integer(kind=4), parameter :: nunit = 100
logical :: mchk(nse)
real(kind=8) :: del, dnorfl, e, efl, emax, emin, epiv, eps, interp, &
nuelec, s, sagi1(nse), sagr1(nse), totvol, dos(sec+1), &
dos2(ntype, sec)
real(kind=8) :: res(20000,50), anumel(20000), dummm(20000), &
edum(20000), dums1(20000), dump1(20000), dums2(20000), dump2(20000), &
dumxz(20000), dumxy(20000), dum3r(20000), dumx2(20000), dumsA(20000), &
dumpA(20000), dumsB(20000), dumpB(20000), densfl(12), weight(jsz), &
qq(jsz,3), spec(20000,jsz)
complex(kind=8) :: sag(nse), sagcon(nse)
character(len=100) :: file1, file2, method
if (verbose) print 1000
nchk = 0; iss1 = 1; n = 0
totvol = 0.0d0
open(7, file='cpaper.out', blank='zero')
write(file1, '(A)') 'cpamat1.dat'
write(file2, '(A)') 'cpamat2.dat'
verbose = .true.; vlvl = 3
call readin(ndim, nuelec, sagr1, sagi1)
! If mode 2, program already run; Calculate superconductivity only
if (mode.eq.2) goto 9999

```

```

call setOnsites
verbose = .false.; vlvl = 2
call kpts(jsz,qq,weight,totvol)
call readSec(hma,vsa,file1)
call readSec(hmb,vsb,file2)
call setInitHam
open(9,file='green.dat',blank='zero')
1111 if(nchk.eq.2) goto 1234
sag(:) = cmplx(sagr1(:),sagi1(:),8)
if(nchk.eq.0) nmode = 1
if(nchk.eq.1) nmode = 2
if(nchk.eq.1) epiv = epiv - del
e = epiv
sig(:) = sag(:)
do ixyz = iss1, 20000
! sag(:) = cmplx(sagr1(:),sagi1(:),8)
if (mode.eq.3) goto 8888
sig(:) = sag(:)
write(method,'(A)') 'Newton'
call calcSig(weight,totvol,e,eps,mchk,numit,method,sagr1,sagi1)
if (all(mchk)) then
sag(:) = sig(:)
sagcon(:) = sagcon(:) + sig(:)
n = n + 1
! goto 9991
else ! Didn't converge so estimate with some other self-energies
do l = 1, nse
if (mchk(l).eqv..false.) then
! Estimate with average of good self-energies
! sig(l) = sagcon(l)/dble(n)
! Estimate next self-energy as the average of the good one

```

```

sag(1) = sagcon(1)/dble(n)

print *, 'Using-average-sig(1):',l, sagcon(1)/dble(n)

end if

! if (mchk(1).eq..false.) sig(1) = cmplx(sagr1(1),sagi1(1),8)

end do

print 1002

write(7,5004)e

write(*,5004)e

goto 870

end if

! nchk = nchk + 1

! goto 1111

! 9991 continue

write(7,1015)n,(sig(i),i=1,4),e

write(7,1016) (sig(i),i=5,8),e

! verbose = .true.

if (verbose) then

write(*,1015)n,(sig(i),i=1,4),e

write(*,1016) (sig(i),i=5,8),e

end if

! verbose = .false.

8888 continue

call cpaDOS(dos,dos2,spec(n,:),weight,totvol,e,eps)

! For mode 3 only, since n isn't increased without this

if (mode.eq.3) n = n + 1

res(n,1) = e

res(n,2) = dble(sig(1))

res(n,3) = aimag(sig(1))

res(n,4) = dble(sig(2))

res(n,5) = aimag(sig(2))

res(n,6) = dble(sig(3))

```

```

res(n,7) = aimag(sig(3))
res(n,8) = dble(sig(4))
res(n,9) = aimag(sig(4))
res(n,10) = dble(sig(5))
res(n,11) = aimag(sig(5))
res(n,12) = dble(sig(6))
res(n,13) = aimag(sig(6))
res(n,14) = dble(sig(7))
res(n,15) = aimag(sig(7))
res(n,16) = dble(sig(8))
res(n,17) = aimag(sig(8))
res(n,18) = dos(1) + dos(10) !Fe-s
res(n,19) = sum(dos(2:3)) + sum(dos(11:12)) !Fe-p(x,y)
res(n,20) = dos(4) + dos(13) !Fe-p(z)
res(n,21) = sum(dos(5:6)) + sum(dos(14:15)) !Fe-d(xz,yz)
res(n,22) = dos(7) + dos(16) !Fe-d(xy)
res(n,23) = dos(8) + dos(17) !Fe-d(3r^2-z^2)
res(n,24) = dos(9) + dos(18) !Fe-d(x^2+y^2)
res(n,25) = dos(19) + dos(28) !Se/Te-s
res(n,26) = sum(dos(20:21)) + sum(dos(29:30)) !Se/Te-p(x,y)
res(n,27) = dos(22) + dos(31) !Se/Te-p(z)
res(n,28) = dos2(1,19) + dos2(1,28) !Se-s
res(n,29) = sum(dos2(1,20:21)) + sum(dos2(1,29:30)) !Se-p(x,y)
res(n,30) = dos2(1,22) + dos2(1,31) !Se-p(z)
res(n,31) = dos2(2,19) + dos2(2,28) !Te-s
res(n,32) = sum(dos2(2,20:21)) + sum(dos2(2,29:30)) !Te-p(x,y)
res(n,33) = dos2(2,22) + dos2(2,31) !Te-p(z)
res(n,34) = dos(sec+1) !Total DOS
write(7,1030)e,(sig(i),i=1,4),dos(sec+1)

```

870 continue

if (nmode.eq.2) goto 51

```

e = e + del

if(e.le.emax) cycle ! next iteration of n loop

iss = n

iss1 = iss + 1

nchk = nchk + 1

goto 1111

51      e = e - del

if(e.ge.emin) cycle ! next iteration of ixyz loop

exit

end do ! End of ixyz loop

1234 continue

itop = n

open(8,file='sigma.dat')

open(9,file='spectral.dat')

write(7,3000)

write(7,3010)

l = itop + 1

19 = 0

do 11 = iss1, itop

l = l - 1

19 = 19 + 1

edum(19) = res(1,1)

dums1(19) = res(1,18)*2.0d0

dump1(19) = (res(1,19) + res(1,20))*2.0d0

dumxz(19) = res(1,21)*2.0d0

dumxy(19) = res(1,22)*2.0d0

dum3r(19) = res(1,23)*2.0d0

dumx2(19) = res(1,24)*2.0d0

dums2(19) = res(1,25)*2.0d0

dump2(19) = (res(1,26) + res(1,27))*2.0d0

dumsA(19) = res(1,28)*2.0d0

```

```

dumpA(19) = (res(1,29) + res(1,30))*2.0d0
dumsB(19) = res(1,31)*2.0d0
dumpB(19) = (res(1,32) + res(1,33))*2.0d0
dumm(19) = res(1,34)*2.0d0
write(7,3030)(res(1,m),m=1,9)
write(7,3040)(res(1,m),m=10,17)
write(8,3030)(res(1,m),m=1,9)
write(8,3040)(res(1,m),m=10,17)
write(9,3045) res(1,1),(spec(1,m),m=1,jsz)

end do

do 1 = 1, iss
  19 = 19 + 1
  edum(19) = res(1,1)
  dums1(19) = res(1,18)*2.0d0
  dump1(19) = (res(1,19) + res(1,20))*2.0d0
  dumxz(19) = res(1,21)*2.0d0
  dumxy(19) = res(1,22)*2.0d0
  dum3r(19) = res(1,23)*2.0d0
  dumx2(19) = res(1,24)*2.0d0
  dums2(19) = res(1,25)*2.0d0
  dump2(19) = (res(1,26) + res(1,27))*2.0d0
  dumsA(19) = res(1,28)*2.0d0
  dumpA(19) = (res(1,29) + res(1,30))*2.0d0
  dumsB(19) = res(1,31)*2.0d0
  dumpB(19) = (res(1,32) + res(1,33))*2.0d0
  dummm(19) = res(1,34)*2.0d0
  write(7,3030)(res(1,m),m=1,9)
  write(7,3040)(res(1,m),m=10,17)
  write(8,3030)(res(1,m),m=1,9)
  write(8,3040)(res(1,m),m=10,17)
  write(9,3045) res(1,1),(spec(1,m),m=1,jsz)

```

```

end do

close(8)

close(9)

num99 = itop - 1

call simp(edum,dumm,anumel,num99,verbose ,vlvl)

anumel(1) = 0.0d0

anumel(itop) = anumel(num99) + dumm(i ss)*del

open(8,file='dosdat.cpa.plot')

write(7,3000)

write(7,3050)

write(8,3060)

l = itop + 1

19 = 0

do ll = iss1 , itop

l = l - 1

19 = 19 + 1

res(1,35) = anumel(19)

write(7,3070) res(1,1),res(1,18),res(1,19)+res(1,20),res(1,21),&

res(1,22),res(1,23),res(1,24),res(1,25),res(1,26)+res(1,27),&

res(1,34),res(1,35),ll

write(8,3080) res(1,1),(res(1,m),m=18,24),(res(1,m),m=28,35),11

end do

do l = 1, iss

19 = 19 + 1

res(1,35) = anumel(19)

write(7,3070) res(1,1),res(1,18),res(1,19)+res(1,20),res(1,21),&

res(1,22),res(1,23),res(1,24),res(1,25),res(1,26)+res(1,27),&

res(1,34),res(1,35),l

write(8,3080) res(1,1),(res(1,m),m=18,24),(res(1,m),m=28,35),1

end do

close(8)

```

```

mcount = 0

do l = 1, itop

  if (anumel(1).gt.nuelec) then
    if (mcount.ne.0) cycle
    mcount = 1
  end if
end do

!      linear interpolation to find the fermi level

open(10,file='dosapw.itp')

write(10,1003) title

mc = mcount

mcm = mc - 1

s = nuelec

efl = interp(s,anumel,edum(1),mcm,2)

dnorfl = interp(s,anumel,dumm(1),mcm,2)/2.0d0

write(7,841)

densfl(1) = interp(s,anumel,dums1(1),mcm,2)/2.0d0
densfl(2) = interp(s,anumel,dump1(1),mcm,2)/2.0d0
densfl(3) = interp(s,anumel,dumxz(1),mcm,2)/2.0d0
densfl(4) = interp(s,anumel,dumxy(1),mcm,2)/2.0d0
densfl(5) = interp(s,anumel,dum3r(1),mcm,2)/2.0d0
densfl(6) = interp(s,anumel,dumx2(1),mcm,2)/2.0d0
densfl(7) = interp(s,anumel,dums2(1),mcm,2)/2.0d0
densfl(8) = interp(s,anumel,dump2(1),mcm,2)/2.0d0
densfl(9) = interp(s,anumel,dumsA(1),mcm,2)/2.0d0
densfl(10) = interp(s,anumel,dumpA(1),mcm,2)/2.0d0
densfl(11) = interp(s,anumel,dumsB(1),mcm,2)/2.0d0
densfl(12) = interp(s,anumel,dumpB(1),mcm,2)/2.0d0

write(7,839)

write(7,840) efl ,nuelec ,dnorfl ,( densfl(i) ,i=1,8)
write(10,842) efl ,nuelec ,dnorfl ,( densfl(i) ,i=1,12)

```

```

close(7)
close(9)
close(10)

9999 continue

call cpaGG(efl,nuelec,dnorfl,densfl)
if (verbose) print 2000

return

839  format(/,'Fermi-energy---Electrons---Total_DOS---Fe-s---Fe-p---Fe-&
--xy---Fe-xz---Fe-3r^2-z^2---Fe-x^2-y^2---Se/Te-s---Se/Te-p',//)
840  format(2f10.5      ,3x,7f10.5//)
841  format(/65x,11h (per spin)  )
842  format(15(F10.6,1x))
1000 format(/,'Begin subroutine mainn')
1001 format(/,"Didn't converge for energy",F8.5,/,"Trying",A, &
" method instead",/)
1002 format(/,"Still unable to converge . Something is wrong",/)
1003 format(A75)
1015 format(5X,I5,8F15.8,F10.6)
1016 format(10X,8F15.8,F10.6)
1030 format(/1X,F9.5,8F12.8,10X,F10.5//)
2000 format('End_mainn',/)
3000 format(1H1,///)
3010 format(20X,'Energy -Complex-self-energies -(s,-px,-py,-pz)',//)
3030 format(F9.5,3X,4(2(G12.5,1X),2X))
3040 format(12X,4(2(G12.5,1X),2X))
3045 format(1F10.6,10X,1000(F10.6,1X))
3050 format(10x,'Energy , -Fe-s , -Fe-p(x,y,z) , -Fe-d(xz,yz) , -Fe-d(xz) , -Fe-&
-d(3r^2-z^2) , -Fe-d(x^2-y^2) , -Se/Te-s , -Se/Te-p(x,y,z) , -&
-Total_DOS, -electrons , -iteration ',/)
3060 format(10x,'Energy , -Fe-s , -Fe-p(x,y) , -Fe-p(z) , -Fe-d(xz,yz) , -&
-Fe-d(xz) , -Fe-d(3r^2-z^2) , -Fe-d(x^2-y^2) , -Se-s , -Se-p(x,y) , -Se-p(z) , -&

```

```

...Te-s , ...Te-p(x,y) , ...Te-p(z) , ...TotalDOS, ...electrons , ...iteration' , /)
3070  format(2x,11f10.4,1x,i5)
3080  format(2x,16f10.4,1x,i5)
5004  format('...sigma didn't converge for e=' , f10.4, /)
end subroutine mainn

subroutine readin(nd, ne, sagr1, sagi1)
!-----!
!  Reads inputs from cpaper.dat and writes some information to output file.
!-----!
!  Variables:
!  ci/cr - Convergence criterion for real and imaginary parts of Green's
!          function, respectively
!  del - Energy shift for site ?
!  es/ep - Initial onsite s & p energies for Se ?
!  nd - # of dimension (# of secular equations; probably should remove)
!  ne - Number of electrons
!  ons(natom(2),nse) - Onsite parameters of Se and Te respectively
!-----!

use global
use converge
use concentration
use onsites
implicit none
common /d2/ emin, emax, eps, del, epiv
integer(kind=4) :: i
integer(kind=4), intent(out) :: nd
real(kind=8) :: del, epiv, eps, es, ep, emin, emax
real(kind=8), intent(out) :: ne, sagi1(nse), sagr1(nse)
character(len=500) :: modestr
if (verbose) print 1000

```

```

open(5,file='cpaper.dat',blank='zero')

read(5,1001) title
write(7,1001) title

read(5,1013) mode
read (5,*) nd,ne,cr,ci

select case (mode)

case (1)
  write(modestr,'(A)') 'Program is running in mode 1.. This will run the &
  .... CPA program in its entirety and calculate the superconductivity &
  .... properties based on the Gaspari-Gyorffy and McMillan theories &
  .... using an approximation of the Hopfield parameter using the &
  .... calculated density of states. '

case (2)
  write(modestr,'(A)') 'Program is running in mode 2.. This will only &
  .... run the cpaGG subroutine to calculate the superconductivity &
  .... properties based on the Gaspari-Gyorffy and McMillan theories &
  .... using an approximation of the Hopfield parameter using the &
  .... calculated density of states. '

case (3)
  write(modestr,'(A)') 'Program is running in mode 3.. This will run a &
  .... virtual crystal approximation (VCA) of the system with DOS and &
  .... Gaspari-Gyorffy calculations. '

case default
  write(modestr,'(A)') 'No mode was selected.. Please include a valid &
  .... mode in your input file and run the code again. '

print 1012, mode, modestr

stop

end select

write(7,1012) mode, modestr
write(7,1002) nd,ne,cr,ci

do i = 1, sec

```

```

read(5,*)ons(1,i), ons(2,i)

end do

write(7,1008)

write(7,1009)ons(1,:)

write(7,1010)

write(7,1009)ons(2,:)

read(5,*) es,ep

write(7,1004) es,ep

read(5,*) con,emin,emax,del,epiv

read(5,*) (sagr1(i), sagi1(i), i=1,nse)

write(7,1005) con,emin,emax,del,epiv,(sagr1(i), sagi1(i), i=1,nse)

read(5,*) eps

close(5)

write(7,1006) eps, jsz

write(7,1007) cr, ci

if (verbose.and.vlvl.ge.2) then

    print 1001, title

    print 1012, mode, modestr

    print 1002, nd,ne,cr,ci

    print 1008

    print 1009, ons(1,:)

    print 1010

    print 1009, ons(2,:)

    print 1004, es,ep

    print 1005, con,emin,emax,del,epiv,(sagr1(i), sagi1(i), i=1,nse)

    print 1006, eps, jsz

    print 1007, cr, ci

end if

if (con.lt.0.0d0.or.con.gt.1.0d0) then

    print 1011

stop

```

```

end if

if (verbose) print 2000

return

1000 format( /, 'Begin_subroutine_readin' )
1001 format(A75)
1002 format(I5,5X,3F10.7)
1003 format(2F9.5)
1004 format(2F15.10)
1005 format(5F10.4/2(4(2F10.4),/))
1006 format(// 'eps=_',F15.6,10X,'k-points:_',i5//)
1007 format(//, 'Convergence_criterion_(real_and_imaginary) /',2F15.9,/)
1008 format(//, 'Onsite_parameters_of_Selenium',/)
1009 format(4((9F12.8,1X),/))
1010 format(//, 'Onsite_parameters_of_Tellurium',/)
1011 format(//, 'Concentration_is_not_an_element_of_[0:1]',/, 'Check &
_cpaper.dat_and_rerun',/)
1012 format(//, 'Mode:_',I1,/,A,/)
1013 format(5X,I5)

2000 format( 'End_readin',/)

end subroutine readin

subroutine setOnsites
!_____
! Sets up the global onsite energies
!_____
! Variables:
! ons_bar(sec) - Averaged onsite energies
! f1000 - Formatting string for printing matrices verbosely
!_____
use global
use concentration

```

```

use onsites
implicit none
integer(kind=4) :: l, 11
character(len=100) :: f1000
if (verbose) print 1000
onsA(:, :) = (0.0d0, 0.0d0)
onsB(:, :) = (0.0d0, 0.0d0)
onsAvg(:, :) = (0.0d0, 0.0d0)
ons_bar(:) = (con*ons(1,:)+ (1.0d0-con)*ons(2,:))

do l = 1, sec
  if (l.ge.19.and.l.le.22) then
    l1 = l - 18
    onsA(l1,l1) = cmplx(ons(1,1),0.0d0,8)
    onsB(l1,l1) = cmplx(ons(2,1),0.0d0,8)
    onsAvg(l1,l1) = cmplx(ons_bar(1),0.0d0,8)
  else if (l.ge.28.and.l.le.31) then
    l1 = l - 23
    onsA(l1,l1) = cmplx(ons(1,1),0.0d0,8)
    onsB(l1,l1) = cmplx(ons(2,1),0.0d0,8)
    onsAvg(l1,l1) = cmplx(ons_bar(1),0.0d0,8)
  end if
end do
write(f1000, '(A,I1,A)') "(," ,nse ,"(2(F10.6,1x)))"
if (verbose.and.vlvl.ge.2) then
  print 1001
  print f1000, (onsA(1,1), l=1,nse)
  print 1002
  print f1000, (onsB(1,1), l=1,nse)
  print 1003
  print f1000, (onsAvg(1,1), l=1,nse)
end if

```

```

if (verbose) print 2000
return
1000 format( / , 'Begin_subroutine_setOnsites')
1001 format( / , 'Onsite_energies_for_system_A_that_will_be_replaced')
1002 format( / , 'Onsite_energies_for_system_B_that_will_be_replaced')
1003 format( / , 'Averaged_onsite_energies_to_be_replaced_by_self-energies')
2000 format( 'End_setOnsites' , /)
end subroutine setOnsites

subroutine kpts(kp,q,wt,swt)
!_____
! Reads in the k-point information; Direction vector, weight at given
! k-point and total weight at all k-points
!_____
! Variables:
! kp - Number of k-points
! q(kp,3) - k-point vector
! wt(kp) - Weights for each k-point
! swt - Total weight
!_____
use global
implicit none
integer(kind=4) :: i, j
integer(kind=4), intent(in) :: kp
real(kind=8), intent(out) :: q(kp,3), swt, wt(kp)
if (verbose) print 1000
swt = 0.0d0; q(:, :) = 0.0d0; wt(:) = 0.0d0
open(10, file='cpaweights.dat')
read(10,*)
do i = 1, kp
  read(10,1001)(q(i,j),j=1,3),wt(i)

```

```

swt = swt + wt(i)

end do

if (verbose.and.vlvl.ge.1) then

do i = 1, kp

print 1001, (q(i,j),j=1,3),wt(i)

end do

end if

close(10)

write(7,1002) swt

if (verbose.and.vlvl.ge.1) print 1002, swt

if (verbose) print 2000

return

1000 format( /, 'Begin_subroutine_kpts' )

1001 format(3F10.6,1X,1F10.6)

1002 format( 'sum_of_weights_is ',e16.7)

2000 format( 'End_kpts' ,/)

end subroutine kpts

subroutine readSec(h,g, fname)

!-----  

! Reads in the secular equations of the system given by the output of the  

! Static code.  

!-----  

! Variables:  

! h(jsz,sec,sec) - Real part of the Hamiltonian for each k-point  

! j(jsz,sec,sec) - Imaginary part of the Hamiltonian for each k-point  

! fname - The name of file to be read  

!  

use global

implicit none

integer(kind=4) :: i, j, k, n

```

```

real(kind=8), intent(out) :: h(jsz,sec,sec), g(jsz,sec,sec)
character(len=100), intent(in) :: fname
if (verbose) print 1000

n = sec

g(:,:,:) = 0.0d0; h(:,:, :) = 0.0d0

open(16,file=fname,blank='zero')

do i = 1, jsz
  do j = 1, 4
    read(16,*)
    if(verbose.and.vlvl.ge.5) print *, ''
  end do
  do j = 1, sec
    do k = 1, j
      read(16,1001) h(i,j,k), g(i,j,k)
      if(verbose.and.vlvl.ge.5) print 1001, h(i,j,k), g(i,j,k)
    end do
  end do
end do

!$OMP PARALLEL &
!$OMP SHARED(i, n, g, h) &
!$OMP PRIVATE(j, k)
!$OMP DO
  do j = 1, n
    do k = 1, n
      g(i,j,k) = -g(i,k,j)
      h(i,j,k) = h(i,k,j)
    end do
  end do
!$OMP END DO
!$OMP END PARALLEL
end do
close(16)

```

```

if (verbose) print 2000
return
1000 format( / , 'Begin_subroutine_readSec ')
1001 format(18X,2F15.10)
2000 format( 'End_readSec' , / )
end subroutine

subroutine setInitHam
!_____
! Sets up the initial Hamiltonian to be modified at each specific energy
!_____
! Variables:
! con - The concentration of the first atom type (e.g. FeSe_[con]Te-[1-con]
! ham(jsz,sec,sec) - Hamiltonian of the system
! H1(jsz,sec,sec) - Hamiltonian of system A
! H2(jsz,sec,sec) - Hamiltonian of system B
! f1000 - Formatting string for printing matrices verbosely
!_____
use global
use concentration
use hamiltonians
implicit none
integer(kind=4) :: i, kpts
complex(kind=8) :: H1(jsz,sec,sec), H2(jsz,sec,sec)
character(len=100) :: f1000
if (verbose) print 1000
kpts = 1
H1(:,:,:,:) = cmplx(hma(:,:,:,:),vsa(:,:,:,:),8)
H2(:,:,:,:) = cmplx(hmb(:,:,:,:),vsb(:,:,:,:),8)
ham(:,:,:,:) = (con*H1(:,:,:,:) + (1.0d0-con)*H2(:,:,:,:))
write(f1000,'(A,I1,A)' "(," ,sec ,"(2(F10.6,1x)))"

```

```

if (verbose.and.vlvl.ge.2) then
    if (vlvl.ge.3) kpts = jsz
    do i = 1, kpts
        print 1001
        print f1000, transpose(H1(i,:,:))
        print 1002
        print f1000, transpose(H2(i,:,:))
        print 1003
        print f1000, transpose(ham(i,:,:))
    end do
end if
if (verbose) print 2000
return
1000 format( /, 'Begin_subroutine_setInitHam')
1001 format( /, 'Hamiltonian_for_system_A')
1002 format( /, 'Hamiltonian_for_system_B')
1003 format( /, 'Averaged_Hamiltonian_before_complex_energy_added_and_&
    _onsite_energies_replaced_with_self-energies')
2000 format( 'End_setInitHam', /)
end subroutine setInitHam

subroutine calcSig(wt,tot,e,eps,mchk,numit,method,sagr1,sagil)
!-----
! Solves for the self-energies, and thus the Green's function, using the
! Newton-Raphson method.
!-----
! Variables:
! G(sec,sec) - Green's function
! sig(nse) - Self-energies of the disordered states
! H(jsz,sec,sec) - Hamiltonian of the system
! wt(jsz) - Weights at each k-point in the Brillouin zone

```

```

! tot - Total weight from all k-points
! dels(2) - Change in the self-energies of the disordered s states
! delp(6) - Change in the self-energies of the disordered p states
! mchk - Flag to specify whether routine converged or not
! numit - Maximum number of iterations for the procedure
! method - String used to decide which zero finding procedure to use
!
```

---

```

use global
use converge
use hamiltonians, only : ham
use sigma
implicit none
integer(kind=4) :: i, n, irep, reset(nse)
integer(kind=4), intent(in) :: numit
logical, intent(out) :: mchk(nse)
real(kind=8), intent(in) :: wt(jsz), tot, e, eps, sagr1(nse), sagil(nse)
complex(kind=8) :: del(nse), H(jsz,sec,sec), G(sec,sec), &
sigs(2,nse)
character(len=100), intent(in) :: method
reset = 0
do n = 1, numit
  if (verbose) print 1000
  del(:) = (0.0d0,0.0d0)
  write(7,1001)n,(sig(i),i=1,4)
  write(7,1002)(sig(i),i=5,8)
  if (verbose.and.vlvl.ge.1) then
    write(*,1001)n,(sig(i),i=1,4)
    write(*,1002)(sig(i),i=5,8)
  end if
  irep = 0
  mchk(:) = .false.

```

```

sigs (:,:) = (0.0d0,0.0d0)

H(:,:,:) = -ham(:,:,:)

call setHam(H,e,eps)
call greens(H,G,wt,tot)

! if (n.eq.1) then
!     write(9,1004) e, G(19,19), G(20,20), G(21,21), G(22,22), G(28,28), &
!                 G(29,29), G(30,30), G(31,31), (sig(i), i=1,4)
! end if

if (verbose.and.vlvl.ge.1) print 1008, trim(method)

select case (method)

case ('Newton')
    sigs(1,:) = sig(:)
    call newton(G,sigs(1,:),del)
case ('Fixed')
    sigs(1,:) = sig(:)
!     call fixpt(G,sigs,del)
case ('False-Position')
!     call falsi(G,del)
case ('Bisect')
!     call bisect(G,del)
case default
    sigs(1,:) = sig(:)
    call newton(G,sigs(1,:),del)
end select

sig(:) = sigs(1,:)

if (verbose.and.vlvl.ge.1) print 1003, del
do i = 1, nse
    if (abs(dble(del(i))).le.cr.and.abs(aimag(del(i))).le.ci) &
        mchk(i) = .true.
end do

if (all(mchk)) then

```

```

if (verbose.and.vlvl.ge.2) print 1005

do i = 1, nse

if (aimag(sig(i)).gt.1.0d-15) then
    irep = 1
    if (verbose.and.vlvl.ge.2) print 1006, i,abs(aimag(sig(i)))
    sig(i) = cmplx(dble(sig(i)), -aimag(sig(i)),8)
elseif (aimag(sig(i)).gt.0.0d0.and.aimag(sig(i)).lt.1.0d0-15) then
    if (verbose.and.vlvl.ge.2) print 1006, i,abs(aimag(sig(i)))
    sig(i) = cmplx(dble(sig(i)),0.0d0,8)
else
    if (verbose.and.vlvl.ge.2.and.i.eq.1) print 1007
end if
end do

else
do i = 1, nse
    if (dble(sig(i)).lt.-4.0d0*abs(sagr1(i)).or. &
        dble(sig(i)).gt.4.0d0*abs(sagr1(i))) then
        reset(i) = reset(i) + 1
        print *, 'RESET:',reset
        if (reset(i).ge.2) return
        sig(i) = cmplx(sagr1(i),sagi1(i),8)
    end if
end do
end if

if (irep.eq.1) cycle
if (all(mchk).or.n.eq.numit) then
    write(9,1004) e, G(19,19), G(20,20), G(21,21), G(22,22), G(28,28), &
    G(29,29), G(30,30), G(31,31), (sig(i), i=1,4)
    if (verbose) print 2000
    exit
end if

```

```

end do

if (verbose) print 2000

return

1000 format( /, 'Begin_subroutine_calcSig' )
1001 format( 2X, I5 , 4(F14.9,E14.6) )
1002 format( 7X, 4(F14.9,E14.6) )
1003 format( 4(2(F12.8,1X)) )
1004 format( F8.5 , 1X, 12(2(F12.8,1X)) )
1005 format( " Didn't you just converge? " )
1006 format( " Yes, but |imaginary[ sig( , I2 , )]| is greater than zero. " , &
E15.8 )
1007 format( " Yes, you are correct" )
1008 format( /, "Running ", A, " -method for finding the self-energies." , / )
2000 format( 'End_calcSig' , / )

end subroutine calcSig

subroutine setHam(H, e, eps)

!_____
! Sets up the Hiltonian to be used in the greens and cpaDOS
! subroutines
!_____
! Variables:
! H(jsz,sec,sec) - Hamiltonian of the system at specific energy level
! ons_bar(sec) - Averaged onsite energies
! sig(nse) - Self-energies for disordered states
! f1000 - Formatting string for printing matrices verbosely
!_____
use global
use concentration
use onsite, only : ons_bar
use sigma

```

```

implicit none

integer(kind=4) :: i, l, kpts
real(kind=8), intent(in) :: e, eps
complex(kind=8), intent(inout) :: H(jsz,sec,sec)
character(len=100) :: f1000
if (verbose) print 1000
do l = 1, sec
    H(:,l,1) = H(:,l,1) + cmplx(e,eps,8)
    if (mode.eq.1) then
        if (l.ge.19.and.l.le.22) then
            H(:,l,1) = H(:,l,1) - sig(1-18) + ons_bar(l)
        else if (l.ge.28.and.l.le.31) then
            H(:,l,1) = H(:,l,1) - sig(1-23) + ons_bar(l)
        end if
    end if
end do
write(f1000,'(A,I1,A)') "(",sec,")"
if (verbose.and.vlvl.ge.2) then
    if (vlvl.ge.3) kpts = jsz
    do i = 1, kpts
        print 1001
        print f1000, transpose(H(i,:,:))
    end do
end if
if (verbose) print 2000
return
1000 format(/,'Begin subroutine setHam')
1001 format(/,'Averaged Hamiltonian with complex energy added and &
onsite energies replaced with self-energies')
2000 format('End setHam',/)
end subroutine setHam

```

```

subroutine greens(H,G,wt,tot)
!-----
! Calculates Green's function for the coherent potential approximation.
!-----
! Variables:
! H(jsz,sec,sec) - Hamiltonian of the system
! wt(jsz) - Weight at the k-points
! tot - Total weight of all k-points
! G(sec,sec) - Green's function
! sig(nse) - Self-energies for disordered states
! f1000 - Formatting string for printing matrices verbosely
!-----
use global
implicit none
integer(kind=4) :: i, l, ll
real(kind=8), intent(in) :: wt(jsz), tot
complex(kind=8), intent(out) :: G(sec,sec)
complex(kind=8), intent(inout) :: H(jsz,sec,sec)
character(len=100) :: f1000
if (verbose) print 1000
G(:, :) = (0.0d0, 0.0d0)
write(f1000, '(A,I1,A)' "(," sec, "(2(F10.6,1x)))"
if (verbose.and.vlvl.ge.2) then
    print 1001
    print f1000, H(1,:,:)
end if
do i = 1, jsz
    call cmplxInv(H(i,:,:), sec, verbose, vlvl)
! this loop is only for Se/Te s & p disorder (currently)
do l = 19, 22
    ll = l + 9

```

```

G(1,1) = G(1,1) + H(i,1,1)*wt(i)
G(11,11) = G(11,11) + H(i,11,11)*wt(i)

end do

end do

G(:, :) = G(:, :) / tot

if (verbose.and.vlvl.ge.2) print f1000, G
if (verbose) print 2000

return

1000 format(/, 'Begin subroutine greens')
1001 format(/, 'Hamiltonian at first k-point (usually Gamma)')
2000 format('End greens',/)

end subroutine greens

subroutine cmplxInv(A,n,verbose,vlvl)
!-----
! Solves for the inverse of a complex square matrix of size nxn. This is
! done by using Crout's LU decomposition with partial pivoting.
!-----
! Variables:
! n - rank of matrix A
! A(n,n) - complex matrix to be inversed
! B(n,n) - Identity matrix
! p(n) - pivots for Crout's algorithm
! f**** - formatting strings
! verbose - Logical for debugging flags (.true. = debug info on)
! vlvl - Level of debugging verboseness
!-----
implicit none

integer(kind=4) :: i, p(n)
integer(kind=4), intent(in):: n, vlvl
logical, intent(in) :: verbose

```

```

complex(kind=8) :: AA(n,n), B(n,n)
complex(kind=8), intent(inout) :: A(n,n)
character(len=100) :: f1000
if (verbose) print 1000
write(f1000,"(A,I1,A)" "(,n,((2F10.5,1X)))")
AA = A; B = 0.0d0
do i = 1, n
  B(i,i) = cmplx(1.0d0,0.0d0,8)
end do
if (verbose.and.vlvl.ge.3) then
  print *, 'A-(real+imaginary)'
  print f1000, transpose(AA)
  print *, 'B'
  print f1000, transpose(B)
end if
! Do LU decomposition using Crout's algorithm with partial pivoting on A
call ccrlu(AA,n,p)
if (verbose.and.vlvl.ge.3) then
  print *, 'LU-(real+imaginary)'
  print f1000, transpose(AA)
end if
! Now use the PLU decomposition to solve for the inverse of A by columns
!$OMP PARALLEL &
!$OMP SHARED(AA, n, p, b) &
!$OMP PRIVATE(i)
!$OMP DO
do i = 1, n
  call clubk(AA,n,p,b(i,:),verbose,vlvl)
  if (verbose.and.vlvl.ge.2) then
    print *, 'b'
    print 1001, b(i,:)
  end if
end do

```

```

    end if

end do

!$OMP END DO
!$OMP END PARALLEL

! Write matrix B (inverse of A) to matrix A

A = B

if (verbose.and.vlvl.ge.2) then
    print *, 'Inverse of A'
    print f1000, A
end if

if (verbose) print 2000

return

1000 format( /, 'Begin subroutine cmplxInv')
1001 format(2F10.5)
1002 format(18X,1F15.10)
2000 format( 'End_cmplxInv', /)
end subroutine cmplxInv

subroutine ccrlu(A,n,p)

!-----
!> LU decompostion subroutine with pivots for square matrix using
!! Crout's algorithm (from rosetta code)
!-----

! Variables:
!> @param n - Rank of matrix A
!> @param A(n,n) - Complex matrix of size nxn to be decomposed
!> @param p(n) - Pivot vector
!-----

implicit none

integer(kind=4) :: i, j, k, piv
integer(kind=4), intent(in) :: n

```

```

integer(kind=4), intent(out) :: p(n)
real(kind=8), parameter :: tiny = 1.0d-15
complex(kind=8), intent(inout) :: A(n,n)
p = (/ (i, i=1, n) /)
do k = 1, n-1
    piv = k - 1 + maxloc(abs(a(p(k:),k)),1)
    if (piv.ne.k) then
        p(/k, piv/) = p(/piv, k/)
    end if
    a(p(k+1:),k) = a(p(k+1:),k)/a(p(k),k)
    ! if (a(p(k+1:),k).le.tiny) a(p(k+1:),k) = 0.0d0
    forall (j = k+1:n)
        a(p(k+1:),j) = a(p(k+1:),j)-a(p(k+1:),k)*a(p(k),j)
    ! if (a(p(k+1:),j).le.tiny) a(p(k+1:),j) = 0.0d0
    end forall
end do
return
end subroutine ccrlu

subroutine clubk(A, n, piv, b, verbose, v1v1)
!-----
!> Solves A*x = b with partial pivoting from Crout's LU
!!      [ \ f$(P*L)*U = P*A\ f$ ]
!-----
! Variables:
!> @param n - Rank of matrix A
!> @param piv(n) - Pivot vector from subroutine ccrlu
!> @param A(n,n) - Complex matrix that is decomposed by subroutine ccrlu
!> @param L(n,n) - Lower decomposition of matrix a
!> @param U(n,n) - Upper decomposition of matrix a
!> @param P(n,n) - Pivot matrix

```

```

!> @param y(n) - (U*x = y)
!> @param x(n) - Working vector (b will equal x at the end)
!> @param b(n) - Input and solution of A*x = b [ $\backslash f\$$  (P*L)*y = b  $\backslash f\$$ ]
!> @param verbose - Logical for debugging flags (.true. = debug info on)
!> @param vlvl - Level of debugging verboseness
!-----
implicit none
integer(kind=4) :: i, j, P(n,n)
integer(kind=4), intent(in) :: n, piv(n), vlvl
logical, intent(in) :: verbose
complex(kind=8) :: L(n,n), U(n,n), y(n), x(n)
complex(kind=8), intent(in) :: A(n,n)
complex(kind=8), intent(inout) :: b(n)
character(len=100) :: f1000
if (verbose) print 1000
P = 0; L = 0.0d0; U = 0.0d0; x = 0.0d0; y = 0.0d0
do i = 1, n
  P(i,i) = 1
  L(i,i) = 1.0d0
end do
do i = 1, n
  L(i,:i-1) = A(piv(i),:i-1)
end do
do i = 1, n
  U(i,i:) = A(piv(i),i:)
end do
P(:,piv) = P
b = matmul(dble(P),b)
if (verbose.and.vlvl.ge.4) then
  write(f1000,"(A,I1,A)" ) "(," ,n,") (2(F10.5,1X)))"
  print *, 'P'

```

```

print f1000, transpose(dble(P))

print *, 'L'

print f1000, transpose(L)

print *, 'U'

print f1000, transpose(U)

print *, 'b'

print 1001, b

end if

y(1) = b(1)/L(1,1)

do i = 2, n

y(i) = b(i)/L(i,i)

do j = 1, i-1

y(i) = y(i) - L(i,j)*y(j)/L(i,i)

end do

end do

if (verbose.and.vlvl.ge.3) then

print *, 'y'

print 1001, y

end if

x(n) = y(n)/U(n,n)

do i = n-1, 1, -1

x(i) = y(i)/U(i,i)

do j = i+1, n

x(i) = x(i) - U(i,j)*x(j)/U(i,i)

end do

end do

if (verbose.and.vlvl.ge.2) then

print *, 'x'

print 1001, x

end if

b = x

```

```

if (verbose) print 2000
1000 format(/,'Begin subroutine clubk')
1001 format(2F10.5)
2000 format('End.clubk',/)
end subroutine clubk

subroutine newton(G,sig,del)
!-----
! Sets up the matrices to be inverted for the elements that have a self-
! energy
!-----
! Variables:
! dels(2) - Change in the s states
! delp(6) - Change in the p states
! G(sec,sec) - Green's function calculated from greens subroutine
! ge(nse,nse) - Diagonally reduced Green's matrix
! usi(nse,nse) - Diagonally reduced self-energy matrix
! up(nse,nse) - Matrix of ge*usi
! su(nse,nse) - Matrix to be inverted
! term(nse,nse) - Final matrix with concentrations. Results are the changes
! in states (del**)
! ons(2,sec) - All onsite parameters for Se and Te
! Se/Te(nse,nse) - Complex versions of onsite matices for calculations
!-----
use global
use concentration
use onsites
implicit none
integer(kind=4) :: l
complex(kind=8) :: ge(nse), term(nse), F(nse), dF(nse), alpha(nse), &
beta(nse)

```

```

complex(kind=8), intent(in) :: G(sec,sec)
complex(kind=8), intent(out) :: del(nse)
complex(kind=8), intent(inout) :: sig(nse)

if (verbose) print 1000

del(:) = (0.0d0,0.0d0)
!delp(:) = (0.0d0,0.0d0)

if(verbose.and.vlvl.ge.1) print 1001, sig
ge(1) = G(19,19)
ge(2) = G(20,20)
ge(3) = G(21,21)
ge(4) = G(22,22)
ge(5) = G(28,28)
ge(6) = G(29,29)
ge(7) = G(30,30)
ge(8) = G(31,31)

do l = 1, nse

alpha(l) = 1.0d0 - onsB(l,1)*ge(l) - onsA(l,1)*ge(l)
beta(l) = ge(l)*onsA(l,1)*onsB(l,1) - onsAvg(l,1)
F(l) = ge(l)*sig(l)**2.0d0 + alpha(l)*sig(l) + beta(l)
dF(l) = alpha(l) + 2.0d0*ge(l)*sig(l)
term(l) = sig(l) - F(l)/dF(l)
del(l) = sig(l) - term(l)

end do

!dels(1) = sig(1) - term(1)
!dels(2) = sig(5) - term(5)
!delp(1) = sig(2) - term(2)
!delp(2) = sig(3) - term(3)
!delp(3) = sig(4) - term(4)
!delp(4) = sig(6) - term(6)
!delp(5) = sig(7) - term(7)
!delp(6) = sig(8) - term(8)

```

```

!verbose = .true.; vlvl = 3
if(verbose.and.vlvl.ge.1) then
  if(vlvl.ge.2) then
    print 1004
    print 1003, F(:)
    print 1003, dF(:)
    print 1003, term(:)
    print 1003, -alpha(:)/(2.0d0*ge(:))
  end if
  print 1002, del
end if
!verbose = .false.; vlvl = 3
do l = 1, nse
  sig(l) = term(l)
end do
if(verbose.and.vlvl.ge.1) print 1001, sig
if(verbose) print 2000
return
1000 format(/,'Begin subroutine newton')
1001 format('Sigma: ',/4(2(F10.6,1X)))
1002 format('Delta_sig: ',/4(2(E12.5,2X)))
1003 format(/,8(2F10.6,1x),/)
1004 format(/,'F, dF, term')
2000 format('End newton',/)
end subroutine newton

subroutine cpaDOS(dos,dos2,spec,w,tot,e,eps)
!_____
! Solves for the DOS of the system.
!_____
! Variables:

```

```

! w(jsz) - Weights at each k-point
! tot - Total weight
! dos(sec+1) - Total and decomposed DOS of the system
! H(jsz,sec,sec) - Working Hamiltonian matrix
! f1000 - Formatting string for printing matrices verbosely
!-----

use global
use hamiltonians
use onsites
use sigma
implicit none
integer(kind=4) :: i, l, 12
real(kind=8) :: gr(sec,sec), gi(sec,sec)
real(kind=8), intent(in) :: w(jsz), tot, e, eps
real(kind=8), intent(out) :: dos(sec+1), dos2(ntype,sec), spec(jsz)
complex(kind=8) :: H(jsz,sec,sec)
character(len=100) :: f1000
if (verbose) print 1000
dos(:) = 0.0d0
dos2(:, :) = 0.0d0
spec(:) = 0.0d0
H(:, :, :) = -ham(:, :, :)
call setHam(H, e, eps)
write(f1000, '(A,I1,A)') "(,sec,"(2(F10.6,1x)))"
if (verbose.and.vlvl.ge.3) then
    print *, 'H:'
    print f1000, transpose(H(1,:,:))
end if
do i = 1, jsz
    call cmplxInv(H(i,:,:), sec, verbose, vlvl)
    gr(:, :) = dble(H(i,:,:))

```

```

gi (:,:) = aimag(H(i,:,:))

do l = 1, sec

dos(l) = dos(l) - pp*w(i)/tot*gi(l,l)

spec(i) = spec(i) - pp*gi(l,l)

if (((l.ge.19.and.l.le.22).or.(l.ge.28.and.l.le.31)).and.mode.eq.1) then

  if (l.ge.19.and.l.le.22) l2 = l - 18
  if (l.ge.28.and.l.le.31) l2 = l - 23

dos2(1,l) = dos2(1,l) - pp*w(i)/tot*(gr(1,l)*aimag(sig(l2))+ &
gi(1,l)*dble(sig(l2))-gi(1,l)*ons(2,l))/(ons(1,l)-ons(2,l))
dos2(2,l) = dos2(2,l) - pp*w(i)/tot*(gr(1,l)*aimag(sig(l2))+ &
gi(1,l)*dble(sig(l2))-gi(1,l)*ons(1,l))/(ons(2,l)-ons(1,l))

else if (((l.ge.19.and.l.le.22).or.(l.ge.28.and.l.le.31)) &
.and.mode.eq.3) then

dos2(1,l) = dos2(1,l) -pp*w(i)/tot*gi(1,l)

end if

end do

end do

dos(sec+1) = sum(dos(1:sec))

if (verbose.and.vlvl.ge.1) then

print 1001, e, dos(:)
print 1003, e, dos2(1,:)
print 1004, e, dos2(2,:)
print 1005, e, spec(:)

end if

print 1002, e, dos(sec+1)

if (verbose) print 2000

1000 format(/,'Start subroutine cpaDOS')
1001 format('DOS_for_energy',F10.6,':',/,37F10.6)
1002 format('DOS_for_energy',F10.6,':',5X,F10.6)
1003 format("Atom_type_1's_DOS_for_energy",F10.6,':',/,37F10.6)
1004 format("Atom_type_2's_DOS_for_energy",F10.6,':',/,37F10.6)

```

```

1005 format("Spectral_function_for_energy",F10.6,:"/,904F10.6)
2000 format('End_cpaDOS',/)
end subroutine cpaDOS

subroutine simp(xx, fx, ax, nx, verbose, vlvl)
!-----
! Need to verify the purpose of this subroutine.
!-----
! Variables:
! verbose - Logical for debugging flags (.true. = debug info on)
! vlvl - Level of debugging verboseness
!-----
implicit none
integer(kind=4) :: ix
integer(kind=4), intent(in) :: nx, vlvl
logical :: verbose
real(kind=8) :: delx
real(kind=8), intent(in) :: fx(2000), xx(2000)
real(kind=8), intent(out) :: ax(2000)
if (verbose) print 1000
delx = xx(2) - xx(1)
ax(1) = 0.0d0
do ix = 2, nx, 2
  select case(nx-ix)
    case(0)
      ax(nx) = delx*(-fx(nx-2)+8.0d0*fx(nx-1)+5.0d0*fx(nx))/12.0d0 &
      + ax(nx-1)
    return
    case default
      ax(ix) = delx*(5.0d0*fx(ix-1)+8.0d0*fx(ix)-fx(ix+1))/12.0d0 &
      + ax(ix-1)
  end select
end do

```

```
    ax(ix+1) = delx*(fx(ix-1)+4.0d0*fx(ix)+fx(ix+1))/3.0d0 + ax(ix-1)

end select

end do

if (verbose.and.vlvl.ge.2) print 1002, ax

if (verbose) print 2000

return

1000 format( /, 'Begin_subroutine_simp' )

1002 format('Electrons',F10.7)

2000 format('End_simp',/)

end subroutine simp
```

## Bibliography

## Bibliography

- [1] J. Bardeen, L. N. Cooper, and J. R. Schrieffer, “Theory of Superconductivity,” *Phys. Rev.*, vol. 108, pp. 1175–1204, Dec. 1957.
- [2] J. G. Bednorz and K. A. Müller, “Possible high T<sub>c</sub> superconductivity in the BaLaCuO system,” *Zeitschrift für Phys. B Condens. Matter*, vol. 64, pp. 189–193, June 1986.
- [3] M. Mehl and D. Papaconstantopoulos, “Applications of a tight-binding total-energy method for transition and noble metals: Elastic constants, vacancies, and surfaces of monatomic metals,” *Phys. Rev. B*, vol. 54, pp. 4519–4530, Aug. 1996.
- [4] A. Subedi, L. Zhang, D. Singh, and M. Du, “Density functional study of FeS, FeSe, and FeTe: Electronic structure, magnetism, phonons, and superconductivity,” *Phys. Rev. B*, vol. 78, p. 134514, Oct. 2008.
- [5] D. Louca, K. Horigane, A. Llobet, R. Arita, S. Ji, N. Katayama, S. Konbu, K. Nakamura, T.-Y. Koo, P. Tong, and K. Yamada, “Local atomic structure of superconducting FeSe- $\{1x\}$ Te- $\{x\}$ ,” *Phys. Rev. B*, vol. 81, p. 134524, Apr. 2010.
- [6] T. Bazhirov and M. L. Cohen, “Spin-resolved electron-phonon coupling in FeSe and KFe<sub>2</sub>Se<sub>2</sub>,” *Phys. Rev. B*, vol. 86, no. 134517, pp. 1–8, 2012.
- [7] W. Kohn and L. J. Sham, “Self-Consistent Equations Including Exchange and Correlation Effects,” *Phys. Rev.*, vol. 140, pp. A1133–A1138, Nov. 1965.
- [8] J. Slater, “An Augmented Plane Wave Method for the Periodic Potential Problem,” *Phys. Rev.*, vol. 92, pp. 603–608, Nov. 1953.
- [9] L. Hedin and B. I. Lundqvist, “Explicit local exchange-correlation potentials,” *J. Phys. C Solid State Phys.*, vol. 4, pp. 2064–2083, Oct. 1971.
- [10] M. Born and R. Oppenheimer, “Zur Quantentheorie der Moleküle,” *Ann. Phys.*, vol. 389, no. 20, pp. 457–484, 1927.
- [11] A. P. Koufos and D. A. Papaconstantopoulos, “Electronic structure of francium,” *Int. J. Quantum Chem.*, vol. 113, pp. 2070–2077, Sept. 2013.
- [12] J. Slater, “Wave Functions in a Periodic Potential,” *Phys. Rev.*, vol. 51, pp. 846–851, May 1937.
- [13] O. K. Andersen, “Linear methods in band theory,” *Phys. Rev. B*, vol. 12, pp. 3060–3083, Oct. 1975.

- [14] F. Birch, “Finite strain isotherm and velocities for single-crystal and polycrystalline NaCl at high pressures and 300K,” *J. Geophys. Res.*, vol. 83, no. B3, p. 1257, 1978.
- [15] M. J. Mehl, B. M. Klein, and D. A. Papaconstantopoulos, “First-Principles Calculation of Elastic Properties.pdf,” in *Intermet. Compounds Vol. 1, Princ.* (J. H. Westbrook and R. L. Fleischer, eds.), pp. 195–210, John Wiley and Sons, 1994.
- [16] G. Lehmann and M. Taut, “On the Numerical Calculation of the Density of States and Related Properties,” *Phys. Status Solidi*, vol. 54, pp. 469–477, Dec. 1972.
- [17] M. J. Gillan, “Calculation of the vacancy formation energy in aluminium,” *J. Phys. Condens. Matter*, vol. 1, pp. 689–711, Jan. 1989.
- [18] G. Sprouse, L. Orozco, J. Simsarian, and W. Zhao, “Laser-trapped francium, a new laboratory for precision measurements,” *Nucl. Phys. A*, vol. 630, pp. 316–320, Feb. 1998.
- [19] M. Sigalas, N. Bacalis, D. Papaconstantopoulos, M. Mehl, and A. Switendick, “Total-energy calculations of solid H, Li, Na, K, Rb, and Cs,” *Phys. Rev. B*, vol. 42, pp. 11637–11643, Dec. 1990.
- [20] D. Papaconstantopoulos and D. Singh, “Reply to Comment on Total-energy calculations of solid H, Li, Na, K, Rb, and Cs ,” *Phys. Rev. B*, vol. 45, pp. 7507–7508, Apr. 1992.
- [21] S.-h. Wei and H. Krakauer, “Local-Density-Functional Calculation of the Pressure-Induced Metallization of BaSe and BaTe,” *Phys. Rev. Lett.*, vol. 55, pp. 1200–1203, Sept. 1985.
- [22] D. Singh, “Ground-state properties of lanthanum: Treatment of extended-core states,” *Phys. Rev. B*, vol. 43, pp. 6388–6392, Mar. 1991.
- [23] C. Kittel, *Introduction to solid state physics*. John Wiley and Sons, 2005.
- [24] L. Shi and D. Papaconstantopoulos, “Theoretical predictions of superconductivity in alkali metals under high pressure,” *Phys. Rev. B*, vol. 73, p. 184516, May 2006.
- [25] K. Herzfeld, “On Atomic Properties which make an Element a Metal,” *Phys. Rev.*, vol. 29, pp. 701–705, May 1927.
- [26] K. Goettel, J. Eggert, I. Silvera, and W. Moss, “Optical Evidence for the Metallization of Xenon at 132(5) GPa,” *Phys. Rev. Lett.*, vol. 62, pp. 665–668, Feb. 1989.
- [27] M. Eremets, E. Gregoryanz, V. Struzhkin, H. Mao, R. Hemley, N. Mulders, and N. Zimmerman, “Electrical conductivity of xenon at megabar pressures,” *Phys. Rev. Lett.*, vol. 85, pp. 2797–800, Sept. 2000.
- [28] L. Veeser, C. Ekdahl, H. Oona, P. Rodriguez, G. Schmitt, J. Solem, S. Younger, S. Baker, C. Hudson, W. Lewis, B. Marshall, W. Turley, A. Bykov, G. Boriskov, M. Dolotenko, N. Egorov, N. Kolokolchikov, M. Kozlov, Y. Kuropatkin, and A. Volkov,

- “Isentropic Compression of Argon and Krypton Using an MC-1 Flux Compression Generator,” in *Megagauss Magn. F. Gener. its Appl. to Sci. Ultra-High Pulsed-Power Technol. - Proc. VIIIf Int. Conf. Megagauss Magn. F. Gener. Relat. Top.*, (Singapore), pp. 237–240, World Scientific Publishing Co. Pte. Ltd., 2004.
- [29] A. Polian, J. Itie, E. Dartige, A. Fontaine, and G. Tourillon, “X-ray absorption spectroscopy on solid krypton up to 20 GPa,” *Phys. Rev. B*, vol. 39, no. 5, pp. 3369–3373, 1989.
  - [30] A. K. McMahan, “Structural transitions and metallization in compressed solid argon,” *Phys. Rev. B*, vol. 33, pp. 5344–5349, Apr. 1986.
  - [31] J. Boettger, “Equation of state and metallization of neon,” *Phys. Rev. B*, vol. 33, no. 8, pp. 6788–6791, 1986.
  - [32] E. V. Zarochentsev and E. P. Troitskaya, “Equation of state of rare-gas crystals near their metallization,” *Phys. Solid State*, vol. 43, pp. 1345–1352, July 2001.
  - [33] I. Kwon, L. Collins, J. Kress, and N. Troullier, “First-principles study of solid Ar and Kr under high compression,” *Phys. Rev. B*, vol. 52, pp. 15165–15169, Dec. 1995.
  - [34] J. Hama and K. Suito, “Equation of state and metallization in compressed solid krypton,” *Phys. Lett. A*, vol. 140, pp. 117–121, Sept. 1989.
  - [35] H. Chacham, X. Zhu, and S. Louie, “Pressure-induced insulator-metal transitions in solid xenon and hydrogen: A first-principles quasiparticle study,” *Phys. Rev. B*, vol. 46, pp. 6688–6699, Sept. 1992.
  - [36] R. Reichlin, K. Brister, A. McMahan, M. Ross, S. Martin, Y. Vohra, and A. Ruoff, “Evidence for the Insulator-Metal Transition in Xenon from Optical, X-Ray, and Band-Structure Studies to 170 GPa,” *Phys. Rev. Lett.*, vol. 62, pp. 669–672, Feb. 1989.
  - [37] T. M. McQueen, Q. Huang, V. Ksenofontov, C. Felser, Q. Xu, H. Zandbergen, Y. S. Hor, J. Allred, a. J. Williams, D. Qu, J. Checkelsky, N. P. Ong, and R. J. Cava, “Extreme sensitivity of superconductivity to stoichiometry in Fe- $\{1+\delta\}$ Se,” *Phys. Rev. B*, vol. 79, p. 014522, Jan. 2009.
  - [38] S. Medvedev, T. M. McQueen, I. a. Troyan, T. Palasyuk, M. I. Eremets, R. J. Cava, S. Naghavi, F. Casper, V. Ksenofontov, G. Wortmann, and C. Felser, “Electronic and magnetic phase diagram of beta-Fe(1.01)Se with superconductivity at 36.7 K under pressure.,” *Nat. Mater.*, vol. 8, pp. 630–3, Aug. 2009.
  - [39] Y. Mizuguchi, F. Tomioka, S. Tsuda, T. Yamaguchi, and Y. Takano, “Superconductivity at 27 K in tetragonal FeSe under high pressure,” *Appl. Phys. Lett.*, vol. 93, no. 15, p. 8, 2008.
  - [40] P. Diko, V. Antal, V. Kavečansky, C. Yang, and I. Chen, “Microstructure and phase transformations in FeSe superconductor,” *Phys. C Supercond.*, vol. 476, pp. 29–31, June 2012.
  - [41] P. P. Ewald and C. Hermann, *Strukturbericht, 1913-1928*,. Leipzig, Akademische Verlagsgesellschaft, 1931.

- [42] a. Yamasaki, Y. Matsui, S. Imada, K. Takase, H. Azuma, T. Muro, Y. Kato, a. Higashiyama, a. Sekiyama, S. Suga, M. Yabashi, K. Tamasaku, T. Ishikawa, K. Terashima, H. Kobori, a. Sugimura, N. Umeyama, H. Sato, Y. Hara, N. Miyagawa, and S. I. Ikeda, “Electron correlation in the FeSe superconductor studied by bulk-sensitive photoemission spectroscopy,” *Phys. Rev. B*, vol. 82, p. 184511, Nov. 2010.
- [43] P. P. Singh, “Effects of disorder in FeSe: an ab initio study.,” *J. Phys. Condens. Matter*, vol. 22, p. 135501, Apr. 2010.
- [44] R. S. Kumar, Y. Zhang, S. Sinogeikin, Y. Xiao, S. Kumar, P. Chow, A. L. Cornelius, and C. Chen, “Crystal and electronic structure of FeSe at high pressure and low temperature.,” *J. Phys. Chem. B*, vol. 114, pp. 12597–606, Oct. 2010.
- [45] V. Ksenofontov, G. Wortmann, and A. Chumakov, “Density of phonon states in superconducting FeSe as a function of temperature and pressure,” *Phys. Rev. B*, vol. 81, no. 18, p. 184510, 2010.
- [46] M. J. Winiarski, M. Samsel-Czekaa, and A. Ciechan, “Strain effects on the electronic structure of the iron selenide superconductor,” *EPL (Europhysics Lett.)*, vol. 100, p. 47005, Nov. 2012.
- [47] A. P. Koufos, D. A. Papaconstantopoulos, and M. J. Mehl, “First-principles study of the electronic structure of iron-selenium: Implications for electron-phonon superconductivity,” *Phys. Rev. B*, vol. 89, p. 035150, Jan. 2014.
- [48] a. S. Panfilov, V. a. Pashchenko, G. E. Grechnev, V. a. Desnenko, a. V. Fedorchenco, a. G. Grechnev, a. N. Bludov, S. L. Gnatchenko, D. a. Chareev, E. S. Mitrofanova, and a. N. Vasiliev, “Interplay of superconductivity and magnetism in  $\text{FeSe}_{1-x}\text{Te}_x$  compounds. Pressure effects,” *ArXiv*, p. 7, Nov. 2013.
- [49] P. Blaha, K. Schwarz, G. Madsen, D. Kvasnicka, and J. Luitz, “WIEN2k, An Augmented Plane Wave + Local Orbitals Program for Calculating Crystal Properties,” 2001.
- [50] J. P. Perdew, K. A. Jackson, M. R. Pederson, D. J. Singh, and C. Fiolhais, “Atoms, molecules, solids, and surfaces: Applications of the generalized gradient approximation for exchange and correlation,” *Phys. Rev. B*, vol. 46, pp. 6671–6687, Sept. 1992.
- [51] D. Papaconstantopoulos, L. Boyer, B. Klein, A. Williams, V. Moruzzi, and J. Janak, “Calculations of the superconducting properties of 32 metals with Z49,” *Phys. Rev. B*, vol. 15, pp. 4221–4226, May 1977.
- [52] G. Gaspari and B. Gyorffy, “Electron-Phonon Interactions, d Resonances, and Superconductivity in Transition Metals,” *Phys. Rev. Lett.*, vol. 28, pp. 801–805, Mar. 1972.
- [53] R. W. Gómez, V. Marquina, J. L. Pérez-Mazariego, R. Escamilla, R. Escudero, M. Quintana, J. J. Hernández-Gómez, R. Ridaura, and M. L. Marquina, “Effects of Substituting Se with Te in the FeSe Compound: Structural, Magnetization and Mössbauer Studies,” *J. Supercond. Nov. Magn.*, vol. 23, pp. 551–557, Mar. 2010.

- [54] S. Chandra and a.K.M.a. Islam, “Elastic properties of mono- and poly-crystalline PbO-type FeSe<sub>1+x</sub>Te<sub>x</sub> (x=01.0): A first-principles study,” *Phys. C Supercond.*, vol. 470, pp. 2072–2075, Dec. 2010.
- [55] P. E. Blöchl, “Projector augmented-wave method,” *Phys. Rev. B*, vol. 50, pp. 17953–17979, Dec. 1994.
- [56] R. S. Kumar, Y. Zhang, S. Sinogeikin, Y. Xiao, S. Kumar, P. Chow, A. L. Cornelius, and C. Chen, “Crystal and electronic structure of FeSe at high pressure and low temperature.,” *J. Phys. Chem. B*, vol. 114, pp. 12597–606, Oct. 2010.
- [57] B. Joseph, a. Iadecola, a. Puri, L. Simonelli, Y. Mizuguchi, Y. Takano, and N. L. Saini, “Evidence of local structural inhomogeneity in FeSe<sub>{1x}</sub>Te<sub>{x}</sub> from extended x-ray absorption fine structure,” *Phys. Rev. B*, vol. 82, p. 020502, July 2010.
- [58] R. Hu, E. S. Bozin, J. B. Warren, and C. Petrovic, “Superconductivity, magnetism, and stoichiometry of single crystals of Fe<sub>{1+y}</sub>(Te<sub>{1x}</sub>S<sub>{x}</sub>)<sub>{z}</sub>,” *Phys. Rev. B*, vol. 80, p. 214514, Dec. 2009.
- [59] D. M. Finlayson, D. Greig, J. P. Llewellyn, and T. Smith, “Some Electrical Characteristics of Single Crystal Iron Monotelluride,” *Proc. Phys. Soc. Sect. B*, vol. 69, pp. 860–862, Aug. 1956.
- [60] J.-E. Jørgensen, J. S. Olsen, and L. Gerward, “Compressibility of Fe 1.087 Te: a high pressure X-ray diffraction study,” *High Press. Res.*, vol. 31, pp. 603–610, Dec. 2011.
- [61] W. McMillan, “Transition Temperature of Strong-Coupled Superconductors,” *Phys. Rev.*, vol. 167, pp. 331–344, Mar. 1968.
- [62] J. Hopfield, “Angular Momentum and Transition-Metal Superconductivity,” *Phys. Rev.*, vol. 186, pp. 443–451, Oct. 1969.
- [63] V. Moruzzi, J. Janak, and K. Schwarz, “Calculated thermal properties of metals,” *Phys. Rev. B*, vol. 37, pp. 790–799, Jan. 1988.
- [64] T. Bazhirov, J. Noffsinger, and M. L. Cohen, “Superconductivity and electron-phonon coupling in lithium at high pressures,” *Phys. Rev. B*, vol. 82, p. 184509, Nov. 2010.
- [65] Z. M. Stadnik, P. Wang, J. Zukrowski, T. Noji, and Y. Koike, “A Mössbauer effect study of single crystals of the non-superconducting parent compound Fe1.09Te and the superconductor FeSe0.4Te0.6.,” *J. Phys. Condens. Matter*, vol. 25, p. 416008, Oct. 2013.
- [66] F.-C. Hsu, J.-Y. Luo, K.-W. Yeh, T.-K. Chen, T.-W. Huang, P. M. Wu, Y.-C. Lee, Y.-L. Huang, Y.-Y. Chu, D.-C. Yan, and M.-K. Wu, “Superconductivity in the PbO-type structure alpha-FeSe.,” *Proc. Natl. Acad. Sci. U. S. A.*, vol. 105, pp. 14262–4, Sept. 2008.
- [67] G. F. Chen, Z. G. Chen, J. Dong, W. Z. Hu, G. Li, X. D. Zhang, P. Zheng, J. L. Luo, and N. L. Wang, “Electronic properties of single-crystalline Fe<sub>{1.05}</sub>Te and Fe<sub>{1.03}</sub>Se<sub>{0.30}</sub>Te<sub>{0.70}</sub>,” *Phys. Rev. B*, vol. 79, p. 140509, Apr. 2009.

- [68] D. A. Papaconstantopoulos, M. J. Mehl, and M. D. Johannes, “Tight-binding Hamiltonian for LaOFeAs,” *Phys. Rev. B*, vol. 82, pp. 054503–1 – 054503–6, Aug. 2010.
- [69] I. Mazin, D. Singh, M. Johannes, and M. Du, “Unconventional Superconductivity with a Sign Reversal in the Order Parameter of  $\text{LaFeAsO}_{\{1-x\}}\text{F}_{\{x\}}$ ,” *Phys. Rev. Lett.*, vol. 101, no. 5, pp. 057003–1 – 057003–4, 2008.
- [70] L. Boeri, O. V. Dolgov, and a. a. Golubov, “Is  $\text{LaFeAsO}_{\{1-x\}}\text{F}_{\{x\}}$  an Electron-Phonon Superconductor?,” *Phys. Rev. Lett.*, vol. 101, p. 026403, July 2008.
- [71] H. Takahashi, K. Igawa, K. Arii, Y. Kamihara, M. Hirano, and H. Hosono, “Superconductivity at 43 K in an iron-based layered compound  $\text{LaO}(1-x)\text{F}(x)\text{FeAs.}$ ,” *Nature*, vol. 453, pp. 376–8, May 2008.
- [72] J. C. Slater and G. F. Koster, “Simplified LCAO Method for the Periodic Potential Problem,” *Phys. Rev.*, vol. 94, pp. 1498–1524, June 1954.
- [73] R. S. Mulliken, “Bonding Power of Electrons and Theory of Valence.,” *Chem. Rev.*, vol. 9, pp. 347–388, Dec. 1931.
- [74] W. B. Jensen, “The Origin of the Sigma, Pi, Delta Notation for Chemical Bonds,” *J. Chem. Educ.*, vol. 90, pp. 802–803, June 2013.
- [75] K. Ohno, K. Esfarjani, and Y. Kawazoe, *Computational Materials Science*, vol. 129 of *Springer Series in Solid-State Sciences*. Berlin, Heidelberg: Springer Berlin Heidelberg, 1999.
- [76] P. Soven, “Coherent-Potential Model of Substitutional Disordered Alloys,” *Phys. Rev.*, vol. 156, pp. 809–813, Apr. 1967.
- [77] P. L. DeVries, *A First Course in Computational Physics*. John Wiley and Sons, 2010.
- [78] T. J. Ypma, “Historical Development of the NewtonRaphson Method,” *SIAM Rev.*, vol. 37, pp. 531–551, Dec. 1995.

# Curriculum Vitae

**Alexander Philip Koufos** was born in Reston, Virginia, and graduated from George Mason University with a B.S. degree in Physics and Mathematics in 2008. He earned his M.S. in Computational Sciences from George Mason University in 2010. In 2014, he acquired his Ph.D. in Computational Sciences and Informatics also from George Mason University. During his time at the university, he was held various leadership roles in clubs, societies, and student organizations. He was also a fellow of the George Mason University (GMU) National Science Foundation (NSF) Graduate STEM Fellows in K-12 Education (GK-12) Program, known as SUNRISE: Schools, University 'N'(and) Resources.

His areas of expertise are in computational solid state physics and include band structure calculations and theory of superconductivity. He is proficient in Fortran and python, modifying and creating computational programs to perform band structure calculations. He has experience in Density Functional Theory programs, such as Wien2k and Elk. He is also an expert in the Naval Research Laboratory suite of band structure programs, including the NRL-Tight-Binding and NRL-Linearized Augmented Plane Wave codes.

## Education

Ph.D., *Computational Sciences and Informatics* George Mason University, 2014  
M.S., *Computational Sciences (concentration in computational materials and chemical sciences)* George Mason University, 2010  
B.S., *Physics and Mathematics (concentrations in atomic physics and applied mathematics)* George Mason University, 2008

## Academic Positions

Graduate Research Assistant - George Mason University Aug. 2008–May 2009  
Graduate Research Fellow (NSF GK-12 SUNRISE Fellowship) - George Mason University Jun. 2009–May 2011  
Graduate Research Assistant - George Mason University Jun. 2011–Dec 2014

## Refereed Journal Publications

1. Koufos, A. P. and Papaconstantopoulos, D. *Electronic Structure of Francium*, International Journal of Quantum Chemistry, 113 pg. 2070-2077 (2013)
2. Koufos, A. P., Papaconstantopoulos, D., and Mehl, M. *First-principles study of the electronic structure of iron-selenium: Implications for electron-phonon superconductivity*, Physical Review B 89, 035150 (2014)

**Research Presentations**

American Physical Society March Meeting (New Orleans, LA) - Poster Presentation (2008)  
George Mason University–William and Mary REU Conference (Fairfax, VA) - Oral and Poster Presentation (2008)

American Physical Society March Meeting (Portland, OR) - Oral Presentation #X15.015 (2010)

NRL-GMU Mini Conference (Fairfax, VA) - Poster Presentation (2011)

Electronic Structure Workshop - ES2013 (Williamsburg, VA) - Poster Presentation (2013)

**Leadership Positions**

GMU Physics Club - Treasurer (2003)

GMU Physics Club - Vice President (2004)

GMU SPACS Graduate Student Association - Co-Founder and Treasurer (2011–2012)

GMU COS Graduate Student Association - Co-Founder (2012–2013)

**Professional Society Memberships**

American Physical Society

American Astronomical Society

National Society of Collegiate Scholars